

**Laser Forming of Metal Foam:
Mechanisms, Efficiency and Prediction**

Tizian Bucher

**Submitted in partial fulfillment of the
requirements for the degree of
Doctor of Philosophy
in the Graduate School of Arts and Sciences**

COLUMBIA UNIVERSITY

2019

ABSTRACT

Laser Forming of Metal Foam: Mechanisms, Efficiency, and Prediction

Tizian Bucher

This thesis deals with metal foam, a relatively new material whose tremendous potential has been identified early on. The material is an excellent shock absorber and also has a very high strength-to-weight ratio, properties that are highly desirable particularly within the aerospace and automotive industries. Despite the material's immense potential, hardly any metal foam products have made it past the prototype stage. The reason is that the material is difficult to manufacture in the shapes required in industrial applications. Oftentimes, applications require sheets to be bent into specific shapes, yet bending is not possible with conventional methods. Laser forming is currently the only method that shows promise to bend metal foam panels to a range of shapes.

In this thesis, the analysis of laser forming of metal foam was taken far beyond the experimental work that has been delivered thus far. A thorough analysis was performed of the thermo-mechanical bending mechanism that governs the deformation of metal foam during laser forming. This knowledge was then used to explain the effect of the process condition on the bending efficiency and the bending limit. Additionally, the impact of laser forming on the metal foam properties was explored. Experimental results were complemented by numerical results that were validated both thermally (using infrared imaging) as well as mechanically (using digital image correlation). Numerical models with different levels of geometrical complexities were used, and the effect of the model geometry on the predictive accuracy was explored.

In the second half of the thesis, the aforementioned effort was extended to metal foam sandwich panels, in which metal foam is sandwiched between two sheets of solid metal. The material again has a high strength-to-weight ratio and excellent shock absorption capacity, while

also being stiff and core-protective. Just like metal foam alone, metal foam sandwich panels are typically manufactured in flat sheets, and failure-free bending can only be achieved using lasers.

The analysis was again initiated with the bending mechanism. It was revisited whether the foam core still follows the same bending mechanism, and how its deformation is affected by the interaction with the solid facesheets. This insight was then used to elucidate the bending efficiency and limit at different process conditions, as well as the impact of the process on the material performance. Additionally, the effect of the sandwich panel manufacturing method on the process outcome was investigated. This was achieved by contrasting two sandwich panel types with a different foam core structure, foam core composition, facesheet composition and facesheet attachment method. Lastly, three-dimensional deformation of metal foam sandwich panels into typical non-Euclidean shapes such as bowl and saddle shapes was explored. It was shown that a significant amount of 3D deformation can be induced. At the same time, it was discussed that the achievable deformation is limited to moderate curvatures, since only a limited amount of in-plane strains may be induced using laser forming.

The aforementioned experimental efforts were again accompanied by numerical efforts. Sandwich panel models with different levels of geometrical complexity were used to study all aspects pertaining to the process, and the properties to the facesheet/foam core interface were discussed.

Overall, the work in this thesis demonstrated that laser forming is capable of bending metal foam panels and metal foam sandwich panels up to large bending angles without causing failures, while maintaining the favorable properties of the material. Conceptual, experimental and numerical groundwork was laid towards a successful implementation of the material in industrial applications.

Table of Contents

List of Figures	vi
List of Tables	xxii
Chapter 1: Introduction	1
1.1 Metal Foam	1
1.2 Sandwich Panels with Metal Foam Cores	2
1.3 Manufacturing Processes	4
1.4 Laser Forming.....	7
1.5 Experiments	9
1.5.1 Materials	9
1.5.1.1 AlSi7 Metal Foam.....	9
1.5.1.2 Sandwich Panel Foam Core & Facesheets.....	12
1.5.2 Experimental Methods	14
1.5.2.1 Non-Dimensional Analysis of Process Conditions.....	15
1.5.2.2 Thermal Imaging.....	17
1.5.2.3 Digital Image Correlation	20
1.6 Simulation.....	23
1.6.1 Uncoupling.....	23
1.6.2 Foam Geometries	30
1.6.2.1 Kelvin-cell Model.....	31
1.6.2.2 Voxel Model	32
1.6.2.3 Equivalent Model.....	34
1.6.3 Heat Transfer through Metal Foam.....	36
1.6.3.1 Gas Conduction through Cavities	37
1.6.3.2 Natural Convection in Cavities.....	37

1.6.3.3 Thermal Radiation through Foam.....	38
1.6.4 Sandwich Modeling.....	41
1.6.4.1 Interface.....	41
1.6.4.2 2D Sandwich Models.....	47
1.6.4.3 3D Sandwich Models.....	48
1.6.5 Initial Conditions and Boundary Conditions.....	49
1.6.6 User Subroutines.....	49
1.6.6.1 2D Dflux.....	49
1.6.6.2 3D radial Dflux.....	52
1.6.6.3 3D circular Dflux.....	53
1.6.6.4 Gapcon.....	54
1.6.6.5 FILM.....	55
1.7 Organization and Objectives of Dissertation.....	56
Chapter 2: Effect of Geometrical Modeling on the Prediction of Laser-Induced Heat	
Transfer in Metal Foam.....	59
2.1 Introduction.....	59
2.2 Background.....	62
2.2.1 Heat Transfer in Metal Foams.....	62
2.2.2 Numerical Models.....	63
2.2.2.1 Equivalent Model.....	64
2.2.2.2 Explicit Porous Models.....	66
2.3 Experimental Procedures.....	68
2.4 Results & Discussion.....	70
2.4.1 Thermal Imager Calibration.....	70
2.4.2 Stationary Heating Source.....	71

2.4.3 Moving Heating Source	75
2.4.4 Fourier Number.....	77
2.4.5 Numerical Model Comparison.....	78
2.5 Conclusions.....	84
Acknowledgment	85
Chapter 3: Laser Induced Mechanical Response of Metal Foam during Laser Forming ...	86
3.1 Introduction.....	86
3.2 Background.....	89
3.2.1 Metal Foam Mechanics and Deformation.....	89
3.2.2 Bending Mechanism	91
3.2.3 Numerical Simulations.....	92
3.3 Experimental Procedures	95
3.4 Results & Discussion	97
3.4.1 Bending Mechanism	97
3.4.2 Bending Limit	101
3.4.3 Impact of Laser Forming on Metal Foam Performance.....	105
3.4.4 Alternative Numerical Models.....	109
3.5 Conclusions.....	111
Acknowledgment	112
Chapter 4: Laser Forming of Sandwich Panels with Metal Foam Cores	113
4.1 Introduction.....	113
4.2 Background.....	115
4.2.1 Sandwich Panel Manufacture and Bending.....	115
4.2.2 Laser Forming.....	118
4.3 Numerical Simulation.....	120

4.4 Experimental Methods	123
4.5 Results & Discussion	125
4.5.1 Bending Mechanism	125
4.5.2 Bending Efficiency & Limit	132
4.5.3 Other Process Conditions.....	136
4.5.4 Numerical Model Comparison.....	139
4.6 Conclusions.....	142
Acknowledgment	143
 Chapter 5: Laser Forming of Metal Foam Sandwich Panels: Effect of Manufacturing	
Method	144
5.1 Introduction.....	144
5.2 Background.....	146
5.2.1 Sandwich Panel Manufacturing Methods	146
5.2.2 Thermally-Induced Stresses at the Interface.....	148
5.2.3 Numerical Simulation	152
5.3 Experimental Methods	155
5.4 Results & Discussion	156
5.4.1 Bending Efficiency & Limit	156
5.4.2 Effect of Facesheet.....	158
5.4.3 Effect of Foam Core.....	160
5.4.4 Thermal Response of Sandwich Panel.....	162
5.4.5 Mechanical Response of Sandwich Panel.....	164
5.4.6 Importance of Facesheet Adhesion Quality	168
5.4 Conclusions.....	170
Acknowledgment	171

Chapter 6: 3D Laser Forming of Metal Foam Sandwich Panels.....	172
6.1 Introduction.....	172
6.2 Background.....	175
6.2.1 Laser Forming of Euclidean Geometries	175
6.2.2 Shaping of Non-Euclidean Geometries	177
6.2.3 Numerical Simulation	180
6.3. Experimental Methods.....	183
6.4. Results & Discussion	184
6.4.1 Bowl Shape	184
6.4.2 Saddle Shape.....	187
6.4.3 Bending Mechanism	190
6.4.4 Effect of Scan Line Length.....	193
6.5. Conclusions.....	199
Acknowledgements.....	200
Chapter 7: Conclusions	201
7.1 Laser Forming of Metal Foam	201
7.2 Numerical Simulation of Laser Forming of Metal Foam	204
7.3 Future Work.....	206
References.....	210
Appendix.....	218

List of Figures

Figure	Caption	Page
Figure 1	(a) In closed-cell metal foam, cavities are entirely surrounded by a cell wall [4]. (b) In open-cell metal foam, cavities are connected to each other [5].	1
Figure 2	Closed-cell metal foam excels as car bumper, shown in green in the left figure, as well as crash box, shown in blue in the left figure. The right figure shows the metal foam filling of a crash box after a collision test [6].	2
Figure 3	Metal foam sandwich panels would excel as parabolic mirrors in solar power plants, shown in (a) [9], due to their high stiffness and strength-to-weight ratio. Their excellent shock and noise absorption capacity would also make them ideal for airplane turbine engine casing, shown in (b) [11].	3
Figure 4	(a) One near-net-shape method to manufacture metal foam sandwich panels is to start with compressed metal and foaming agents powders (precursor), place it between facesheets and heat the assembly near the metal melting temperature. The foaming agent releases a gas, turning the precursor into a foam [9]. (b) 3D printing is the second near-net-shape method [14].	5
Figure 5	Many different types of failures occur during 3-point bending of metal foam sandwich panels. Most typical are core shear failures (c,d), delamination (b,c), and facesheet yield (e). Even the ideal scenario, shown in (a), is not desirable, because the facesheet penetrates deeply into the metal foam [15].	6
Figure 6	Laser forming setup. The specimen is loosely clamped on one side and laser scanned across the entire width at a diameter D , scan speed v and power P [18]. Depending on the bending mechanism, the specimen may bend towards or away from the laser.	7
Figure 7	Metal foam that was used in chapters 2 & 3.	10
Figure 8	Phase diagram for a binary aluminum-silicon alloy system [32].	10
Figure 9	(a) Schematic of the structure of a hypo-eutectic Al-Si alloy, showing the Al-rich α -phase on the left, the grainy eutectic β -phase on the right as well as Si-rich lamellas in black. (b) Optical microscopy picture of a hypo-	11

eutectic Al-Si alloy, along with schematic showing the same structure as in (a) [33].

Figure 10	Compressive stress-strain curve of metal foam. Initially, the response is almost linear in segment 1. In segment 2, the cells crush and absorb energy. In segment 3, the foam starts to densify, causing an exponential increase in the compressive stress [34].	11
Figure 11	(a) Type I sandwich panel that was analyzed in chapter 4. (b) Type II sandwich panel that was compared with the type I sandwich panel in chapter 5.	12
Figure 12	(a) Uncoated aluminum block, (b) aluminum block coated with high-emissivity graphite paint. (c) Non-uniform temperature distribution measured on the shiny block shown in (a), and (d) uniform temperature distribution measured on the coated block shown in (b).	19
Figure 13	Temperature reading on the painted aluminum block (leaving ϵ constant) after heating the block in the tube furnace to (a) 100°C, (b) 200°C, (c) 300°C, and (d) 400°C.	19
Figure 14	Strain distribution in y-direction after laser forming a metal foam specimen to a 45 degree angle. The data was only extracted from the stationary part above the bending axis.	23
Figure 15	(a) Stacked Kelvin-cell geometries [38]. (b) Kelvin-cell model that was obtained by cutting arrays of Kelvin-cells out of a solid block, after a laser forming simulation.	31
Figure 16	(a) In a micro-CT data cloud, there are high-absorption points for aluminum, shown as black dots, and low-absorption points for air (no dots). For each arrangement within a cube, there is a different interpolation scheme to divide the high-absorption area (solid) from the low-absorption area (air) [39]. The individual interpolated surfaces are then stitched together to obtain a closed volume, shown in (b) [40].	33
Figure 17	Voxel model of the metal foam that was used in chapters 2 & 3.	33
Figure 18	Equivalent model after a laser forming simulation.	34

Figure 19	The stress-strain response of metal foam in uniaxial tension and compression is nearly the same up to the tensile failure point [41]. Based on this fact it is possible to assume a symmetric yield surface and isotropic hardening.	35
Figure 20	Initial and subsequent yield surfaces of metal foam. The yield surface is symmetric and expands uniformly (the same in tension and compression) due to the isotropic hardening assumption [42].	36
Figure 21	Typical EDS line scan across the interface of a type I sandwich panel, showing the magnesium content. The interface is the intermediate region between the high mg-content facesheet and the low mg-content foam core.	41
Figure 22	The interface is infinitesimally thin, thus only the interfacial normal and shear tractions are looked at. Due to the traction continuity at the interface, the two layers may deform differently by u^+ and u^- , respectively, giving rise to a jump discontinuity u across the interface [45].	43
Figure 23	Data fit of the results in [46], which allowed establishing a temperature-dependent function for the gap conductance.	45
Figure 24	Sandwich panel that is loaded by a lateral force F [49]. Each layer stretches by $t+\delta t$, and the interface expands by Δ .	46
Figure 25	The ratio $\alpha = Kt/E$ must be at least 25 for the effective stiffness E_{eff} of the entire sandwich panel to be the same magnitude as the stiffness E of the joined layers [49].	47
Figure 26	(a) Equivalent sandwich panel model, (b) Kelvin-cell sandwich panel model, (c) type I sandwich panel specimen (left) and corresponding voxel model (right), (d) type II sandwich panel specimen (left) and corresponding voxel model (right).	48
Figure 27	3D equivalent sandwich panel model used for the (a) bowl shape and the (b) saddle shape. Symmetry constraints were used to reduce the CPU-intensity. The models were also constrained at two vertically aligned points to mimic the experimental fixture.	48

Figure 28	Closed-cell aluminum foam specimen after laser forming.	61
Figure 29	(a) Equivalent model, (b) Kelvin-cell model and (c) voxel model.	63
Figure 30	Determining the equivalent thermal conductivity using the visual method by calculating the cross-sectional areas and the angular orientations of the cell walls.	66
Figure 31	Experimental setup.	68
Figure 32	Experimental and numerical temperature history response during steel sheet laser forming at 800 W – 50 mm/s (high) and 400 W – 25 mm/s (low).	70
Figure 33	(a) and (c) show the experimental top and bottom temperature distributions, respectively, and (b) and (d) show the numerical (Kelvin-cell) top and bottom temperature distributions, respectively, after a 2 s exposure to a 30 W laser with a 6mm radius.	72
Figure 34	(a) Experimental and (b) numerical (Kelvin-cell) temperature distribution from the laser center to the edge of the laser source after a 30 W laser exposure with a 6mm radius. The experimental data is averaged over 15 specimens and standard errors are shown.	73
Figure 35	(a) Experimental and (b) numerical (Kelvin-cell) temperature history plots during a 2 s exposure to a 30 W defocused laser beam with a 6mm radius. The experimental data is averaged over 15 specimens and standard errors are shown.	74
Figure 36	(a) and (c) show the experimental top and bottom temperature history plots, (b) and (d) show the numerical (Kelvin-cell) top and bottom temperature history plots at scanning speeds 2.5 mm/s, 3.33 mm/s and 5 mm/s, respectively. The laser power was 50 W with a beam radius of 6mm. The experimental results were averaged over 20 test runs and standard errors are shown.	76
Figure 37	Experimental and numerical (Kelvin-cell) maximum temperature gradients during 50 W scans with a 6mm beam radius at 2.5 mm/s, 3.33 mm/s and 5 mm/s, respectively. Standard errors are shown for the experimental data.	77

Figure 38	Typical color contours of the (a) equivalent model, (b) Kelvin-cell model and (c) voxel model during a laser scan. Legends are omitted since the color contours are used for a qualitative comparison.	80
Figure 39	Heat flux vectors in cross-sections of the (a) equivalent model, (b) Kelvin-cell model and (c) voxel model during laser irradiation. Legends are omitted since the plots are used for a qualitative comparison.	81
Figure 40	Experimental and numerical (equivalent, Kelvin-cell and voxel model) top and bottom surface temperature history plots during a 2 s laser pulse at 30 W with a defocused beam radius of 6mm.	82
Figure 41	Experimental and numerical (equivalent, Kelvin-cell and voxel model) top temperature history plots during a 50 W scan at 5mm/s with a defocused beam radius of 6 mm.	83
Figure 42	Experimental and numerical (equivalent, Kelvin-cell and voxel model) maximum top surface temperatures during 50 W laser scans at 2.5 mm/s, 3.33 mm/s and 5 mm/s, respectively. Standard errors are shown for the experimental data.	84
Figure 43	Uniaxial compressive stress-strain data (engineering) of four compression specimens (curves 1-4) made with the same metal foam that was used in this study [34]. The stress-strain curve can be divided into three segments: (1) a linear regime, followed by (2) a plateau where cell crushing occurs and a large amount of energy is absorbed, followed by (3) foam densification. Due to their crushability, metal foams can withstand much lower compressive stresses than solid metals.	89
Figure 44	Two approaches were used to model metal foam. In the first (“equivalent”) model, shown in (a), a solid geometry was used and equivalent foam properties were assigned. In the second (“Kelvin”) model, shown in (b), the foam geometry was explicitly modeled, and solid aluminum properties were assigned. The cavity geometry was approximated by a Kelvin-cell geometry.	92
Figure 45	(a) Experimental setup. The laser was scanned in x -direction. The bottom specimen surface was spray-painted white with a black speckle pattern. Digital images were taken in between consecutive laser scans. (b) Example strain distribution (ϵ_{yy} , Lagrangian strain) on the bottom surface of a laser	95

formed specimen at a bending angle of 45° . The strain was only extracted on the clamped half of the specimen above the bending axis to avoid effects related to out-of-plane rotations [37].

- Figure 46 Section of the top surface of the specimen on the laser scan line (a) before laser forming, (b) after 1 scan and (c) after 10 scans at 90 W and 5 mm/s. Even at this low power, localized melting of thin cell walls occurred, marked in white. Melting started after the first scan and progressed with each consecutive scan, forming u-shaped trenches in the cell walls and reducing the amount of compressible material. Melting stopped once the thickness of the remaining cell wall sections increased. 98
- Figure 47 Cross-section of a foam specimen after 5 laser scans at 180 W and 10 mm/s. The laser was scanned into the page. The white arrows show where cell walls were bent during laser forming, indicating that the foam cannot withstand high compressive stresses. 98
- Figure 48 Comparison of the tensile strain (ϵ_{yy}) on the bottom surface (determined via DIC) in 4-point bending and laser forming (at 180 W and 10 mm/s). ϵ_{yy} is the strain resulting from a combination of cell collapsing and cell wall deformation. Standard errors are shown, calculated over all the pixels of the averaged areas (see Sec. 3.3). In 4-point bending, the strain increased exponentially before a catastrophic failure, whereas in laser forming there was a stable linear strain growth with increasing bending angle. Laser forming yielded a larger maximum ϵ_{yy} , due to heat-induced softening, yet ϵ_{yy} did not grow proportionally to the bending angle, and hence tensile stretching cannot be the main cause of bending. 98
- Figure 49 Strain distributions (ϵ_{yy}) in (a) metal foam during 4-point bending, (b), metal foam during laser forming, and (c) a steel sheet during laser forming. (d) Ratio of top surface (compressive) strain over bottom surface (tensile) strain at the bending axis, calculated for all three simulations. In 4-point bending, bending was equally caused by compressive and tensile strains. In laser forming, the large ratios indicate that compressive deformation was the main cause for bending. 99
- Figure 50 Relative density distribution after a single scan at 180 W and 10 mm/s. The baseline relative density is 0.112, and a relative density of 1 indicates complete densification. Densification occurred throughout the top 80% of the foam, leaving only a small tensile region on the bottom surface. Therefore, laser forming shifts the neutral axis downwards, and deformation is dominated by compressive shortening. 100

Figure 51	(a) Experimental and (b) numerical bending angles and tensile strain data (ϵ_{yy}) at large bending angles. “High” refers to the condition 180 W 10 mm/s, “low” refers to 90 W 5 mm/s. Standard errors are shown for the strain results, calculated over all the pixels of the averaged area (see Sec. 3.3). In both the experiment and the simulation, the bending angle and strain plots leveled off at a large number of scans. In the numerical simulation, the limit at 180 W and 10 mm/s was reached at a larger bending angle, since the model did not consider melting, as well as changes in the moment of area, laser absorption and thermal conductivity with increasing densification.	102
Figure 52	Comparison of numerical data before and after correcting for density-dependence. Without correction, both the bending angle and strain increment decreased only slightly with increasing scans, induced by tensile strain hardening on the bottom surface. After incorporating density-dependent variables, a distinct limiting behavior could be observed.	104
Figure 53	Bottom surface of a specimen scanned at 90 W and 5 mm/s at bending angles of (a) 1°, (b) 11.6°, and (c) 16.3°. Due to some naturally occurring stress concentrations, micro-cracks already occurred at low bending angles of 1°. As the bending angle became larger, those micro-cracks increased in size, and new micro-cracks formed (b,c). However, the micro-cracks remained isolated from each other at this stage and thus hardly affected the structural integrity of the foam.	105
Figure 54	(a) Foam specimen at a bending angle of 45°, after being laser formed at 180 W and 10 mm/s, with a cross-section shown in (b). At large bending angles, the isolated cracks on the bottom surface grew larger and started to coalesce, shown in (a). In close proximity to the bending axis, cells at the top surface were crushed significantly, shown in (b), but the foam was still far away from complete densification.	106
Figure 55	Resistance curves determined using the J-integral method, ASTM 813-89, for a closed-cell foam with a very similar composition and porosity [79]. The white and black data points represent two test specimens. Unlike in a brittle material, where the J_R -value would be horizontal beyond an unstable crack length, it keeps on increasing in metal foam, indicating that the foam fracture toughness is maintained even as the crack grows larger. Therefore, micro-cracks do not lead to an unstable fracture, and even larger cracks do not completely remove the structural integrity of the foam.	106
Figure 56	Fracture surfaces in (a) mechanically fractured and (b) laser formed metal foam specimens. The fracture surface in (a) consists of a mix of dimples	108

and clean surfaces with sharp edges, indicating a mix of ductile and brittle fracture. The material on the surface of (b), on the other hand, appears to have been stretched severely, indicating a more ductile fracture.

- Figure 57 Relative density distribution at a bending angle of 45° . The baseline relative density is 0.112, and a relative density of 1 indicates complete densification. The densified region was highly localized around the bending axis. Over a small area close to the top surface, the relative density increased by a factor of 2.5, which is still far away from complete densification. Foam expansion occurred close to the bottom surface, coinciding with the region where cracks appeared in Fig. 54(a). 108
- Figure 58 Bending angles predicted by the Kelvin model in comparison with the predictions of the equivalent model and the experimental values. Standard errors are shown for the experimental data. Due to its superior geometrical accuracy, the Kelvin model yielded results that were closer to the experimental results. Nevertheless, the model still overestimated the bending angle, particularly at the high condition (180 W, 10 mm/s), since it did not account for melting, as well as changes in the laser absorption (due to using an uncoupled modeling approach). 109
- Figure 59 Thermal strain distribution in a micro-CT based “voxel” model during a laser scan at 90 W and 5 mm/s. The downward deformation represents the initial counter-bending that occurs during the laser scan. The voxel model has a higher level of geometrical accuracy, which could potentially be used to predict crack-initiation sites and cell wall bending. 110
- Figure 60 An example showing a metal foam sandwich (89% porosity, total thickness 10 mm, facesheets thickness 1 mm) which has a 17.4 times higher moment of area about the y axis than a solid with the same cross-sectional area (thickness 3.2 mm). Hence, metal foam sandwiches have a higher stiffness to bending deformation. The cross-sections were divided into squares of 0.1 mm length, whose moment of area were calculated individually and added using the parallel axis theorem. The y and z axes refer to the number of squares per coordinate direction. The total number of squares was the same for the solid and sandwich. 117
- Figure 61 Two different geometries were used to model the foam core: (a) solid geometry (“equivalent model”), whereby foam properties were assigned, and (b) Kelvin cell geometry (“Kelvin model”), where each cavity was approximated by a Kelvin-cell. Not visible are the cohesive layers that were inserted between the facesheets and the foam core. 122

- Figure 62 Experimental setup. The specimens were scanned in x-direction, and a thermally insulating material was inserted between the specimen and the holder. The dial indicator was removed during laser scans. 124
- Figure 63 Cross-sections of sandwich panels scanned at (a) $D = 4$ mm and $v = 30$ mm/s (100 scans) and (b) $D = 12$ mm and $v = 10$ mm/s (24 scans), and cross-sections of isolated facesheets scanned at (c) $D = 4$ mm and $v = 30$ mm/s (7 scans), and (d) $D = 12$ mm and $v = 10$ mm/s (6 scans). The power and area energies were $P = 800$ W and 6.67 J/mm² in all cases, respectively, and the final bending angle was 15° . The top facesheet bent via the TGM in (a) and (c), the BM in (d), and the UM in (b). 126
- Figure 64 Simulated temperature distributions at a cross-section (yz -plane) as the laser passes, both in the entire sandwich (equivalent sandwich model) and in an isolated facesheet. At $D = 4$ mm and $v = 30$ mm/s, a steep temperature gradient exists in the top facesheet, regardless of whether the facesheet is isolated or in sandwich configuration, indicating that the TGM is always the governing mechanism. At $D = 12$ mm and $v = 10$ mm/s, there is hardly any gradient over the top facesheet in both scenarios, indicating that the BM and the UM govern in the isolated and sandwich configurations, respectively. 127
- Figure 65 Experimental and numerical temperature histories on the bottom sandwich panel surface at $D = 4$ mm and $D = 12$ mm. At $D = 12$ mm there is a more significant temperature rise, indicating that more heat is transferred across the top facesheet. At $D = 4$ mm, little heat reaches the bottom surface, implying the presence of a temperature gradient in the top facesheet. 128
- Figure 66 Density distribution after a laser scan at (a) $D = 4$ mm and $v = 30$ mm/s, and (b) $D = 12$ mm and $v = 10$ mm/s. The initial density is 100%. At both conditions, the foam core densified as postulated by the MTGM. At $D = 4$ mm, the densification has a higher magnitude, but occurs more locally. At $D = 12$ mm, densification occurs over a much greater area, allowing for a more efficient deformation at large bending angles. A deformation scaling factor of 5 was used. Half of the specimen is shown due to symmetry. 129
- Figure 67 Vertical plastic strain distribution in z -direction (ϵ_{33}) at the scan line at $D = 4$ mm and $v = 30$ mm/s (a) right before the laser passes, (b) as the laser passes, and (c) after the laser scan. Right as the laser passes, the top facesheet (top 3 element layers) expands upwards and downwards near the scan line, compressing the foam underneath. The foam, in turn, densifies due to the MTGM and “pulls” the facesheet down, causing tensile strains in the top facesheet. A deformation scaling factor of 5 was used. Half of the 131

specimen is shown due to symmetry.

- Figure 68 Experimental bending angles over 8 scans at $D = 4$ mm with $v = 30$ mm/s, and $D = 12$ mm with $v = 10$ mm/s. The power and area energy are constant at $P = 800$ W and $AE = 6.67$ J/mm², respectively. The bending angles are averaged over 5 specimens, standard errors are shown. At $D = 12$ mm, bending is more efficient than at $D = 4$ mm. 132
- Figure 69 Plastic strain distribution after a laser scan at (a) $D = 4$ mm with $v = 30$ mm/s and (b) $D = 12$ mm with $v = 10$ mm/s. At $D = 4$ mm, significant compressive shortening only occurred over a small segment of the top facesheet (top 3 element layers), unlike at $D = 12$ mm, where the entire top facesheet contributed to compressive shortening, and compressive strains extended further from the laser scan line. A deformation scaling factor of 5 was used. Half of the specimen is shown due to symmetry. 133
- Figure 70 At $D = 4$ mm, appreciable bending angles can only be obtained by performing parallel scans, as shown in (a), where 2 scans were performed per scan line and offset by 1 mm. At $D = 12$ mm, large bending angles up to 65° and beyond can be obtained over a single scan line, as shown in (b). 134
- Figure 71 Cross-section of a sandwich specimen bent to 65° at $D = 12$ mm and $v = 10$ mm/s. The top facesheet thickened significantly, and foam densification occurred over a large area. Yet the strength of the top facesheet is maintained, if not increased. Much less densification occurred than in mechanical bending. 135
- Figure 72 Experimental bending angles over 8 scans at spot sizes ranging from $D = 4$ mm to $D = 12$ mm. The power and area energy are constant at $P = 800$ W and $AE = 6.67$ J/mm², respectively. The bending angles are averaged over 5 specimens, standard errors are shown. At small spot sizes, the bending curves level off more rapidly due to an increased amount of paint evaporation and a higher sensitivity to facesheet thickening. 137
- Figure 73 Experimental bending angles after 1 scan and 8 scans at spot sizes ranging from $D = 4$ mm to $D = 12$ mm. The power and area energy are constant at $P = 800$ W and $AE = 6.67$ J/mm², respectively. The bending angles are averaged over 5 specimens, standard errors are shown. 138
- Figure 74 Experimental and numerical bending angles after a single scan at a spot size of $D = 12$ mm and a power of $P = 800$ W. The experimental results were 138

averaged over 5 specimens, standard errors are shown. With increasing scan speed, the area energy and thus the bending angle decrease. A considerable range of area energies can be used.

- Figure 75 Temperature distribution in a sandwich specimen scanned at $D = 12$ mm and $v = 10$ mm/s using a (a) equivalent sandwich model and a (b) Kelvin sandwich model. Half of the specimen is shown due to symmetry. 139
- Figure 76 Simulated temperature distributions at a cross-section (yz -plane) as the laser passes the section, predicted by the equivalent and Kelvin models, for the conditions $D = 4$ mm with $v = 30$ mm/s, and $D = 12$ mm with $v = 10$ mm/s. In the Kelvin sandwich model, the top facesheet temperatures and the temperature drop across the interface are greater due to the additional geometrical restriction of the heat flow at the interface. 140
- Figure 77 Plastic strain distribution in the Kelvin sandwich model after a laser scan at $D = 4$ mm with $v = 30$ mm/s. A deformation scaling factor of 10 was used. Half of the specimen is shown due to symmetry. In (a), a cavity is located underneath the facesheet at the scan line, and the facesheet can expand downwards unrestrictedly. In (b), a cell wall is located underneath the facesheet, and the downward expansion of the facesheet is restricted. 141
- Figure 78 Experimental and numerical bending angles after a single laser scan at $D = 4$ mm and $v = 30$ mm/s, and $D = 12$ mm and $v = 10$ mm/s ($P = 800$ W = const.). The Kelvin model is more sensitive to changes in process conditions due to its higher geometrical accuracy. Both models over-predicted the bending angles at $D = 4$ mm because they did not account for paint evaporation and localized melting. 142
- Figure 79 (a) Type I sandwich panel, (b) type II sandwich panel. 146
- Figure 80 Schematic of two layers of thicknesses s_1 and s_2 that are joined by an interface of thickness η , with a close-up of the traction components at the interface [93]. 149
- Figure 81 Typical EDS line scan of a type I sandwich panel specimen, showing the magnesium content. The scan was performed across the interface between the facesheet and the foam core. The interface is the intermediary region between the high Mg-content facesheet and the low Mg-content foam. 150

Figure 82	(a) Equivalent sandwich model, (b) Kelvin-cell sandwich model, (c) type I sandwich panel specimen (left) and corresponding voxel model (right), (d) type II sandwich panel specimen (left) and corresponding voxel model (right).	153
Figure 83	Bending angles of both sandwich panel types over 8 laser scans at a large spot size ($D = 12$ mm, $v = 10$ mm/s) and a small spot size ($D = 4$ mm, $v = 30$ mm/s), the power was constant at $P = 800$ W. The results were averaged over 3 specimens, standard errors are shown.	157
Figure 84	The bending limit of the (a) type I and (b) type II sandwich panel at a large spot size ($D = 12$ mm, $v = 10$ mm/s) were around 65° and around 45° , respectively. In the type I sandwich panel, the top facesheet mostly deformed inwards, whereas it mostly deformed outwards in the type II sandwich panel.	157
Figure 85	Bending angles of the “isolated” facesheets (not attached to foam core) at a small spot size ($D = 4$ mm, $v = 30$ mm/s). The type I facesheet, made of AW 5005, bent more efficiently than the type II facesheet, which was made of Al 1060.	158
Figure 86	Plastic strain distribution in y-direction after a laser scan at ($D = 12$ mm, $v = 10$ mm/s). AW 5005 facesheet properties were used in (a), and Al 1060 facesheet properties were used in (b). The remaining geometrical and material properties were identical. The deformation was scaled by a factor of 10 for viewing clarity. Only half of the model is shown due to symmetry.	159
Figure 87	Foam pucks were sandwiched between two solid aluminum disks. A laser with spot size $D = 12$ mm was applied to the top surface of the assembly and the temperature was measured underneath. The measured heat diffusion through the type I and type II foams was very similar. The results were averaged over 2 specimens that were tested from both directions, standard deviations are shown.	160
Figure 88	The moment of area of the type I foam is on average 18% greater than the moment of area of the type II foam, making it stiffer to bending deformation.	161
Figure 89	Temperature history on the bottom surface of the sandwich panels during laser scans at a large spot size ($D = 12$ mm, $v = 10$ mm/s) and a small spot	163

size ($D = 4$ mm, $v = 30$ mm/s). 4 specimens were tested for each sandwich panel type, standard deviations are shown.

- Figure 90 Temperature distribution in voxel models of (a) type I sandwich panels and (b) type II sandwich panels, during a scan at a large spot size ($D = 12$ mm, $v = 10$ mm/s). The laser was scanned in x -direction. The models were sliced along the laser scan line for viewing clarity. 164
- Figure 91 Cross-sections of type I and type II sandwich panels that were bent to the bending limit. The laser was scanned into the page. At a small spot size ($D = 4$ mm, $v = 30$ mm/s), the bending limit of the type I sandwich panel is around 15° (a), and for the type II sandwich panel it is around 12° (b). At a large spot size ($D = 12$ mm, $v = 10$ mm/s) the limit is (c) around 65° for the type I sandwich panel and (d) around 45° for the type II sandwich panel. 165
- Figure 92 Plastic strain distributions in y -direction in a type II sandwich panel after a laser scan at a large spot size ($D = 12$ mm, $v = 10$ mm/s), shown using a voxel model. The deformation was scaled by a factor of 10 for viewing clarity. The laser was scanned into the page, and the laser center was on the dashed line. 166
- Figure 93 Plastic strain distributions in y -direction in a Kelvin-cell sandwich model after a laser scan at a large spot size ($D = 12$ mm, $v = 10$ mm/s). Only half of the model is shown due to symmetry. In (a), the foam core was constructed such that cavities are underneath the top facesheet at the symmetry plane, whereas in (b) mostly cell walls are underneath the top facesheet. The remaining properties of both models are identical. The deformation was scaled by a factor of 10 for viewing clarity. 167
- Figure 94 (a) A cross-section of the type II sandwich panel, obtained using a micro-CT scan, shows that there are regions of detachment between the facesheet and the foam core. This detachment is detrimental to laser forming, since the maximum achievable bending angle drops from 45° to around 15° at a large spot size ($D = 12$ mm, $v = 10$ mm/s), shown in (b). 168
- Figure 95 Plastic strain distributions in y -direction after a laser scan at a large spot size ($D = 12$ mm, $v = 10$ mm/s). In (a), the adhesion between the top facesheet and the foam core is intact, whereas in (b) the top facesheet is detached from the foam core over a half the spot size of $D = 12$ mm. Only half of the model is shown due to symmetry. The deformation was scaled by a factor of 10 for viewing clarity. 170

Figure 96	The channel shape on the left is a Euclidean geometry. It can be obtained by bending strains alone, and the bending deformation is in the yz - plane. The bowl and saddle shapes are non-Euclidean geometries. Deforming a flat sheet into bowls and saddles requires both bending and in-plane strains, and the deformation occurs in three dimensions.	176
Figure 97	Radial scan pattern that was used to obtain the (a) bowl shape and (b) saddle shape. Solid lines were performed on the top surface, dashed lines on the bottom surface. The numbering indicates the scan sequence. Scans were initiated on the outside and ended at the center. The diagrams apply for the condition of $D = 12$ mm and $v = 10$ mm/s. For $D = 4$ mm and $v = 30$ mm/s, the same overall area was treated, but the laser scans were closer together.	178
Figure 98	(a) Bowl model and (b) saddle model. In both cases, only one quarter of the specimen was modeled, and an x and y symmetry was employed. Both models were fixed at two vertically aligned points using encastre constraints.	180
Figure 99	Isometric and side view of bowl shape (a) after 300 scans at a laser spot size of $D = 4$ mm with scan speed of $v = 30$ mm/s, and (b) after 160 scans at a laser spot size of $D = 12$ mm with scan speed of $v = 10$ mm/s. The laser power was $P = 800$ W in both cases.	184
Figure 100	Average radial deflection of the bowls in Fig. 99, shown with standard deviations. At a large spot size of $D = 12$ mm, a higher deflection was obtained even though the number of scans was lower than at a small spot size of $D = 4$ mm.	185
Figure 101	Bowl shape predicted by the numerical model in Fig. 98(a), after performing one iteration of the scan pattern in Fig. 97(a). The model was mirrored in x and y - direction. The spot size was $D = 12$ mm and the scan speed was $v = 10$ mm/s. The deformation was magnified by a factor of 10 for viewing clarity.	186
Figure 102	Comparison of experimental and numerical deflections of the bowl shape at (a) a laser spot size of $D = 4$ mm with scan speed of $v = 30$ mm/s, and (b) a laser spot size of $D = 12$ mm with scan speed of $v = 10$ mm/s. One iteration of the scan pattern in Figs. 97(a) and 99(a) were performed. Average deflections and standard deviations are shown for the experimental data.	186

Figure 103	Saddle shape (a) after 288 scans at a laser spot size of $D = 4$ mm with scan speed of $v = 30$ mm/s, and (b) after 168 scans at a laser spot size of $D = 12$ mm with scan speed of $v = 10$ mm/s. The laser power was $P = 800$ W in both cases.	187
Figure 104	Average deflection of the saddles in Fig. 103, measured at the outer edges marked as edge 1 and edge 2 in Fig. 105. The large spot size of $D = 12$ mm again yielded a higher amount of deformation than the small spot size of $D = 4$ mm.	188
Figure 105	Saddle shape predicted by the numerical model in Fig. 98(b) after mirroring the result in both x and y direction. The spot size was $D = 4$ mm and the scan speed was $v = 30$ mm/s. The deformation was magnified by a factor of 10 for viewing clarity. Only half the scans of Figs. 103 and 104 were modeled, skipping every other scan, to reduce the computational intensity.	189
Figure 106	Comparison of experimental and numerical deflections of the saddle shape at (a) a laser spot size of $D = 4$ mm with scan speed of $v = 30$ mm/s, and (b) a laser spot size of $D = 12$ mm with scan speed of $v = 10$ mm/s after one iteration of the scan pattern. Average deflections are shown for the experimental data.	189
Figure 107	Temperature distributions across the sandwich panel thickness right as the laser passes the cross-section, predicted by the numerical models. At $D = 12$ mm, there is hardly any gradient across the top facesheet, satisfying the thermal prerequisites for the UM. At $D = 4$ mm, there is a steep gradient across the top facesheet, satisfying the thermal prerequisites for the TGM. In both cases, there is a steep gradient across the foam, satisfying the thermal prerequisites for the MTGM.	190
Figure 108	Cross-sections cut perpendicular to the scan path at (a) $D = 4$ mm and $v = 30$ mm/s, and (b) $D = 12$ mm and $v = 10$ mm/s. The laser was scanned into the page. The cross-sections look very similar to cross-sections obtained in 2D laser forming [91].	191
Figure 109	Plastic strain distributions in $y -$ direction (PE22) at a cross-section that is perpendicular to the laser scan at (a) $D = 4$ mm and $v = 30$ mm/s (3D case), and (b) $D = 12$ mm and $v = 10$ mm/s (3D case), and (c) $D = 12$ mm and $v = 10$ mm/s (2D case). The laser scan was performed on the symmetry plane, hence only half of the specimen is shown. The deformation was magnified by a factor of 10 for viewing clarity. The foam thickness differed between	192

the 2D (c) and 3D (a,b) cases to reflect the experimental specimens used.

- Figure 110 Circular scan pattern that was used to obtain the bowl shape at $D = 12$ mm and $v = 10$ mm/s. The overall scan length is the same as in the radial scan pattern of Fig. 97(a). The radii are $R_1 = 30$ mm, $R_2 = 36.5$ mm, $R_3 = 43.1$ mm, $R_4 = 49.6$ mm. At $D = 4$ mm and $v = 30$ mm/s, the same overall area was treated, but 10 laser radii were used that were closer to one another. 195
- Figure 111 Comparison between the average deflections of the bowl shape achieved using radial and circular scan paths. Standard deviation are shown. Much more deformation could be achieved using radial scan patterns. 195
- Figure 112 Bowl shape obtained using a circular scan pattern. The spot size was $D = 12$ mm and the scan speed was $v = 10$ mm/s. The deformation was magnified by a factor of 10 for viewing clarity. The plastic strain magnitude is lower than when using a radial scan pattern (Fig. 101). 196
- Figure 113 Temperature distributions during (a) a radial laser scan, (b) a circular scan far away from the edge, and (c) a circular scan close to the edge. In circular scans, the temperature gradient is reduced, and the material surrounding the irradiated region undergoes more heating, especially if the scan is performed close to the edge. 197
- Figure 114 Plastic strain distributions in y – direction after (a) a single laser scan close to the edge and (b) after 4 laser scans. The compressive strain increases with increasing distance from the edge, and its magnitude is higher on the side facing the center of the specimen. 198

List of Tables

Table	Caption	Page
Table 1	Al 1060 undergoes more thermal softening and has a much lower flow stress than AW 5005.	13
Table 2	The type I foam core (AlSi10) is slightly stiffer and undergoes less thermal softening than the type II foam core (Al 99.7).	13
Table 3	The nine dimensional parameters that are used for the Buckingham Pi analysis. In the second row, the regular material units are shown, whereas in the third row the units are written in terms of the four fundamental units, the mass M , the length L , the time t , and the temperature T .	15
Table 4	The moment of area (about $z = 0$) of a metal foam with 89% porosity is 43.4 times higher than the area moment of a solid with the same cross-sectional area. As a consequence, metal foam has a much higher bending stiffness.	90

Acknowledgments

I would like to thank all the people without whose support this endeavor would not have been possible. First of all, I would like to acknowledge my advisor Prof. Y. Lawrence Yao for his advice, guidance and counsel throughout my Ph.D, as well as my lab mates for the productive and fun times we have spent together. I would also like to acknowledge Bob Stark, Mohamed Haroun, Andrei Shylo, and Bill Miller for their help on numerous projects, as well as giving me access to milling machines and the universal strength tester. Furthermore I would like to thank Prof. Jeffrey Kysar for giving me access to the DIC equipment. The financial support from the National Science Foundation and Columbia University is gratefully appreciated. Finally, I would like to thank the collaborators from Boeing for our exchange in ideas. This work used the supercomputing facilities at XSEDE.

I would like to dedicate this thesis to my parents, to whom I am greatly indebted for their unconditional support. Gifted with perhaps more skills, intelligence, hard-working attitude and drive for perfection than myself, they had everything necessary to excel at a high school, college, and they could have even pursued a Ph.D. However, they were lacking the most important thing, the opportunity, which prevented them from pursuing any higher education. This thesis gives a sense of my accomplishment, but it truly ought to be looked at as the accomplishment of my parents. Starting from absolutely nothing, they worked relentlessly to provide my brother and me with all the opportunities one could wish for regarding education, sports, and music. It is needless to say that I would not have become half the person I am today without their herculean effort and dedication.

I would also like to thank my brother Cyril for being an excellent role model and continuously providing me with abundant inspiration.

Last but not least, I would like to thank my wife and best friend Gabrielle for all the wonderful time we have spent together during college (during which, thank god, I never ever had to talk about engineering), the many delicious meals that we cooked, and the many memories we already share.

Chapter 1: Introduction

1.1 Metal Foam

Metal foam is a relatively new material that was introduced in the middle of the 20th century [1]. It has the same structure as sponges, but is made out of metal, a combination that gives rise to truly unique material properties that have been nearly fully characterized over the past couple of decades [2,3]. Metal foams are generally classified into two categories: (1) closed-cell foams, in which cell walls completely encapsulate each cavity (Fig. 1(a)), and (2) open-cell foams, in which individual cavities are connected with one another (Fig. 1(b)).

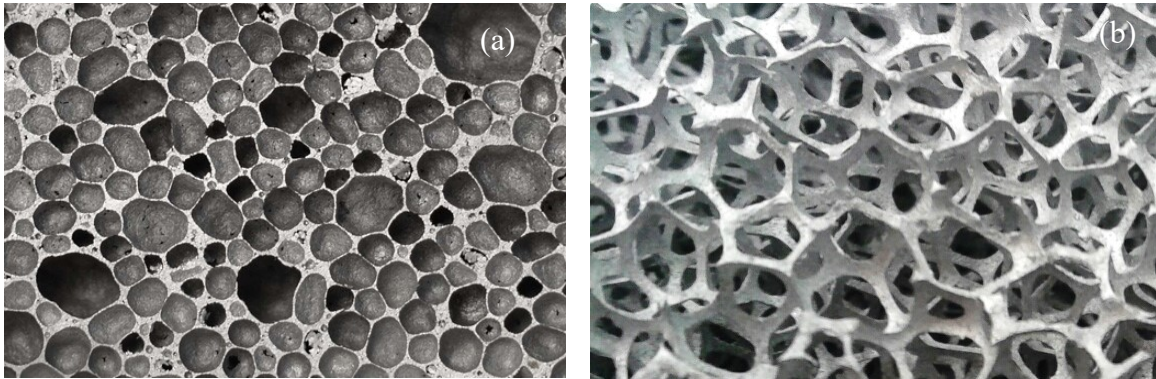


Figure 1: (a) In closed-cell metal foam, cavities are entirely surrounded by a cell wall [4]. (b) In open-cell metal foam, cavities are connected to each other [5].

Closed-cell metals foams are exceptional shock absorbers and perfectly suited for crash-absorption applications such as car bumpers or car crash boxes [6]. Moreover, they have a very high strength-to-weight ratio, making them ideal for space applications such as rocket components or space shuttle parts [7]. Closed-cell metal foams have also been reported to have exceptional noise-absorption capabilities [2]. They are rather good thermal insulators, and particularly suitable for fire-retardance or fire-proofing applications, since they are not flammable unlike some polymer foams that are currently used for insulations [8]. Many more

potential applications exist that are summarized in [7,9], including architectural applications, train/boat hulls, machine vibration dampers, or even cooking ware.

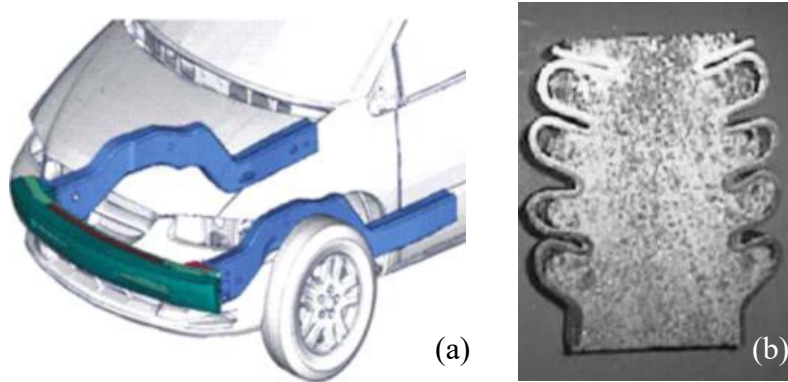


Figure 2: Closed-cell metal foam excels as car bumper, shown in green in the left figure, as well as crash box, shown in blue in the left figure. The right figure shows the metal foam filling of a crash box after a collision test [6].

Open-cell metal-foams excel as heat sinks, since their high conductivity allows for quick heat dissipation. Furthermore, they are an ideal material for ultra-light components, because they can be manufactured at extremely low densities. Open-cell foams are also often used as catalysts [9]. In this thesis, only closed-cell metal foams were investigated, since they are more suitable for structural applications and have more unique properties than open-cell foams. Additionally, the project was focused on low-density metal foams with porosities of 70% and greater, since they are lowest in weight while having the greatest shock absorption capacity.

1.2 Sandwich Panels with Metal Foam Cores

In many applications, metal foam is not used in bulk, because it is difficult to integrate into engineering structures, and its cell walls can easily be damaged. Instead, metal foam is often encapsulated by solid sheet metal. The most common way this is done is by cutting a slender metal foam panel and attaching solid metal sheets (“facesheets”) on both sides of the metal foam. The resulting composite is called “sandwich panel”. Sandwich panels can be manufactured with many different types of foam cores, such as open and closed-cell metallic or polymer foams. In

this project it was focused on the most common type of sandwich panels, consisting of a closed-cell metal foam core, for the same reasons that were mentioned previously.

Just like bulk metal foam, metal foam sandwich panels have an exceptional shock-absorption capacity and high strength-to-weight ratio, making them a viable option for many car components [10]. At the same time, they are much stiffer than metal foam sheets due to the metallic facesheets, and offer protection of the foam core. Their dimensional stability and low weight makes them well suited for parabolic mirrors in solar plants shown in Fig. 3(a). Perhaps one of the greatest potentials of sandwich panels lies in the aerospace industry. Sandwich panels could potentially be used as turbine casings, shown in Fig. 3(b), since they can arrest turbine blades in case of a failure, while also reducing the engine noise and being comparatively light [11]. Sandwich panels would also be well suited for airplane noses as they can protect the aircraft from bird impacts [12]. They could even serve as a substitute for honeycomb structures, which are frequently used in aircraft nowadays. Unlike honeycomb structures, sandwich panels are not unidirectional and have the same rotational stiffness about every bending axis. Moreover, they can be manufactured to doubly-curved surfaces, and offer a greater flexibility in the foam density, structure (open or closed-cell), and composition.

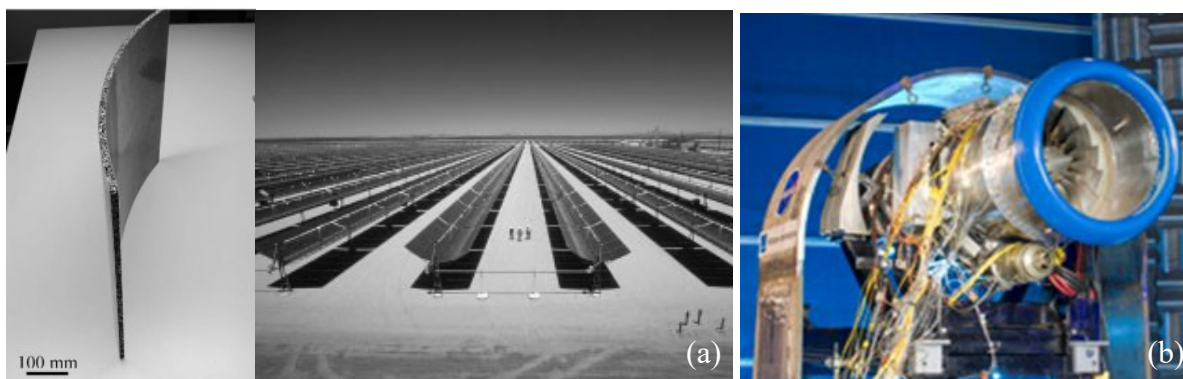


Figure 3: Metal foam sandwich panels would excel as parabolic mirrors in solar power plants, shown in (a) [9], due to their high stiffness and strength-to-weight ratio. Their excellent shock and noise absorption capacity would also make them ideal for airplane turbine engine casing, shown in (b) [11].

1.3 Manufacturing Processes

Even though numerous potential applications have been identified in which metal foam and metal foam sandwich panels would excel, metal foam products have hardly ever made it past the prototype stage. The reason is that metal foam products are extremely challenging to manufacture in the shapes that are required in engineering applications.

There do exist two near-net-shape processes that directly manufacture metal foam parts in the final shape. The first process is based on powder metallurgy and drawn schematically in Fig. 4(a). In this process metal and so called “foaming agent” powders are mixed and compressed to a precursor block. The precursor is then inserted into a mold and heated to a temperature at which the foaming agent releases a gas and turns the precursor into a foam. At the same time the metal powders are sintered together due to the elevated temperatures. The foamed precursor expands and eventually fills out the mold, creating a fully foamed part with the negative shape of the mold. The same technique can be applied to manufacture custom-shaped sandwich panels. The only difference is that prior to heating the precursor inside the mold, it is sandwiched between solid metal facesheets, and the assembly is bent to the required shape. During heating, the precursor again turns into a foam, and creates metallic bonds to the adjacent facesheets due to the elevated temperatures and the pressures that develop inside the mold [9].

While being rather convenient, this process has several drawbacks. First, the foaming process requires a mold, and sandwich panels even require two molds for the initial deformation and foaming. Moreover, these molds have to fit into an oven, and an excessive amount of trial and error is required to obtain the best precursor shapes and foaming conditions. Hence, this manufacturing process is only profitable for a very large production volume and is limited to

moderately sized parts. Another drawback is that the manufacturing process usually yields non-uniform density and cell-distributions, because the metal foam is created in irregular shapes.

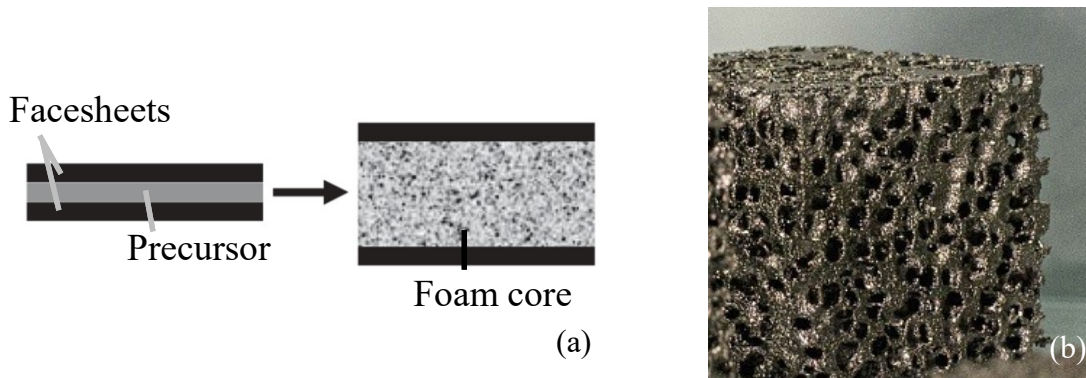


Figure 4: (a) One near-net-shape method to manufacture metal foam sandwich panels is to start with compressed metal and foaming agents powders (precursor), place it between facesheets and heat the assembly near the metal melting temperature. The foaming agent releases a gas, turning the precursor into a foam [9]. (b) 3D printing is the second near-net-shape method [14].

The second near-net-shape process is 3D printing shown in Fig. 4(b). With the recent developments in the field of additive manufacturing, molds can be 3D printed in the negative shape of the desired foam geometry, which can then be filled with molten metal to obtain a metallic foam. While offering a lot of flexibility in the foam structure and the choice of the base metal, 3D printing has the drawback of being extremely slow and only suitable for small parts with small production volumes.

The alternative to near-net-shape processes is to manufacture generic metal foam shapes, such as slabs and sheets, and subsequently bend them into the required shapes. This approach has the advantage of being more cost effective, while also yielding more uniform foam densities and cell distributions. The drawback of this approach is that it is exceedingly difficult to bend metal foam. Several mechanical bending methods have been attempted, all reporting dissatisfying results. 3 and 4 – point bending, for instance, cause many different types of failures [15,16]. Core shear failures are for instance very common (Fig. 5(a)), due to the high tensile stresses that arise and that readily exceed the tensile strength of metal foam. Other common failures are

indentations of the foam, either by the indenter, or, in the case of the sandwich, by the facesheet (Fig. 5(b)). Further failures include facesheet wrinkling or failure, or facesheet delamination, shown in Figs. 5(c) – 5(e).

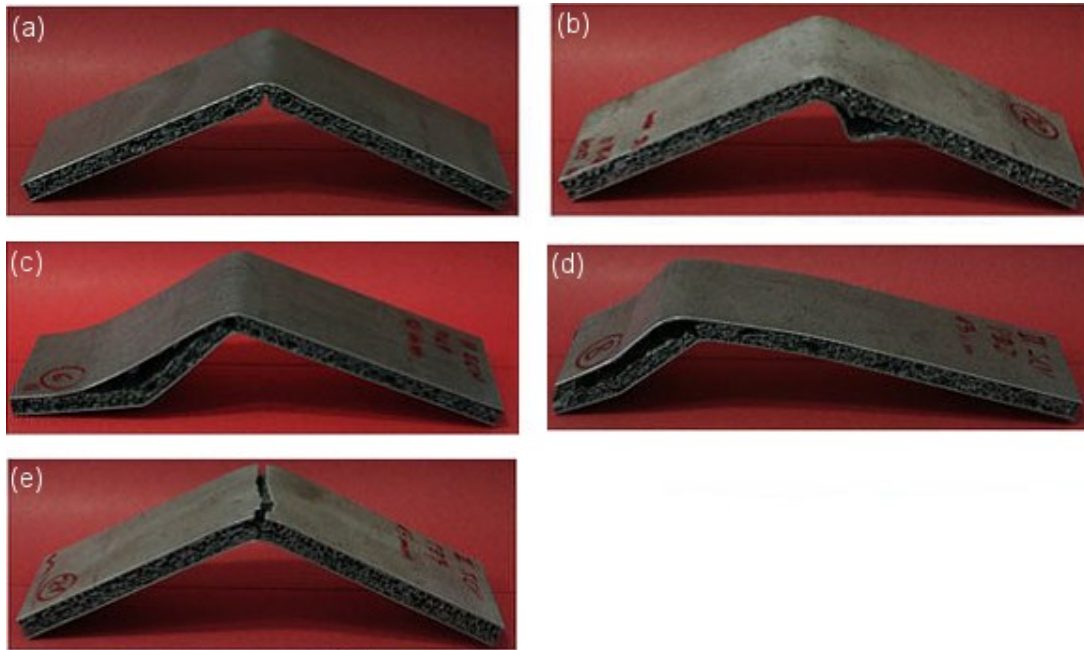


Figure 5: Many different types of failures occur during 3-point bending of metal foam sandwich panels. Most typical are core shear failures (c,d), delamination (b,c), and facesheet yield (e). Even the ideal scenario, shown in (a), is not desirable, because the facesheet penetrates deeply into the metal foam [15].

Some of the aforementioned failures are due to the concentrated loads exerted by the indenter. Hydroforming was attempted in response to those failures, since the uniformly applied water pressure removes the necessity of point loads and can create more smooth curvatures [17]. The experiments that were conducted were successful in avoiding indentation or core-shear failures, but at the same time the process significantly compressed the foam core and reduced its compressibility. Also, the process can only be used for sandwich panels, as the metal foam structure is too fragile to withstand the high water pressures.

The only manufacturing process that can avoid all of the aforementioned failures is laser forming. Laser forming is a non-contact process that causes mechanical deformation through

laser-induced heating and the subsequent thermal expansion. The process does not need any part-specific tools and can generate a wide range of part geometries. Any part sizes from small electronic chip components to large-sized panels can be laser formed, and the process fills the low to medium production volume niche that the powder metallurgy and 3D printing processes fail to occupy.

1.4 Laser Forming

The laser forming process itself is extremely straightforward. The specimen is loosely clamped as shown in Fig. 6, and the laser is scanned over the entire length of the specimen at a scan speed v , power P , and laser spot size D . Material parameters include the sheet thickness t and the sheet size, along with the material-specific properties.

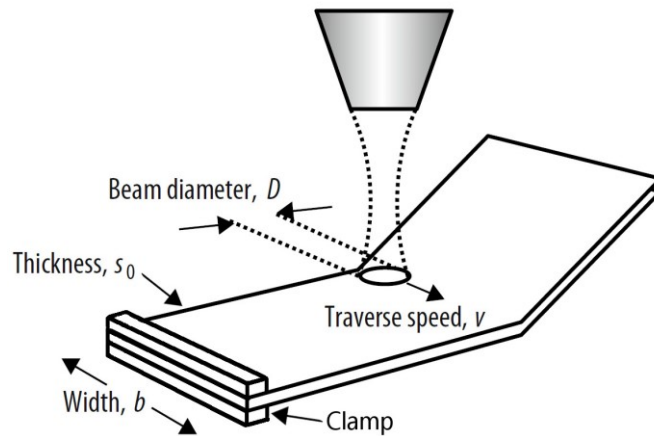


Figure 6: Laser forming setup. The specimen is loosely clamped on one side and laser scanned across the entire width at a diameter D , scan speed v and power P [18]. Depending on the bending mechanism, the specimen may bend towards or away from the laser.

For more than three decades, countless studies have been performed on laser forming, and the process has been used to bend a variety of materials including steel, aluminum, nickel, chromium, silicon [19], and even bi and tri-layer materials [20], and metal-polymer composites [21]. The process is best understood for solid sheet metals, and three major thermo-mechanical mechanisms have been devised that explain the bending behavior [22].

The first mechanism, called temperature gradient mechanism (TGM), governs the case where the sheet thickness is about the same size or greater than the laser spot size. In that case, a steep temperature gradient establishes through the sheet thickness during forming, and only the portion immediately underneath the laser heats up significantly. This section tries to expand, but is hindered from doing so by the “cold” surrounding material. Instead of expanding, the material is plastically compressed, which shortens the top section of the sheet relative to the bottom section. The same phenomenon occurs along the entire laser scan, and the sheet ultimately bends towards the laser.

The second mechanism, called buckling mechanism (BM), governs the scenario where the laser spot size is much greater than the sheet thickness. As a consequence, the entire sheet heats up uniformly throughout the thickness and tries to expand. This time, the heated segment is restricted laterally, giving rise to uniaxial compressive stresses that buckle the heated material away or towards the laser. The buckled region is translated along the laser scan, and the sheet ultimately bends in the direction opposite to the buckling direction.

The third mechanism, called upsetting mechanism (UM), governs the same scenario as the BM, except that the material is geometrically prevented from buckling. Instead of buckling, the section thickens, which causes bending for geometries such as pipes [23] or sandwich panels, as shown in Chapter 4.

Other bending mechanisms have been proposed that are slightly modified versions of the above three mechanisms. Examples include the coupling mechanism (CM), which is combination of the TGM and the UM [24], the martensite expansion mechanism (MEM) that includes martensite formation in steels, or the residual stress point/relaxation mechanisms

(RSPM, RSRM) that address the residual stresses that develop during stationary laser pulses or laser scans [25].

In this decade, laser forming has first been used to bend metal foams. Several studies have been published, showing that open-cell [26,27], closed-cell [28], and closed-cell foams with exterior skins [29] can be bent up to 45° and beyond. Successful results were reported with different foam structures [28], and with porosities ranging from 30% up to 90% [26,30]. Most of these studies assumed, without experimental or numerical proof, that the TGM governs bending of the metal foam, due to the large sheet thickness. However, this study analyzed the bending mechanisms with more rigor and found that none of the three standard bending mechanisms (TGM, BM, UM) directly apply to laser forming of metal foam and metal foam sandwich panels. Instead, a modified temperature gradient mechanism (MTGM) holds for laser forming of metal foam (see chapters 2 & 3), and laser forming of sandwich panels with metal foam cores is governed by a combination of mechanisms (see chapter 4).

1.5 Experiments

1.5.1 Materials

1.5.1.1 AlSi7 Metal Foam

In chapters 2 and 3, an aluminum foam with 7 weight percent silicon was used that is shown in Fig. 7. The foam was manufactured by melting an aluminum-silicon alloy, adding calcium to increase the viscosity, and subsequently adding a “foaming agent” TiH₂. When subjected to the heat, the foaming agent releases a hydrogen gas and creates cavities inside the aluminum melt. As time progresses, an increasing amount of cavities are generated, and the existing cavities grow larger (hence the density decreases). When the desired pore size and density are reached,

the material is cooled down, and the metallic foam is obtained. Throughout the thesis, this method is referred to as the “melt-foaming method” [31].



Figure 7: Metal foam that was used in chapters 2 & 3.

The foam used in this project had a density of 279 kg/m^3 and an average pore size of 4 mm. The silicon was added to increase the stiffness and strength of the foam. Side effects of adding silicon are a reduced thermal conductivity and a reduced thermal expansion coefficient. The AlSi7 alloy material can be categorized as a hypo-eutectic silicon alloy, since the silicon weight percentage is below the eutectic 12.6 wt %, as shown in the phase diagram of Fig. 8.

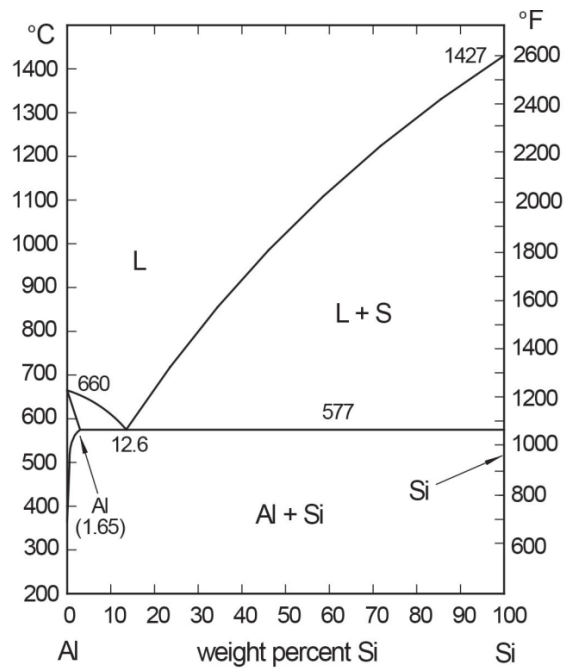


Figure 8: Phase diagram for a binary aluminum-silicon alloy system [32].

The major phases that are present are an Al-rich α -phase, a eutectic β -phase as well as Si-rich lamellas as shown schematically in Fig. 9(a). A typical microscopy picture is shown in Fig. 9(b).

The density and structure of the lamellas depends on the rate at which the alloy was cooled.

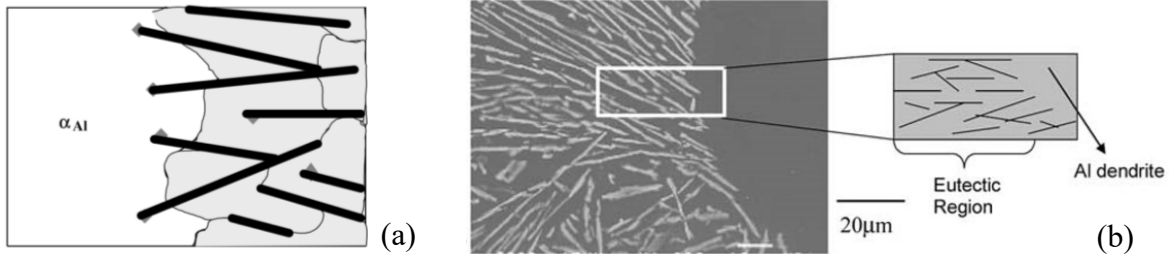


Figure 9: (a) Schematic of the structure of a hypo-eutectic Al-Si alloy, showing the Al-rich α -phase on the left, the grainy eutectic β -phase on the right as well as Si-rich lamellas in black. (b) Optical microscopy picture of a hypo-eutectic Al-Si alloy, along with schematic showing the same structure as in (a) [33].

Due to its low density, the metal foam has a low thermal conductivity of around 9 W/mK compared to the bulk thermal conductivity of 170 W/mK. The specific heat and thermal expansion coefficient are roughly the same as in solid AlSi7, but Young's Modulus is smaller by a factor of 27. Additionally, the flow stress is roughly an order of magnitude smaller than the flow stress of the corresponding solid, and the compressive stress-strain curve has a characteristic plateau (segment 2 in Fig. 10) that is responsible for the excellent shock absorption capacity of metal foam.

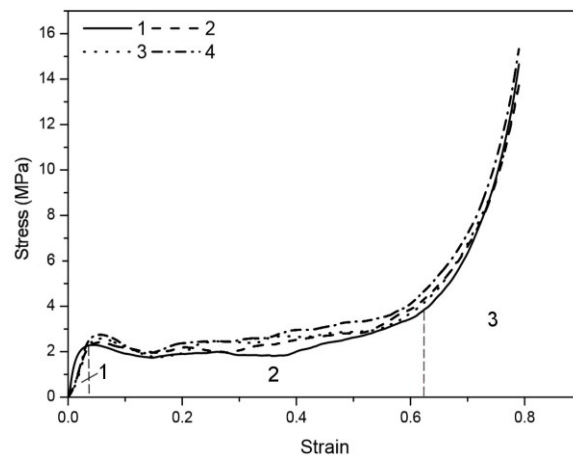


Figure 10: Compressive stress-strain curve of metal foam. Initially, the response is almost linear in segment 1. In segment 2, the cells crush and absorb energy. In segment 3, the foam starts to densify, causing an exponential increase in the compressive stress [34].

1.5.1.2 Sandwich Panel Foam Core & Facesheets

In chapter 4, a sandwich panel with an AlSi10 foam core was used (10 wt % silicon). This metal foam type also falls into the category of hypo-eutectic alloys and its properties are very similar to the foam properties discussed in Sec. 1.5.1.1. The facesheets were made of the AW 5005 alloy, containing magnesium as the major alloy element. The sandwich was manufactured using a powder-metallurgy method that was already briefly introduced in Sec. 1.3. In this process, AlSi10 and foaming agent powder mixture are compressed into a precursor and inserted between two AW 5005 facesheets. The assembly is then heated in a furnace, during which the foaming agent releases a gas and turns the precursor into a foam. Since the lateral expansion of the sandwich is restricted, the foam and facesheets are subjected to both high temperatures and pressures, promoting the formation of metallic bonds between the foam and the facesheets that generate a strong adhesion between the components [9]. The resulting sandwich panel is shown in Fig. 11(a) and has an average density and pore size of around 700 kg/m^3 and 2 mm, respectively. Throughout the remainder of this thesis, this sandwich type is referred to as *type I* sandwich panel.

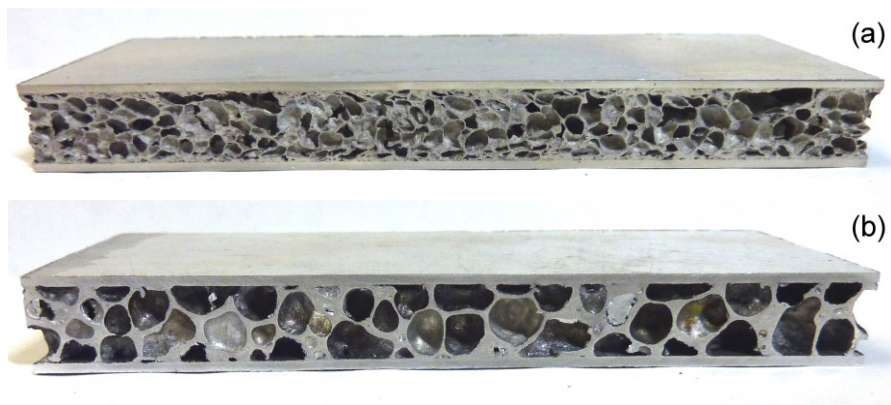


Figure 11: (a) Type I sandwich panel that was analyzed in chapter 4. (b) Type II sandwich panel that was compared with the type I sandwich panel in chapter 5.

In chapter 5, a second sandwich panel type was introduced, shown in Fig. 11(b). It is referred to as *type II* sandwich panel, has different material compositions and was manufactured in a fundamentally different way. The facesheet consisted of Al 1060, whose thermal properties are very similar to the ones of the AW 5005 alloy that was used for the type I facesheet. The mechanical properties of Al 1060 differ significantly, however, and its flow stress is much lower than in AW 5005. Moreover, Al 1060 undergoes substantially more thermal softening than AW 5005.

Table 1: Al 1060 undergoes more thermal softening and has a much lower flow stress than AW 5005.

		AW 5005	Al 1060 (Al 99.7)
Young's Modulus (GPa)	Room temp	69.5	70.7
	200°C	66.5	63.2
	400°C	64	52.6
Flow Stress (MPa)	Room temp	82.4	43.3
	200°C	58.6	27.5
	400°C	33.6	11.3

The type II foam core differs from the type I foam core both in its composition and manufacturing method. The foam was manufactured using the same method as the foam in chapters 1 and 2, except that no silicon was added. The average cavity size was still around 4 mm, and the foam had a high aluminum content (> 99.7 wt %). Due to its high purity, the type II foam core material is softer than the type I foam core material.

Table 2: The type I foam core (AlSi10) is slightly stiffer and undergoes less thermal softening than the type II foam core (Al 99.7).

		AlSi10	Al 99.7
Young's Modulus (GPa)	Room temp	73.9	70.7
	200°C	68.2	63.2
	400°C	58.0	52.6
Flow Stress (MPa)	Room temp	55.9	43.3
	200°C	40.2	27.5
	400°C	16.8	11.3

Finally, the type II sandwich panel used a different facesheet adhesion method than the type I sandwich panel. Unlike in the type I sandwich panel, where a bond between the facesheets and the foam core was established during the foaming process, the bond was established in a separate step in the type II sandwich panel. The bond was achieved by sandwiching the foam between the facesheets after adding some pure aluminum powder to the interface. The assembly was then heated under a vacuum condition (*vacuum sintering*) near the melting temperature of aluminum, causing the powder to sinter and establish a metallic bond between the facesheets and the foam core.

All the specimens in the study were cut to a length of 100 mm, a width of 35 mm, and a thickness of 10 mm, in order to allow for a comparison with the results obtained in previous studies [28,29].

1.5.2 Experimental Methods

In chapters 2 and 3, the AlSi7 foam was laser formed using a Nd:YAG laser with a maximum power of $P_{max} = 2,000$ W and a wavelength of $\lambda = 1,064$ nm. The laser was used in a continuous wave (CW) mode. To increase the laser absorption and avoid oxidation of the metal surface, the specimens were spray-painted with graphite paint and tested under a protective nitrogen environment, respectively. The power was varied between $P = 30 - 180$ W, the scan speed was varied between $v = 2.5 - 10$ mm/s, and the spot size was kept constant at $D = 12$ mm.

In chapter 4, the sandwich panel with the AlSi10 foam core was laser formed using a CO₂ laser with a maximum power of $P_{max} = 1,500$ W and a wavelength of $\lambda = 10,600$ nm. The laser was again used in CW mode, and the specimens were spray painted with graphite paint. The power was maintained at $P = 800$ W, the scan speed was varied between $v = 10 - 30$ mm/s, and the spot size was varied between $D = 4 - 12$ mm.

In all cases the deflection of the specimens were measured using a dial indicator. When measuring the deflection of the AlSi7 foam, a thin metal sheets was attached to the surface at the location of the measurement to prevent the dial indicator to penetrate into cavities and distort the results.

1.5.2.1 Non-Dimensional Analysis of Process Conditions

In chapters 4-6, it is shown that metal foam sandwich panels can be laser formed using two fundamentally different process parameter regimes. The first regime involves a laser spot size of $D = 4$ mm and a scan speed of $v = 30$ mm/s, while the second regime involves a laser spot size of $D = 12$ mm and a scan speed of $v = 10$ mm/s. The power was $P = 800$ W in both regimes to maintain a constant area energy. Due to the constant energy input, the two regimes could directly be compared, and statements could be made about their relative efficiencies.

In order to define in a non-dimensional manner how these process parameters relate to the specimen geometry, a non-dimensional Buckingham Pi analysis was performed. The non-dimensional relations were obtained by assuming that the bending angle α_B is a function of the laser absorption coefficient A , the power P , the scan speed v , the spot size D , the linear expansion coefficient α_{th} , the sheet thickness s , the specific heat c_p , and the density ρ .

$$\alpha_B = f(A, P, v, D, \rho, \alpha_{th}, s, c_p) \quad (1.1)$$

All of these nine parameters ($n = 9$) were described in terms of four units ($K = 4$), the mass M , the length L , the time t , and the temperature T .

Table 3: The nine dimensional parameters that are used for the Buckingham Pi analysis. In the second row, the regular material units are shown, whereas in the third row the units are written in terms of the four fundamental units, the mass M , the length L , the time t , and the temperature T .

Parameter	α_B	A	P	v	D	α_{th}	s	c_p	ρ
SI Unit	-	-	$\left[\frac{J}{s} \right]$	$\left[\frac{m}{s} \right]$	$[m]$	$\left[\frac{1}{K} \right]$	$[m]$	$\left[\frac{J}{kgK} \right]$	$\left[\frac{kg}{m^3} \right]$

Alt. Unit	-	-	$\left[\frac{ML^2}{t^3}\right]$	$\left[\frac{L}{t}\right]$	$[L]$	$\left[\frac{I}{T}\right]$	$[L]$	$\left[\frac{L^2}{Tt^2}\right]$	$\left[\frac{M}{L^3}\right]$
------------------	---	---	---------------------------------	----------------------------	-------	----------------------------	-------	---------------------------------	------------------------------

Hence, this analysis yielded $n - K = 5$ non-dimensional parameters. The unique parameters in the above table are the power, the scan speed, the spot size, and the thermal expansion coefficient. The remaining parameters, with the exception of the bending angle and the absorption coefficient, can be described in terms of the unique parameters. The first two non-dimensional parameters of the Buckingham Pi analysis are simply $\Pi_1 = \alpha_B$ and $\Pi_2 = A$. The third non-dimensional parameter was calculated as follows:

$$\Pi_3 = P^a v^b D^c \alpha_{th}^d S \quad \text{and} \quad \left(\frac{ML^2}{t^3}\right)^a \left(\frac{L}{t}\right)^b L^c \left(\frac{I}{T}\right)^d L = M^0 t^0 L^0 T^0 \quad (1.2)$$

Equating the exponential parameters in the second relation and solving for a , b , c , and d yields:

$$\left. \begin{array}{l} a = b = c = 0 \\ c = -1 \end{array} \right\} \Rightarrow \Pi_3 = \frac{S}{D} \quad (1.3)$$

Similarly, the fourth non-dimensional parameter was evaluated:

$$\Pi_4 = P^e v^f D^g \alpha_{th}^h c_p \quad \text{and} \quad \left(\frac{ML^2}{t^3}\right)^e \left(\frac{L}{t}\right)^f L^g \left(\frac{I}{T}\right)^h \left(\frac{L^2}{Tt^2}\right) = M^0 t^0 L^0 T^0 \quad (1.4)$$

Solving for e , f , g , and h :

$$\left. \begin{array}{l} e = g = 0 \\ f = -2 \\ h = -1 \end{array} \right\} \Rightarrow \Pi_4 = \frac{c_p}{\alpha_{th} v^2} \quad (1.5)$$

Finally, the fifth non-dimensional parameter was evaluated:

$$\Pi_5 = P^i v^j D^k \alpha_{th}^l \rho \quad \text{and} \quad \left(\frac{ML^2}{t^3}\right)^i \left(\frac{L}{t}\right)^j L^k \left(\frac{I}{T}\right)^l \left(\frac{M}{L^3}\right) = M^0 t^0 L^0 T^0 \quad (1.6)$$

Solving for i , j , k , and l :

$$\left. \begin{array}{l} i = -1 \\ j = 3 \\ k = 2 \\ l = 0 \end{array} \right\} \Rightarrow \Pi_5 = \frac{v^3 D^2 \rho}{P} \quad (1.7)$$

From these calculations, the following relationship may be established:

$$\Pi_1 = f(\Pi_2, \Pi_3, \Pi_4, \Pi_5) \quad (1.8)$$

$$\Rightarrow \alpha_B = f\left(A, \frac{s}{D}, \frac{c_p}{\alpha_{th} v^2}, \frac{v^3 D^2 \rho}{P}\right) \quad (1.9)$$

In essence, the Buckingham Pi analysis allowed reducing the number of variables from nine to five. These five remaining non-dimensional variables can now be used to describe the process conditions in relation to the material parameters. Specifically the third non-dimensional parameter, $\Pi_3 = \frac{s}{D}$, gives meaningful insight into the relative size of the laser spot. In the first regime, the laser spot of $D = 4$ mm yielded $\Pi_3 = \frac{s}{D} = 2.5$, whereas the second regime with $D = 12$ mm yielded $\Pi_3 = \frac{s}{D} = 0.833$. Therefore, in the first regime the laser spot size was substantially smaller than the sandwich panel sheet thickness, hence the process condition is referred to as *small* throughout the remainder of the thesis. In the second regime, on the other hand, the laser spot size was roughly equal to the sandwich panel thickness, and is henceforth referred to as *large*.

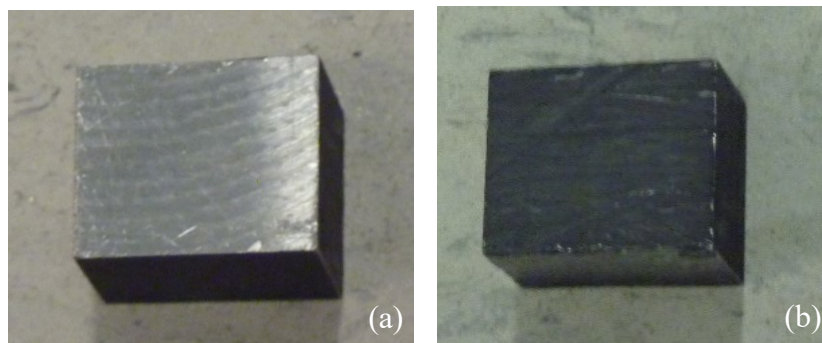
1.5.2.2 Thermal Imaging

Throughout chapters 2, 4, and 5, an infrared (IR) camera was used to obtain temperature measurements during and in between consecutive laser scans. Unlike thermocouples, which have to establish a physical contact with the specimen and have a low spatial and temporal resolution,

thermal imaging is a non-contact method that is capable of measuring the temperatures of even thin cell walls at a high frame rate of 120 Hz.

In order to obtain reliable temperature measurements, the material emissivity had to be calibrated. The emissivity represents the amount of infrared irradiation any body emits that has a higher temperature than 0 K. The amount of irradiation is highest if the tested material is a perfect black body (which also absorbs 100 % of incident radiation), represented by an emissivity $\varepsilon = 1$, and the emissivity is zero ($\varepsilon = 0$) for a perfect white body. Any material with an emissivity of $0 < \varepsilon < 1$ is considered a grey body.

In many materials, including aluminum, the emissivity is not only a strong function of temperature, but also highly dependent on the surface finish. This is demonstrated in Fig. 12(c), showing an aluminum cube (Fig. 12(a)) with side length of 15 mm that was uniformly heated to 100°C in a tube furnace. Despite the uniform temperature of the block, strong temperature variations are visible in the thermal image due to the shiny surface finish of the aluminum block. Uniform temperature measurements, shown in Fig. 12(d), can only be obtained when spray-painting the block with black graphite paint (as shown in Fig. 12(b)), which is a material that has a very high emissivity.



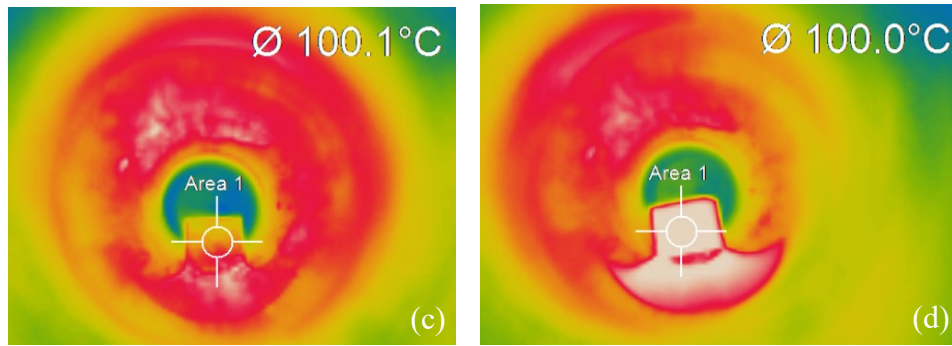


Figure 12: (a) Uncoated aluminum block, (b) aluminum block coated with high-emissivity graphite paint. (c) Non-uniform temperature distribution measured on the shiny block shown in (a), and (d) uniform temperature distribution measured on the coated block shown in (b).

The additional benefit of spray-painting the surface with black graphite paint is that unlike aluminum, the paint has a nearly constant emissivity over a higher temperature range. This is demonstrated in Figs. 13(a) – Figs.13(d), showing the temperature readings of the aluminum block after being heated to 100°C, 200°C, 300°C and 400°C in a tube furnace. In each case, the emissivity value was left constant at $\epsilon = 0.92$, and a good agreement with the furnace temperature was obtained in each case.

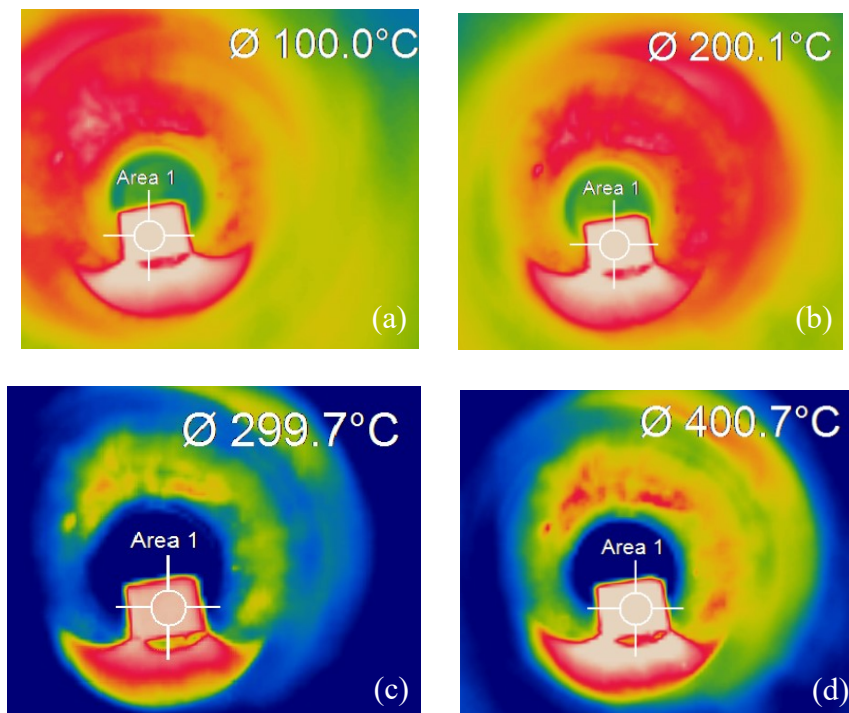


Figure 13: Temperature reading on the painted aluminum block (leaving ε constant) after heating the block in the tube furnace to (a) 100°C, (b) 200°C, (c) 300°C, and (d) 400°C.

In chapter 2, the IR camera was used without filter since laser forming was performed at a wavelength ($\lambda_{Nd:Yag} = 1,064$ nm) outside of the measurement range of 7 – 13 μm . In chapter 4, on the other hand, the IR camera was used with a CO₂ laser whose wavelength of $\lambda_{CO_2} = 10.6$ μm was exactly within the measurement range. To prevent damaging the IR camera, a wide band pass filter was used from EOC (IWBP 7650-10000) with a cut-on wavelength of $7,650 \pm 100$ nm and a cut-off wavelength of $10,000 \pm 100$ nm. The filter passed all the irradiation between 7,650 – 10,000 nm and rejected all the irradiation outside of this range.

The consequence of using a filter was that the camera measurement had to be re-calibrated. The IR camera is constructed such that its detectors equally absorb all the irradiances between 7 – 13 μm . The camera thus comes up with an average incident irradiation value, which is then used to calculate the temperature based on calibration tests performed by the manufacturer. When using a filter, the absorption window is reduced, and hence the camera comes up with an average irradiation value based on a reduced amount of incident irradiation. If the same irradiation – temperature relation is used, the camera returns a temperature value that is too low. To correct for the absorption window reduction, the aluminum block from Figs. 12 and 13 was again heated to different temperatures in a tube furnace, and the measured temperatures were compared with the actual temperatures. Based on the deviations, a temperature-dependent scaling factor was obtained, which was multiplied to the temperature measurements that were performed in chapter 4.

1.5.2.3 Digital Image Correlation

In chapter 3, the strain distributions in metal foam were determined using digital image correlation (DIC). DIC is a non-contact measurement technique that measures the displacements

in a material based on the change of a speckle-pattern. From the displacement field, different types of strain measures are then calculated.

The requirement for DIC is a random speckle pattern with the highest possible contrast to the background color (typically black speckles on a white background) [35]. Moreover, the average speckle should cover 3 – 5 pixels on a digital camera [36]. During the material deformation, sequential images are taken and compared with one another. For a small amount of deformation, all images are compared to the initial reference image of the un-deformed body. If the deformations are very large, the difference between the current image and the image is too great, and no correlation can be established. In those cases, each image is compared with the previous image, rather than the initial reference image. This method is called “incremental correlation”.

Regardless of the type of correlation, the DIC software runs the same algorithms to compare the digital images. The images are divided into subsets, whose size is specified by the user, and it is analyzed whether each subset of the picture has been translated from the reference configuration to the current configuration (i.e. from one state of deformation to the next). This is done by translating the subset by a step-size, whose value is also specified by the user. The comparison between the two images is initiated at the so-called “seed”, which is placed at a representative location where the deformations are comparatively small. In a dogbone specimen, for instance, the seed would not be placed right inside the necking region, but outside in a region where the deformation is moderate. The DIC software then starts the image comparison at the seed, using the parameters specified by the user, and moves the subset around until the average deviation in the grey levels becomes minimal between the two images. Once the position with the best agreement has been found, the displacement of that part of the image has been evaluated,

and it is moved on to the next subset one step-size away, until the translations are determined over the entire measurement area.

After completing the translational analysis, the procedure is repeated, but this time it is evaluated whether there has been a rotation between the reference configuration and the current configuration. In order to do that, the subset is translated to the position of best fit, evaluated in the previous step, and is rotated by different degrees. For each rotation, the deviation from the reference is evaluated, and the rotation with the best agreement is determined. The same process is repeated once more, evaluating the amount of normal stretching and shear deformation the subset has undergone. Using those four metrics, the full displacement and rotational fields are determined over the entire speckle surface, and the corresponding strain fields can be calculated.

The DIC technique has been developed for cases where the deformation takes place inside a plane that is perpendicular to the digital camera, as is for instance the case in a dogbone test. Rather often, however, the deformations are not restricted to a single plane, and the tested specimen translates and rotates away from or towards the camera. These translations and rotations will cause additional differences between the compared images and thus yield “erroneous” strains during the DIC measurement. To correct for those strains, calibration tests need to be performed in which the strain magnitudes are determined during translations and rotations without actual material deformation [37].

In experiments performed in chapter 3, data was extracted from the stationary portion of the specimen, not the portion that rotates away from the camera, to avoid out-of-plane effects (see Fig. 14). In DIC measurements of 4 – point bending experiments (chapter 3), on the other hand, out-of-plane translations had to be accounted for using the aforementioned calibration technique. In all DIC experiments, the strain values were averaged over 5 mm from the bending axis to

account for the irregularity in the foam structure, as well as the fact that some cell walls were too thin for a measurement to be possible.

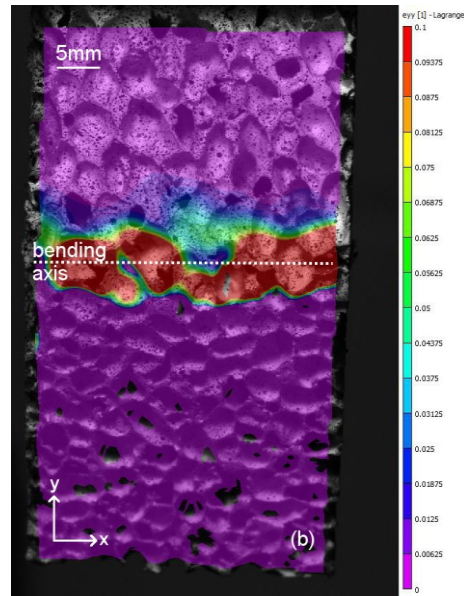


Figure 14: Strain distribution in y -direction after laser forming a metal foam specimen to a 45 degree angle. The data was only extracted from the stationary part above the bending axis.

1.6 Simulation

1.6.1 Uncoupling

In most cases, the thermal and mechanical parts of the laser forming simulation are performed separately. The thermal analysis is performed first, and its results are used as an initial condition in the mechanical analysis that is performed subsequently. This approach is more computationally efficient than performing a coupled thermo-mechanical analysis, and it is valid provided that the mechanical analysis does not affect the thermal analysis, i.e. the mechanical deformation does not cause a significant temperature increase. In laser forming, this condition is obviously met, since any heat generated by mechanical deformation is negligible compared to the tremendous heat input of the laser source. Nevertheless, this point can be painstakingly proved with an excessively long derivation, to satisfy all skeptics that like an overdose of theory.

To prove this point, we start with the balance of energy, which is the basis from which the governing equation of thermo-elasticity can be obtained. First, the balance of energy is written in integral form:

$$\frac{d}{dt} \int_V \rho \left(\varepsilon + \frac{1}{2} \underline{v} \underline{v} \right) dV = - \int_S \rho \left(\varepsilon + \frac{1}{2} \underline{v} \underline{v} \right) (\underline{v} \underline{n}) dS + \int_S \underline{v} \underline{t} dS + \int_V \underline{v} \rho \underline{b} dV - \int_S \underline{q} \underline{n} dS + \int_V \rho r dV \quad (1.10)$$

where ρ is the density, ε the internal energy, v the velocity, S the control surface, V the volume, b the body force, n the normal vector, t the traction, q the heat flux, and r the heat generation. This formulation can be converted to the differential form:

$$\rho \frac{D\varepsilon}{Dt} = \underline{T} : \text{grad}(\underline{v}) - \text{div}(\underline{q}) + \rho r \quad (1.11)$$

where T is the stress tensor. Moreover, the velocity gradient can be rewritten in terms of the strain rate $\underline{\dot{E}}_{ij}$ and the rotation rate $\underline{\dot{\Omega}}_{ij}$:

$$\text{grad}(\underline{v}) = v_{i,j} = \frac{1}{2} (v_{i,j} + v_{j,i}) + \frac{1}{2} (v_{i,j} - v_{j,i}) = \underline{\dot{E}}_{ij} + \underline{\dot{\Omega}}_{ij} \quad (1.12)$$

The double product of the stress tensor and the rotation tensor is zero since the stress tensor is symmetric but the rotation tensor is anti-symmetric. Hence we obtain:

$$\rho \frac{D\varepsilon}{Dt} = \underline{T} : \underline{\dot{E}} - \text{div}(\underline{q}) + \rho r \quad (1.13)$$

Further relations can be derived from the axiom of entropy inequality:

$$\frac{d}{dt} \int_V \rho \eta dV \geq - \int_S \rho \eta (\underline{v} \underline{n}) dS - \int_S \frac{1}{\theta} \underline{q} \underline{n} dS + \int_V \rho \frac{r}{\theta} dV \quad (1.14)$$

where η is the entropy and θ is the temperature. This relation may also be written in differential form as:

$$\rho \frac{D\eta}{Dt} + \text{div} \left(\frac{\underline{q}}{\theta} \right) - \rho \frac{r}{\theta} \geq 0 \quad (1.15)$$

The material derivative in the entropy η can be written in terms of the internal energy ε , the free energy density ψ and the temperature θ using the relation $\eta = \frac{\varepsilon - \psi}{\theta}$:

$$\underline{T} : \underline{D} - \rho \left(\frac{D\psi}{Dt} + \eta \frac{D\theta}{Dt} \right) - \frac{q}{\theta} \text{grad}(\theta) \geq 0 \quad (1.16)$$

At this point it is assumed that the free energy density ψ is a function of only the Cauchy Green deformation tensor C and the temperature θ , $\psi = \psi(\underline{C}, \theta)$. After going through the derivatives, the following relation is obtained:

$$-\rho \left(\frac{\partial \psi}{\partial \theta} + \eta \right) \frac{D\theta}{Dt} - \frac{1}{\theta} q \text{grad}(\theta) + \left(\underline{T} + 2\rho \underline{F} \frac{\partial \psi}{\partial \underline{C}} \underline{F}^T \right) : \underline{D} \geq 0 \quad (1.17)$$

This inequality must hold for arbitrary changes in \underline{D} (which is the symmetric part of $\text{grad}(\underline{v}) = \underline{L}$), $\frac{D\theta}{Dt}$ and $\text{grad}(\theta)$. Therefore, the contents of the brackets must be zero.

Additionally, we make the assumption that both the strains and rotations are infinitesimally small, which allows writing the equations on the right:

$$\left. \begin{array}{l} (1) \eta = -\frac{\partial \psi}{\partial \theta} \\ (2) \underline{q} = \underline{0} \\ (3) \underline{T} = 2\rho \underline{F} \frac{\partial \psi}{\partial \underline{C}} \underline{F}^T \end{array} \right\} \begin{array}{l} \text{small strain \& rotations} \\ \underline{F} \approx \underline{I} \\ d\underline{C} = 2d\underline{E} \end{array} \left\{ \begin{array}{l} (1) \eta = -\frac{\partial \psi}{\partial \theta} \\ (2) \underline{q} = \underline{0} \\ (3) \underline{T} \approx \rho \frac{\partial \psi}{\partial \underline{E}} \end{array} \right. \quad (1.18)$$

At this point we assume that the material is isotropic, and thus the free energy density function must be invariant under a transformation \underline{Q} (i.e. $\psi(\underline{Q} \cdot \underline{E} \cdot \underline{Q}^T) = \psi(\underline{E})$). It is known that the three invariants of the strain tensor are isotropic function, however, the third invariant $I_3 = \det(\underline{E})$ produces cubic terms that become non-linear. Therefore, the free energy density

function is chosen to only be a function of the first two invariants. Moreover, unlike in elasticity, the free energy density function is also chosen to be a function of temperature.

$$\psi(\underline{E}, \theta) = \psi(I_1, I_2, \theta) \quad (1.19)$$

Since the I_2 contains I_1 , they can just be replaced by J_1 and J_2 :

$$\left. \begin{aligned} I_1 &= \text{tr}(\underline{E}) \\ I_2 &= \frac{1}{2} \left[(\text{tr}(\underline{E}))^2 - \text{tr}(\underline{E}^2) \right] = \frac{1}{2} \left[I_1^2 - \text{tr}(\underline{E}^2) \right] \end{aligned} \right\} \Rightarrow \begin{aligned} J_1 &= \text{tr}(\underline{E}) \\ J_2 &= \text{tr}(\underline{E}^2) \end{aligned} \quad (1.20)$$

The free energy density function may now be written in terms of those two invariants and the temperature:

$$\psi(J_1, J_2, \theta) = \frac{1}{\rho} \left[\frac{\lambda}{2} J_1^2 + \mu J_2 - (3\lambda + 2\mu) \alpha T_0 \theta J_1 \right] \quad (1.21)$$

The derivative of the free energy density with respect to the strain tensor is:

$$\begin{aligned} \frac{\partial \psi}{\partial \underline{E}} &= \frac{1}{\rho} \left[\lambda J_1 \frac{\partial J_1}{\partial \underline{E}} + \mu \frac{\partial J_2}{\partial \underline{E}} - (3\lambda + 2\mu) \alpha \theta \frac{\partial J_1}{\partial \underline{E}} \right] \\ &= \frac{1}{\rho} \left[\lambda (\text{tr} \underline{E}) \underline{I} + 2\mu \underline{E} - (3\lambda + 2\mu) \alpha \theta \underline{I} \right] \end{aligned} \quad (1.22)$$

and the derivatives of the invariants are:

$$\begin{aligned} \left(\frac{\partial J_1}{\partial \underline{E}} \right)_{ij} &= \frac{\partial E_{kk}}{\partial E_{ij}} = \delta_{ki} \delta_{kj} = \delta_{ij} = (\underline{I})_{ij} \\ \left(\frac{\partial J_2}{\partial \underline{E}} \right)_{ij} &= \frac{\partial (E_{kl} E_{lk})}{\partial E_{ij}} = \frac{\partial E_{kl}}{\partial E_{ij}} E_{lk} + E_{kl} \frac{\partial E_{lk}}{\partial E_{ij}} = \delta_{ki} \delta_{lj} E_{lk} + E_{kl} \delta_{li} \delta_{kj} = 2E_{ij} = 2(\underline{E})_{ij} \end{aligned} \quad (1.23)$$

This may be substituted into eq. 1.18 to obtain the stress as a function of strain and temperature:

$$\underline{T} = \rho \frac{\partial \psi}{\partial \underline{E}} = \lambda (\text{tr} \underline{E}) \underline{I} + 2\mu \underline{E} - (3\lambda + 2\mu) \alpha \theta \underline{I} \quad (1.24)$$

Now we can go back to the differential form of the energy equation and derive the governing equation of thermo-elasticity:

$$\rho \frac{D\varepsilon}{Dt} = \underline{T} : \dot{\underline{E}} - \text{div}(\underline{q}) + \rho r \quad (1.25)$$

The tensor double product is equal to:

$$\begin{aligned} \underline{T} : \dot{\underline{E}} &= [\lambda(\text{tr}\underline{E})\underline{I} + 2\mu\underline{E} - (3\lambda + 2\mu)\alpha\theta\underline{I}] : \dot{\underline{E}} \\ &= [\lambda(\text{tr}\underline{E})\underline{I} : \dot{\underline{E}} + 2\mu\underline{E} : \dot{\underline{E}} - (3\lambda + 2\mu)\alpha\theta\underline{I} : \dot{\underline{E}}] \end{aligned} \quad (1.26)$$

The divergence of the heat flux may be re-written using Fourier's law:

$$\text{div}(\underline{q})_i = \frac{\partial q_i}{\partial x_i} = \frac{\partial}{\partial x_i} \left(-k \frac{\partial \theta}{\partial x_i} \right) = -k \frac{\partial^2 \theta}{\partial x_i^2} = -k\theta_{,ii} \quad (1.27)$$

Substituting these two expressions back into the energy equation yields:

$$\rho \frac{D\varepsilon}{Dt} = \lambda(\text{tr}\underline{E})\underline{I} : \dot{\underline{E}} + 2\mu\underline{E} : \dot{\underline{E}} - (3\lambda + 2\mu)\alpha\theta\underline{I} : \dot{\underline{E}} - k\theta_{,ii} + \rho r \quad (1.28)$$

The internal energy ε needs to be substituted by the following expression:

$$\varepsilon = \eta\theta + \psi \quad (1.29)$$

Hence the total derivative becomes:

$$\begin{aligned} \frac{D\varepsilon}{Dt} &= \frac{\partial \varepsilon}{\partial \eta} \frac{D\eta}{Dt} + \frac{\partial \varepsilon}{\partial \theta} \frac{D\theta}{Dt} + \frac{\partial \varepsilon}{\partial \psi} \frac{D\psi}{Dt} \\ &= \theta \frac{D\eta}{Dt} + \eta \frac{D\theta}{Dt} + \frac{D\psi}{Dt} \end{aligned} \quad (1.30)$$

As was seen earlier, the entropy is equal to $\eta = -\frac{\partial \psi}{\partial \theta}$. Moreover, it is assumed that the entropy is a function of the small strain tensor and the temperature, $\eta = \eta(\underline{E}, \theta)$, and as a consequence $\dot{\eta} = \dot{\eta}(\dot{\underline{E}}, \dot{\theta})$. Therefore, the material derivatives can be written as:

$$\begin{aligned} \frac{D\varepsilon}{Dt} &= \theta \left(\frac{\partial \eta}{\partial \underline{E}} \dot{\underline{E}} + \frac{\partial \eta}{\partial \theta} \dot{\theta} \right) - \frac{\partial \psi}{\partial \theta} \frac{D\theta}{Dt} + \frac{D\psi}{Dt} \\ &= -\theta \frac{\partial^2 \psi}{\partial \theta^2} \dot{\theta} + \frac{1}{\rho} [\lambda(\text{tr}\underline{E})\underline{I} : \dot{\underline{E}} + 2\mu\underline{E} : \dot{\underline{E}} - (3\lambda + 2\mu)\alpha\theta_0 \underline{J}_1] \end{aligned} \quad (1.31)$$

This expression is substituted back into the energy equation to obtain the governing equation:

$$-\theta \frac{\partial^2 \psi}{\partial \theta^2} \dot{\theta} = -(3\lambda + 2\mu)\alpha\theta_0 \dot{J}_1 + k\theta_{,ii} + \rho r \quad (1.32)$$

which after rearranging becomes:

$$k\theta_{,ii} = \rho c_E \dot{\theta} + (3\lambda + 2\mu)\alpha\theta_0 \left(\frac{\dot{E}}{\theta}\right)_{kk} + \rho r \quad (1.33)$$

Another way to think about this governing equation is that it simply represents the heat equation $k\nabla\theta = \rho c_v \dot{\theta} + \rho r$ plus an additional internal variable, which is in this case the strain. The strain cannot be added to the equation in scalar form since it is a tensor. Therefore, the derivative of the trace of the strain tensor is included into the equation, which is a scalar. The term further comes with some constant terms, including the initial temperature θ_0 , the thermal diffusivity α and the Lamé constants λ and μ .

It can be assumed that there is no heat generation within the body, thus ρr can be dropped. Moreover, the coefficient c_E can be replaced by the heat capacity at constant volume c_v . In order to make statements about uncoupling, the equation needs to be rewritten the following way:

$$\begin{aligned} k\theta_{,ii} &= \rho c_v \dot{\theta} + \frac{(3\lambda + 2\mu)(\lambda + 2\mu)}{(3\lambda + 2\mu)(\lambda + 2\mu)} \frac{\alpha \rho^2 c_v \dot{\theta}}{\alpha \rho^2 c_v \dot{\theta}} (3\lambda + 2\mu)\alpha\theta_0 \left(\frac{\dot{E}}{\theta}\right)_{kk} \\ &= \rho c_v \dot{\theta} + \rho c_v \dot{\theta} \frac{(3\lambda + 2\mu)^2 \alpha^2 \theta_0}{\rho^2 c_v \frac{(\lambda + 2\mu)}{\rho}} \left(\frac{\lambda + 2\mu}{3\lambda + 2\mu}\right) \frac{\left(\frac{\dot{E}}{\theta}\right)_{kk}}{\alpha \dot{\theta}} \\ &= \rho c_v \dot{\theta} + \rho c_v \dot{\theta} \frac{(3\lambda + 2\mu)^2 \alpha^2 \theta_0}{\rho^2 c_v v_e^2} \left(\frac{\lambda + 2\mu}{3\lambda + 2\mu}\right) \frac{\left(\frac{\dot{E}}{\theta}\right)_{kk}}{\alpha \dot{\theta}} \end{aligned} \quad (1.34)$$

In the last equation, the substitution $\frac{(\lambda + 2\mu)}{\rho} \equiv v_e^2$ was performed. Furthermore, the substitution

$\frac{(3\lambda + 2\mu)^2 \alpha^2 \theta_0}{\rho^2 c_v v_e^2} = \delta$ can be made to simplify the equation:

$$k\theta_{,ii} = \rho c_v \dot{\theta} \left[1 + \delta \left(\frac{\lambda + 2\mu}{3\lambda + 2\mu} \right) \frac{\left(\frac{\dot{E}}{\theta}\right)_{kk}}{\alpha \dot{\theta}} \right] \quad (1.35)$$

From this equation it can be seen that the coupling term, which contains δ , is negligible if its magnitude is much smaller than 1:

$$\delta \left(\frac{\lambda + 2\mu}{3\lambda + 2\mu} \right) \frac{(\dot{E})_{kk}}{\alpha \dot{\theta}} \ll 1 \quad (1.36)$$

The calculation can be performed using the material properties of aluminum foam:

$$\begin{aligned} E &= 1.5 \text{ GPa (approx.)} \\ \nu &= 0.33 \\ \alpha &= 21.93 \cdot 10^{-6} \frac{1}{K} \\ \rho &= 279 \frac{\text{kg}}{\text{m}^3} \\ c_v &= 837 \frac{\text{J}}{\text{kgK}} \end{aligned} \quad (1.37)$$

The Lamé constants can then be calculated as follows:

$$\begin{aligned} \lambda &= \frac{\nu E}{(1+\nu)(1-2\nu)} = \frac{0.33 \cdot 1.5 \text{ GPa}}{(1+0.33)(1-2 \cdot 0.33)} = 1.095 \text{ GPa} \\ \mu &= \frac{E}{2(1+\nu)} = \frac{1.5 \text{ GPa}}{2(1+0.33)} = 0.564 \text{ GPa} \end{aligned} \quad (1.38)$$

From the Lamé constants ν_i and δ can be calculated:

$$\begin{aligned} \nu_i &= \sqrt{\frac{\lambda + 2\mu}{\rho}} = \sqrt{\frac{(1.095 \cdot 10^9 \text{ Pa}) + 2(0.564 \cdot 10^9 \text{ Pa})}{279 \frac{\text{kg}}{\text{m}^3}}} = 2822.7 \left(\frac{\text{Pa} \cdot \text{m}^3}{\text{kg}} \right)^{1/2} \\ \delta &= \frac{(3\lambda + 2\mu)^2 \alpha^2 \theta_0}{\rho^2 c_v \nu_i^2} = \frac{(3(1.095 \text{ GPa}) + 2(0.564 \text{ GPa}))^2 \left(21.93 \cdot 10^{-6} \frac{1}{K} \right)^2 (300 \text{ K})}{\left(279 \frac{\text{kg}}{\text{m}^3} \right)^2 \left(837 \frac{\text{J}}{\text{kgK}} \right) (2822.7)^2 \frac{\text{Pa} \cdot \text{m}^3}{\text{kg}}} = 0.0054 \end{aligned} \quad (1.39)$$

In laser forming experiments of aluminum foam, both the rate of change of temperature and the strain rate are low. For a standard laser scan at a scan speed of 5mm/s, the maximum temperature

rate of change is $\dot{\theta} = 300 \frac{K}{s}$, and the maximum strain rate in the direction perpendicular to the

scan line is $\dot{E} = 0.025$, yielding:

$$\delta \left(\frac{\lambda + 2\mu}{3\lambda + 2\mu} \right) \frac{\dot{E}}{\alpha \dot{\theta}} = (0.0054) \left(\frac{1.095 \text{ GPa} + 2(0.564 \text{ GPa})}{3(1.095 \text{ GPa}) + 2(0.564 \text{ GPa})} \right) \frac{(0.025)}{\left(21.93 \cdot 10^{-6} \frac{1}{K} \right) \left(300 \frac{K}{s} \right)} = 0.01 \ll 1 \quad (1.40)$$

Since the result of the above equation is much smaller than 1, the term involving δ and the strain rate can be dropped, leaving only the thermal part. Therefore, for the given analysis we are allowed to uncouple the thermal and mechanical problem and treat them independently without inducing much error.

1.6.2 Foam Geometries

In previous laser forming studies that were performed in our lab, the model geometry did not require any special considerations, since the studies were performed on solid metal. When modeling metal foam, however, many geometrical representations with different levels of accuracy may be used, and it had to be evaluated which approach leads to the best results. Three different approaches were contrasted in this thesis, falling into two categories. In the first category, called *explicit models*, the metal foam shape is modeled explicitly, and material properties are assigned of the material that comprises the foam. Two different types of explicit models with different levels of geometrical accuracy were contrasted, a *Kelvin-cell model* and a *Voxel model*, which are explained in more detail in the following sections. In the second category, called *equivalent models*, the foam is simply represented by a rectangular box, and metal foam properties are assigned (i.e. the properties of the combination of solid material and cavities).

1.6.2.1 Kelvin-cell Model

The Kelvin-cell model assumes that a single foam cavity may be approximated by a Kelvin cell, shown in Fig. 15(a), consisting of a combination of hexagons and squares. Additionally, the Kelvin-cell model assumes that the foam can be represented in a repeatable manner, where the Kelvin-cell acts as a “unit” cell that is repeated throughout the model. Hence, many Kelvin cells are aligned and subsequently cut out of a solid model, yielding the model shown in Fig. 15(b).

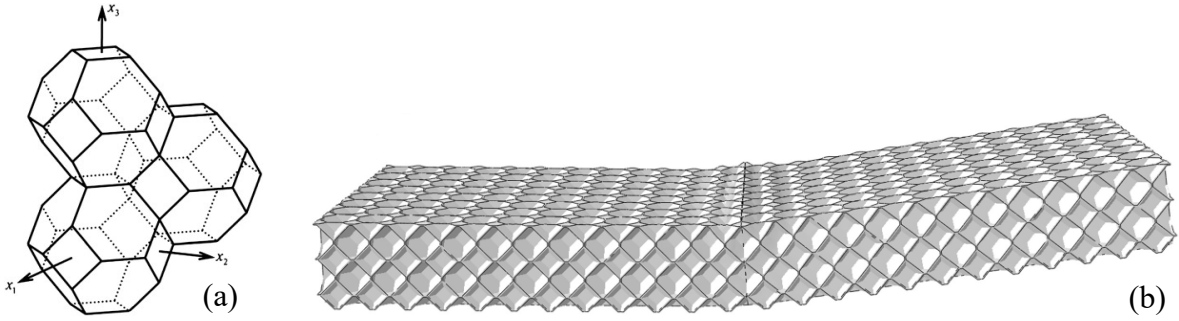


Figure 15: (a) Stacked Kelvin-cell geometries [38]. (b) Kelvin-cell model that was obtained by cutting arrays of Kelvin-cells out of a solid block, after a laser forming simulation.

Since solid material properties are assigned to the model (i.e. bulk aluminum properties), a constitutive relation had to be used that describes the behavior of bulk aluminum. It was assumed that the aluminum is incompressible, and that yielding only occurs due to deviatoric (shear) stresses pursuant the Von Mises Criterion. Mathematically, the yield criterion can be written as:

$$F = \left(\frac{1}{3} \sqrt{(\sigma_1 - \sigma_2)^2 + (\sigma_2 - \sigma_3)^2 + (\sigma_3 - \sigma_1)^2} \right)^{1/2} - \sigma_f = 0 \quad (1.42)$$

where σ_1 , σ_2 , σ_3 are the principal stresses and σ_f is the tensile flow stress (assuming that the tensile and compressive yield strengths are the same). When $F < 0$, the deformation is elastic. When $F = 0$, plastic deformation occurs following the Von Mises flow rule:

$$d\varepsilon^{pl} = d\lambda \cdot \frac{\partial F(\sigma, \kappa)}{\partial \sigma} \quad (1.43)$$

where $d\varepsilon^{pl}$ is the plastic strain increment and $d\lambda$ is the consistency parameter. Plastic strain increments are used instead of plastic strain rates because strain rates are very low and the processes are “infinitely” slow compared with the material relaxation time τ . Finally, it was assumed that hardening is isotropic (strain hardening) pursuant:

$$\sigma_f = K \left(\varepsilon^{pl} \right)^n \quad (1.44)$$

where K is the strength coefficient and n is the strain hardening exponent.

1.6.2.2 Voxel Model

The previously discussed Kelvin-cell model uses a rather crude geometrical approximation to represent the foam geometry and falls short in two regards. First, it assumes that the foam geometry follows a repeated pattern and fails to account for the randomness in the cavity arrangement. Second, the model uses a constant wall thickness throughout, which does not correspond to reality, where solid material is accumulated between cavities.

To address these issues, a model was created that is based on a micro computed tomography (micro-CT) scan, creating an “exact” replica of the foam shape. Several routes may be taken to convert the micro-CT data cloud into a solid model that can be used in finite elements. The first method divides the data cloud into “cubes” and interpolates the surface between high-absorption points (solid) and low-absorption points (air), as shown in Fig. 16(a). Afterwards, a *marching cube* algorithm is employed to stitch the individual interpolated surfaces together to create a closed solid as shown in Fig. 16(b).

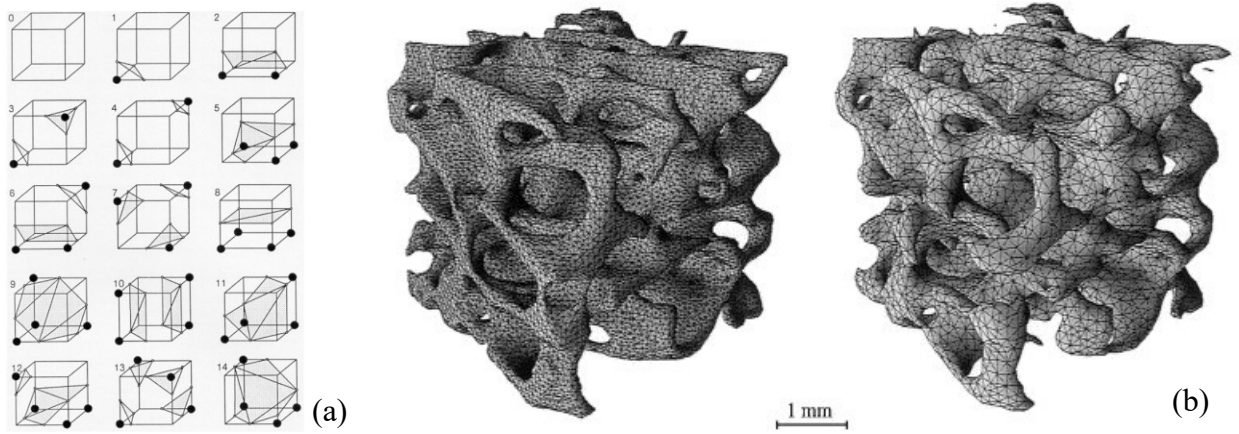


Figure 16: (a) In a micro-CT data cloud, there are high-absorption points for aluminum, shown as black dots, and low-absorption points for air (no dots). For each arrangement within a cube, there is a different interpolation scheme to divide the high-absorption area (solid) from the low-absorption area (air) [39]. The individual interpolated surfaces are then stitched together to obtain a closed volume, shown in (b) [40].

The aforementioned approach is extremely accurate because the resulting parts have a smooth surface and very closely resemble the scanned original. As successful as the approach is in creating models of trabecular bones (Fig. 16(b)), however, it turned out to be not successful when used for metal foam. The reason is that the metal foam features were too small, requiring either an exceedingly dense mesh or a highly accurate micro-CT scan.

In its stead, a different method was used, in which high-absorption data points of the micro-CT data cloud were converted into cubical volumes, called *voxels*. The resulting model is called a *voxel model*, shown in Fig.17. Voxel models were established both for the foam in chapters 2 & 3, as well as for the type I and II sandwich panels in chapter 5.

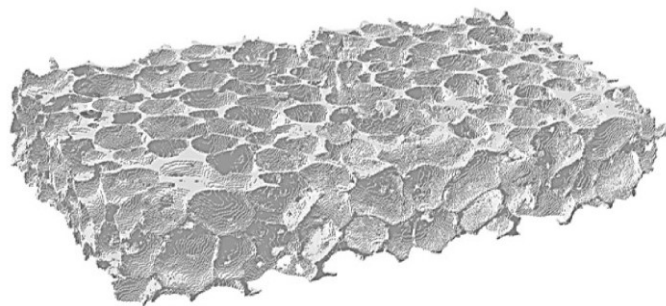


Figure 17: Voxel model of the metal foam that was used in chapters 2 & 3.

Just like the Kelvin-cell model, the voxel model is assigned bulk aluminum properties and is thus described by a bulk aluminum constitutive model. It was again assumed that the material is incompressible and that Von Mises' Criterion holds.

1.6.2.3 Equivalent Model

In the equivalent model, a fundamentally different approach was taken. The foam geometry was simply represented by a solid rectangular box, shown in Fig. 18, and foam properties were assigned.

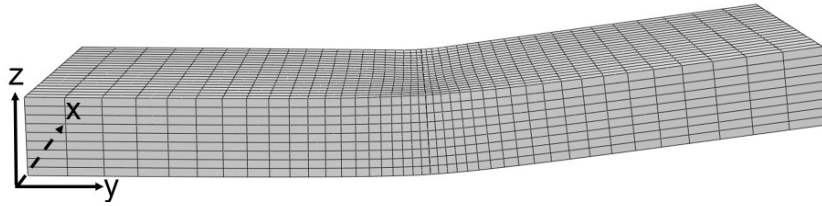


Figure 18: Equivalent model after a laser forming simulation.

Due to the geometrical simplicity, it is possible to model the foam with a fraction of the elements used in the Kelvin-cell and Voxel models, allowing for the simulation of multi-scan processes. The drawback of the equivalent model is that foam properties need to be assigned that are challenging to obtain. Another difficulty is that a foam constitutive model needs to be used, which is more complex than a solid constitutive model, since the foam can yield due to hydrostatic pressure in addition to deviatoric (shear) stresses. This is reflected in the more complicated yield criterion [41]:

$$F = \left[\frac{1}{1 + (\beta/3)^2} (\sigma_e^2 + \beta^2 \sigma_m^2) \right]^{1/2} - Y \leq 0 \quad (1.45)$$

where σ_e is the Von Mises equivalent stress, σ_m the hydrostatic stress, Y the yield strength and β the aspect ratio of the yield surface. When $F < 0$, elastic deformation occurs, while $F = 0$ initiates plastic deformation following the flow rule:

$$\dot{\epsilon}_{ij}^p = \frac{\dot{Y}}{H} \frac{\partial F}{\partial \sigma_{ij}} \quad (1.46)$$

where $\dot{\epsilon}_{ij}^p$ is the plastic strain rate, and H is the hardening modulus defined as:

$$H = \frac{\sigma_e}{\hat{\sigma}} h_\sigma + \left(1 - \frac{\sigma_e}{\hat{\sigma}}\right) h_p \quad (1.47)$$

where h_σ and h_p are the tangent moduli in uniaxial and hydrostatic compression, respectively, and $\hat{\sigma}$ is equal to the first term in the yield criterion. The above *foam crushable constitutive model*, as it is called in Abaqus, makes several assumptions. The first assumption is that the yield surface is symmetric, implying that the yield strength in compression and tension are identical. This assumption has been verified for a similar foam, whose compressive and tensile stress-strain curves are shown in Fig. 19.

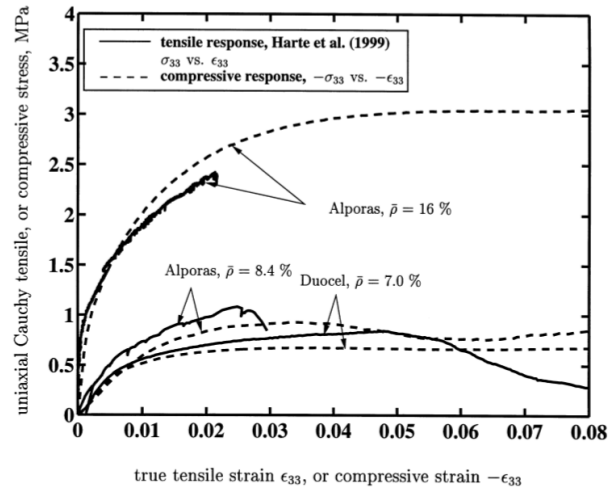


Figure 19: The stress-strain response of metal foam in uniaxial tension and compression is nearly the same up to the tensile failure point [41]. Based on this fact it is possible to assume a symmetric yield surface and isotropic hardening.

The second assumption of the foam crushable constitutive model is that hardening occurs in an isotropic manner. In other words the yield surface grows uniformly in all directions, as shown in Fig. 20.

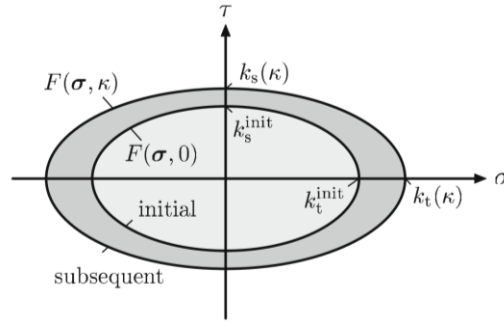


Figure 20: Initial and subsequent yield surfaces of metal foam. The yield surface is symmetric and expands uniformly (the same in tension and compression) due to the isotropic hardening assumption [42].

The implication is that the material hardens the same way in compression and tension. This assumption is obviously incorrect for large strains, since metal foam absorbs a lot of energy in compression and shows a distinct plateau in the stress-strain curve (see Fig. 10), whereas it breaks rather catastrophically in tension at a moderate amount of deformation. However, the assumption is correct if the tensile strains are rather small, which is the case throughout this study as will be discussed in detail in chapter 3.

In Abaqus, the consequence of the aforementioned assumptions is that the user only needs to specify the flow stresses in uniaxial compression. Abaqus automatically assumes that the flow stresses are the same in uniaxial tension.

1.6.3 Heat Transfer through Metal Foam

Thus far, the model geometries were discussed, along with some of the assumptions that were used for each modeling approach. What requires further discussion is how the different heat transfer mechanisms were dealt with. In metal foam, heat is transferred in five different ways: (1) conduction through solid material, (2) gas conduction through cavities, (3) natural convection from the specimen to the ambient, (4) natural convection through the cavities, (5) thermal radiation. (1) and (4) were accounted for in all models. The remaining heat transfer mechanisms were not accounted for, however, because they are negligible compared to (1) and (4) (except in

the equivalent model where they were indirectly lumped into the equivalent thermal conductivity). In the following sections it will be proved that neglecting the said heat transfer mechanisms yields acceptable results.

1.6.3.1 Gas Conduction through Cavities

In some polymers, gas conduction through the cavities can contribute up to 50% of the total heat transfer since the heat conductivity of polymers is extremely low. For aluminum foam, the situation is different because aluminum is highly conductive. Suppose that the equivalent thermal conductivity of aluminum foam $k_{Al,net}$ can be calculated by multiplying the bulk aluminum thermal conductivity k_{Al} by the solid volume fraction ρ/ρ_s as well as a factor of 2/3 to account for the tortuous shape of the cell walls:

$$k_{Al,net} = \left(\frac{\rho}{\rho_s} \right) \cdot \frac{2}{3} \cdot k_{Al} = \left(\frac{279.26 \frac{kg}{m^3}}{2650 \frac{kg}{m^3}} \right) \cdot \frac{2}{3} \cdot \left(135 \frac{W}{mK} \right) = \underline{\underline{9.484 \frac{W}{mK}}} \quad (1.48)$$

Similarly, the gas thermal conductivity can be obtained by multiplying the thermal conductivity of air k_{air} by the gaseous volume fraction, which is 1 minus the solid volume fraction:

$$k_{Air,net} = \left(1 - \frac{\rho}{\rho_s} \right) \cdot k_{air} = \left(1 - \frac{279.26 \frac{kg}{m^3}}{2650 \frac{kg}{m^3}} \right) \cdot \left(0.025 \frac{W}{mK} \right) = \underline{\underline{0.0224 \frac{W}{mK}}} \quad (1.49)$$

From these results it can be seen that the net gas thermal conductivity only accounts for 0.236% of the overall conduction, under the reasonable assumption that the hydrogen in the cavities was replaced by air. Hence, gas conduction may safely be neglected.

1.6.3.2 Natural Convection in Cavities

Previous studies [3] have shown that the Grashof number is a good measure to determine whether natural convection will occur inside cavities or not:

$$Gr = \frac{g \cdot \beta \cdot \Delta T_c \cdot l^3 \cdot \rho^2}{\mu^2} \quad (1.50)$$

where g is the gravitational acceleration, β the gas volume expansion coefficient ($1/T_{avg}$ for an ideal gas, where T_{avg} is the average cavity temperature), ΔT_c the temperature gradient across one cell, l the average cell diameter, and μ the dynamic viscosity of the gas. In essence, the Grashof number calculates the ratio of buoyant forces to viscous forces. It was shown that if the Grashof number is smaller than 1000, viscous forces dominate over buoyant forces, and natural convection is mostly suppressed. At Grashof numbers greater than 1000, on the other hand, significant buoyant forces arise that cause natural convection.

The Grashof number was calculated for the worst-case scenario where a 600°C gradient is across a single cavity, corresponding to the case where one side of the cavity is at room temperature and the other side near the melting temperature:

$$\begin{aligned} \Rightarrow Gr &= \frac{g \cdot \beta \cdot \Delta T_c \cdot l_{avg}^3 \cdot \rho_{air}^2}{\mu_{air}^2} = \frac{g \cdot \frac{1}{T_{avg}} \cdot T_{avg} \cdot l_{avg}^3 \cdot \rho_{air}^2}{\mu_{air}^2} = \frac{g \cdot l_{avg}^3 \cdot \rho_{air}^2}{\mu_{air}^2} \\ &= \frac{\left(9.81 \frac{m}{s^2}\right) (0.0043 m)^3 \left(0.5804 \frac{kg}{m^3}\right)^2}{\left(305.8 \cdot 10^{-7} \frac{Ns}{m^2}\right)^2} = \underline{\underline{280.97 < 1000}} \end{aligned} \quad (1.51)$$

Since even the worst-case scenario yields a Grashof number smaller than 1000, natural convection in cavities may also be safely neglected.

1.6.3.3 Thermal Radiation through Foam

The third type of heat transfer through the foam is thermal radiation. In order to derive an equivalent radiative “conductivity” for aluminum foam that may be compared to the solid conductivity, it first needs to be looked at Boltzmann’s law, which describes the heat flux q_r^0

passing from a surface of a high temperature T_1 (top of foam specimen) to a surface of a lower temperature T_0 (bottom of foam specimen) through thermal radiation:

$$q_r^0 = \beta_l \sigma (T_1^4 - T_0^4) \quad (1.52)$$

where σ is Boltzmann's constant and β_l the emissivity of aluminum (~ 0.5). In the case of laser forming the high temperature surface is the top specimen surface that is exposed to the laser, and the low temperature surface is the bottom specimen surface. Boltzmann's law assumes that a vacuum is between the high and low temperature surfaces, which differs from the laser forming scenario where the radiation propagation inside the foam is a result of a complex interplay between solid absorption and cell wall reflection. To account for these factors, it is assumed that the thermal radiation inside the foam attenuates according to the Beer-Lambert law. The Beer-Lambert law is often used in laser materials processing to determine the laser intensity distribution inside a solid that is being treated, where I_0 is the initial irradiation intensity and $I(z)$ is the irradiation intensity at a depth z from the surface:

$$I(z) = I_0 e^{-\gamma z} \quad (1.53)$$

For the case of laser processing $\gamma = \frac{4\pi k}{\lambda}$, where k is the extinction coefficient and λ is the laser wavelength. For the case of radiative heat transfer, the irradiation intensity I can be replaced by the radiative heat flux q_r , whereby q_{r0} is the initial heat flux and $q_r(t)$ is the heat flux at a depth t . Additionally, the reduced density of the foam needs to be taken into account by multiplying the exponent by the solid volume fraction ρ/ρ_s . Using these modifications, the Beer-Lambert law becomes:

$$q_r = q_r^0 e^{-k \frac{\rho}{\rho_s} t} \quad (1.54)$$

This form of the Beer-Lambert law can now be substituted into Boltzmann's law to obtain:

$$q_r = 4\beta_1\sigma(T_1^4 - T_0^4)e^{-k\frac{\rho}{\rho_s}t} \quad (1.55)$$

At this point two approximations are made. First, the temperature gradients are replaced by average temperatures, substituting $(T_1^4 - T_0^4) \approx 4\Delta T \cdot T_{avg}^3$. Second, Fourier's law is introduced to come up with the "radiative conductivity" k_{rad} , and the spatial temperature derivative in Fourier's Law is replaced by the specimen thickness t and the applied temperature gradient $\frac{dT}{dx} \approx -\frac{\Delta T}{t}$.

The resulting relationship then becomes:

$$q_r = -k_{rad} \frac{dT}{dx} \approx k_{rad} \frac{\Delta T}{t} = 4\beta_1\sigma \Delta T T_{avg}^3 t e^{-k\frac{\rho}{\rho_s}t} \quad (1.56)$$

$$\Rightarrow k_{rad} = 4\beta_1\sigma T_{avg}^3 t e^{-k\frac{\rho}{\rho_s}t} \quad (1.57)$$

In the case of laser forming, the following values correspond to the worst-case scenario where a 600°C temperature gradient is across the foam specimen.

$$\begin{aligned} \beta_1 &\approx 0.5 \quad (\text{from camera test}) \\ T_{avg} &= \frac{300+900}{2} = 600K \quad (\text{extreme case}) \\ t &= 10mm = 0.01m \\ \rho &= 279.26 \frac{kg}{m^3} \\ \rho &= 2560 \frac{kg}{m^3} \end{aligned} \quad (1.58)$$

The extinction coefficient is $k = 8.5 \text{ m}^2/\text{kg}$ for a Nd:YAG laser as per [18]. Using these values, the radiative conductivity becomes:

$$\begin{aligned} k_{rad} &= 4 \cdot \beta_1 \cdot \sigma \cdot T_{avg}^3 \cdot t \cdot e^{-k\frac{\rho}{\rho_s}t} \\ &= 4 \cdot 0.5 \cdot \left(5.67 \cdot 10^{-8} \frac{W}{m^2 K^4} \right) (600K)^3 (0.01m) \cdot \exp\left(-8.5 \cdot \left(\frac{279.26}{2560} \right) (0.01m) \right) = \underline{\underline{0.2428 \frac{W}{mK}}} \end{aligned} \quad (1.59)$$

Hence, in an absolute worst-case scenario where a 600°C gradient is across the foam specimen, thermal radiation only accounts for around 3% of the overall heat transfer and can thus be ignored.

1.6.4 Sandwich Modeling

Sandwich panels consist of a foam core, two facesheets, and two interfaces. For the foam core, the same modeling techniques were used as discussed in Sec. 1.6.2. The facesheet was modeled the same way as standard sheet metal in previous studies [43,44]. It was assumed that the material is incompressible and only yields in shear. The same governing equations were used as in Sec. 1.6.2.1.

1.6.4.1 Interface

The interface is a unique component of the sandwich panel, and much effort was spent to develop a sound understanding of the different modeling techniques that are available. The difficulty about dealing with the interfaces between the facesheets and the foam core is that they are infinitesimally thin, as can be seen from the energy-dispersive X-ray spectroscopy (EDS) line scan in Fig. 21 that was taken across the interface of a type I sandwich panel.

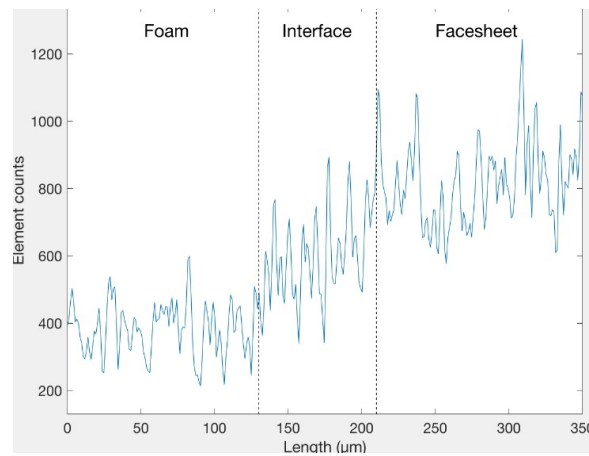


Figure 21: Typical EDS line scan across the interface of a type I sandwich panel, showing the magnesium content. The interface is the intermediate region between the high mg-content facesheet and the low mg-content foam core.

The magnesium content was measured on a line across the interface. The facesheet (AlMg1) has a high magnesium content compared to the foam core (AlSi7), and the interface represents the region in between where the magnesium content gradually drops. In the type I sandwich panel, the average interface thickness was measured to be 80 μm , and in the type II sandwich panel the average thickness was 120 μm .

One way to model an interface that is exceedingly thin compared to the remaining dimensions of the sandwich is to simply omit the interface altogether and directly join the facesheets to the foam core. Even though this modeling technique works and yields almost identical results as two improved methods that will be discussed shortly, it is not desirable because several material properties of the facesheets and the foam core differ by more than an order of magnitude. Notably the stiffness and yield strength of the facesheet are 69.5 GPa and 82.5 MPa, respectively, while they are only 2.75 GPa and 6.6 MPa in the metal foam (type I sandwich panel). Due to these drastic differences in the material properties, numerical difficulties can arise, especially in conditions where the facesheet undergoes substantially more heating than the foam core.

A second method to deal with the interface is to model it as a solid 3D layer. This approach is by far the most inefficient, not only because the mesh of the interfacial layer would be tiny, but also because the mesh of the adjacent facesheets and foam core would have to be refined excessively.

The best method is to “disregard” the stress-strain behavior of the interface itself, and to describe the stress-state at the interface in terms of normal and shear tractions as well as jump displacements across the interface. In essence, the tractions at the facesheet surface and the foam

core surface are the same (traction continuity), but the two layers might deform differently, which is why there is an “imaginary” jump discontinuity across the interface as illustrated in Fig.

22

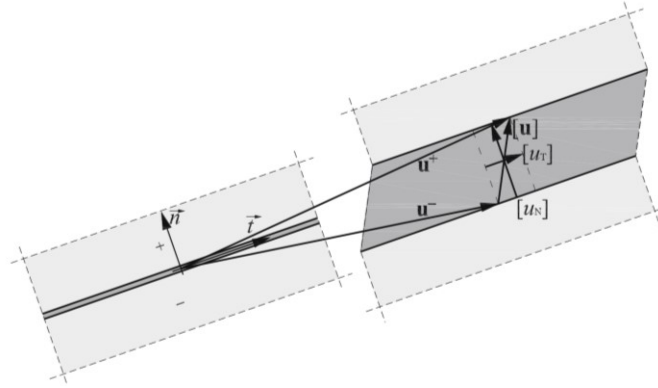


Figure 22: The interface is infinitesimally thin, thus only the interfacial normal and shear tractions are looked at. Due to the traction continuity at the interface, the two layers may deform differently by u^+ and u^- , respectively, giving rise to a jump discontinuity u across the interface [45].

It was further assumed that the tractions and jump displacements are linearly related up until failure. Failures (delamination) due to laser forming were not observed though.

Two modeling methods can be used in Abaqus to simulate the aforementioned behavior. The first method involves *cohesive surfaces* that are specified as *contact interactions* (surface-to-surface contact). The properties of the interface are specified in an *interaction property*, namely the interfacial stiffness as well as the failure parameters (onset, propagation). The second method involves *cohesive elements* that are added to the foam core surface as an “offset layer”. Both approaches yield exactly the same thermal and mechanical results, but the latter was used, since it allows visualizing the damage progress in the cohesive layer. This feature ultimately became irrelevant, because no delamination was observed that was caused by laser forming.

The cohesive element layer was created by meshing the foam core, creating an orphan mesh (mesh – create mesh part), and then creating the offset layer (mesh – edit – mesh - offset layer) by selecting the top surface of the foam. Surfaces were created on either side of each cohesive

layer in the part definition (by temporarily making the foam disappear with *display groups*). These surfaces were subsequently used to define the adhesion between the facesheets, the cohesive layer, and the foam core via surface-to-surface contact interactions (thermal analysis) and tie constraints (mechanical analysis). In the thermal analysis, the material properties of the foam were assigned to the cohesive layer (otherwise Abaqus refuses to run the job), and linear thermal elements DC3D8 were assigned. In the mechanical analysis, a “cohesive” material section was used and cohesive elements COH3D8 were assigned to the cohesive layer.

Two more aspects require further discussion. The first aspect is the heat transfer between the facesheet and the foam core. In both sandwich panel types, the adhesion between the facesheets and the foam core is established via metallic diffusion bonds, which have more imperfections (voids, etc.) than bonds obtained through complete melting. Hence, the adhesion between the facesheets and the foam core is imperfect, and consequently there is some thermal resistance at the interface. This thermal resistance was taken into account in the interaction property of the thermal analysis. Due to the lack of references pertaining gap conductance measurements in sandwich composites, as well as the inherent difficulty of such a measurement, it was assumed that the gap conductance follows the same temperature dependence as solid metallic layers in direct contact. Several references that performed such experiments reported a mild linear increase in the gap conductance with temperature, followed by an exponential increase near the melting point [46-48]. The exponential increase in the gap conductance near the melting point is as expected, since heating “wettens” the surfaces and dramatically increases the contact area. In chapters 4 & 5, the data from [46] was used, shown in Fig.23.

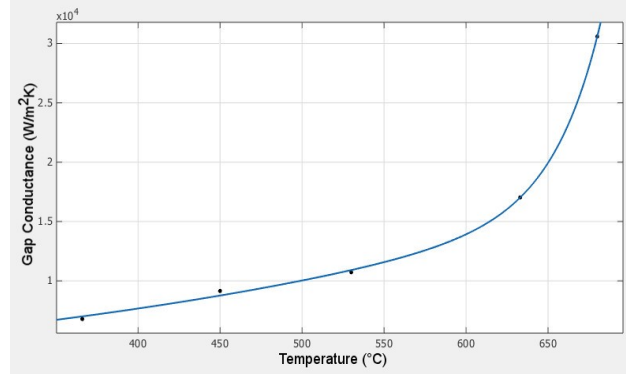


Figure 23: Data fit of the results in [46], which allowed establishing a temperature-dependent function for the gap conductance.

The data fit yielded the following relation, which was used in the *gapcon* subroutine that will be discussed in Sec. 1.6.6.3.

$$G(T_A) = 2646 \cdot \exp(0.002659 \cdot T_A) + 6.145 \cdot 10^{-7} \cdot \exp(0.03511 \cdot T_A) \quad (1.60)$$

The second aspect requiring discussion is the stiffness of the cohesive layer. Throughout the analysis it was assumed that the shear stiffnesses are zero, and that the tractions are directly related to the jump displacements of the corresponding coordinate direction. The normal stiffnesses, often referred to as *penalty stiffness*, could not be determined experimentally due to the small thickness of the interface. Instead, a value was chosen for it such that the interface does not affect the overall “equivalent” stiffness of the sandwich panel. To illustrate the influence of the interfacial stiffness on the equivalent sandwich stiffness, the scenario is analyzed where the sandwich panel is loaded by a lateral load F as shown below.

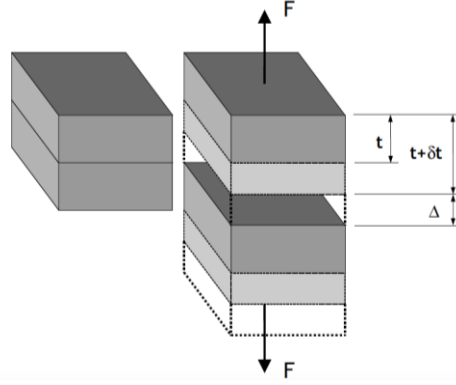


Figure 24: Sandwich panel that is loaded by a lateral force F [49]. Each layer stretches by $t+\delta t$, and the interface expands by Δ .

If the joined layers are identical, they expand from their initial thickness t to a final thickness $t+\delta t$. Assuming that the interface itself stretches from an infinitesimal thickness to a finite thickness Δ , the overall deformation is $2\delta+\Delta$. The effective strain of the sandwich then becomes:

$$\varepsilon_{eff} = \frac{\delta t + \delta t + \Delta}{t} = \frac{2\delta t + \Delta}{t} = \varepsilon + \frac{\Delta}{t} \quad (1.61)$$

Due to the stress continuity at the interface, the stress can be written in terms of the facesheet strain ε and Young's Modulus E , or the corresponding effective strain ε_{eff} and Young's Modulus E_{eff} , or the interfacial stiffness K and deformation Δ :

$$\sigma = E\varepsilon = E_{eff}\varepsilon_{eff} = K\Delta \quad (1.62)$$

Substituting the first expression, we obtain:

$$\sigma = E_{eff}\varepsilon_{eff} = E_{eff} \left(\varepsilon + \frac{\Delta}{t} \right) \quad (1.63)$$

Substituting $\Delta = E\varepsilon/K$, this becomes:

$$\sigma = E\varepsilon = E_{eff} \left(\varepsilon + \frac{E\varepsilon}{Kt} \right) \quad (1.64)$$

Finally, solving for the equivalent stiffness E_{eff} , the following expression is obtained:

$$E_{eff} = \frac{E\varepsilon}{\left(\varepsilon + \frac{E\varepsilon}{Kt}\right)} = E \left(\frac{1}{1 + \frac{E}{Kt}} \right) \quad (1.65)$$

From this equation it is apparent that the equivalent sandwich stiffness is unaffected by the cohesive layer if the interfacial stiffness K is as large as possible. Turon et al. showed that this requirement is satisfied if the interfacial stiffness is at least 25 times greater than the stiffnesses of the joined layers (where $\alpha = Kt/E$), as shown in Fig. 25.

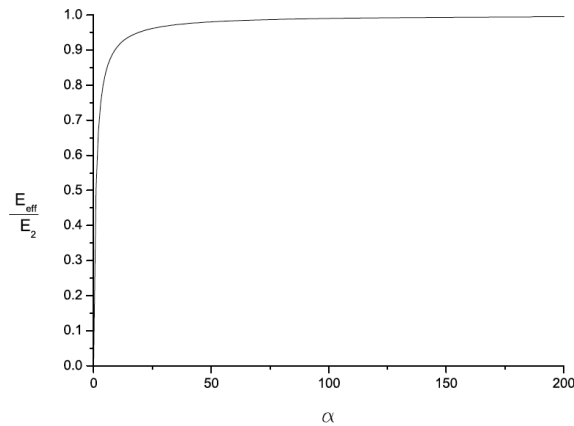


Figure 25: The ratio $\alpha = Kt/E$ must be at least 25 for the effective stiffness E_{eff} of the entire sandwich panel to be the same magnitude as the stiffness E of the joined layers [49].

However, the interfacial stiffness cannot be arbitrarily high either, since that introduces spurious oscillations in the analysis and creates convergence difficulties. In this study, successful results were obtained using a 50-times greater interfacial stiffness than the facesheet stiffness.

1.6.4.2 2D Sandwich Models

For the analysis of straight (“2D”) laser scans, three different model types were used. In the first model, the foam core was modeled using the equivalent approach that was introduced in Sec. 1.6.2.3. The resulting model is shown in Fig. 26(a).

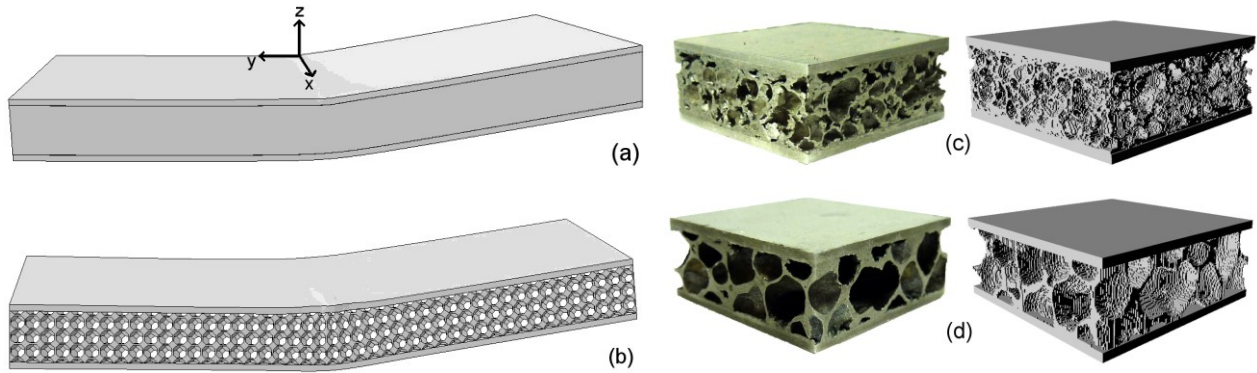


Figure 26: (a) Equivalent sandwich panel model, (b) Kelvin-cell sandwich panel model, (c) type I sandwich panel specimen (left) and corresponding voxel model (right), (d) type II sandwich panel specimen (left) and corresponding voxel model (right).

The second model used a Kelvin-cell approach for the foam core, introduced in Sec. 1.6.2.1 and shown in Fig. 26(b). Finally, a voxel model was created both for the type I (Fig. 26(c)) and type II (Fig. 26(d)) sandwich panels. All the model types used the same facesheet properties, mesh and geometries, as well as facesheet adhesion method.

1.6.4.3 3D Sandwich Models

For the simulation of 3D laser forming in chapter 6, the models in Fig. 27(a) and 27(b) were used for the bowl and saddle shapes, respectively. Due to the CPU intensity of this simulation, only a quarter of the bowl and saddle shapes were modeled, and symmetry constrains were used in x and y – direction. This induces some error, as the problem is not truly symmetric, but the errors are small since a good agreement between experimental and numerical data can be obtained. The models were additional constrained (encastre) at two vertically aligned points at the center.

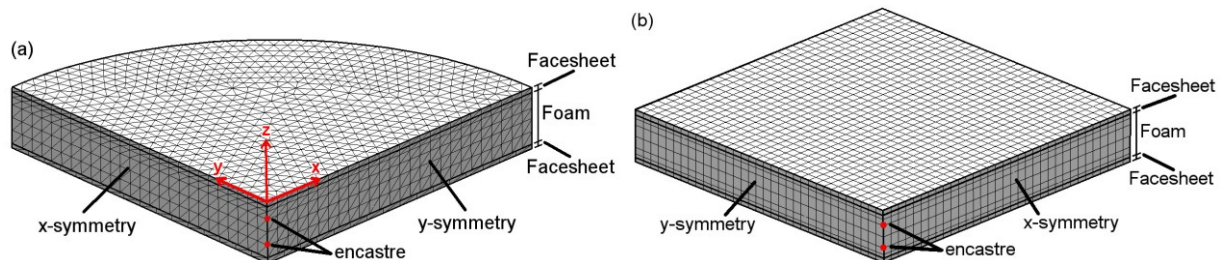


Figure 27: 3D equivalent sandwich panel model used for the (a) bowl shape and the (b) saddle shape. Symmetry constraints were used to reduce the CPU-intensity. The models were also constrained at two vertically aligned points to mimic the experimental fixture.

1.6.5 Initial Conditions and Boundary Conditions

In all simulations, with the exception of micro CT models in chapter 5, only half of the specimen was modeled due to symmetry. Also, the analysis was uncoupled into a thermal and a subsequent mechanical part, as was previously mentioned.

In the thermal analysis, the initial temperature of the entire model was set equal to room temperature. A user defined surface flux was specified on the top specimen surface, and the laser shape was defined using the subroutine *dflux* (see Sec. 1.6.6.1). In the subroutine, the absorption coefficient was set equal to 0.6. Natural convection was modeled on all sides except the symmetry plane, and a heat transfer coefficient of 10 W/m²K was used. Zero heat flux was specified across the symmetry plane.

The results of the thermal analysis were then used as a pre-defined field for the mechanical analysis. Based on the temperature changes, the stresses were calculated via the thermal expansion coefficient. A symmetry boundary condition was used at the center of the laser scan, which sets the displacement in *y*-direction as well as the rotations about the *x* and *z*-axes equal to zero. The displacements in *x* and *z*-direction were restricted at two vertically aligned points at the symmetry plane. Rotations about the *y*-axis were not restricted.

1.6.6 User Subroutines

1.6.6.1 2D Dflux

In the *dflux* subroutine the laser spot with a Gaussian heat flux distribution is generated. In the example below, the laser is scanned in *x*-direction by 80 mm at a power of 360 W, a spot size

of 5 mm and a scan speed of 10 mm/s. The flux is calculated once the laser is at (0,0) minus the radius, until the laser reached (0.08,0) plus a laser radius.

```

SUBROUTINE DFLUX(FLUX,SOL,KSTEP,KINC,TIME,NOEL,NPT,COORDS,
1 JLTYP,TEMP,PRESS,SNAME)

INCLUDE 'ABA_PARAM.INC'
DIMENSION FLUX(2), TIME(2), COORDS(3)
CHARACTER*80 SNAME

REAL R0, AB, P, V, RK, QMAX
REAL X1, Y1, X2, Y2, X0, Y0, X, Y, R
R0=0.005
AB=0.60
P=360
V=0.01
RK=2.9957/(R0**2)
QMAX=(AB*P)*RK/3.1415926

C
C IF (KSTEP.EQ.1) THEN
C
X1=0
Y1=0
X2=0.08
Y2=0
X0=-R0+X1
Y0=Y1
X=X0+V*TIME(2)
Y=Y0

C
IF((X.LT.(X1-R0)) .OR. (X .GT. (X2+R0))) THEN
FLUX(1)=0.
ELSE
R=SQRT((X-COORDS(1))**2.0+(Y-COORDS(2))**2.0)
FLUX(1)=QMAX*EXP(-RK*R*R)
ENDIF
ENDIF

RETURN
END

```

In order to obtain the equations used in the subroutine, it needs to be started with the following equations describing the energy E of the laser source:

$$E(r, \phi) = E_0 \cdot \left(\frac{\sqrt{2}r}{w} \right)^l \cdot L_p^l \cdot \left(\frac{2r^2}{w^2} \right) \cdot e^{-\left(\frac{r^2}{w^2} \right)} \cdot \cos(l\phi) \quad (1.66)$$

$$L_p^l(x) = e^x \cdot \left(\frac{x^{-l}}{p!} \right) \cdot \frac{d^p}{dx^p} \cdot (e^{-x} \cdot x^{p+l})$$

where r is the radial position, w the beam radius, E_0 the maximum energy, and the variables p and l the number of radial zero fields and number of angular zero fields, respectively. For a Gaussian beam, both p and l are equal to zero, hence:

$$L_0^l(x) = e^x \cdot x^{-l} \cdot \frac{d^0}{dx^0} \cdot (e^{-x} \cdot x^l) = e^x \cdot x^{-l} \cdot e^{-x} \cdot x^l = 1$$

$$E(r, \phi) = E_0 \cdot \left(\frac{\sqrt{2}r}{w} \right)^l \cdot L_p^l \left(\frac{2r^2}{w^2} \right) \cdot e^{\left(-\frac{r^2}{w^2} \right)} \cdot \cos(l\phi) = E_0 \cdot 1 \cdot 1 \cdot e^{\left(-\frac{r^2}{w^2} \right)} \cdot \cos(0) \quad (1.67)$$

$$\Rightarrow E(r, \phi) = E_0 \cdot e^{\left(-\frac{r^2}{w^2} \right)} \quad (1.68)$$

The above equation describes the theoretical energy distribution in the Gaussian beam. In order to convert the energy equation to the heat flux and make it usable for the subroutine, the following thermodynamic relation needs to be used:

$$dE = dQ + dW \quad (1.69)$$

Since the laser does not perform any work ($dW = 0$), the change in energy uniquely comes from the change in heat. Therefore, the energy equation can be written as a heat flux equation:

$$q = Q_{\max} \cdot e^{(-RK \cdot R^2)} \quad (1.70)$$

Q_{\max} is the maximum heat flow and defined as:

$$Q_{\max} = \frac{A \cdot P \cdot w}{\pi} \quad (1.71)$$

where A is the absorption coefficient and P the laser power. The radial position R is the distance between the point (x, y) , for which the heat flux is being calculated, to the current center of the laser beam (x_0, y_0) :

$$R = \sqrt{(x_c - x)^2 + (y_c - y)^2} \quad (1.72)$$

1.6.6.2 3D radial Dflux

If the laser scan is to be performed from any arbitrary point (x_1, y_1) to a second arbitrary point (x_2, y_2) , several if-statements need to be included to ensure a correct directionality of the laser. Depending on the directionality in x and y , the parameters a and b change sign, altering the incremental change of the current position (x, y) . Additionally, the slope m is calculated, requiring additional if-statements to cover the scenarios where the denominator becomes zero. An example code is shown below, scanning from $(0,0)$ to $(0.01,0.02)$:

```
IF (KSTEP.EQ.1) THEN

X1=0.0
X2= 0.01
Y1=0.0
Y2=0.02

If ((Y2 == 0) . AND. (X2 .GT. 0)) THEN
a = 1
b = 0
ELSE IF( (Y2 == 0) .AND. (X2 .LT. 0)) THEN
a = -1
b = 0
ELSE If ((X2 == 0) . AND. (Y2 .GT. 0)) THEN
a = 0
b = 1
ELSE IF( (X2 == 0) .AND. (Y2 .LT. 0)) THEN
a = 0
b = -1
ELSE IF( (X2 / Y2).GT.(0) .AND. (X2 .GT. 0)) THEN
a = 1
b = 1
ELSE IF ( (X2 / Y2).LT.(0) .AND. (X2 .LT. 0)) THEN
a = -1
b = 1
ELSE IF ( (X2 / Y2).GT.(0) .AND. (X2 .LT. 0)) THEN
a = -1
b = -1
ELSE
a = 1
b = -1
ENDIF

IF(X2 . GT . (0)) THEN
c = 1
ELSE
c = -1
ENDIF
```

```

IF(Y2 . GT . (0)) THEN
d = 1
ELSE
d = -1
ENDIF

IF ((X2 - X1) == 0) THEN
m = 0
p = 1

ELSE
m = ABS((Y2 - Y1) / (X2 - X1))
p = ABS((Y2 - Y1) / (X2 - X1))
ENDIF

X0 = X2 + a * SQRT( R0** 2.0 / (1+m**2.0))
Y0 = Y2 + b * p * SQRT( R0**2.0 / (1+m**2.0))
X = X0 - a * SQRT(( V * TIME(1))**2.0 / (1+m**2.0))
Y = Y0 - b * p * SQRT( ( V * TIME(1)) ** 2.0/ (1+m**2.0))

IF((c * X .LT. c * X1 ) .OR. (c * X .GT. c* X0)) THEN
    FLUX(1)=0.
ELSE IF ((d * Y .LT. d * Y1 ) .OR. (d * Y .GT. d* Y0)) THEN
    FLUX(1)=0.
ELSE
    R=SQRT((X-COORDS(1))**2.0+(Y-COORDS(2))**2.0)
    FLUX(1)=QMAX*EXP(-RK*R*R)
ENDIF
ENDIF

```

1.6.6.3 3D circular Dflux

Finally, by changing from Cartesian coordinates to polar coordinates the *dflux* subroutine can also be used to perform circular scans, as shown below. The starting position is denoted by (x_s, y_s) , where x_s refers to the scan radius if y_s is zero. x_s is corrected by the laser radius $R0$ to ensure that the center of the laser lies on the desired radius. The circular frequency of the scan, which ultimately determines the speed of revolution, is denoted by Wn and calculated from the linear speed v that is specified by the user. The current position (x, y) is then calculated via sines and cosines. The final if-statement ensures that laser firing continues until a complete revolution is completed.

```

IF (KSTEP.EQ.1) THEN

Xs = -.02006
Ys = 0

```

```

X0 = Xs - R0
Y0 = Ys

rad1 = SQRT(X0**2)
Wn = V / rad1

X = X0 * COS(Wn* TIME(1))
Y = X0 * SIN(Wn* TIME(1))

IF(TIME(1) * Wn .LT. 6.283185 ) THEN
    R=SQRT((X-COORDS(1))**2.0+(Y-COORDS(2))**2.0)
    FLUX(1)=QMAX*EXP(-RK*R*R)

ELSE
Flux(1) = 0

ENDIF
ENDIF

```

1.6.6.4 Gapcon

In Sec. 1.6.4.1 it was discussed that a temperature-dependent gap conductance value was used in the simulations. In Abaqus, this was implemented using the *gapcon* subroutine shown below. Only the first component of *AK* had to be specified, which is the gap conductance itself. The remaining components were the derivatives of the gap-conductance, that were set to zero, since the gap conductance was assumed to be time-invariant.

```

SUBROUTINE GAPCON(AK,D,FLOWM,TEMP,PREDEF,TIME,CINAME,SLNAME,
1 MSNAME,COORDS,NOEL,NODE,NPRED,KSTEP,KINC)

INCLUDE 'ABA_PARAM.INC'

CHARACTER*80 CINAME,SLNAME,MSNAME

DIMENSION AK(5),D(2), FLOWM(2), TEMP(2), PREDEF(2,*),
1 TIME(2), COORDS(3)

REAL A, B, G, H
A=2646
B=0.002659
G=0.0000006145
H=0.03511
AK(1)=A*EXP(B*TEMP(2))+G*EXP(H*TEMP(2))
AK(2)=0
AK(3)=0

RETURN

```

END

1.6.6.5 FILM

Throughout most of the work in this thesis, a constant natural convection coefficient of 10 W/m²K was used, which has been routinely done in previous numerical investigations of laser forming. In reality, however, the heat transfer coefficient changes with the temperature of the workpiece, because the viscosity and thermal conductivity of the surrounding air changes with temperature. To account for changes in the heat transfer coefficient h , a correlation for unstable natural convection over a horizontal plate can be used:

$$h = \frac{k_{air}}{L_c} Nu_{L_c} = \frac{k_{air} P}{A_c} 0.15 (Ra_{L_c})^{(1/3)} = \frac{k_{air} P}{A_c} 0.15 \left(\frac{g \beta |T_w - T_\infty| L_c^3}{\nu_{air}^2} \right)^{(1/3)} Pr \quad (1.73)$$

where k_{air} is the thermal conductivity of the air, L_c the critical length, A_c the specimen area, P the specimen circumference, Nu_{L_c} the Nusselt number, Ra_{L_c} the Rayleigh number, g the acceleration of gravity, T_w the average plate temperature, T_∞ the ambient temperature, β the inverse of the ambient temperature, and ν_{air} is the kinematic viscosity of air. The Prandtl number is nearly constant with temperature, but the thermal conductivity and the kinematic viscosity of air vary considerably with temperature, along with the temperature gradient $|T_w - T_\infty|$. When accounting for all the temperature dependences, a worst-case scenario with an average workpiece temperature of 600°C yields a roughly 25% higher heat transfer coefficient than a scenario where the average workpiece temperature is 200°C (but remains close to 10 W/m²K). In Abaqus, the temperature-dependence can be incorporated in a FILM subroutine by writing the thermal conductivity and kinematic viscosity as a function of the temperature (TEMP), and calculating the heat transfer coefficient at each location as shown in the code below.

While using a FILM subroutine can slightly increase the model accuracy, it most of the time does not justify the resulting increase in CPU intensity. During laser forming, heating is extremely localized, and convective heat transfer is generally insignificant compared to conductive heat transfer that occurs through the bulk material.

```

SUBROUTINE FILM(H,SINK,TEMP,KSTEP,KINC,TIME,NOEL,NPT, 1
COORDS,JL TYP,FIELD,NFIELD,SNAME,NODE,AREA) C INCLUDE
'ABA_PARAM.INC' C DIMENSION H(2),TIME(2),COORDS(3), FIELD(NFIELD)
CHARACTER*80 SNAME

REAL HC, HR, HH, RE, PR, K, B, KIN, DEN, THETA, EPS, TA, V

C H(1)= heat transfer coefficient
C H(2)=derivative of heat transfer coefficient
C HH=total heat transfer coefficient
C RE=Reynolds number
C PR=Prandtl number
C K=thermal conductivity of the cooling gas (W/mK)
C KIN=kinematic viscosity (in Reynolds number)
C DEN=density of the gas jet
C THETA=Boltzmann constant
C EPS=emissivity
C TA=ambient temperature
C TS=surface temperature
C LC=critical distance
C V=kinematic viscosity

RE=100
K=function 1
V=function 2
THETA=5.6703*10**-8
EPS=0.918
TA=298
G=9.81

PR=0.688

H(1)=K/LC*0.15*((G*(TEMP-TA)*LC**3)/(TA*V**2))*PR

SINK=298

RETURN
END

```

1.7 Organization and Objectives of Dissertation

In this thesis, the behavior of metal foam during laser forming was investigated first. The problem was divided into two parts, a thermal part (chapter 2) and a mechanical part (chapter 3).

In the thermal part, a detailed analysis was performed of how the laser is absorbed in the foam, as well as how heat distributes through the foam. Based on the findings it was discussed which bending mechanism is favored from a thermal perspective. In the mechanical part, the deformation behavior of the foam was analyzed, specifically the cell wall crushing that occurs during laser forming. From the results conclusions were drawn about the mechanical aspects of the bending mechanism. It was shown that the overall bending mechanism that governs the deformation of metal foam during laser forming differs from the traditional bending mechanisms that have been identified for sheet metal. It was further discussed what the implications of the bending mechanism are on the structural integrity of the metal foam, as well as its performance as crash absorber. In both the thermal and mechanical analyses (chapters 2 & 3), numerical models with different levels of geometrical complexity were contrasted.

In chapter 4, laser forming of sandwich panels was investigated, bringing together the extensive knowledge that has been developed in metal foam laser forming (chapters 2 & 3) and sheet metal laser forming (previous theses). The bending mechanisms were revisited, and it was shown that separated mechanisms govern the deformation of the sheet metal facesheets and the foam core. Also, the bending efficiency and limit were analyzed and related to specific process conditions. Finally, numerical modeling techniques were analyzed, with a special focus on the facesheet/foam core interface, a new component that has never been dealt with in previous laser forming analyses.

In chapter 5, two fundamentally different sandwich panel types were compared in order to determine the impact of the panel composition and manufacturing method on the outcome of laser forming processes. The impact of each component/facet was analyzed independently as well as collectively. It was shown that the facesheet/foam core interaction has the greatest impact

on the bending efficiency and bending limit. Various numerical models were used throughout the analysis to illustrate different aspects.

In chapter 6, finally, 3D laser forming of metal foam sandwich panels was explored. The material was laser-formed into the two fundamental non-Euclidean geometries, the bowl and saddle shapes. It was demonstrated that a substantial amount of deformation can be achieved, yet the deformation is reduced compared to the deformation that can be achieved in 2D laser forming. Using experimental and numerical evidence, it was shown that this discrepancy is not due to a change in the bending mechanism, but related to the type of deformation that is required to obtain non-Euclidean geometries. The study was concluded by analyzing the effect of the laser scan length of the process outcome.

Chapter 2: Effect of Geometrical Modeling on the Prediction of Laser-Induced Heat Transfer in Metal Foam

2.1 Introduction

Aluminum-foam (Al-foam) is a relatively new material that has stimulated a lot of interest due to its high strength to weight ratio and its excellent shock and noise absorption properties [50]. Al-foam can be manufactured in many different ways, yet it is most commonly manufactured in flat panels [51]. In many engineering applications such as car bumpers or spacecraft components, however, Al-foam needs to be in specific shapes. Since near-net shape manufacturing is difficult and expensive, it becomes necessary to bend Al-foam to the desired shape. Bending Al-foam is not trivial because the cell walls can only sustain low stresses and crack easily. As a consequence, conventional mechanical bending methods cause fracture and cell collapse [16,52]. Therefore, an alternative bending method is needed.

Laser forming is an alternative advanced manufacturing method used to bend materials. The process is well understood for solid materials, and many aspects of the process have been studied previously. Li et al., for instance, studied laser forming under constant line energy as well as strain rate effects during laser forming [43,53]. Cheng et al. studied cooling effects during multi-scan experiments and microstructural changes in steel during laser forming [44,54]. The laser forming process has also been studied for sheets of varying thicknesses [55], and algorithms have been developed for process synthesis [56].

Previous studies have shown that laser forming can successfully bend metal foams as well. Guglielmotti et al. [29] and Quadrini et al. [57] investigated the feasibility of laser forming of Al-

foam sandwich panels and open-cell Al-foams for different power levels, scanning speeds, sheet thicknesses and foam densities. They found that laser forming of Al-foam is possible without cell collapse and skin delamination. The maximum number of scan lines was found to be limited by foam densification, melting, and crack growth on the bottom surface. The optimum processing conditions and the corresponding maximum bending angles were determined. The experimental results were limited to bending angle measurements, and heat transfer issues were not addressed. Moreover, no numerical studies have been performed yet.

Santo et al. [28] and Quadrini et al. [58] extended the previous parametrical study to large-pore open-cell Al-foams. They first introduced numerical schemes that explicitly modeled the foam geometry. Uncoupled sequential thermal and mechanical models were used, and the material data for AlSi7Mg was temperature-dependent. The numerical model was indirectly validated using a 3-point bending test, but no comparison was made between experimental and numerical laser forming results. The heat transfer results were limited to color contour plots and time-history curves at selected points, and no detailed discussion was performed of the underlying heat transfer aspects of laser forming.

In addition, the microstructural changes in Al-foam during laser forming have been studied, as well as the effect of heat treatments on the mechanical properties of Al-foam [59,60]. Again, no comparison was made between numerical and experimental data, and similar heat transfer results were reported as in the previous studies.

More recently, Zhang et al. used laser forming on closed-cell Al-foam [61]. They developed two types of numerical models in uncoupled thermo-mechanical analyses. The first model assumed a solid geometry and used foam material properties, while the second model used an

explicit geometry with solid material properties. The models were employed to analyze both the temperature history during laser scans as well as the mechanical response of the foam during laser forming. Zhang et al. was the first group to compare numerical bending angles with experimentally measured bending angles. However, the heat transfer results of the numerical simulations were not verified experimentally. Moreover, a highly simplified explicit porous model was used, as will be discussed later.

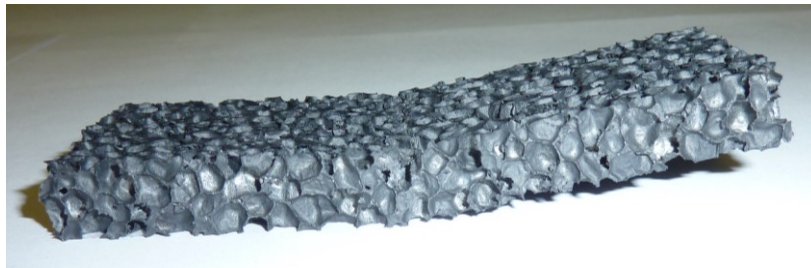


Figure 28: Closed-cell aluminum foam specimen after laser forming.

The current study was focused on the heat transfer aspects of laser forming of closed-cell Al-foam that is shown in Fig. 28. While laser forming is a thermo-mechanical process, one may uncouple the thermal process from the mechanical process and use the thermal results as initial conditions for the mechanical analysis. Hence, a good understanding of the heat flow and the transient temperature profiles during laser forming is vital to explain why and under which circumstances foams can bend. Especially from a numerical standpoint, accurate thermal simulations are the key to performing successful mechanical simulations. In order to determine the best way to model Al-foam, several numerical models with different levels of geometrical complexities were compared. The models included an equivalent model with a solid geometry, a Kelvin-cell model with a Kelvin-cell geometry, and a voxel model with a geometry that was based on an X-ray computed-tomography (CT) scan. The numerical models were then validated

by experimental data, which was obtained using an infrared camera to measure the transient response of Al-foam during laser pulses and laser scans.

2.2 Background

2.2.1 Heat Transfer in Metal Foams

There are four different mechanisms through which heat can be transferred in foams: (1) solid conduction, (2) gas conduction through the cavities, (3) natural convection inside the cavities and (4) radiation heat transfer. Since the thermal conductivities of metals are generally very large, most of the heat transfer occurs through solid conduction. In the current study, the maximum contribution of gas conduction was calculated to be around 0.2%, which is negligible. Natural convection inside the cavities is governed by the Grashof number

$$Gr = \frac{g\beta\Delta T_c d^3 \rho_g^2}{\mu_g^2} \quad (2.1)$$

where g is the gravitational acceleration, β is the volumetric expansion coefficient of the gas, ΔT_c is the maximum temperature gradient over a single cavity, d is the cavity diameter, ρ_g and μ_g are the density and dynamic viscosity of the gas, respectively. The Grashof number describes the ratio of buoyant forces to viscous forces. If $Gr < 1000$, viscous forces are dominant over buoyant forces, and natural convection is suppressed [62]. In the current study, the Grashof number was one order of magnitude smaller than the threshold and thus the contribution of natural convection inside the cavities was negligible. Finally, the radiation heat flux in metal foams is governed by a combination of Boltzmann's law and the Beer Lambert law [3]

$$k_{rad} = 4\varepsilon\sigma T_{avg}^3 t e^{-k_s \frac{\rho_f}{\rho_s} t} \quad (2.2)$$

where ε is the emissivity, σ is the Boltzmann constant, T_{avg} is the average between the top and the bottom surface temperatures, t is the sheet thickness, k_s is the solid thermal conductivity, and ρ_f/ρ_s is the solid volume fraction. In the current study, the maximum contribution of radiative heat transfer was calculated to be around 3% of the total heat transfer. Therefore, radiation had a higher impact than gas conduction and gas convection, but its contribution was still negligible.

2.2.2 Numerical Models

Numerical simulations of the laser forming process are very powerful since they can determine the best processing parameters without having to perform an excessive amount of experiments. For metal foams, numerical simulations become even more important since foams can have different densities and mass distributions, and thus the number of process parameters is even greater than in solid laser forming.

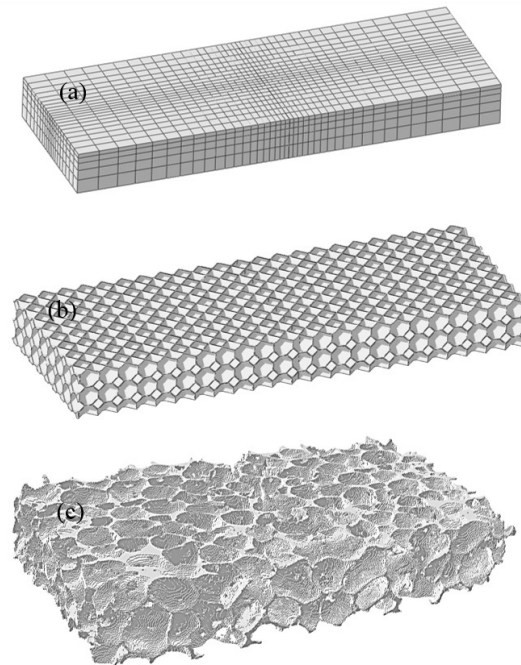


Figure 29: (a) Equivalent model, (b) Kelvin-cell model and (c) voxel model.

In this study, three different numerical models were used and are shown in Fig. 29. The first model strove to simulate the complex laser forming process with the simplest possible model geometry, which is a solid. In the second model, the foam geometry was approximated using a Kelvin-cell geometry, which will be referred to as Kelvin-cell model. The goal was to use an approximate geometry that is easy to generate but still as representative of the actual foam geometry as possible. The third and final model, which will be referred to as voxel model, aimed to replicate the exact foam geometry by using an FEM model that was based on an X-ray computed tomography (CT) scan. The first model is called an equivalent model, while the latter two models fall into the category of explicit porous models.

2.2.2.1 Equivalent Model

Equivalent models have a solid geometry and use foam material properties. They are rather widely applicable and have been used for different types of laser processes in the past. Mukarami et al. [63], for instance, used an equivalent model for laser welding of porous lotus-type magnesium, and Yilbas et al. [64] used an equivalent model for laser cutting of Al-foam. In both cases, phase changes had to be taken into consideration, which were of no concern in the current study. Moreover, Mukarami et al. used anisotropic material properties due to the elongated shapes of the pores, whereas this study assumed isotropic material behavior. An equivalent model was also used by Zhang et al. to model laser-forming of Al-foam [61]. In their study, however, the solid volume fraction of the Al-foam was more than twice the solid volume fraction of the foam that was used in this study, which was only 11%. This study thus investigated whether even low-density closed-cell foams may be approximated with a solid geometry.

The main challenge associated with equivalent models is the determination of the equivalent material properties. For a heat transfer analysis, three material properties are required: the

density, specific heat and thermal conductivity. The density of the foam can be measured, and the equivalent specific heat of the foam is approximately equal to the specific heat of the solid material out of which the foam is made [2-3,63]. The equivalent thermal conductivity, on the other hand, needs to be determined. In most cases, temperature-dependent data only exists for the solid material out of which the foam is made but not for the foam itself. Therefore, it becomes necessary to relate the equivalent thermal conductivity to the corresponding solid thermal conductivity. This can be done with many different methods that are summarized in [42,65]. In this study, three different methods were compared to highlight the important role that foam properties play in equivalent models. In the first two methods, the foam thermal conductivity k_{eq} was related to the solid thermal conductivity k_s through the volume fraction ρ_f/ρ_s and a shape factor f_z :

$$k_{eq} = k_s \frac{\rho_f}{\rho_s} f_z \quad (2.3)$$

The first method determined the shape factor by assuming that the foam structure may be represented as a Voronoi model with the random morphological microstructure that was proposed by Lu et al. [66]. In the second method, the shape factor was visually determined by measuring the cross-sectional areas A_i and the angular orientations γ_i of the cell walls as shown in Fig. 30 [67]:

$$f_z = \frac{\sum_{i=1}^n A_i \cos^2(\gamma_i)}{\sum_{i=1}^n A_i} \quad (2.4)$$

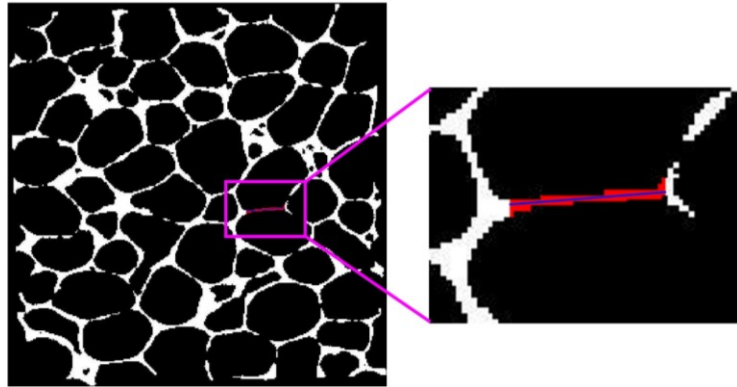


Figure 30: Determining the equivalent thermal conductivity using the visual method by calculating the cross-sectional areas and the angular orientations of the cell walls.

Finally, in the third method, experimental laser-forming data was used to tune the equivalent thermal conductivity while all the remaining variables and processing parameters were left constant.

2.2.2.2 *Explicit Porous Models*

Explicit porous models use solid material properties and aim to replicate the closed-cell foam geometry. They generally fall into two categories, which may be called approximate models and “exact” CT-based models. Approximate models assume a unit cell geometry and repeat the geometry to generate a full-scale model. Zhang et al., for instance, used spherical unit cells in a closed-packed arrangement to simulate closed-cell Al-foam [61]. While being extremely simple to model, spherical cavity models have the major disadvantage that the minimum volume fraction is limited to 27%. Moreover, they overestimate the material accumulation at cell intersections and underestimate the minimum cell wall thickness. An alternative unit cell geometry is the Kelvin cell, which was used in this study and has also been used for compression and impact tests by De Giorgi et al. [68] and Mills et al [69], respectively. In both studies, the Kelvin-cell model was exclusively used for mechanical analyses, and no thermal simulations

were performed. Furthermore, the foam cell wall thicknesses were very thin in both studies, which allowed for the simplification of the geometry by using shell elements. In the current study, however, no such simplifications could be used. De Giorgi et al. also introduced a more sophisticated approximated model that used randomly oriented ellipsoids of different sizes [68]. The resulting micro-structure was rather close to the real foam, and a good agreement was achieved with experimental compression test data. However, the model required sophisticated algorithms to generate the random geometry, which defeated the original purpose of using an approximated geometry.

The second category of explicit porous models is based on CT-scans. CT-scans use X-rays and can thus measure the internal structure of Al-foam at a high resolution. The result of a CT-scan is a point cloud that gives the attenuation coefficient at every point of the measured object. For aluminum foams that are filled with air cavities, the point cloud contains zeros for air and finite values for aluminum. In order to obtain a FEM model from the CT-scan, the point cloud needs to be translated into a solid geometry. This was done by simply converting each solid data point of the point cloud into cubical volumes, called voxels. The advantage of this approach over other existing approaches explained in [42] is that the implementation is straightforward to perform and directly generates a solid geometry that can be used in a FE software.

The numerical simulations were performed in the commercial FEM software ABAQUS. The governing equation for the numerical simulations was Fourier's law:

$$q = -k\nabla T \quad (2.5)$$

Linear 8-node brick elements DC3D8 were used for the equivalent and the voxel model, and linear 4-node tetrahedrons DC3D4 were used for the Kelvin-cell model. For the equivalent model, a refined mesh was used close to the laser scan line to ensure that high temperature

gradients could be captured. A FORTRAN subroutine DFLUX was employed to model the Gaussian laser beam. An algorithm was used within the subroutine to adjust the beam radius with varying depth. The absorption coefficient of the model was set equal to the experimentally measured absorption coefficient that will be discussed in Sec. 2.4.1.

2.3 Experimental Procedures

A hypoeutectic closed-cell Al-foam was used containing 7 weight percent silicon. The foam was manufactured at the Northeastern University of China using a melt-foaming method that is explained in [2], using TiH_2 as a foaming agent and Calcium to increase the viscosity of the liquid aluminum. Its volume fraction was 11% and its density was 279 kg/m^3 . Temperature-dependent material properties of AlSi7 were extracted from [70]. The Al-foam was manufactured in the form of large bricks that were afterwards cut into $100\text{mm} \times 35\text{mm} \times 50\text{mm}$ blocks using end mill tools. These blocks were afterwards sliced using slitting cutters to obtain a total of 20 specimens with dimensions of $100\text{mm} \times 35\text{mm} \times 10\text{mm}$.

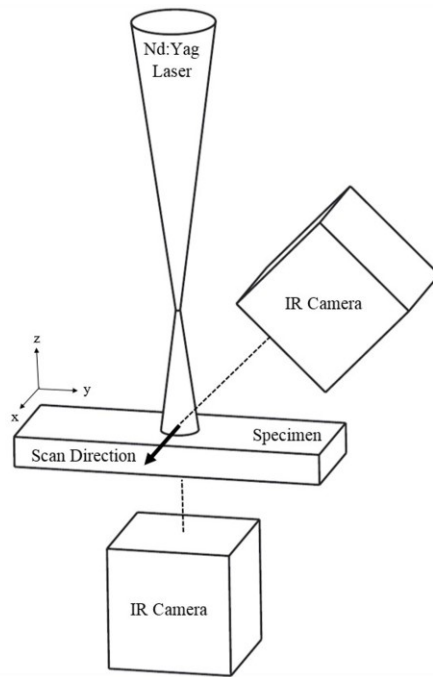


Figure 31: Experimental setup.

A GSI-Lumonics 2kW Nd:Yag laser was used with a minimum spot size of 1mm and a wavelength of 1064nm. The specimens were clamped onto a 6 degree-of-freedom Stäubli RX1300 robot and scanned underneath the laser source as shown in Fig. 31. A long-wavelength infrared camera with a maximum frame rate of 120Hz was used to generate close-up thermal measurements. A specimen holder stage was made that allowed mounting the IR camera below and on the top of the specimen. The top surface was imaged at a 45° angle to prevent the IR camera from interfering with the laser.

Stationary laser experiments were performed at 30W using a defocused laser beam with a 6mm radius. The laser center was aimed at cell wall intersections to minimize the amount of radiation absorbed within the cavities. During the laser application, the top and bottom temperature distributions were measured in real time at 120Hz. The tests were repeated at multiple locations on several specimens to statistically account for the irregularities in the foam structure.

Laser scan experiments were performed at 50W using a defocused laser beam radius of 6mm. The specimens were scanned across the entire width at scanning speeds of 2.5mm/s, 3.33mm/s and 5mm/s. The temperatures were again measured in real time at 120Hz on the top and bottom surfaces. The specimens were scanned in the x-direction close to the center of the specimen. Multiple scans were performed on several specimens, and for each scan the y-position was varied slightly.

2.4 Results & Discussion

2.4.1 Thermal Imager Calibration

Aluminum is a grey body with a low emissivity, and its emissivity can change dramatically as a function of position, surface texture and temperature. In order to minimize the uncertainty in the emissivity value, the test specimens were coated with black graphite paint, which is a material known to have a very high emissivity. To measure the emissivity of the graphite paint, a coated aluminum specimen was heated to 100°C, 200°C, 300°C and 400°C in a tube furnace, and the emissivity value in the IR camera was adjusted until the measured temperature matched the furnace temperature. The emissivity remained constant at 0.92 for all temperatures. As a result, a constant emissivity of 0.92 was used for all experiments.

The spatial resolution of the IR camera is limited to the smallest area a single pixel can detect. This was calculated to be 0.05mm×0.05mm for a 23° lens operated at a minimum measurement distance of 20mm. Since the average foam wall thickness was approximately 85µm, the spatial resolution was sufficient to detect most of the geometrical details.

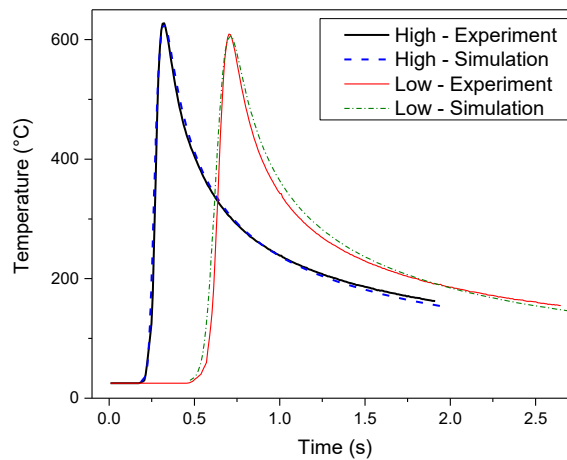


Figure 32: Experimental and numerical temperature history response during steel sheet laser forming at 800W – 50mm/s (high) and 400W – 25mm/s (low).

The IR camera response time was tested by imaging a high-speed steel sheet forming process at powers of 800W (high) and 400W (low) with scanning speeds 50mm/s and 25mm/s, respectively. The temperature was measured on the top surface. Since the camera measurement range was limited to 150-900°C, the experimental results were extrapolated below 150°C. Figure 32 shows a comparison between the experimental results and numerical results that were generated with a model that was used in previous studies by Li et al. [53] and Bao et al. [71]. The numerical model could be used as a reference since it had been validated by comparing the simulated bending angles with experimentally measured bending angles. A very good agreement was achieved between the simulation and the experiment, indicating that the camera response time is sufficient to capture transient temperature phenomena during laser forming processes.

2.4.2 Stationary Heating Source

In laser forming processes, power levels are normally chosen such that no melting and detrimental microstructural changes occur even at the highest experienced temperature. In the current study, the power levels had to be chosen more conservatively to prevent even thin walls from melting. However, no special consideration was given to microstructural changes since it was assumed that microstructural changes have a negligible effect on the heat transfer.

To ensure that no melting occurs, a low power of 30W was used with a large defocused laser beam radius of 6mm. Note that in Secs. 2.4.2 and 2.4.3, only the Kelvin-cell model was used for the numerical simulations. Since the Kelvin-cell model represents a good middle ground between the simplicity of the equivalent model and the complexity of the voxel model, it was used representatively for all the numerical models. The comparison between the three models will be performed in Sec. 2.4.5.

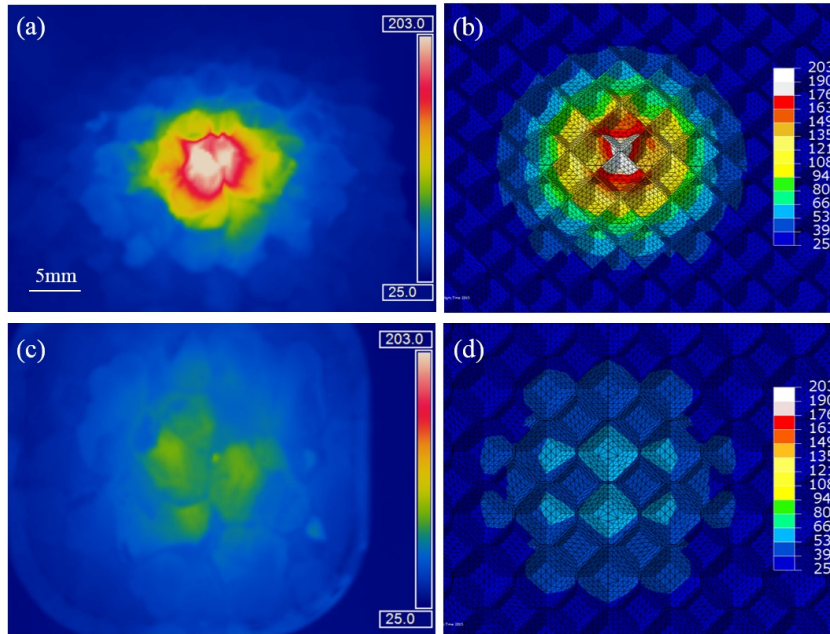


Figure 33: (a) and (c) show the experimental top and bottom temperature distributions, respectively, and (b) and (d) show the numerical (Kelvin-cell) top and bottom temperature distributions, respectively, after a 2s exposure to a 30W laser with a 6mm radius.

Figures 33(a) and 33(b) show the experimental and numerical temperature distribution on the top surface. The top surface was imaged at an angle of 45° after the completion of the 2s pulse at 30W. In general, a good agreement was achieved between the experimental and numerical color contours. Figures 33(c) and 33(d) show the corresponding experimental and numerical color contours on the bottom surface. In the experiment, the maximum temperature magnitudes were slightly higher than the numerical ones, which can be attributed to the geometrical assumptions of the Kelvin-cell model. In the real foam, the cell walls were very thin and were oriented almost perfectly perpendicular to the top surface. As a consequence, the laser irradiation was mostly absorbed within the cavities, and the heat could easily conduct to the bottom of the specimen. In the Kelvin-cell model on the other hand, the cell walls were thicker (since the thickness was constant in the entire model) and the cell walls were oriented at an angle relative to the top surface (see Sec. 2.4.5). Therefore, the cell walls could absorb a majority of the incoming heat

flux, and the heat needed to conduct through a greater distance to reach the bottom surface. This discrepancy in the absorption could be remedied by using spherical cavities as was done by Zhang et al. [61]. However, the minimum volume fraction of spherical cavity models is around 27%, which is much higher than the 11% volume fraction of the foam that was used in this study. The volume fraction could potentially be reduced by randomizing the cavity geometry, size and orientation as was done for ellipsoidal cavities by De Giorgi et al. [68]. Yet, that approach significantly increases the model complexity and thus reduces the benefit of using an approximate geometry. It can be concluded that the Kelvin-cell model has the advantage of achieving a volume fraction of precisely 11% while being rather simple to model, but it comes at the cost of a rather crude geometrical approximation.

Figure 34 shows the experimental and numerical radial temperature distributions on the top surface after 0.5s, 1s and 2s during the laser pulse. In both the experiment and the simulation the temperature distribution maintained the same profile throughout the laser pulse, which approximately mirrored the Gaussian profile of the incoming laser irradiation. During the laser pulse, the temperature profile simply shifted up, indicating that the material underwent uniform heating throughout the pulse.

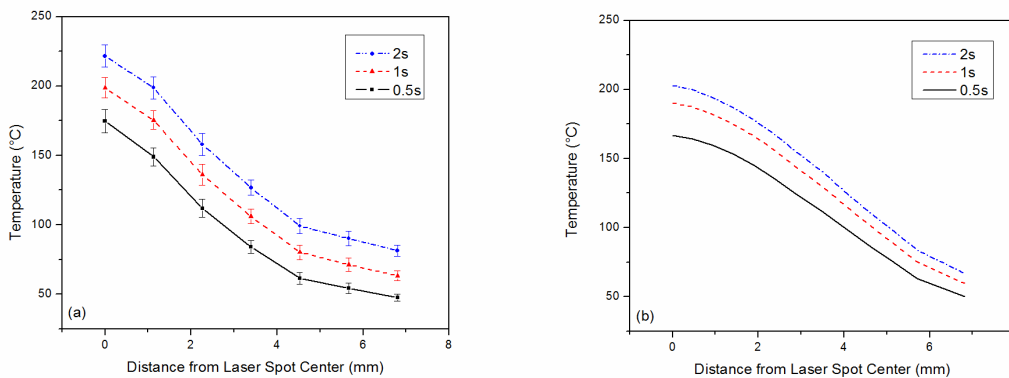


Figure 34: (a) Experimental and (b) numerical (Kelvin-cell) temperature distribution from the laser center to the edge of the laser source after a 30W laser exposure with a 6mm radius. The experimental data is averaged over 15 specimens and standard errors are shown.

Figure 35 shows the experimental and numerical temperature history on the top and bottom surface during the 2s laser pulse. It also shows the transient temperature gradient that was calculated by subtracting the bottom temperature from the top temperature. Overall, a very good agreement was achieved between the experimental and numerical results for the top, bottom and the gradient. The bottom numerical temperature was again slightly lower than the experimental one for the same reason that was explained earlier. As a consequence, the Kelvin-cell model slightly overestimated the gradient. From both the experiment and the simulation it is evident that a steep temperature gradient develops quickly when Al-foam is subjected to a laser pulse. The experimental and numerical time constants of the gradient were 0.18s and 0.2s, respectively. It can further be observed that the bottom temperature rise was delayed relative to the top. Interestingly, once the bottom temperature started to rise, it kept rising at the same rate as the top, such that a constant gradient was maintained throughout the rest of the laser exposure.

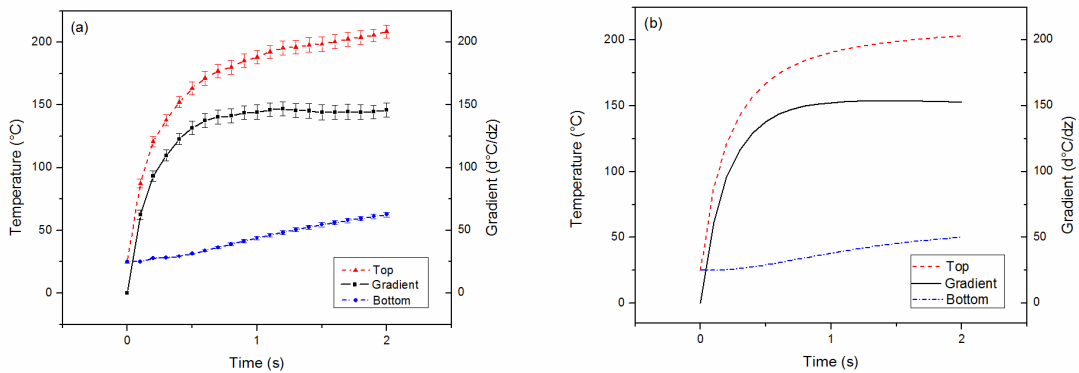


Figure 35: (a) Experimental and (b) numerical (Kelvin-cell) temperature history plots during a 2s exposure to a 30W defocused laser beam with a 6mm radius. The experimental data is averaged over 15 specimens and standard errors are shown.

2.4.3 Moving Heating Source

Figures 36(a) and 36(b) show the top experimental and numerical temperature history plots during laser scans at 50W with a 6mm radius at scanning speeds 2.5mm/s, 3.33mm/s and 5mm/s. Note that the laser powers had to be kept low to prevent thin cell structures from melting, as explained in Sec. 2.4.2. In order to maintain similar line energies as in solid laser forming, the scanning speeds had to be reduced as well. Further note that the experimental plots were extrapolated below 150°C due to the camera range limit. To explain these results, two phenomena need to be discussed that occur when the laser scanning speed is increased. Firstly, the incoming heat flux is reduced since the material is subjected to the laser for a shorter amount of time. Secondly, there is less time for the heat to diffuse away from the top surface, as shown by Li et al. [53]. These phenomena work against each other since the former decreases the top temperature while the latter increases it. As can be seen in Figs. 36(a) and 36(b), the first phenomenon was dominant in the experiment because the temperature increased significantly with decreasing scanning speed. In the simulation on the other hand, the temperature difference was much smaller, indicating that the second phenomenon was dominant. This discrepancy is related to the difference in the absorption that was explained in Sec. 2.4.2. In the experiment, the heat could quickly diffuse to the bottom, even at elevated scanning speeds. In the Kelvin-cell model, on the other hand, the heat remained trapped close to the top surface. At higher scanning speeds, the heat was unable to diffuse away quickly, and the temperature therefore increased substantially. The bottom temperature history plots of Figs. 36(c) and 36(d) confirm these observations since the experimental temperatures were much greater than the numerical ones.

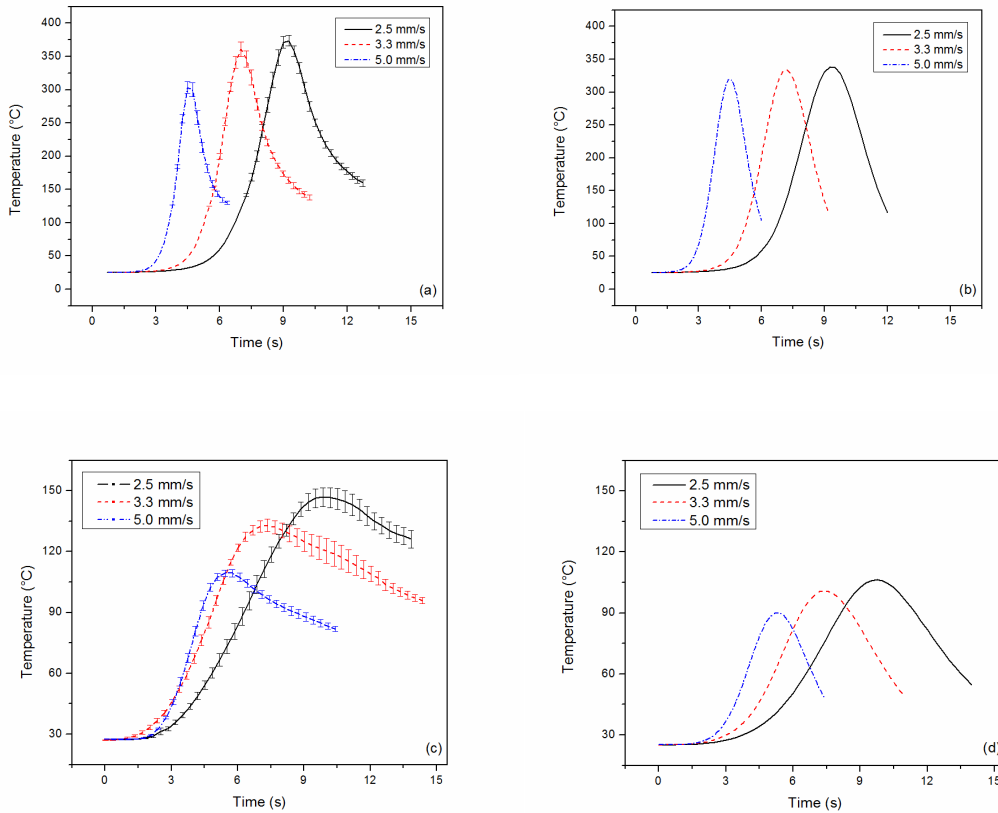


Figure 36: (a) and (c) show the experimental top and bottom temperature history plots, (b) and (d) show the numerical (Kelvin-cell) top and bottom temperature history plots at scanning speeds 2.5mm/s, 3.33mm/s and 5mm/s, respectively. The laser power was 50W with a beam radius of 6mm. The experimental results were averaged over 20 test runs and standard errors are shown.

Figure 37 shows the maximum experimental and numerical temperature gradients during a 50W laser scan at 2.5mm/s, 3.33mm/s and 5mm/s. The gradients were obtained by subtracting the bottom temperature distributions from the top temperature distributions and extracting the maximum values. The experimental and numerical gradients differed in magnitude since the numerical bottom temperatures in Fig. 37 were lower than the experimental bottom temperatures. In both the experiment and the simulation, the gradient decreased with increasing scanning speed. This result is intuitive because the gradient had less time to establish with increasing scanning speed. Moreover, it is obvious from the results in Fig. 37 that the decrease in the top

temperature with increasing speed was greater than the corresponding decrease in the bottom temperature.

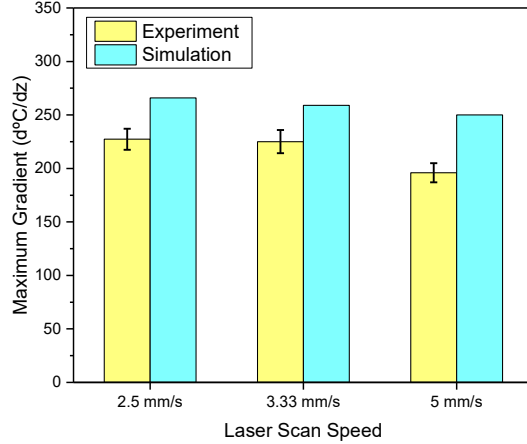


Figure 37: Experimental and numerical (Kelvin-cell) maximum temperature gradients during 50W scans with a 6mm beam radius at 2.5mm/s, 3.33mm/s and 5mm/s, respectively. Standard errors are shown for the experimental data.

2.4.4 Fourier Number

In laser forming of solid metals, three bending mechanisms have been identified, which are the temperature gradient mechanism (TGM), buckling mechanism (BM) and upsetting mechanism (UM) [22]. Moreover, the Fourier number was found to be a good indicator of which bending mechanism is dominant. It can be expressed as

$$Fo = \frac{D\alpha}{vt^2} \quad (2.6)$$

where D is the laser diameter, α is the foam thermal diffusivity, v is the laser scanning speed and t is the sheet thickness. For $Fo < 1$, TGM is expected to be the dominating mechanism, whereas $Fo > 1$ indicates that BM or UM are the dominating mechanisms. In order to determine whether the same threshold is valid for foams, the foam Fourier numbers need to be compared to the corresponding solid Fourier numbers. In foams, the laser diameters are generally bigger and the scanning speeds are lower than in solids since the laser power needs to be kept low. At the same

time, foams have much smaller thermal diffusivities compared to solids, while foam sheet thicknesses are comparatively larger. Since the Fourier number is inversely proportional to the square of the thickness and only linearly dependent on the remaining variables, the Fourier numbers of foams should generally be lower than the corresponding solid Fourier numbers. Thus, based on this analysis TGM should always be the dominant bending mechanism.

Moreover, even if the Fourier number was greater than 1, BM and UM could not occur in foams. In order for BM and UM to be dominant, the material needs to be able to develop high compressive stresses to allow buckling or thickening. Due to the thin cell walls, however, foams crush before such high compressive stresses can develop. Therefore, it is not necessary to specify a threshold on the Fourier number since TGM is the only possible bending mechanism for foams.

2.4.5 Numerical Model Comparison

In this section, the equivalent, Kelvin-cell and voxel models are compared with each other and with experimental results. Before starting the comparison, several comments need to be made about the equivalent model. Since equivalent models use a simple solid geometry, extreme care needs to be taken in the determination of the equivalent thermal conductivity. The three different approaches introduced in the background were contrasted. The Voronoi-structure method and the visual method yielded shape factors of 0.43 and 0.46, which resulted in equivalent thermal conductivities of $k_{eq} = 8.1\text{W/mK}$ and $k_{eq} = 8.7\text{W/mK}$, respectively. The experimentally tuned equivalent thermal conductivity turned out to be $k_{eq} = 10.5\text{W/mK}$. Thus, there was a rather significant disparity in the results, which is based on the underlying assumptions of the different methods. In the Voronoi-structure method, it was assumed that the foam structure could be approximated by randomly oriented honeycombs with constant wall thicknesses. Since solid aluminum is accumulated between cavities in the actual foam, the

geometrical approximations in the Voronoi-structure were still too crude despite the randomized cell distribution. A higher level of accuracy was achieved with the visual method in which the cell wall areas and the cell wall orientations were taken into account. However, the model accuracy was still limited since the mass distribution was not taken into account. This becomes clear from the fact that the visual method would predict the same shape factors for foams with huge and tiny cells as long as their cell walls have the same overall area and average orientation. In this specific case, the experimentally tuned thermal conductivity yielded the best results since it was directly tuned with laser-forming thermal data. Overall, this comparison emphasized that the choice of the equivalent thermal conductivity evaluation method has a high impact on the performance of the equivalent model, especially for foams with small solid volume fractions.

Figure 38 shows typical color contour plots of the equivalent, Kelvin-cell and voxel model during a laser scan. In the equivalent model, all the incoming laser irradiation was absorbed at the top surface ($z=10\text{mm}$). Therefore, heating was extremely localized and the isotherms were very shallow close to the top surface. Moreover, the isotherms were rather wide in the x and y -direction, indicating that the heat could easily escape along the side of the specimen. As a consequence, less heat could reach the bottom surface, and the temperature magnitude on the bottom surface was reduced. In the Kelvin-cell model, the laser irradiation could penetrate into the material, which caused the isotherms to be spaced farther apart in the z -direction. Yet, since the cell walls were oriented at an angle at the top surface, a majority of the incoming heat flux was still absorbed close to the top surface. In the voxel model, the laser could penetrate deeply into the material since the thin cell walls were almost perpendicular to the top surface. As a consequence, the heat flux was mainly absorbed inside the cavities. The isotherms were thus spaced further apart in the z -direction, indicating that more heat could reach the bottom surface.

Overall, the temperature distribution of the voxel model was most realistic, while the equivalent model induced significant errors due to inaccurate top surface boundary conditions.

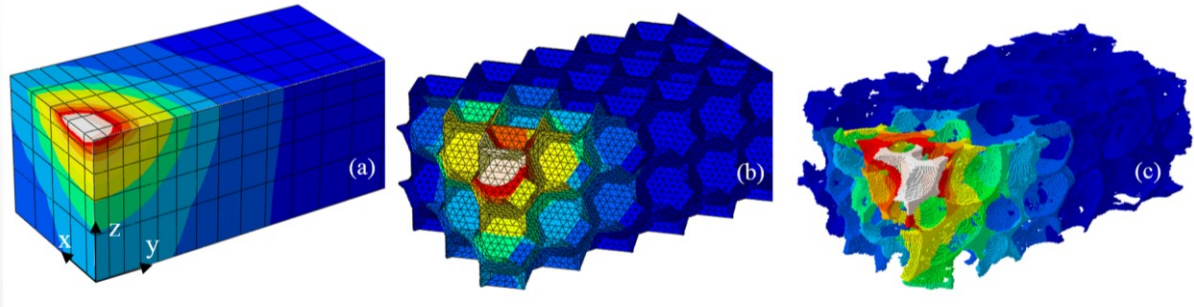


Figure 38: Typical color contours of the (a) equivalent model, (b) Kelvin-cell model and (c) voxel model during a laser scan. Legends are omitted since the color contours are used for a qualitative comparison.

Figure 39 shows the cross-sectional heat flux vectors of the different numerical models during a laser scan. The figure nicely illustrates the differences in the absorption schemes that were discussed in Fig. 38. In the equivalent model, the heat was absorbed entirely at the top surface ($z = 10\text{mm}$), while in the voxel model the heat could penetrate even further into the material than in the Kelvin-cell model due to the different cell wall orientations and thicknesses. The figure further illustrates differences in the heat flow patterns. In the equivalent model, the heat could diffuse away radially from the top surface, which overestimated the heat transfer in y -direction and underestimated the heat transfer to the bottom surface. In the explicit porous models on the other hand, the heat was channeled through the thin cell walls since it was assumed that the heat transfer through the cavities is negligible. As a consequence, the topmost cavities created a barrier for the heat transfer in the y -direction, and less heat could escape along the side of the specimen. In the voxel model, the heat flow was additionally obstructed in locations where cell walls were interrupted or of a small thickness. Thus, the voxel model again provided the most realistic heat flow simulation since it contained the highest level of geometrical details.

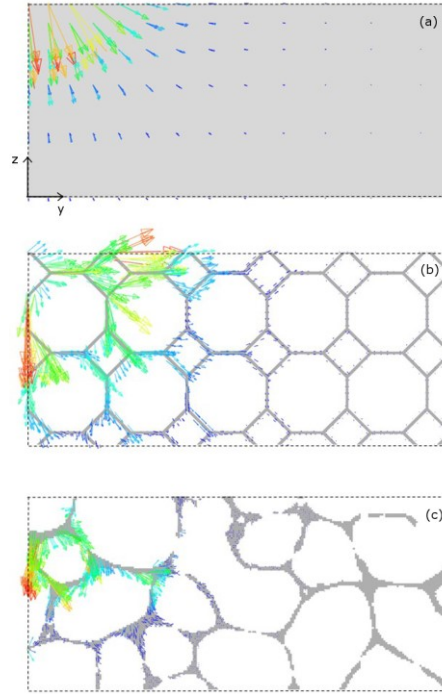


Figure 39: Heat flux vectors in cross-sections of the (a) equivalent model, (b) Kelvin-cell model and (c) voxel model during laser irradiation. Legends are omitted since the plots are used for a qualitative comparison.

Figure 40 compares the top and bottom temperature history plots of the experiment and the three numerical models during a 2s laser pulse with a 6mm radius at 30W. On the top surface, the Kelvin-cell model and the equivalent model agreed well with the experimental results. In the voxel model, however, the temperature rise was delayed. This discrepancy can be related to the surface geometry of the voxel model. During the voxel model generation, each data point of the CT-scan was converted to a cubical element, called a voxel. As a consequence, the surface of the voxel model had a staircase structure, which overestimated the surface area and hence the convective heat losses. Due to the increased convective losses, the rise in the temperature was delayed. On the bottom surface, the equivalent model predicted a very small temperature rise, which is related to the fact that the entire laser irradiation was absorbed at the top surface as shown previously. The Kelvin-cell and voxel model predictions were much closer to the experimental results, which is again consistent with the previous findings. Overall, the

differences between the three models could be mostly attributed to the laser absorption boundary condition on the top surface. If the specimen thickness was increased or the cavity size was reduced, the influence of the top surface boundary condition would be reduced, and thus the three models would yield more similar results.

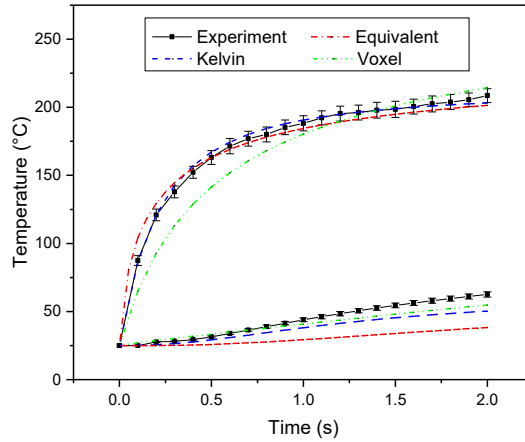


Figure 40: Experimental and numerical (equivalent, Kelvin-cell and voxel model) top and bottom surface temperature history plots during a 2s laser pulse at 30W with a defocused beam radius of 6mm.

The results from Fig. 39 can be used to predict the amount of bending that each model will generate in a thermo-mechanical analysis. Previous studies [43,53] have shown that the bending angle is proportional to the temperature gradient. Therefore, the equivalent model is expected to yield the highest bending angles, whereas the explicit porous models are expected to generate smaller bending angles.

Figure 41 compares the experimental temperature history plots with the numerical plots for a 50W laser scan with a beam radius of 6 mm and at a scanning speed 5 mm/s. The equivalent and Kelvin-cell models yielded similar heating and cooling rates as the experiment. In the voxel model, the heating and cooling rates were slightly reduced due to the overestimation of

convective losses as mentioned previously. In the Kelvin-cell model, the temperature magnitudes were slightly higher than in the experiment as was explained in Sec. 2.4.3.

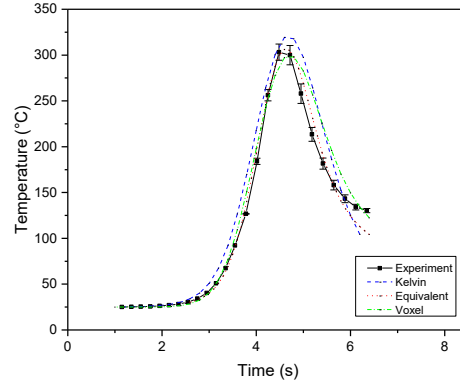


Figure 41: Experimental and numerical (equivalent, Kelvin-cell and voxel model) top temperature history plots during a 50W scan at 5mm/s with a defocused beam radius of 6mm.

Figure 42 shows the maximum experimental and numerical temperatures during 50W scans at 2.5 mm/s, 3.33 mm/s and 5 mm/s. All the numerical models predicted a linear decrease in the maximum temperature with increasing scanning speeds. In the experimental results the trend was not perfectly linear since the standard deviations were rather large. The voxel model was the only model that was able to capture the full temperature drop with increasing scanning speed. This reflects the fact that the temperature distributions and the heat flow patterns of the voxel model were most realistic. The Kelvin-cell and the equivalent model, on the other hand, both underestimated the temperature drop. The equivalent model performed slightly better than the Kelvin-cell model since the heat was able to escape in the y -direction along the side of the specimen. In the Kelvin-cell model, the heat remained trapped close to the top surface and could neither escape through the bottom nor the side. Hence, the temperatures could rise rather high despite the increase in the scanning speed.

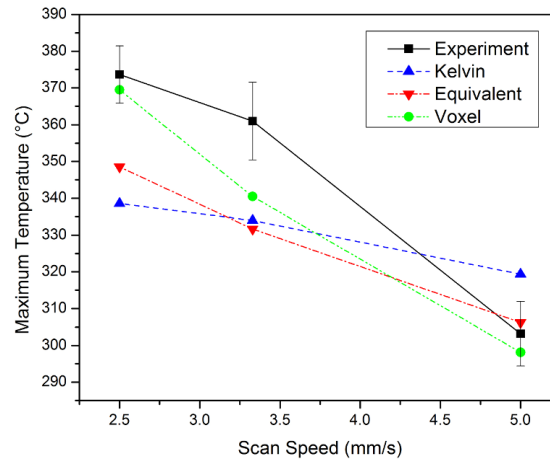


Figure 42: Experimental and numerical (equivalent, Kelvin-cell and voxel model) maximum top surface temperatures during 50W laser scans at 2.5mm/s, 3.33mm/s and 5mm/s, respectively. Standard errors are shown for the experimental data.

2.5 Conclusions

The equivalent, Kelvin-cell and voxel models all predicted steep temperature gradients during laser forming of Al-foam, and this result was both validated by experiments and theory. The advantages and disadvantages of the three numerical models were evaluated. The equivalent model was extremely simple to generate, but introduced significant errors due to the assumption that the entire heat flux is absorbed at the top surface. As a consequence, this model underestimated the bottom surface temperature, which in turn led to a higher predicted temperature gradient. Due to the crude geometrical structure of the equivalent model, the specification of the equivalent material properties was crucial, especially since the solid volume fraction was low. In comparison, the Kelvin-cell model was able to replicate the exact volume fraction of the real foam without significantly increasing the model complexity. Due to the accuracy in the volume fraction, a good agreement was achieved with the experiment for the response to stationary laser sources. At the same time, the shape of the Kelvin-cells overestimated the laser absorption close to the top surface, which limited its response to changes

in laser scanning speeds. Finally, the voxel model could replicate the exact foam geometry, which allowed for the most accurate temperature distributions and heat flow predictions during the laser exposure. As a consequence, the model was highly responsive to changes in processing conditions. The drawbacks of the voxel model were that it was computationally intensive and the staircase structure of its surface caused an overestimation of the surface area and therefore the convective losses.

Acknowledgment

Financial support from Columbia University is acknowledged. In addition, the authors acknowledge the support of Bin Zhou and the Bone Bioengineering Lab at Columbia University during the generation of the CT-scan and the voxel FEM model.

Chapter 3: Laser Induced Mechanical Response of Metal

Foam during Laser Forming

3.1 Introduction

Since its introduction in the first half of the 20th century, metal foam has been the subject of countless research studies. Many researchers have demonstrated the great potential of the material due to its high strength-to-weight ratio and its outstanding noise and shock absorption capacity [3,11]. Its material properties have been studied in great detail [2,42], and numerous potential industrial applications have been identified [9,72].

Despite all these efforts, metal foam products have rarely made it past the prototype stage. The reason is that industrial applications often call for intricately shaped parts that are challenging to manufacture. Near-net-shape manufacturing methods for metal foam do exist, such as 3D printing [13], as well as a powder metallurgy process [10]. The former, however, is a notoriously slow process, limited to small production volumes and part sizes. The latter, in turn, requires molds, limiting it to large production volumes and moderately sized parts.

Metal foam is normally manufactured in generic shapes, such as slabs or sheets, and subsequently bent to the required shape. This approach is less costly, can be implemented on a much larger scale, and yields a more uniform density distribution. The challenge associated with this method is that metal foam is prohibitively difficult to bend due to the foam's high moment of area and bending stiffness. Conventional mechanical bending methods have shown no success to date. 3-point bending, for instance, generates high tensile stresses that exceed the foam failure strength and cause immediate failure [16]. Similarly, hydroforming was shown to cause

excessive densification [17]. Therefore, an alternative bending method is needed that does not exert mechanical forces.

Laser forming has been investigated as an alternative bending method, since it is a non-contact method that does not require part-specific molds. The process is considered an economic option for low to mid production-volumes because it can be used to form arbitrarily sized parts into a wide range of geometries without a mold. Laser forming has been studied extensively for sheet metal forming, and many aspects have been investigated, such as strain rate effects [43] and process synthesis considerations [56].

Within the last decade, several research groups have attempted laser forming of metal foam and reported positive results. Experiments have been conducted with open-cell foams [57], closed-cell foams [61], and closed-cell foams with outside skin [29], each case showing that bending angles up to 45° are feasible. The reported experimental work involves parametrical studies, in which bending angles have been measured for a range of different processing parameters, such as power, spot size, scan speed and cooling methods. Moreover, the process has been studied for a range of metal foam properties, such as densities, pore sizes and sheet thicknesses. Additionally, issues related to microstructure [59] and heat treatments [60] have been addressed, and some predictive capabilities have been developed [28,30,61].

From the aforementioned work, a rather complete picture emerges about the processing window that is required for metal foam laser forming, and some rudimentary numerical capabilities have been developed. However, the existing work has three essential shortcomings.

First, none of the previous studies have addressed the underlying bending mechanism in sufficient detail. So far it has been assumed, without experimental proof, that the temperature gradient mechanism (TGM), identified by Vollertsen [22] for sheet metal laser forming, is

always the governing bending mechanism in metal foam laser forming. While this assumption has been experimentally confirmed from a thermal standpoint [26], metal foam does not meet the requirements of TGM from a mechanical standpoint, as discussed in the next section.

Second, previous studies have observed the existence of a maximum bending angle [29,57], but no comprehensive discussion of the reasons for the limiting behavior has been made. Also, the cited studies failed to address the impact of laser-induced imperfections, which occur during large-bending angle experiments, on the mechanical performance of the foam.

Finally, the cited experimental work is limited to bending angle measurements, and thus the existing numerical models have only been validated via the bending angle [30,61]. Additionally, the process has never been simulated up to large bending angles, and no comparison between models of different geometries has been done.

A step towards addressing the last issue was recently accomplished by measuring the transient temperature distributions in metal foam, using an infrared camera [26]. The obtained results were used to validate three numerical models with different levels of geometrical accuracy. In this study, the efforts from [26] were extended to the analysis of the mechanical aspects of laser forming. This was done by experimentally validating the numerical strain distributions using digital image correlation (DIC). Additionally, the bending mechanism was revisited by comparing metal foam laser forming with steel sheet laser forming, as well as 4-point bending. From the similarities and differences, a modified temperature gradient mechanism (MTGM) has been proposed. Finally, the limiting behavior of metal foam was investigated, both experimentally and numerically, by determining the extent of cell collapsing near the top surface, and monitoring the crack formation on the bottom surface. The impact of both of these imperfections on the foam crushability and structural integrity was investigated.

3.2 Background

3.2.1 Metal Foam Mechanics and Deformation

Metal foam shows fundamentally different deformation behaviors in tension and compression. In tension, the material can undergo only a small amount of plastic deformation and has a low strength. In compression, on the other hand, the stress-strain curve can be divided into three distinct stages, as shown in Fig. 43. Initially, the stress increases linearly with strain, then transitions to a large “plateau” where cells collapse, followed by an exponential increase after the foam is fully compressed. Due to the wide plateau, the area under the stress-strain curve is large, explaining why metal foam is an excellent energy absorber.

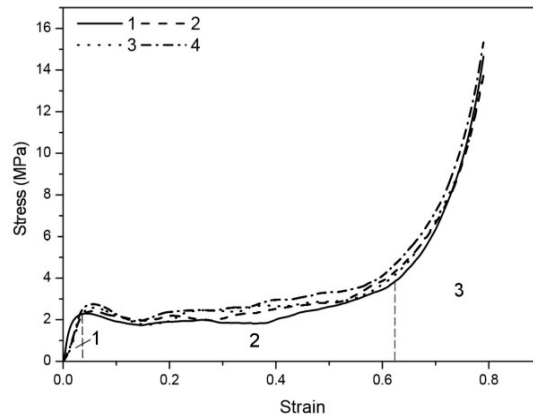


Fig. 43 Uniaxial compressive stress-strain data (engineering) of four compression specimens (curves 1-4) made with the same metal foam that was used in this study [34]. The stress-strain curve can be divided into three segments: (1) a linear regime, followed by (2) a plateau where cell crushing occurs and a large amount of energy is absorbed, followed by (3) foam densification. Due to their crushability, metal foams can withstand much lower compressive stresses than solid metals.

Metal foam bending involves a combination of tensile and compressive deformation. Compared to solid material, metal foam has a very large bending stiffness S , which is defined as the resistance of the material to bending deformation and is denoted by

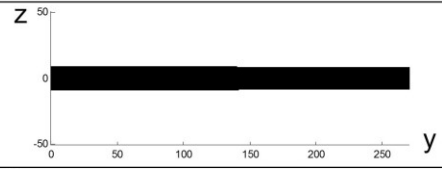
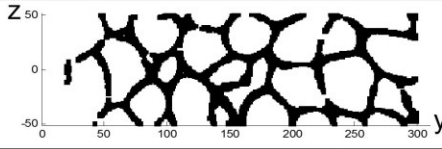
$$S = \frac{B_1 EI}{l^3} \quad (3.1)$$

where B_l is a scaling factor that is boundary and loading condition dependent, E is Young's modulus, I the moment of area, and l the beam length [3]. The reason is that the moment of area of the foam is more than an order of magnitude greater than the moment of area of a solid with the same net cross-sectional area (Table 4), where I is calculated via

$$I = \int_{-s_0/2}^{s_0/2} z^2 y(z) dz \quad (3.2)$$

where s_f is the sheet thickness and $y(z)$ the net section width at height z . Thus, the combination of high bending stiffness and low tensile strength explains why mechanical bending of metal foams is prohibitively difficult.

Table 4 The moment of area (about $z = 0$) of a metal foam with 89% porosity is 43.4 times higher than the area moment of a solid with the same cross-sectional area. As a consequence, metal foam has a much higher bending stiffness.

	Cross-section	Moment of area
Solid		1
Foam		43.4

Unlike solid material, which is in most cases assumed to be incompressible, metal foam can yield both due to deviatoric stresses, as well as hydrostatic stresses. Assuming isotropic behavior, the yield surface is a closed symmetric ellipsoid with aspect ratio α , and the yield criterion involves both Von Mises' equivalent stress σ_e as well as the mean stress σ_m [41]:

$$F = \left[\frac{1}{1 + (\alpha/3)^2} (\sigma_e^2 + \alpha^2 \sigma_m^2) \right]^{1/2} - Y \leq 0 \quad (3.3)$$

where Y is the uniaxial yield strength. When $F < 0$, the material behavior is elastic, and when $F = 0$, plastic deformation occurs pursuant to the following flow rule

$$\dot{\varepsilon}_{ij}^p = \frac{\dot{Y}}{H} \frac{\partial F}{\partial \sigma_{ij}} \quad (3.4)$$

where $\dot{\varepsilon}_{ij}^p$ is the plastic strain rate, and H is the hardening modulus defined as

$$H = \frac{\sigma_e}{\hat{\sigma}} h_\sigma + \left(1 - \frac{\sigma_e}{\hat{\sigma}}\right) h_p \quad (3.5)$$

where h_σ and h_p are the tangent moduli in uniaxial and hydrostatic compression respectively, and $\hat{\sigma}$ is the equivalent stress that is equal to the first term in the yield criterion (eq. (3.5)).

3.2.2 Bending Mechanism

The thermo-mechanical bending mechanisms underlying laser forming are currently only well understood for solid materials [22]. For metal foam laser forming, it has thus far always been assumed, without experimental proof, that the temperature gradient mechanism (TGM) is the governing bending mechanism.

TGM was introduced by Vollertsen [22] for sheet metal laser forming, and it governs the scenario where a steep temperature gradient develops across the thickness of the workpiece. The material immediately below the laser spot heats up and tries to expand, but is restricted by the “cold” surrounding material. Instead of being able to expand, the material point becomes plastically compressed. This phenomenon occurs along the entire scan line, making the material shorter on the top surface and bending the workpiece towards the laser.

From a heat transfer standpoint, experiments have confirmed that steep temperature gradients develop across metal foam during laser forming [26], and thus the prerequisites for TGM are met. When investigating the mechanical aspects of laser forming, however, it becomes questionable whether TGM is valid for metal foam for several reasons.

First, the “shortening” that occurs in TGM via the formation of plastic compressive strain does not seem possible in metal foam, due to its crushability. The reason is that unless metal foam is in the densification stage, its yield strength is less than one 60th of the yield strength of the solid metal it is made of, since its fragile cell walls crush when subjected to large compressive stresses.

A second argument that puts TGM in question is the low tensile strength of metal foam. Even though TGM postulates that bending is mainly caused by compressive strains on the top surface, some tensile deformation occurs near the bottom surface as well. Solid metal can plastically deform in tension and thus accommodate the tensile deformation. Metal foam, on the other hand, can undergo only a small amount of plastic tensile deformation and fractures shortly beyond the linear elastic regime [73]. Thus, bending via TGM should cause an immediate fracture in metal foam. Hence, the traditional TGM does not fully capture the foam response during laser forming and needs to be revisited.

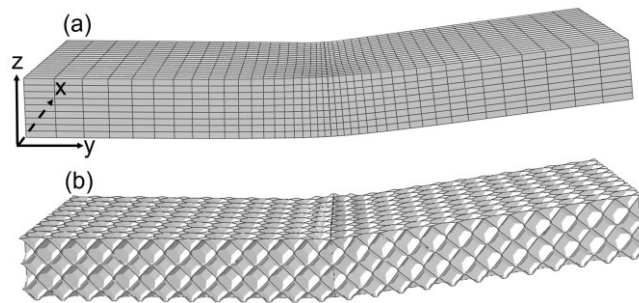


Fig. 44 Two approaches were used to model metal foam. In the first (“equivalent”) model, shown in (a), a solid geometry was used and equivalent foam properties were assigned. In the second (“Kelvin”) model, shown in (b), the foam geometry was explicitly modeled, and solid aluminum properties were assigned. The cavity geometry was approximated by a Kelvin-cell geometry.

3.2.3 Numerical Simulations

The metal foam geometry was modeled using two different approaches shown in Fig. 44, with details explained in [26]. In the first model, “equivalent” model (used in Secs. 3.4.1 - 3.4.3), a solid geometry with equivalent foam properties was used. In the second model, “Kelvin”

model, (used in Sec. 3.4.4), the foam geometry was modeled explicitly, approximating the cavity geometry by a Kelvin-cell geometry, and assigning solid aluminum properties. The simulation was carried out using uncoupled thermo-mechanical analyses, whereby the output of the thermal analysis was used as a predefined field for the mechanical analysis. While this study exclusively discusses the mechanical aspects of the simulation, a detailed investigation of the thermal aspects may be found in [26].

In the equivalent model, the constitutive behavior was modeled using the equations introduced in Sec. 3.2.1, making two major assumptions: (1) the yield surface is symmetric, which has been verified for a similar metal foam [41], and (2) hardening occurs in an isotropic manner. The latter assumption is not valid for large deformations due to the fundamentally different responses of metal foam in tension and compression. Since the tensile strains are small compared to the compressive strains, however, the induced errors are small. In the Kelvin model, the constitutive behavior was modeled using Von Mises' yield criterion and the Levy-Mises flow rule.

The foam mechanical behavior at large bending angles was simulated using the equivalent model. The cell crushing behavior of the foam was modeled in an average sense, by calculating the volumetric plastic strain rate $\dot{\epsilon}_m$ from the flow rule (eq. (3.4)), using the expression [41]

$$\dot{\epsilon}_m = \frac{\alpha^2 \dot{\epsilon}}{[1 + (\alpha/3)^2]^{3/2}} \quad (3.6)$$

where $\dot{\epsilon}$ is the work conjugate strain rate of $\hat{\sigma}$ that can be expressed as $\dot{\epsilon} = \dot{\hat{\sigma}}/H$. The volumetric strain rate can also be written as $\dot{\epsilon}_{ii} = \dot{R}/R$, where R is the relative density and \dot{R} is the relative density variation rate. Integrating this equation gives the current relative density R

$$R = R_0 \exp\left(-\int \dot{\epsilon}_{ii} dt\right) \cong R_0 \exp(-\Delta\epsilon_{ii}) \quad (3.7)$$

where R_0 is the relative density at the previous time increment and $\Delta\epsilon_{ii}$ are the logarithmic “true” strain increments in all directions [52]. Eq. (3.7) was then used to calculate the relative density distributions at a cross-section of the foam.

The simulations were implemented in Abaqus, and densification calculations were performed in Matlab. Multi-scan simulations were performed on the Stampede supercomputer provided by XSEDE [74]. Quadratic elements C3D20 were used for the equivalent model, and linear tetrahedral elements C3D4 were used for the Kelvin model. A y-symmetry boundary condition was used that set displacements in the y-direction (U2) and rotations about the x and z-axes (UR1, UR3) equal to zero. Furthermore, the displacements in x and z (U1, U3) were restricted at two vertically aligned points on the symmetry surface. Rotations about the y-axis (UR2) were not restricted.

The thermal properties were used from [26]. The temperature-dependent thermal expansion coefficient $\alpha_{th}(T)$ of the foam was assumed to be identical to that of the corresponding solid and was extracted from [70]. Temperature-dependent Young’s modulus $E(T)$ was obtained for solid AlSi11 [75] and converted to foam using relations given in [76]. The elastic and plastic Poisson’s ratios ν and ν_p were obtained from [76] and [41], respectively. The flow stress σ_f was obtained from [34], and the temperature dependence was adapted from solid aluminum data [70]. The compressive yield stress ratio σ/p_c was estimated based on [41].

Steel sheet forming simulations were performed using the model in [43]. 4-point bending simulations were based on U-bend simulations developed by Brandal and Yao [77]. The loading block and supports were defined as rigid shells, and a general contact interaction, with zero friction, was used. Loading was exerted by vertically displacing the loading block.

3.3 Experimental Procedures

Closed-cell Al-foam was used, with 7 weight percent silicon, a volume fraction of 11.2% and a density of 279 kg/m^3 . The foam was manufactured employing a melt-foaming method that used TiH_2 as a foaming agent and calcium to increase the viscosity of the liquid aluminum. Slitting cutters and end mill tools were used to cut test specimens to a length, width and thickness of 100 mm, 35 mm and 10 mm, respectively.

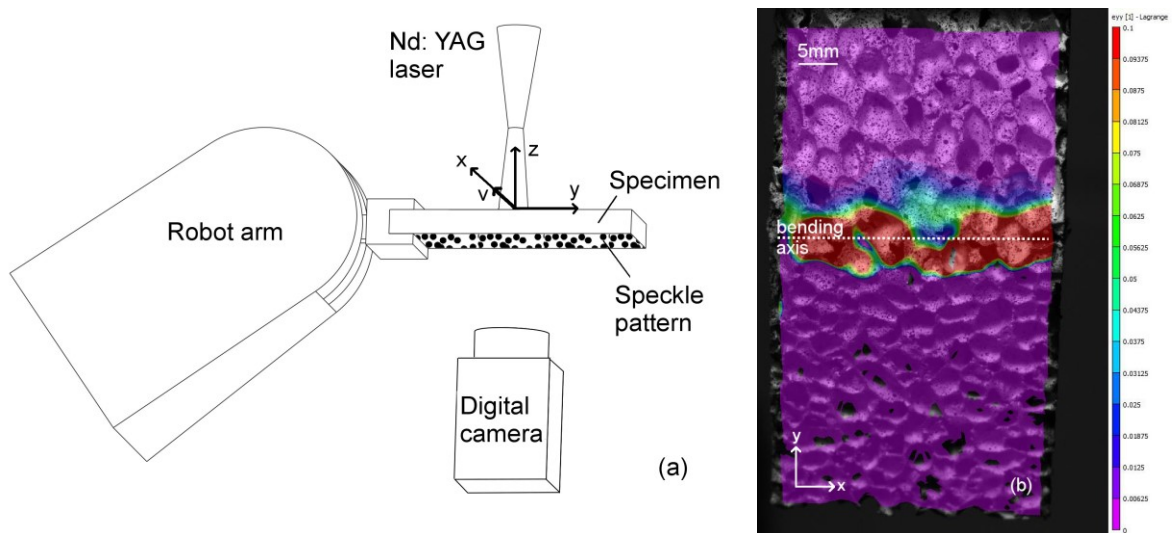


Fig. 45 (a) Experimental setup. The laser was scanned in x-direction. The bottom specimen surface was spray-painted white with a black speckle pattern. Digital images were taken in between consecutive laser scans. (b) Example strain distribution (ϵ_{yy} , Lagrangian strain) on the bottom surface of a laser formed specimen at a bending angle of 45° . The strain was only extracted on the clamped half of the specimen above the bending axis to avoid effects related to out-of-plane rotations [37].

Laser forming experiments were performed using a continuous-wave Nd:YAG laser with a wavelength of 1064 nm. All the experiments were performed using a spot size of 12 mm, and the specimens were positioned below the focal plane to ensure that the laser intensity does not increase inside cavities (Fig. 45(a)). The specimens were clamped at one end using rubber pads to provide thermal insulation. Nitrogen was used as a protective gas to avoid oxidation, and in between successive scans the specimen was allowed to cool to room temperature to prevent heat

accumulation effects. The bending angle was determined by measuring the vertical deflection with a dial indicator.

The specimens were scanned underneath the laser using a 6 DOF Stäubli RX-130 robot. Two representative processing conditions were contrasted with (power, scan speed) of (90 W, 5 mm/s) and (180 W, 10 mm/s), respectively. The line energy $LE = P/v$ was kept constant, since constant LE experiments reveal several aspects of the physical behavior of metal foam and allow for a meaningful comparison with numerical simulations as has been shown in [53].

Digital image correlation (DIC) was used to determine the strain distribution on the bottom specimen surface in between consecutive laser scans (Fig. 45(b)). The DIC experiments were performed by spray-painting the bottom specimen surfaces white and subsequently applying a black speckle pattern. A digital camera with a resolution of 2448 x 2048 pixels was used to take images of the speckle pattern after each laser scan. To achieve the best resolution of about 100 μm , it was ensured that the speckle sizes corresponded to 3-5 pixels on the digital camera [35,36]. The commercial DIC software VIC-2D from Correlated Solutions was used to calculate the Lagrangian strain fields from the digital images, which were subsequently converted to the logarithmic “true” strain fields. All the strains were computed in the tensile direction (ϵ_{yy}). Several calibration tests were performed to ensure that the results were independent of variables such as the subset, stepsize, seed placement and incremental correlation. An example of a processed image is shown in Fig. 45(b), representing a strain distribution (ϵ_{yy}) at a bending angle of 45°.

To avoid strains induced by out-of-plane rotations [37], the strain was only extracted on the clamped half of the specimen above the bending axis (Fig. 45(b)). To minimize the impact of local inhomogeneities, the data was averaged over the entire specimen width and a distance of 5

mm from the bending axis. Standard errors were calculated over all individual pixels within that area.

The laser forming strain distributions were compared with strain distributions in 4-point bending experiments. 4-point bending tests were performed pursuant to a combination of ASTM standards D7249 and C1341. The data was averaged over a rectangle similar to laser forming, and was also corrected for strains caused by out-of-plane displacements [37].

3.4 Results & Discussion

3.4.1 Bending Mechanism

In the background section, it was predicted that metal foam is unable to develop the compressive strains central to the traditional temperature gradient mechanism (TGM), due to its crushability and low compressive strength. Laser forming experiments revealed two aspects of the foam behavior that spoke in favor of this prediction. First, no matter how low within the processing window the laser power was chosen, localized melting of thin cell walls was unavoidable. As shown in Fig. 46, melting initiated at the first laser scan and progressed with each successive laser scan. Thin cell walls started melting from the top surface, forming u-shaped trenches that deepened until either the entire cell wall was melted away, or the cell wall thickness increased. If metal foam bending indeed occurred due to plastic compressive strains, melting would drastically impede bending, because it reduces the amount of compressible material. Experiments have shown the contrary, however, implying that plastic compressive strains cannot be the major cause of bending.

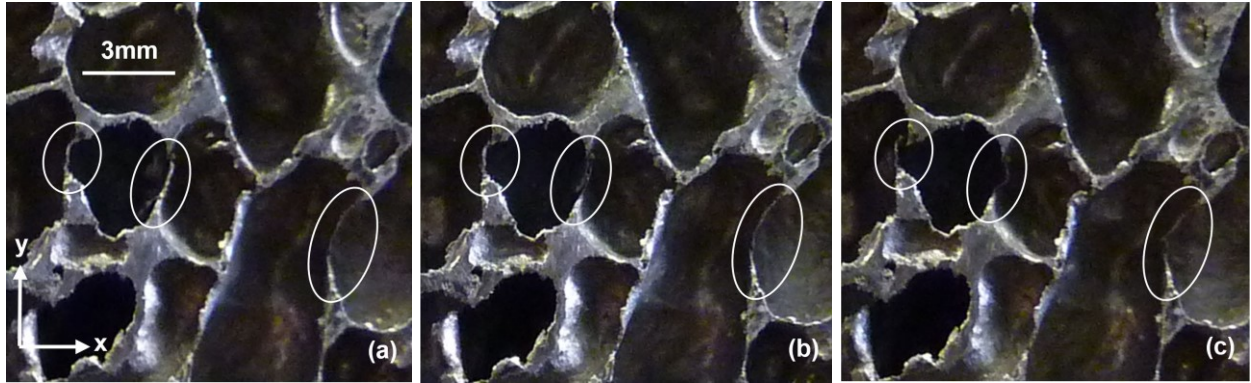


Fig. 46 Section of the top surface of the specimen on the laser scan line (a) before laser forming, (b) after 1 scan and (c) after 10 scans at 90 W and 5 mm/s. Even at this low power, localized melting of thin cell walls occurred, marked in white. Melting started after the first scan and progressed with each consecutive scan, forming u-shaped trenches in the cell walls and reducing the amount of compressible material. Melting stopped once the thickness of the remaining cell wall sections increased.

The second aspect is that cell wall bending occurred close to the bending axis (Fig. 47), clearly indicating that the cell walls are unable to withstand high compressive stresses.



Fig. 47 Cross-section of a foam specimen after 5 laser scans at 180 W and 10 mm/s. The laser was scanned into the page. The white arrows show where cell walls were bent during laser forming, indicating that the foam cannot withstand high compressive stresses.

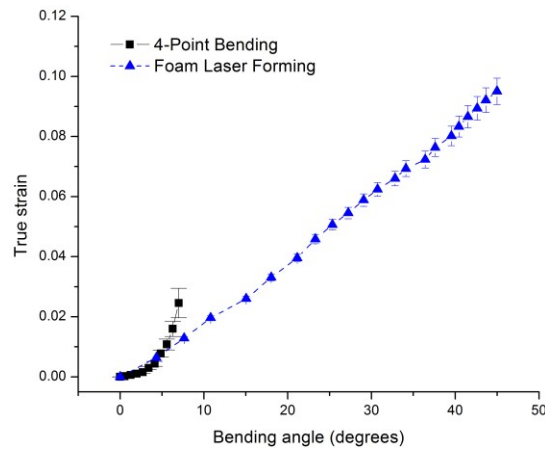


Fig. 48 Comparison of the tensile strain (ϵ_{yy}) on the bottom surface (determined via DIC) in 4-point bending and laser forming (at 180 W and 10 mm/s). ϵ_{yy} is the strain resulting from a combination of cell collapsing and cell wall deformation. Standard errors are shown, calculated over all the pixels of the averaged areas (see Sec. 3.3). In 4-point bending, the strain increased exponentially before a catastrophic failure, whereas in laser forming there was a stable linear strain growth with increasing bending angle. Laser forming yielded a larger maximum ϵ_{yy} , due to heat-induced softening, yet ϵ_{yy} did not grow proportionally to the bending angle, and hence tensile stretching cannot be the main cause of bending.

An alternative explanation is that metal foam bending is mainly caused by tensile stretching near the bottom surface instead of compressive deformation on the top. To investigate this hypothesis, the tensile strain ϵ_{yy} (determined via DIC) was compared for laser forming and 4-point bending (Fig. 48). ϵ_{yy} is the strain resulting from a combination of cell collapsing and cell wall deformation. In laser forming, ϵ_{yy} indeed grew substantially larger than in 4-point bending, due to heat-induced softening. However, while the maximum ϵ_{yy} in laser forming was around 4 times greater than in 4-point bending, the maximum bending angle was greater by a factor of 7. Therefore, ϵ_{yy} did not grow proportionally to the bending angle, hence tensile stretching cannot possibly account for all of the bending deformation.

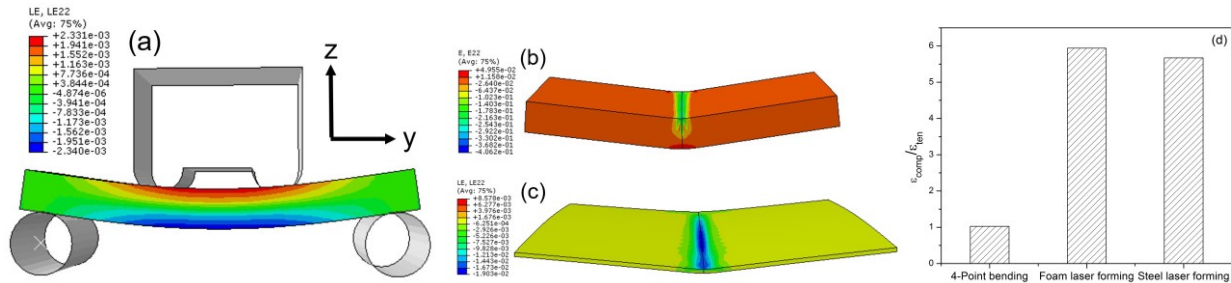


Fig. 49 Strain distributions (ϵ_{yy}) in (a) metal foam during 4-point bending, (b), metal foam during laser forming, and (c) a steel sheet during laser forming. (d) Ratio of top surface (compressive) strain over bottom surface (tensile) strain at the bending axis, calculated for all three simulations. In 4-point bending, bending was equally caused by compressive and tensile strains. In laser forming, the large ratios indicate that compressive deformation was the main cause for bending.

Numerical results confirmed that tensile stretching is not the driving force of the bending deformation. Figure 49(d) shows the ratio of the compressive top surface strain to the tensile bottom surface strain for metal foam laser forming, steel sheet laser forming, and 4-point bending (models shown in Figs. 49(a)-49(c)). The equivalent model was used for the simulation of metal foam, which was experimentally validated in [26,27]. In all cases, the strains were

extracted at the bending axis. For foam and steel laser forming, the ratio was averaged over 10 scans and two typical conditions [foam - (90 W, 5 mm/s; 180 W, 10 mm/s), steel - (400 W, 25 mm/s; 800 W, 50 mm/s)], to obtain a most representative value. For 4-point bending, the ratio was averaged over all the bending angles until the experimental failure angle. The results in Fig. 49(d) clearly show that, whereas compression and tension contributed equally in 4-point bending, compressive deformation was the major cause of bending in laser forming. Interestingly, metal foam and steel sheet laser forming nearly yielded the same ratio, implying that the compressive “shortening” on the top surface should be identical in both metal foam and steel.

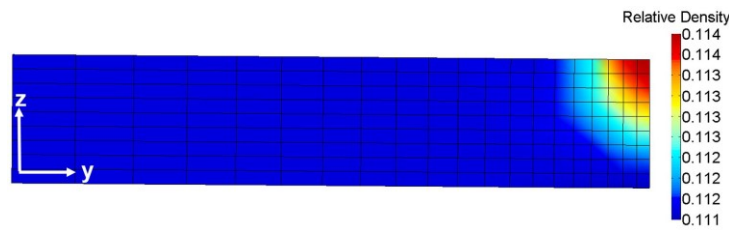


Fig. 50 Relative density distribution after a single scan at 180 W and 10 mm/s. The baseline relative density is 0.112, and a relative density of 1 indicates complete densification. Densification occurred throughout the top 80% of the foam, leaving only a small tensile region on the bottom surface. Therefore, laser forming shifts the neutral axis downwards, and deformation is dominated by compressive shortening.

Numerical relative density distributions at a cross-section, calculated after a single laser scan at 180 W and 10 mm/s (Fig. 50), allow a similar conclusion to be drawn. The baseline relative density is 0.112, and a relative density of 1 indicates complete densification. The densified (compressed) region stretched over the top 80 % of the foam, leaving only a small expanded (tensile) region on the bottom. Therefore, laser forming seems to shift down the neutral axis and limits the amount of tensile deformation occurring, unlike in 4-point bending (Fig. 49(a)), where the neutral axis lies midway through the thickness (assuming small bending angles).

The findings in Figs. 46-50 allow only one explanation: cell wall bending and cell crushing in metal foam laser forming, observed in Fig. 47, is equivalent to plastic compressive strains in steel sheet laser forming.

Using that insight, the bending mechanism of metal foam can be revisited. Metal foam develops steep temperature gradients across its thickness and thus meets the thermal prerequisites of TGM [26]. Similar to solid metal, bending is mainly achieved via compressive deformation, and tensile deformation near the bottom surface only occurs to accommodate the “shortening” on the top surface. The reason for its “shortening” near the top surface, however, differs from conventional TGM. Unlike solid sheet metal, which develops plastic compressive strains, metal foam shortens due to cell wall bending and cell collapsing. Moreover, metal foam does not immediately undergo a tensile fracture on the bottom surface due to heat-induced softening, as well as a downward shift in the neutral axis that limits the amount of tensile deformation. Since metal foam still meets most of the requirements set by TGM, this revised bending mechanism may be called modified temperature gradient mechanism (MTGM).

3.4.2 Bending Limit

For laser forming of solid sheet metal, several studies reported that the bending increment decreases with increasing laser scans [55,80]. In laser forming of metal foam, a similar limiting behavior was observed at two different processing conditions, (high – 180 W; 10 mm/s) and (low – 90 W; 5mm/s), shown in Fig. 51. In the experiment, as well as the simulation, the rate of change of both the bending angles and tensile strains decreased with an increasing number of scans and eventually approached zero, indicating that there is a maximum achievable bending angle.

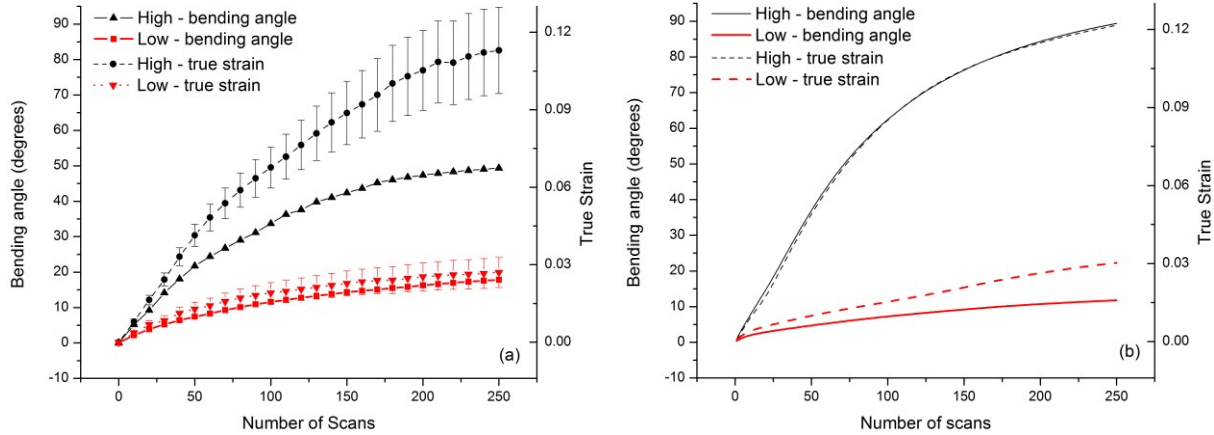


Fig. 51 (a) Experimental and (b) numerical bending angles and tensile strain data (ϵ_{yy}) at large bending angles. “High” refers to the condition 180 W 10 mm/s, “low” refers to 90 W 5 mm/s. Standard errors are shown for the strain results, calculated over all the pixels of the averaged area (see Sec. 3.3). In both the experiment and the simulation, the bending angle and strain plots leveled off at a large number of scans. In the numerical simulation, the limit at 180 W and 10 mm/s was reached at a larger bending angle, since the model did not consider melting, as well as changes in the moment of area, laser absorption and thermal conductivity with increasing densification.

In solid metals, the limiting behavior can be attributed to increases in the sheet thickness, strain hardening on the bottom surface, and variations in the laser absorption due to coating removal and heat-induced surface discoloration [55,78]. In metal foam, on the other hand, thickening does not occur, and neither does strain hardening on the top surface, since the flow stress remains constant until densification. Tensile strain hardening on the bottom surface only occurs to a small extent, because metal foam can only undergo limited amounts of plastic tensile deformation. Variations in the laser absorption do occur in metal foams, since cavities crush and rotate with increasing bending angle, but they are not significant enough to be the major cause of the bending limit. Similarly, melting ceases after a few laser scans and cannot be responsible for the limit either.

Therefore, the bending limit must be caused by a phenomenon that does not occur in sheet metal laser forming, which is cell crushing and the subsequent densification. Densification increases the amount of material away from the central axis of the foam, and hence increases its

moment of area, rendering the foam stiffer. Simultaneously, both Young's Modulus [77] and the flow stress [3] of the foam increase exponentially with its relative density, as shown in

$$\frac{E_f}{E_s} = \frac{(1 - \rho_f / \rho_s)^2}{(1 + (2 - 3\nu_s) \rho_f / \rho_s)} \quad (3.8)$$

$$\frac{\sigma_f}{\sigma_s} \approx 0.3 \left(\phi \frac{\rho_f}{\rho_s} \right)^{3/2} + (1 - \phi) \frac{\rho_f}{\rho_s} \quad (3.9)$$

where E_f, σ_f, ρ_f are the Young's Modulus, yield strength, and density of the foam respectively, and E_s, σ_s, ρ_s the corresponding solid properties. ν_s is the Poisson's ratio of the solid, and ϕ is the percentage of solid material at cell intersections, which was assumed to linearly increase with foam density. These equations show that densification stiffens the foam even further and reduces the amount of plastic deformation. Densification also increases the thermal conductivity, as is shown by [2]

$$\left(\frac{\rho_f}{\rho_s} \right)^{1.8} < \frac{k_f}{k_s} < \left(\frac{\rho_f}{\rho_s} \right)^{1.65} \quad (3.10)$$

where k_f and k_s represent the foam and solid thermal conductivities, respectively. As a consequence, the heat diffusion away from the top surface increases, thereby reducing the amount of thermal expansion and plastic compressive deformation. Hence, densification is the main reason for the bending limit in metal foam laser forming.

From the results in Fig. 51, it is apparent that (180 W; 10 mm/s) yielded a higher maximum bending angle than (90 W; 5 mm/s). The reason is that, for an increased power and speed (at LE = const.), heat has less time to dissipate, thus increasing the temperature rise, thermal expansion, and plastic compressive "shortening" close to the top surface [26,53]. Hence, more densification is required to stop the plastic compression from occurring.

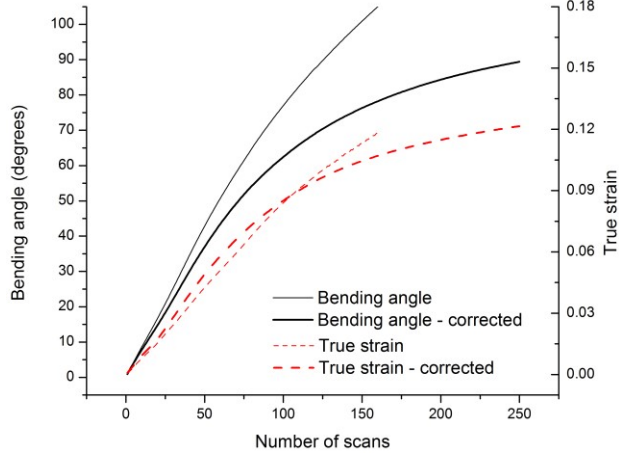


Fig. 52 Comparison of numerical data before and after correcting for density-dependence. Without correction, both the bending angle and strain increment decreased only slightly with increasing scans, induced by tensile strain hardening on the bottom surface. After incorporating density-dependent variables, a distinct limiting behavior could be observed.

Numerical results confirm the above reasoning. Without accounting for densification effects, the bending and strain increment only slightly decreased with increasing laser scans in Fig. 52, whereby the decrease was caused by tensile hardening on the bottom surface. When calculating the density as a field variable using $\rho = \rho_0 e^{-(\epsilon_u)}$ (from eq. (3.7)) and incorporating density-dependent Young's Moduli and flow stresses from eqns. (3.8) and (3.9), both the bending and strain increment decreased much more quickly, and the resulting corrected results agreed better with the experimental trends. Therefore, simulations confirmed that densification-induced changes in the material properties are the major cause of the bending limit.

While the numerical results agreed with the experimental results at 90 W and 5 mm/s, they overestimated the bending angle at 180 W and 10 mm/s, and simultaneously underestimated the tensile strain on the bottom surface. Several approximations in the model led to this error that only became significant at large bending angles and higher powers/speeds. First, melting was neglected, which relaxes stresses in the material and thus reduces the amount of bending. Second, the model failed to account for changes in the moment of area, owing to its solid geometry. Finally, due to it being an uncoupled analysis, the model did not account for changes

in the laser absorption, as well as densification-induced changes in the thermal conductivity, k , whose impact can become significant at large bending angles. This problem could be mediated by using a coupled thermo-mechanical analysis, but doing so currently renders the simulation too CPU-intensive to study laser forming at large bending angles.

3.4.3 Impact of Laser Forming on Metal Foam Performance

Bending deformation in metal foam laser forming is achieved by introducing irreversible plastic deformation, which, as was shown previously, manifests itself mainly through cell crushing and some tensile deformation. This plastic deformation may affect the performance of metal foam as a crash absorber and structural member. In this section, it is demonstrated that the impact of laser-induced imperfections are negligible until large bending angles are reached.

A first type of laser-induced imperfections is crack formation near the bottom surface. Some thin cell walls, which have naturally occurring stress concentrations, while also being favorably aligned with the bending direction, can form micro-cracks already at low bending angles of 1° (Fig. 53(a)). More micro-cracks form with increasing bending angles (Figs. 53(b) and 53(c)), but they are small in size and remain isolated from each other. Once the bending angle approaches 45° , the cracks grow and start coalescing, forming a more visible crack (Fig. 54(a)).

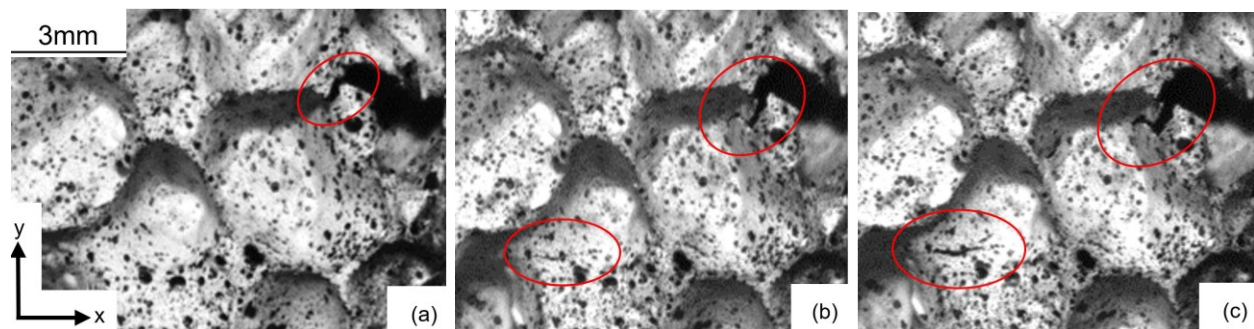


Fig. 53 Bottom surface of a specimen scanned at 90 W and 5 mm/s at bending angles of (a) 1° , (b) 11.6° , and (c) 16.3° . Due to some naturally occurring stress concentrations, micro-cracks already occurred at low bending angles of 1° . As the bending angle became larger, those micro-cracks increased in size, and new

micro-cracks formed (b,c). However, the micro-cracks remained isolated from each other at this stage and thus hardly affected the structural integrity of the foam.

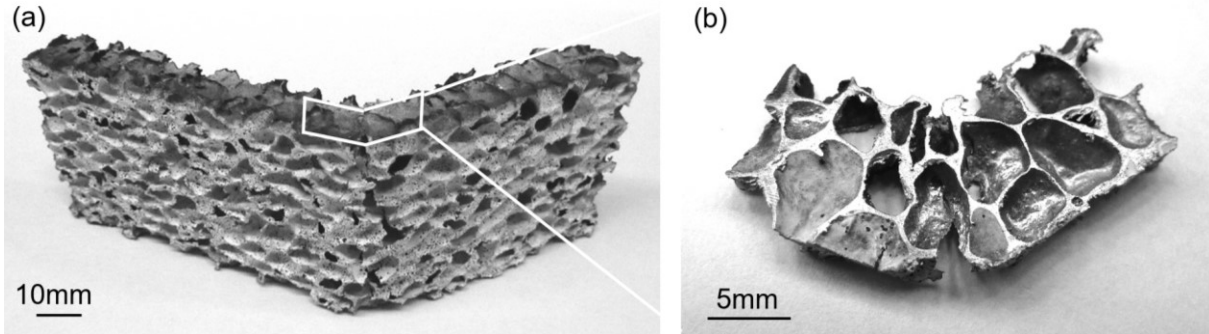


Fig. 54 (a) Foam specimen at a bending angle of 45°, after being laser formed at 180 W and 10 mm/s, with a cross-section shown in (b). At large bending angles, the isolated cracks on the bottom surface grew larger and started to coalesce, shown in (a). In close proximity to the bending axis, cells at the top surface were crushed significantly, shown in (b), but the foam was still far away from complete densification.

The impact of those micro and macro-cracks on the structural strength of metal foam can be determined by analyzing its fracture behavior. Sugimura et al. [79] and McCullough et al. [80] showed that metal foam does not fracture in a “clean” manner. Instead, the cellular structure makes crack propagation rather tortuous, and major cracks in the foam are always preceded, and accompanied by, small side cracks. Therefore, even in the presence of micro-cracks, metal foam is still far away from complete failure, unlike a typical brittle material, in which the smallest crack can initiate a catastrophic failure.

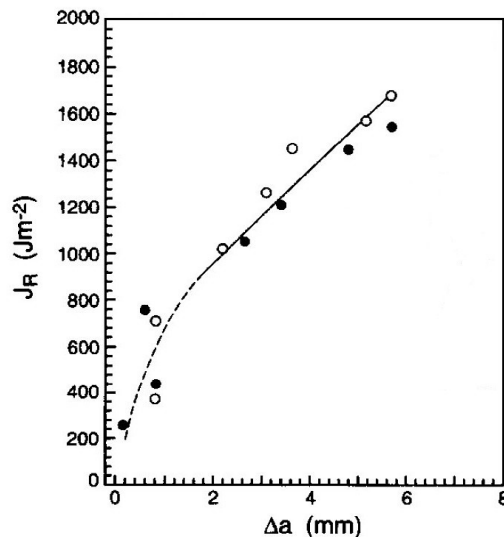


Fig. 55 Resistance curves determined using the J-integral method, ASTM 813-89, for a closed-cell foam with a very similar composition and porosity [79]. The white and black data points represent two test specimens. Unlike in a brittle material, where the J_R -value would be horizontal beyond an unstable crack length, it keeps on increasing in metal foam, indicating that the foam fracture toughness is maintained even as the crack grows larger. Therefore, micro-cracks do not lead to an unstable fracture, and even larger cracks do not completely remove the structural integrity of the foam.

Further insight can be obtained by evaluating the J -value, which is defined as the decrease in potential energy due to the growth of an incremental crack length, Δa [81]. Figure 55 shows the J -integral resistance curve obtained by Sugimura et al. for a similar foam [79]; comparable results were obtained by Mccullough et al. [80]. The exact crack length, up to which the J -integral resistance curve is reliable, depends on the precise specimen geometry, particularly the distance that is available for crack growth as per ASTM E813-89. Regardless of the geometry, however, the J -curve in Fig. 55 shows a clear tendency to increase with crack length, unlike for brittle materials, where the J -curve describes a horizontal line beyond an unstable crack length [82]. Therefore, the micro-cracks observed in Fig. 53 hardly reduce the crack resistance, and even large cracks do not entirely remove the structural integrity of the foam.

While the aforementioned fracture analysis applies to mechanically fractured aluminum foam, it can be shown that the fracture behavior of laser-formed metal foam is even less of concern. Figure 55 shows a comparison between the fracture surfaces in 4-point bending and laser forming. Whereas the fracture surface in 4-point bending contained a mix of rough ductile dimples and clean brittle surfaces with sharp edges, the material on the laser formed fracture surface appears to have been pulled towards the right side, and thus has undergone a substantial amount of plastic deformation before fracture. Hence, the fracture in laser forming was much more ductile, due to a heat-induced reduction of the flow stress, which explains why laser forming yielded much larger tensile strains ϵ_{yy} in Fig. 48. This result further emphasizes that the structural integrity of laser formed metal foam, even more so than untreated foam (in Fig. 55), is hardly affected by micro-cracks until large bending angles are reached.

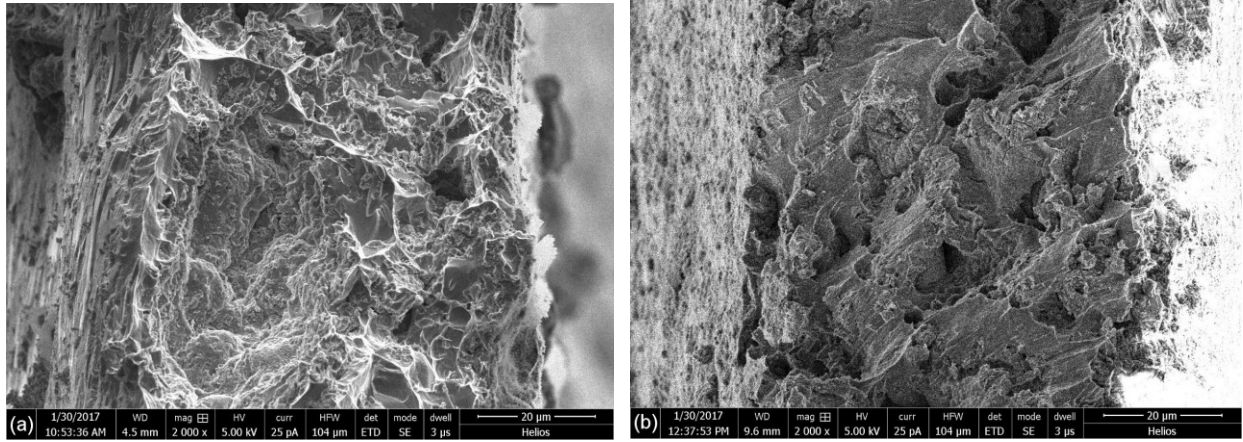


Fig. 56 Fracture surfaces in (a) mechanically fractured and (b) laser formed metal foam specimens. The fracture surface in (a) consists of a mix of dimples and clean surfaces with sharp edges, indicating a mix of ductile and brittle fracture. The material on the surface of (b), on the other hand, appears to have been stretched severely, indicating a more ductile fracture.

The second type of imperfection introduced by laser forming is cell crushing, first discussed in Fig. 47, and now shown intensified at a large bending angle in Fig. 54(b). In order to determine the impact of cell crushing on the foam crushability, the changes in the relative density at large

bending angles were analyzed, shown in Fig. 57. Even at a bending angle of 45° , the maximum relative density achieved was 0.271, which is far away from complete densification of $R = 1$. Figure 57 further shows that the compressed area is highly localized around the bending axis, which is also the case in the experiment (Fig. 54(b)). Therefore, while cell crushing does to an extent reduce the compressibility of metal foam, it occurs in a highly localized manner, and to a degree that does not severely hamper the performance of metal foam as a crash absorber.

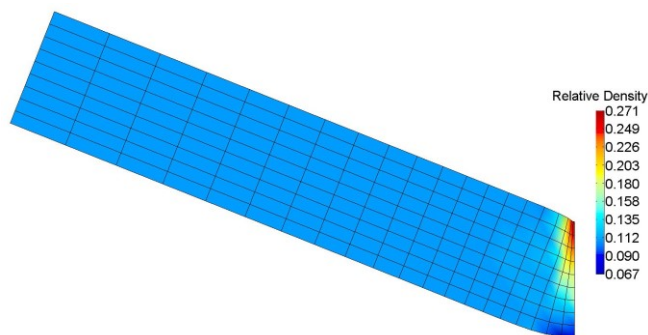


Fig. 57 Relative density distribution at a bending angle of 45°. The baseline relative density is 0.112, and a relative density of 1 indicates complete densification. The densified region was highly localized around the bending axis. Over a small area close to the top surface, the relative density increased by a factor of 2.5, which is still far away from complete densification. Foam expansion occurred close to the bottom surface, coinciding with the region where cracks appeared in Fig. 54(a).

3.4.4 Alternative Numerical Models

So far, the numerical simulations were performed using a solid geometry model, which was found to induce errors due to its inaccurate laser-absorption [26], as well as its inability to model changes in the moment of area with increasing bending angle. These issues can be remedied by explicitly modeling the foam geometry.

Figure 58 shows the bending angle predictions of a Kelvin model for 8 laser scans, in comparison with the equivalent model predictions and the experimental data. The high and low conditions again refer to (180 W; 10 mm/s) and (90 W; 5 mm/s), respectively. On the one hand, the Kelvin model yielded results that more closely matched with the experimental values, due to its improved geometrical accuracy. On the other hand, the model still overestimated the bending angle at 180 W and 10 mm/s, since it did not account for melting, as well as changes in the laser absorption with increasing bending angle (due to using an uncoupled analysis). Also, the model geometry was too simplified to accurately predict crack initiation sites or cell wall bending.

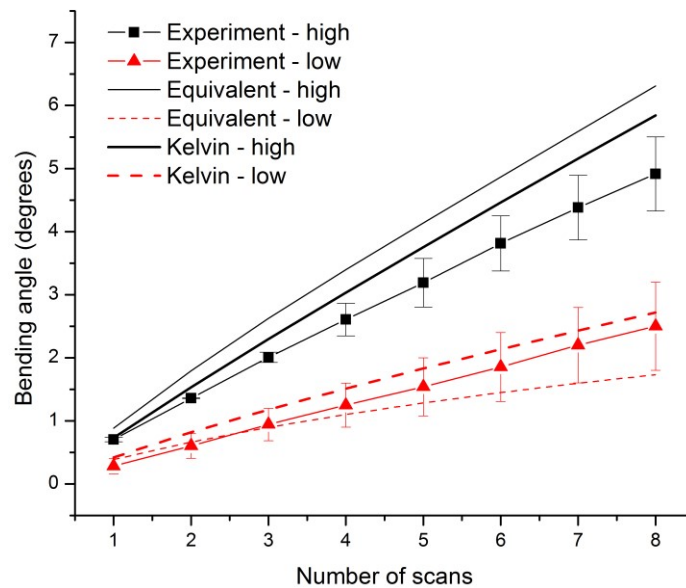


Fig. 58 Bending angles predicted by the Kelvin model in comparison with the predictions of the equivalent model and the experimental values. Standard errors are shown for the experimental data. Due to its superior geometrical accuracy, the Kelvin model yielded results that were closer to the experimental results. Nevertheless, the model still overestimated the bending angle, particularly at the high condition (180 W, 10 mm/s), since it did not account for melting, as well as changes in the laser absorption (due to using an uncoupled modeling approach).

A more accurate geometry can be obtained by “randomly” dispersing unit cells of different sizes throughout the model geometry, as was done by de Giorgi et al. [68] and Roohi et al. [30] for low and high-density foams, respectively. However, the “random” dispersion of the cells still follows systematic algorithms, and the unit cell geometry remains highly simplified.

In order to obtain genuine randomness, a micro-CT based “voxel” model could be used. From a thermal standpoint, it has already been shown that the voxel model can yield good results [26]. Figure 59 demonstrates that the voxel model can also be used to model the mechanical response of the foam, showing the thermal strain distribution during a laser scan at 90 W and 5 mm/s. Due to its geometrical accuracy, particularly its capacity to model even thin cell walls, the voxel model could potentially be used to predict early-stage cracking and cell wall bending.

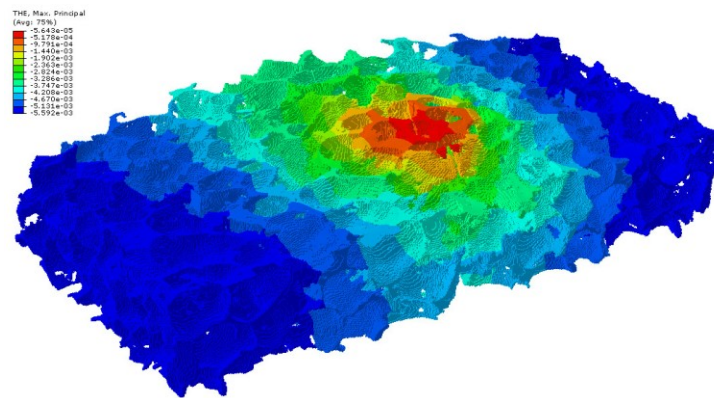


Fig. 59 Thermal strain distribution in a micro-CT based “voxel” model during a laser scan at 90 W and 5 mm/s. The downward deformation represents the initial counter-bending that occurs during the laser scan. The voxel model has a higher level of geometrical accuracy, which could potentially be used to predict crack-initiation sites and cell wall bending.

Despite these advantages, it is often not worth going to the great lengths of using a voxel model, since the modeling technique comes along with several disadvantages. First, each voxel model represents only one particular metal foam specimen, and it becomes necessary to generate a new

voxel model for each specimen if a high level of accuracy is desired. Second, due to its extremely large number of elements, the CPU-intensity increases dramatically, and the specimen size that can be modeled is limited. Due to these significant drawbacks, the equivalent and Kelvin models are in most cases adequate to model the metal foam response during laser forming, despite their limited geometrical accuracy.

3.5 Conclusions

In this study, the mechanical response of metal foam during laser forming was investigated. Metal foam was found to undergo compressive shortening via cell wall bending and cell crushing near the irradiated surface, as opposed to compressive plastic strains that occur in laser forming of solid sheet metal. Based on this deviation from the traditional TGM, a modified temperature gradient mechanism (MTGM) was proposed. From bending angle and strain measurements (determined via DIC), it was found that the achievable bending angle is limited, which can be attributed mostly to densification-induced changes in the thermal conductivity, material stiffness, flow stress, and moment of area. At bending angles around 45° , crack formation and cell crushing were observed. It was shown, however, that these cracks do not negatively impact the structural integrity of the foam, and the extent of the cell crushing has a minor impact on the foam crushability, since the foam remains far away from full densification and the densification is localized.

Numerically, the mechanical response of metal foam was modeled using an equivalent model, which captured the experimental trends despite using a highly simplified geometry. Alternative modeling approaches using different explicit foam geometries were discussed.

Acknowledgment

The authors gratefully acknowledge financial support from the National Science Foundation under grant #CMMI-1725980. This work used the Extreme Science and Engineering Discovery Environment (XSEDE) Stampede through allocation TG-DDM160002, which is supported by National Science Foundation grant number ACI-1548562. The authors are also grateful to Prof. J.W. Kysar and Bob Stark for providing us with the DIC equipment and software.

Chapter 4: Laser Forming of Sandwich Panels with Metal Foam Cores

4.1 Introduction

Metal foam has long been acknowledged for its excellent shock and noise absorption properties, as well as its high strength to weight ratio [2,3]. Despite its desirable characteristics, metal foam alone is generally not suitable for structural applications because its thin cellular structure can easily be damaged and often makes the practical incorporation difficult. In many cases, it is therefore desirable to encapsulate metal foam within a shell of solid metal. Of particular interest are so called “sandwich” panels, where plates of metal foam are “sandwiched” in between solid metal sheets. The metal sheets (“facesheets”) not only protect the foam core from damage, but also significantly improve the stiffness of the composite while maintaining a high strength to weight ratio.

Potential applications for sandwich panels with metal foam core range from various car components [1,10,83] to solar power plants [7] and train/ship structures [6,84]. Perhaps the greatest potential for application exists in the aerospace industry. Specifically, sandwich panels could be used as turbine casings to arrest blades in case of a failure and reduce noise while maintaining low weight [11]. Metal foam sandwich panels could further be used in airplane “noses” to absorb impact energy from bird collisions [10]. In some applications, they could also replace honeycomb structures that are frequently used in modern airplanes. Unlike honeycomb structures, which are anisotropic and cannot be readily curved, metal foam is isotropic and can be bent to doubly-curved shapes [2]. Moreover, the densities and geometries that can be used for honeycomb structures is limited, whereas sandwich panels with metal foam core can be

manufactured in a variety of different densities, cell shapes (using open/closed cell foams), and cell sizes [9].

The challenge associated with using sandwich panels with metal foam core in industrial applications is that they must be manufactured to specific, and oftentimes intricate shapes. It is possible to manufacture sandwich panels directly into the required shape using powder metallurgy processes [9]. This process involves creating a precursor material consisting of compressed metal and foaming agent powders, placing it between solid metal “facesheets”, and bending the assembly to the desired shape. Afterwards, the assembly is moved to a furnace, which causes the foaming agent to release a gas that turns the precursor into a foam. Elevated temperatures cause metallic bonds to form between the foam and adjacent facesheets. While feasible, the drawback of this process is that it requires molds both for the initial forming and subsequent heating. This limits the part size and makes the process very expensive for low production volumes. Furthermore, the structure and density of the resulting foam core is oftentimes irregular because it was produced in a non-uniform shape.

An alternative method to manufacture engineering parts is to start with generic shapes, such as flat panels, and subsequently bend them into the required shapes. This method is significantly cheaper and offers better control over the metal foam properties. At the same time, this method is challenging because sandwich panels with metal foam core are difficult to bend. Mechanical bending has been attempted, such as 3-point bending [15,16] or die stamping [52], but caused many different types of defects and failures. Additionally, 3-point bending has been attempted at elevated temperatures, yet no improvement was observed beyond slightly postponing the onset of failures in mechanical bending at room temperature [85]. Although hydroforming allowed

forming dome-shaped parts, it severely densified the metal foam core and thus diminished the favorable properties of the sandwich panel [17].

A viable alternative to the aforementioned processes is laser forming, since it is based on thermally-induced mechanical deformation and requires no physical contact with the treated material. The process has successfully been used to bend a variety of different metal foams, such as closed-cell foams [16,27], open-cell foams [28], as well as foams with protective skins [29]. Yet, no attempt has been made to apply laser forming to sandwich panels with metal foam cores. Extending the laser forming study to sandwich panels is challenging because the interfaces and interactions between the facesheets and the foam core are critical to the overall material and must be taken into consideration. The existence of an interface significantly complicates the heat transfer and mechanics, and more involved numerical simulations are consequently required to understand these phenomena. These issues, along with a thorough discussion of the bending mechanisms and the applicable process window, are investigated in this study.

4.2 Background

4.2.1 Sandwich Panel Manufacture and Bending

Sandwich panels consist of three components: a foam core (metal foam in this study) and two solid metallic “facesheets” that are attached on either side of the foam core. In some studies, sandwich panels are referred to as materials in which the core and the facesheets are a single part. Examples are metal foams that develop protective skins during powder metallurgical processes [9,29]. More commonly, however, sandwich panels consist of facesheets and a foam core that are distinct entities and initially separated. These sandwich panels have stronger facesheets that better protect the foam core and increase the stiffness of the sandwich panel.

Additionally, these sandwich panels offer a greater flexibility in material composition, since different material types and alloys can be used for the facesheets and the foam core combination.

To manufacture these sandwich panels, the facesheets need to be attached to the core, which can be achieved in different fashions. In this study, a typical method in which a precursor block consisting of compressed aluminum and foaming agent powders was used. The precursor is sandwiched between two facesheets and heated near the melting temperature of the metal powder. During heating, the foaming agent releases a gas that generates cavities inside the precursor and forms the foam. To ensure the sandwich panel has a uniform thickness and that metallic bonds can establish between the foam and the facesheets, expansion in the direction of panel thickness is restricted during the foaming process [9].

While having an exceptional strength and stiffness, the resulting sandwich panels are extremely challenging to bend, due to several reasons. First, the major constituent of the sandwich panels is metal foam, which is unable to withstand the high tensile stresses that develop during mechanical deformation processes [27]. Hence, core shear failures are one of the most prevalent failure types seen in mechanical bending [2,15,16]. Second, sandwich panels are extremely stiff, and their moment of area I is substantially greater than the moment of area of a solid with the same cross-sectional area (Fig. 60), where I is calculated using

$$I = \int_{-s_0/2}^{s_0/2} z^2 y(z) dz \quad (4.1)$$

where s_0 is the sheet thickness [2]. As a consequence, the sandwich panel has a much higher bending stiffness S than the corresponding solid as shown in

$$S = \frac{2EI}{l^3} = \frac{M}{l\delta} \quad (4.2)$$

where l is half the beam length, E is Young's Modulus, and δ is the vertical deflection of the beam during bending [2]. Therefore, a greater bending moment M is required to achieve the same bending deflection δ , which in turn increases the stresses in the foam core, making it even more prone to shear failures. High stresses also develop in the facesheets that can cause facesheet failures or wrinkling [2,15].

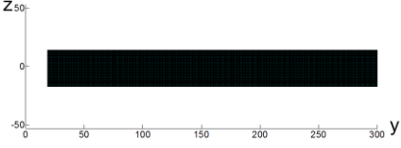
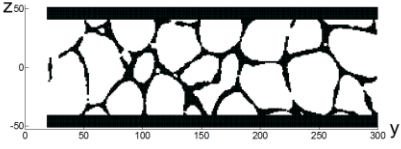
	Cross-section	Moment of area
Solid		1
Sandwich		17.4

Fig. 60 An example showing a metal foam sandwich (89% porosity, total thickness 10 mm, facesheets thickness 1 mm) which has a 17.4 times higher moment of area about the y axis than a solid with the same cross-sectional area (thickness 3.2 mm). Hence, metal foam sandwiches have a higher stiffness to bending deformation. The cross-sections were divided into squares of 0.1 mm length, whose moment of area were calculated individually and added using the parallel axis theorem. The y and z axes refer to the number of squares per coordinate direction. The total number of squares was the same for the solid and sandwich.

Third, deforming sandwich panels is exceedingly difficult due to the presence of the facesheet/foam interfaces. During mechanical bending processes, such as 3-point bending, significant stress discontinuities develop at the interfaces due to the drastic difference in the material properties between the metal foam and the facesheets. Assuming bending occurs about the x -axis (see Fig. 60) and is achieved by a bending moment M , the normal strain at a distance z from the neutral axis can be written as $\varepsilon_{22} = -z/R$ [86], where R is the radius of curvature. The normal stress (in y -direction) then becomes

$$\sigma_{22} = E\varepsilon_{22} = -\frac{Ez}{R} \quad (4.3)$$

where E is Young's Modulus. The sign indicates that the deformation is compressive and tensile above and below the neutral axis, respectively. Since the radius of curvature is constant, the magnitude of the stress discontinuity depends on the difference in Young's Modulus between the facesheet and the foam, which can readily reach a factor of 100. At the interface, this stress discontinuity is experienced as a shear traction and can cause delamination [15,16].

Finally, the interaction between the facesheet and the foam can cause additional undesirable effects. Due to the high compressive stresses that develop during mechanical bending, the facesheet can buckle into the foam core, compressing the foam to a fraction of its original thickness [2,15]. As a consequence, the foam loses a majority of its local compressibility and renders the sandwich useless for shock-absorption applications.

4.2.2 Laser Forming

Laser forming of solid sheet metal is well understood; several mechanisms explain the bending behavior at different process conditions [22]. The first bending mechanism, temperature gradient mechanism (TGM), governs the scenario where the sample sheet thickness is relatively large compared to the laser spot size. Steep temperature gradients develop across the sheet thickness, and heating is highly localized underneath the laser source. As a consequence, the thermal expansion of the heated material is restricted by the cold surrounding material, and plastic compression occurs. Plastic compression is propagated along the entire laser scan, shortens the top of the sheet relative to the bottom, and ultimately bends the material towards the laser. The second mechanism, buckling mechanism (BM), governs the scenario where the laser spot is much larger than the sheet thickness, causing uniform heating across the thickness. The sheet again tries to expand but is hindered by the surrounding material, ultimately buckling away or towards the laser source. The buckled region is propagated along the laser scan, and the sheet

eventually bends in the direction opposite to the buckling direction. The third mechanism, upsetting mechanism (UM), governs the same scenario as the BM, except the section is geometrically prevented from buckling and instead undergoes thickening.

For metal foams, it was shown that none of the above mechanisms exactly apply, and a modified temperature gradient mechanism (MTGM) was proposed [27]. In the MTGM, a steep temperature gradient develops across the thickness just like in the TGM, but the compressive shortening near the top surface occurs via cell crushing as opposed to plastic compressive strains.

For sandwich panels with metal foam cores, the bending mechanism analysis becomes more involved. For one, the interaction between the facesheets and the metal foam must be taken into consideration. The facesheets tend to bend at a higher rate than the metal foam core and are thus “held back”, which can give rise to stresses at the interface. Moreover, there is no bending mechanism that is valid both for solid sheet metal and metal foam, and hence there is no mechanism that can explain the bending behavior of the entire sandwich panel. The TGM and the MTGM, for instance, cannot govern bending of the entire sandwich panel, since the foam deformation is not mainly based on plastic compression, and the facesheet cannot undergo crushing, respectively. The BM cannot be valid either, since the thickness of the composite is too large to undergo buckling. The UM can only partially explain the sandwich deformation for a set of process conditions, as will be shown, but does not explain how the foam core can bend without undergoing fracture. It turns out that the sandwich panel deformation can be explained by a combination of two mechanisms, which interact and give rise to a new phenomenon at the interface between the top facesheet and the foam core.

4.3 Numerical Simulation

Several methods can be used to model sandwich panels. The simplest method is to model the sandwich as a block, divide it into three regions and assign facesheet and foam properties to the corresponding regions [87]. Though extremely simple, the disadvantage of this method is that the facesheet and core are always rigidly connected, and the heat transfer between them is assumed to be perfect (infinite conductance). Since the facesheet and foam core are not fully melted during manufacturing, however, the interface contains micro-voids, and the adhesion is imperfect. Hence, a finite thermal conductance is to be expected, which can only be taken into account by models where the facesheets and the foam core are initially detached.

Initially detached models require a joining method, of which there are again several alternatives. A simplistic method involves joining the facesheet and foam core using tie constraints or contact interactions [15,17]. Both methods can model contact resistances, yet do not allow for any delamination to occur. Cohesive surfaces have the same thermal capabilities, but also allow for delamination to occur when specified damage parameters are exceeded [88]. The same result can be achieved by inserting a thin layer (e.g. 10 μm) at the interface consisting of cohesive elements, with the additional benefit that delamination can be monitored and visualized [89]. Even though delamination did not occur in the current study, this approach was used for both interfaces, in anticipation of future studies where delamination effects become important.

The cohesive element approach assumes the interface layer to be infinitesimally thin, and the deformation is described in terms of the tractions t and the displacement discontinuity u across the interface. The tractions and displacements are linearly related through the stiffness matrix K

$$\begin{bmatrix} t_n \\ t_s \\ t_t \end{bmatrix} = \begin{bmatrix} K_{nn} & 0 & 0 \\ 0 & K_{ss} & 0 \\ 0 & 0 & K_{tt} \end{bmatrix} \begin{bmatrix} u_n \\ u_s \\ u_t \end{bmatrix} \quad (4.4)$$

where the subscripts n , s , t refer to the normal, 1st and 2nd shear directions, respectively. The stiffness of the cohesive layer is set very high to avoid affecting the response of the sandwich [49].

To simulate the imperfect heat transfer at the interfaces, temperature-dependent conductance values $G(T)$ were assigned. $G(T)$ data is currently only available for metals in direct contact that are subjected to a pressure. Several references suggest an exponential increase of G with temperature T [46-48]. For sandwich panels, the conductance should be greater than in direct contact because of the presence of metallic bonds, however due to the lack of available reference data, the $G(T)$ relationship from [46] was used.

The laser forming simulation was performed in an uncoupled manner, using the thermal results as input to the mechanical analysis. The facesheets were modeled using Von Mises' yield criterion, and temperature-dependent material properties were extracted from [70]. Simulations were implemented in the finite element software ABAQUS using DC3D20 and C3D20R elements for the thermal and mechanical analysis, respectively. The top and bottom facesheets were modeled with 3 and 2 elements through the thickness, respectively.

The metal foam was modeled in two different ways. In the first method ("equivalent model"), shown in Fig. 61(a), the foam was modeled as a solid, and metal foam properties were assigned. Yielding was assumed to occur due to deviatoric and hydrostatic stresses, pursuant the criterion

$$F = \left[\frac{1}{1 + (\alpha/3)^2} (\sigma_e^2 + \alpha^2 \sigma_m^2) \right]^{1/2} - Y \leq 0 \quad (4.5)$$

where σ_e is the Von Mises' equivalent stress, σ_m the mean stress, Y the yield strength, and α the aspect ratio of the yield surface [41]. When $F < 0$, the material behavior is elastic, and when $F = 0$, plastic deformation occurs pursuant to the following flow rule

$$\dot{\epsilon}_{ij}^p = \frac{\dot{Y}}{H} \frac{\partial F}{\partial \sigma_{ij}} \quad (4.6)$$

where $\dot{\epsilon}_{ij}^p$ is the plastic strain rate, and H is the hardening modulus defined as

$$H = \frac{\sigma_e}{\hat{\sigma}} h_\sigma + \left(1 - \frac{\sigma_e}{\hat{\sigma}}\right) h_p \quad (4.7)$$

where h_σ and h_p are the tangent moduli in uniaxial and hydrostatic compression, respectively, and $\hat{\sigma}$ is the equivalent stress equal to the first term in eq. (4.5). The assumptions of this model and the sources for the material data are discussed in detail in [26,27]. The x and y mesh refinement was the same as in [27], in z -direction the mesh was more refined towards the interfaces and coarser towards the center of the foam. In the second method ("Kelvin model"), the foam cavity was approximated by a Kelvin cell, shown in Fig. 61(b), and solid AlSi10 properties were assigned. The element types and meshing technique were the same as in [27], with the exception that a cavity size of 2 mm was used, yielding a density of 700 kg/m³.

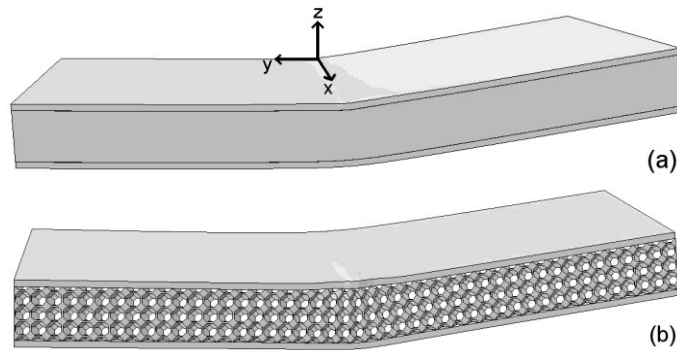


Fig. 61 Two different geometries were used to model the foam core: (a) solid geometry ("equivalent model"), whereby foam properties were assigned, and (b) Kelvin cell geometry ("Kelvin model"), where each cavity was approximated by a Kelvin-cell. Not visible are the cohesive layers that were inserted between the facesheets and the foam core.

In the equivalent model, the cohesive layer was meshed with COH3D8 elements that were half the size of the adjacent metal foam elements. In the Kelvin model the same element size was used for the cohesive layer as in the adjacent metal foam elements. The thermal and mechanical boundary conditions were the same as in prior analyses [26,27], and an absorption coefficient of $A = 0.6$ was used [43].

4.4 Experimental Methods

Sandwich panels manufactured by Havel Metal Foam GmbH were used in this study, consisting of AW 5005 facesheets and AlSi10 metal foam core. The thickness of the sandwiches was 10 mm, and the average density of the metal foam was measured to be 700 kg/m^3 . The manufacturing method was discussed in Sec. 4.2.1. Sandwich specimens were cut to a length of 100 mm and a width of 35 mm and mounted onto a thermally insulated stage as shown in Fig. 62. A CO_2 laser with a wavelength of $10.6 \text{ }\mu\text{m}$ was used to scan the specimens in x -direction. To improve the naturally poor absorption of $10.6 \text{ }\mu\text{m}$ radiation in aluminum [18], the specimens were coated in black graphite paint. The specimens were cooled to room temperature after each laser scan, at which point the deflection was measured with a dial indicator.

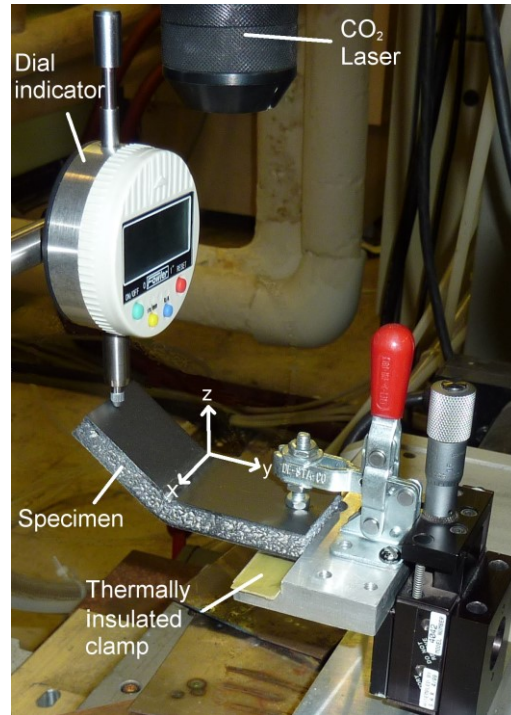


Fig. 62 Experimental setup. The specimens were scanned in x-direction, and a thermally insulating material was inserted between the specimen and the holder. The dial indicator was removed during laser scans.

Two different approaches were taken during the determination of the process conditions. In the first approach, inspiration was drawn from multi-layer composite laser forming studies [21], in which the TGM was induced in the top layer, and the remaining sections of the composite were bent by the resulting bending moment. In the second approach, it was attempted to bend the entire sandwich panel through a laser forming mechanism by subjecting the entire section to a steep temperature gradient. For both approaches, bending was successful, but the bending mechanisms turned out to be different than anticipated, which will be discussed later. The first approach yielded a small spot size of $D = 4$ mm with a high scan speed of $v = 30$ mm/s, whereas the second approach yielded a large spot size of $D = 12$ mm and a lower scan speed of $v = 10$ mm/s. The power was kept at $P = 800$ W to maintain a constant area energy $AE = P/Dv$.

Since both process conditions give rise to fundamentally different bending mechanisms, most of this study was dedicated to the comparison of the two conditions. However, the process

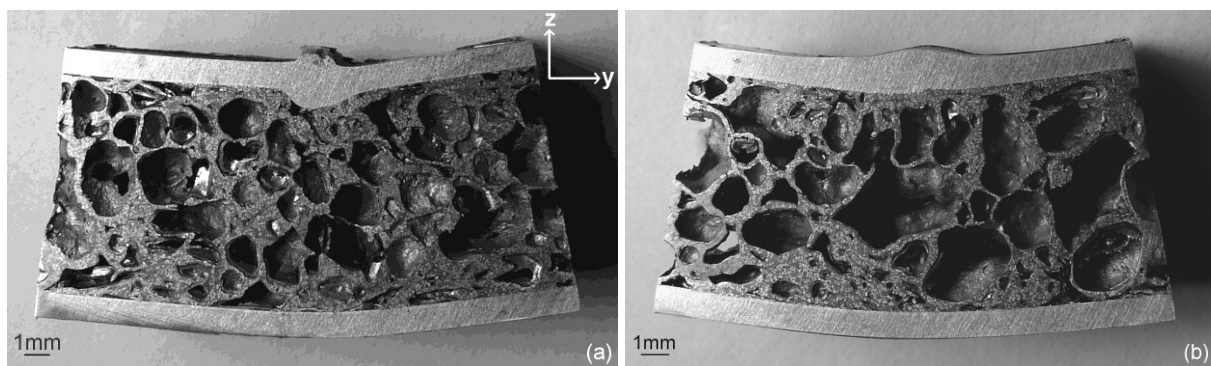
window is not limited to these two conditions, and laser forming can also be achieved with intermediate laser spot sizes between $D = 4 - 12$ mm and scan speeds between $v = 10 - 30$ mm/s, as will be demonstrated in Sec. 4.5.3.

The temperatures on the bottom surface of the sandwich were measured using an IR camera. The IR camera was mounted underneath the specimen, and an aluminum shield was added to the stage to avoid damaging the IR camera. The maximum frame rate of 120 Hz was used, which provided sufficient detail to capture the temperature-time history. The spatial resolution of the IR camera is roughly 0.1 mm at the distance operated, and the temperature resolution is 0.1 K.

4.5 Results & Discussion

4.5.1 Bending Mechanism

To study the bending mechanism, sandwich specimens and “isolated” facesheets that were removed from the sandwich were both laser formed to about 15° . Then, the typical cross-sections of the sandwich specimens (Figs. 63(a) and 63(b)) were compared with cross-sections of “isolated” facesheets (Figs. 63(c) and 63(d)). The process conditions used for (a) and (c) were a small spot size of $D = 4$ mm with a scan speed $v = 30$ mm/s, and for (b) and (d) a large spot size of $D = 12$ mm with a scan speed $v = 10$ mm/s. The power and area energy were constant at $P = 800$ W and $AE = 6.67$ J/mm², respectively.



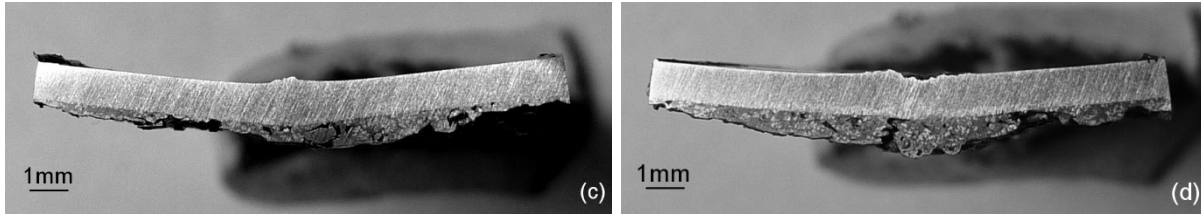


Fig. 63 Cross-sections of sandwich panels scanned at (a) $D = 4$ mm and $v = 30$ mm/s (100 scans) and (b) $D = 12$ mm and $v = 10$ mm/s (24 scans), and cross-sections of isolated facesheets scanned at (c) $D = 4$ mm and $v = 30$ mm/s (7 scans), and (d) $D = 12$ mm and $v = 10$ mm/s (6 scans). The power and area energies were $P = 800$ W and 6.67 J/mm² in all cases, respectively, and the final bending angle was 15° . The top facesheet bent via the TGM in (a) and (c), the BM in (d), and the UM in (b).

The bending of the isolated facesheets is governed by well-known bending mechanisms. At $D = 4$ mm, some thickening occurred on the top surface (Fig. 63(c)), which is an established consequence of TGM-dominated bending [90]. At $D = 12$ mm (Fig. 63(d)), there was insignificant change in the facesheet thickness, and the spot size was substantially greater than the facesheet thickness, indicating that the BM is the governing mechanism [22].

In comparison, it is evident that the bending of sandwich panels is governed by different mechanisms, since the cross-sections look quite different under both process conditions. At $D = 12$ mm (Fig. 63(b)), the top facesheet no longer bent via the BM because it was prevented from buckling by the attached metal foam. Instead, the facesheet thickened, a response that is indicative of the well established UM. The temperature distributions across the thickness, shown in Fig. 66 as the laser passes, confirm this finding. Both in the isolated and sandwich configuration, there was hardly any temperature gradient across the top facesheet, speaking in favor of the BM and the UM, for each configuration respectively.

At $D = 4$ mm (Fig. 63(a)), the top facesheet in the sandwich configuration thickened not just upwards, but also downwards, which is uncharacteristic for the TGM and suggests that a different bending mechanism governs deformation. The thermal results from Fig. 64 suggest the contrary, however, since a steep temperature gradient developed across the top facesheet regardless of whether it was isolated or attached to the foam core.

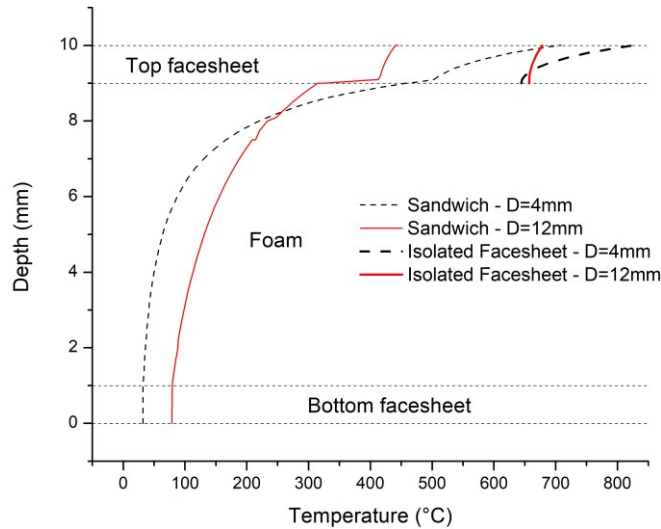


Fig. 64 Simulated temperature distributions at a cross-section (yz -plane) as the laser passes, both in the entire sandwich (equivalent sandwich model) and in an isolated facesheet. At $D = 4$ mm and $v = 30$ mm/s, a steep temperature gradient exists in the top facesheet, regardless of whether the facesheet is isolated or in sandwich configuration, indicating that the TGM is always the governing mechanism. At $D = 12$ mm and $v = 10$ mm/s, there is hardly any gradient over the top facesheet in both scenarios, indicating that the BM and the UM govern in the isolated and sandwich configurations, respectively.

Further evidence can be drawn from the experimental and numerical results in Fig. 65, showing the temperature history at the bottom sandwich panel surface at the scan line. At $D = 12$ mm, a substantial amount of heat was transferred across the sandwich. This indirectly implies that the top facesheet heated up uniformly, again suggesting that the UM governed bending of the top facesheet. At $D = 4$ mm, on the other hand, little heat reached the bottom sandwich surface, suggesting the presence of a temperature drop in the top facesheet, which gives rise to the TGM. It must be noted that in the experiment, a laser shield was placed very close to the bottom sandwich surface to protect the IR camera. This shield absorbed some heat and is responsible for the discrepancy between the experimental and numerical peak temperatures. Also, there is a significant temperature drop across the top interface, which can be attributed to the finite interface conductance. The temperature drop was more significant at $D = 12$ mm than at $D = 4$ mm due to the exponential temperature-dependence of the interface conductance $G(T)$.

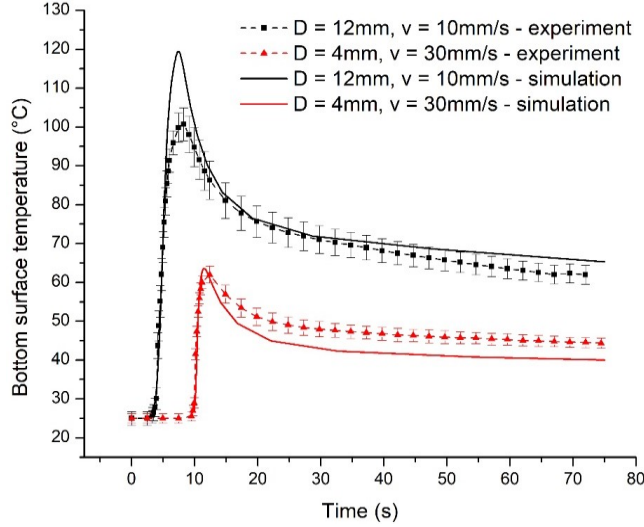


Fig. 65 Experimental and numerical temperature histories on the bottom sandwich panel surface at $D = 4$ mm and $D = 12$ mm. At $D = 12$ mm there is a more significant temperature rise, indicating that more heat is transferred across the top facesheet. At $D = 4$ mm, little heat reaches the bottom surface, implying the presence of a temperature gradient in the top facesheet.

Thus far, the bending mechanism analysis was solely focused on the top facesheet, and evidence was found that the TGM and UM govern facesheet bending at $D = 4$ mm and $D = 12$ mm, respectively. The question now becomes how the rest of the sandwich panel bends. Two pieces of evidence show that the foam core actively bends through a laser forming mechanism as well, rather than bending solely because of the bending moment exerted by the top facesheet. First, steep temperature gradients develop across the foam during the laser scan as shown in Fig. 64, both at $D = 4$ mm and $D = 12$ mm. Second, the metal foam undergoes some densification during the laser scan as shown in Figs. 66(a) and 66(b), which is identical to the densification occurring during laser forming of free-standing metal foam [27]. The density changes were calculated using

$$\frac{\rho}{\rho_0} = e^{-(\varepsilon_{11} + \varepsilon_{22} + \varepsilon_{33})} = e^{-(\varepsilon_{ii})} \quad (4.8)$$

where ρ_0 is the initial density and ε_{ii} are the normal strain components [52]. The initial density ($\rho = \rho_0$) is represented by 100%. Both results imply that the metal foam bent via the MTGM [27].

Experimental results confirm this finding, since some cell-crushing can be seen at small bending angles (Figs. 63(a) and 63(b)), and especially at large bending angles (see Sec. 4.5.2).

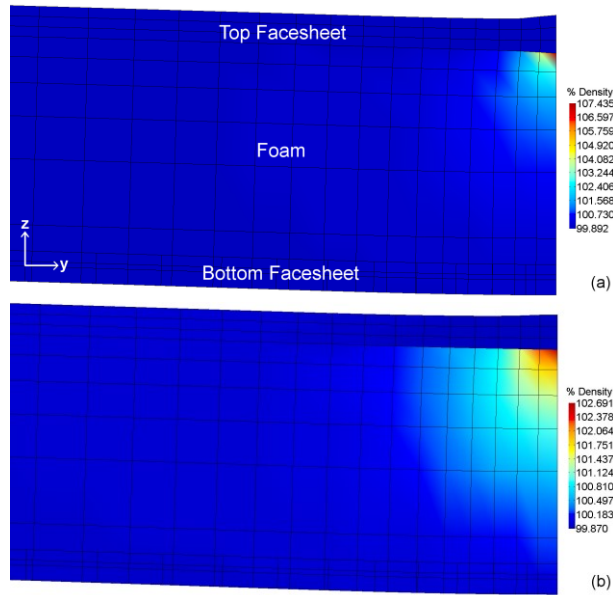


Fig. 66 Density distribution after a laser scan at (a) $D = 4$ mm and $v = 30$ mm/s, and (b) $D = 12$ mm and $v = 10$ mm/s. The initial density is 100%. At both conditions, the foam core densified as postulated by the MTGM. At $D = 4$ mm, the densification has a higher magnitude, but occurs more locally. At $D = 12$ mm, densification occurs over a much greater area, allowing for a more efficient deformation at large bending angles. A deformation scaling factor of 5 was used. Half of the specimen is shown due to symmetry.

Therefore, both the top facesheet and foam core actively contribute to the bending deformation through different bending mechanisms. The last sandwich component requiring an analysis is the bottom facesheet. According to Fig. 64, there is no temperature gradient across the bottom facesheet, and the amount of heating is low as well. Hence, the bottom facesheet is the only component of the sandwich panel that does not actively contribute to bending. Instead, it is bent mechanically by the bending moment exerted by the foam core and the top facesheet.

Having discussed the bending mechanisms, it becomes clear why laser-formed sandwich panels do not undergo any failures mentioned in Sec. 4.2.1. Core shear failures do not occur because the foam deformation through the MTGM is mostly compressive [27]. Similarly, buckling of the top facesheet does not occur, since the top facesheet undergoes compressive

shortening via the TGM. Facesheet wrinkling does not occur either because the facesheets are too thick, and bottom facesheet failures are prevented by heat-induced softening. Facesheet delamination can occur, depending on the joining method. In this study, a very strong joining method was used, which did not give rise to any delamination.

A further topic requiring discussion is the thickening on the bottom surface of the top facesheet (Fig. 63(a)). Two mechanisms can be held responsible for this behavior. First, the metal foam densifies, as shown in Figs. 66(a) and 66(b), and the associated volume reduction leaves a void in the foam to be filled. Since the adhesion between the top facesheet and the metal foam remains intact, the facesheet must fill this void, which it can readily accomplish because it is subject to high compressive stresses and also softened due to the laser-induced heating. Second, the top facesheet expands downwards right as the laser passes. Figure 67 shows the strain distribution ε_{33} in z -direction (a) right before the laser passes, (b) while the laser passes and (c) at the end of the laser scan. Immediately before the laser passes, the top facesheet starts expanding uniformly. As the laser passes, the facesheet rapidly expands both upwards and downwards, inducing a compressive strain in the metal foam underneath. Meanwhile, the foam undergoes some compressive deformation of its own through the MTGM, thereby “pulling” the facesheet down and inducing a tensile strain in the facesheet. This condition is maintained until the end of the laser scan, shown in Fig. 67(c).

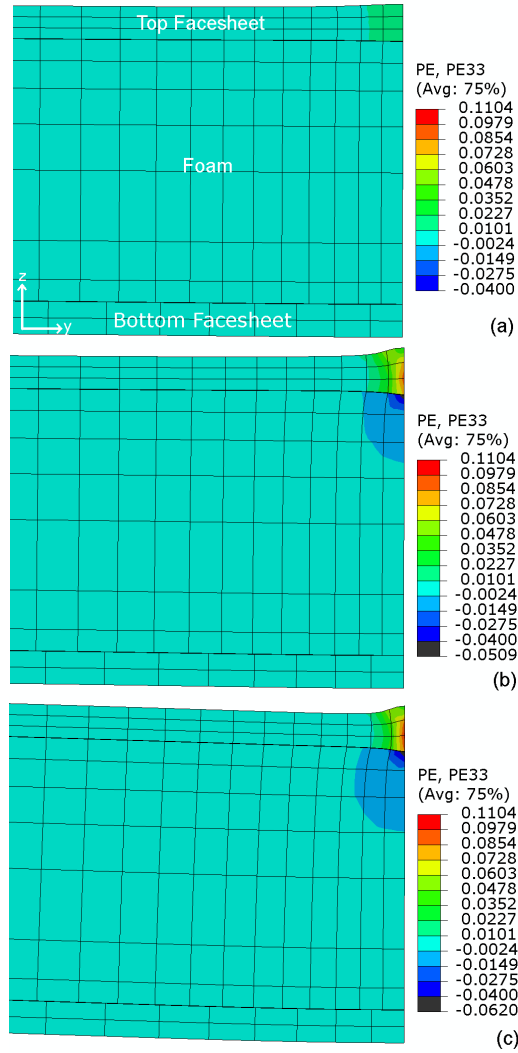


Fig. 67 Vertical plastic strain distribution in z-direction (ϵ_{33}) at the scan line at $D = 4$ mm and $v = 30$ mm/s (a) right before the laser passes, (b) as the laser passes, and (c) after the laser scan. Right as the laser passes, the top facesheet (top 3 element layers) expands upwards and downwards near the scan line, compressing the foam underneath. The foam, in turn, densifies due to the MTGM and “pulls” the facesheet down, causing tensile strains in the top facesheet. A deformation scaling factor of 5 was used. Half of the specimen is shown due to symmetry.

4.5.2 Bending Efficiency & Limit

In the previous section it was shown that small ($D = 4$ mm) and large ($D = 12$ mm) laser spot sizes induce different bending mechanisms in the top facesheet. The bending mechanisms, in turn, significantly impact both the bending efficiency and the bending limit.

Figure 68 shows that the bending angles achieved at $D = 12$ mm were more than twice the bending angles achieved at $D = 4$ mm over 8 laser scans, even though the area energy was constant in both cases ($AE = 6.67$ J/mm²). These results clearly suggest that bending is significantly more efficient at larger laser spot sizes.

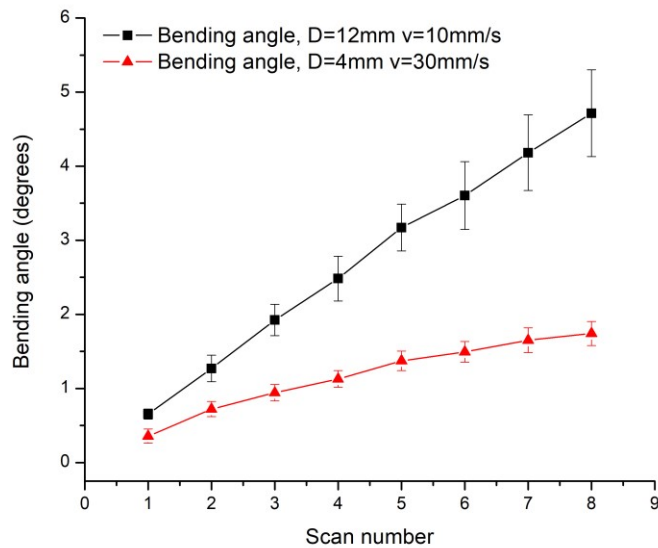


Fig. 68 Experimental bending angles over 8 scans at $D = 4$ mm with $v = 30$ mm/s, and $D = 12$ mm with $v = 10$ mm/s. The power and area energy are constant at $P = 800$ W and $AE = 6.67$ J/mm², respectively. The bending angles are averaged over 5 specimens, standard errors are shown. At $D = 12$ mm, bending is more efficient than at $D = 4$ mm.

To explain the trends observed in Fig. 68, the plastic compressive strain distributions in y -direction (ϵ_{22}^p) were analyzed over a cross-section of the sandwich panel. At $D = 4$ mm (Fig. 69(a)), large compressive strains developed at the center of the top facesheet due to intense heating and the large thermal expansion forces characteristic of the TGM. The remaining

facesheet segments contributed much less to compressive deformation, and the plastically deformed area was generally localized near the laser scan line. At $D = 12$ mm (Fig. 69(b)), the plastically deformed region extended further from the laser scan line, and the compressive strains were more uniformly distributed throughout the top facesheet. Hence, bending was more efficient at $D = 12$ mm because a larger segment of the top facesheet contributed to compressive shortening.

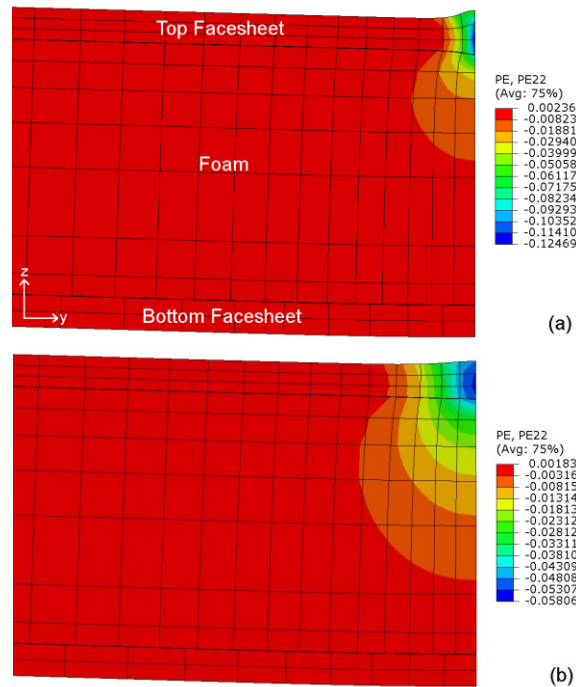


Fig. 69 Plastic strain distribution after a laser scan at (a) $D = 4$ mm with $v = 30$ mm/s and (b) $D = 12$ mm with $v = 10$ mm/s. At $D = 4$ mm, significant compressive shortening only occurred over a small segment of the top facesheet (top 3 element layers), unlike at $D = 12$ mm, where the entire top facesheet contributed to compressive shortening, and compressive strains extended further from the laser scan line. A deformation scaling factor of 5 was used. Half of the specimen is shown due to symmetry.

Furthermore, bending was more efficient at $D = 12$ mm because the foam core bent more efficiently via the MTGM. Unlike at $D = 4$ mm (Fig. 69(a)), where the foam only underwent plastic compression adjacent to the scan line, the plastically compressed region was much larger at $D = 12$ mm (Fig. 69(b)). The same conclusion can be drawn from the densification plots in Figs. 66(a) and (b), as well as experimental results at large bending angles (Fig. 71).

Finally, bending was more efficient at $D = 12$ mm because the bottom facesheet reached higher temperatures during the laser scan, as shown in Fig. 65, and consequentially underwent a higher amount of heat-induced softening than at $D = 4$ mm.

Similar to the bending efficiency, the maximum achievable bending angle is very sensitive to the laser spot size. At $D = 4$ mm, the maximum bending angle is merely $\sim 15^\circ$, as shown in Fig. 63(a). Large bending angles can exclusively be achieved by performing multiple parallel laser scans. In Fig. 70(a), for instance, two scans were performed per scan line, and each scan line was offset by 1 mm. At $D = 12$ mm, on the other hand, bending angles up to 65° and beyond can be achieved over a single scan line as shown in Fig. 70(b).

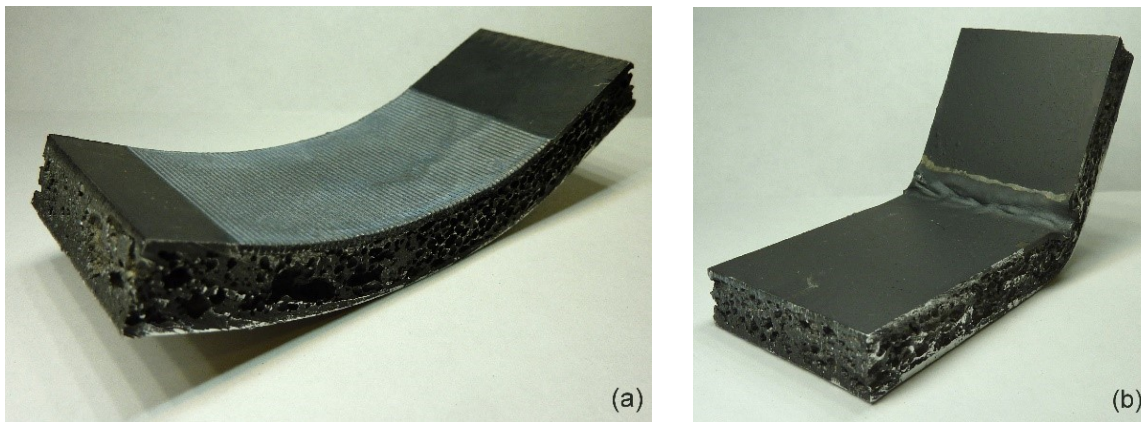


Fig. 70 At $D = 4$ mm, appreciable bending angles can only be obtained by performing parallel scans, as shown in (a), where 2 scans were performed per scan line and offset by 1 mm. At $D = 12$ mm, large bending angles up to 65° and beyond can be obtained over a single scan line, as shown in (b).

One cause for the different limiting behaviors is the bending mechanism that governs the deformation of the top facesheet. At $D = 4$ mm, the top facesheet bends via the TGM, and considerable thickening occurs over the small area around the laser scan line (Fig. 63(a)). This thickening causes a significant drop in the bending angle increment $\Delta\alpha$, since $\Delta\alpha$ is proportional to the inverse of the sheet thickness squared for TGM conditions [22]. Eventually, the facesheet becomes too stiff, and $\Delta\alpha \rightarrow 0$ for the entire sandwich. At $D = 12$ mm, significant thickening occurs as well, especially at large bending angles as shown in Fig. 71. However, the bending

efficiency is less affected, because the temperature distributions in the top facesheet remains mostly uniform due to the large laser spot size, and the thermal prerequisite for the UM is still met.

Another cause for the different limiting behaviors is the efficiency of the foam densification via the MTGM. As mentioned in Sec. 4.5.1, densification occurs very locally at $D = 4$ mm, unlike at $D = 12$ mm where a large segment of the foam densifies, as seen in Fig. 71. Therefore the foam can densify unrestrictedly at $D = 12$ mm, whereas it might locally approach solidification at $D = 4$ mm, reducing the bending efficiency [27].

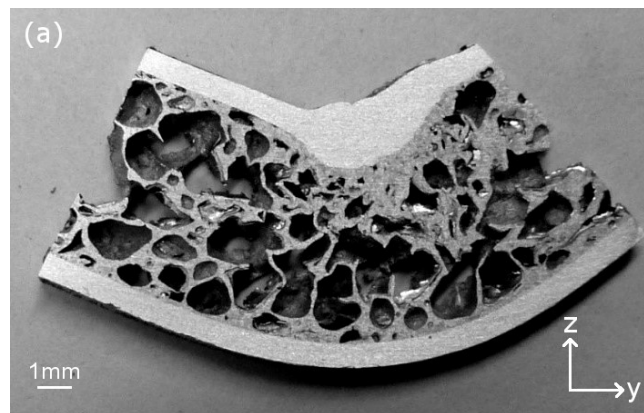


Fig. 71 Cross-section of a sandwich specimen bent to 65° at $D = 12$ mm and $v = 10$ mm/s. The top facesheet thickened significantly, and foam densification occurred over a large area. Yet the strength of the top facesheet is maintained, if not increased. Much less densification occurred than in mechanical bending.

After reviewing the behavior of sandwich panels at large bending angles, the impact of laser forming on sandwich performance can be examined. The first issue to be examined is facesheet thickening. On one hand, a thickened facesheet increases the strength and stiffness of the sandwich panel. Conversely, the thickened segment has undergone numerous rapid heating and cooling cycles that can cause a material embrittlement [44]. However, since the facesheet thickening occurs over a larger scale and aluminum is less susceptible to detrimental embrittlement effects, it is expected that the top facesheet performance is maintained, if not improved. The second issue is foam densification. At $D = 4$ mm, the densification resembles the

densification observed during laser forming of free-standing metal foam [27]. With an increasing number of scans, the densification becomes more localized and thus minimally affects foam crushability. At $D = 12$ mm, the densification is wide-spread, due to the MTGM, as well as the large-scale thickening of the top facesheet. Still, the densification is much smaller than in mechanical bending, where the top facesheet deeply penetrates into the foam core and can reduce its thickness by up to 75% [15,16].

4.5.3 Other Process Conditions

The process window is not limited to the two process conditions that have been compared thus far, but covers the entire spectrum in between. As shown in Fig. 72, any laser spot size between $D = 4$ mm and $D = 12$ mm yields a successful result (at $AE = \text{const.}$). At each spot size, the bending curve slightly leveled off with an increasing number of laser scans. At $D = 4$ mm and $D = 6$ mm, the bending curve leveled off more quickly since the TGM, which is more sensitive to facesheet thickening (see Sec. 4.5.2), was dominant in the top facesheet. Also, the paint wore off faster due to the higher temperatures that developed in the top facesheet. At $D = 10$ mm and $D = 12$ mm, the bending curves leveled off the least, since the BM, which is less sensitive to facesheet thickening, was dominant in the top facesheet. Also, the temperatures in the top facesheet were the lowest and caused the least amount of paint evaporation. Finally, $D = 8$ mm was somewhere in between, and only leveled off at a high number of laser scans.

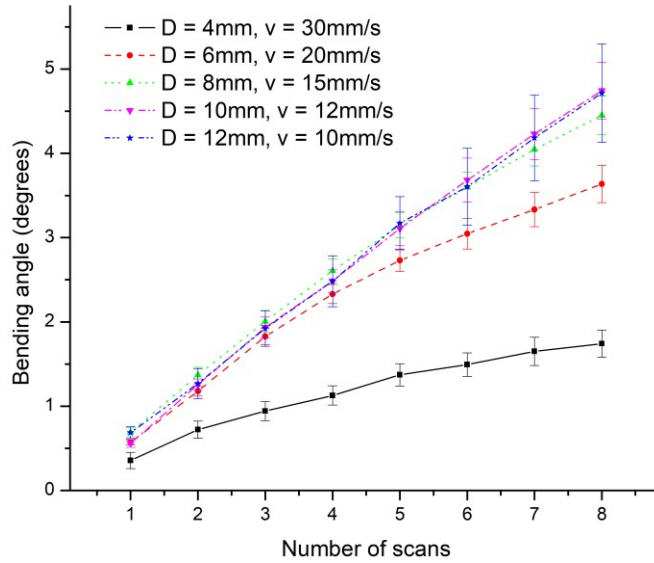


Fig. 72 Experimental bending angles over 8 scans at spot sizes ranging from $D = 4$ mm to $D = 12$ mm. The power and area energy are constant at $P = 800$ W and $AE = 6.67$ J/mm², respectively. The bending angles are averaged over 5 specimens, standard errors are shown. At small spot sizes, the bending curves level off more rapidly due to an increased amount of paint evaporation and a higher sensitivity to facesheet thickening.

More insight into the bending efficiency can be obtained by comparing the bending angles achieved by each condition after one and eight laser scans, shown in Fig. 73. After one scan, there was a distinct increase in the bending angle from $D = 4$ mm to $D = 8$ mm, which became even more pronounced after 8 scans. Again, the reason is that as the spot size increases, less paint evaporation occurs, and the bending mechanism is less sensitive to facesheet thickening. Additionally, at $D = 4$ mm and $D = 6$ mm, facesheet temperatures were very close to melting temperatures (see Fig. 64), hence localized melting could occur, releasing part of the compressive stresses. Figure 72 further shows a slight drop in the bending angle from $D = 8$ mm to $D = 12$ mm after one laser scan. After eight scans, this trend disappeared, and the bending angles leveled off beyond $D = 8$ mm. The initial trend is related to the fact that increasing scan speeds at constant input energies reduce heat diffusion time, thereby increasing the temperatures and thus the bending angles [53]. This effect is negated after multiple scans, since larger spot sizes experience less paint evaporation and are less sensitive to facesheet thickening.

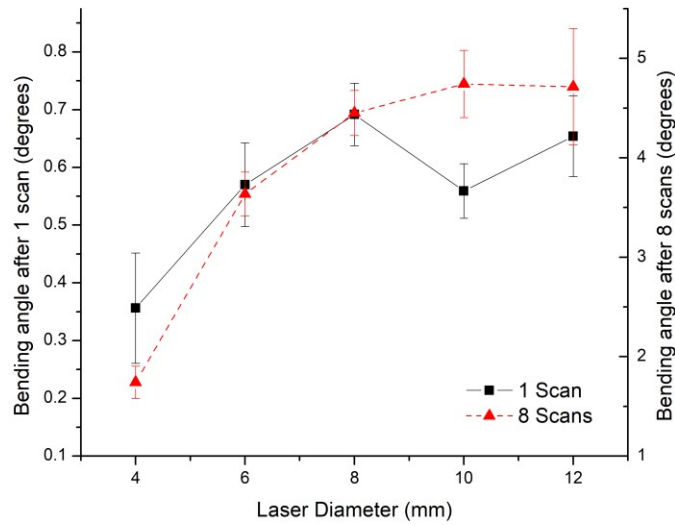


Fig. 73 Experimental bending angles after 1 scan and 8 scans at spot sizes ranging from $D = 4$ mm to $D = 12$ mm. The power and area energy are constant at $P = 800$ W and $AE = 6.67$ J/mm², respectively. The bending angles are averaged over 5 specimens, standard errors are shown.

Laser forming of sandwich panels is not only possible with a range of spot sizes, but there is also a considerable amount of freedom in the choice of the area energy. As shown in Fig. 74, a 40% change in the scan speed (and hence the area energy) still yielded appreciable bending angles. The spot size and the power were maintained at $D = 12$ mm and $P = 800$ W, respectively. Increasing the scan speed caused a drop in the area energy and hence a reduction of the bending angle, a trend that is well captured by the simulation.

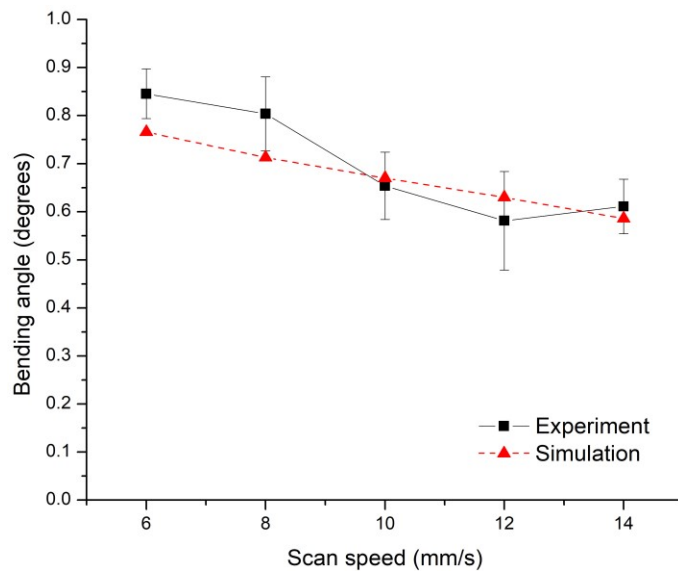


Fig. 74 Experimental and numerical bending angles after a single scan at a spot size of $D = 12$ mm and a power of $P = 800$ W. The experimental results were averaged over 5 specimens, standard errors are shown. With increasing scan speed, the area energy and thus the bending angle decrease. A considerable range of area energies can be used.

4.5.4 Numerical Model Comparison

Thus far, all the presented numerical results were generated using an equivalent sandwich model shown in Fig. 61(a). In this section, the equivalent sandwich model is compared with the Kelvin sandwich model shown in Fig. 61(b), in which the cavities of the foam core are explicitly modeled using Kelvin-cell geometries.

On one hand, the foam model geometry appears to be less important in sandwich panels than in free-standing foams [26], because the laser absorption in the top facesheet is the same regardless of the foam geometry. Also, the temperature distributions during laser scans are very similar in both models, as shown in Fig. 75 for $D = 12$ mm, $v = 10$ mm/s, and $P = 800$ W.

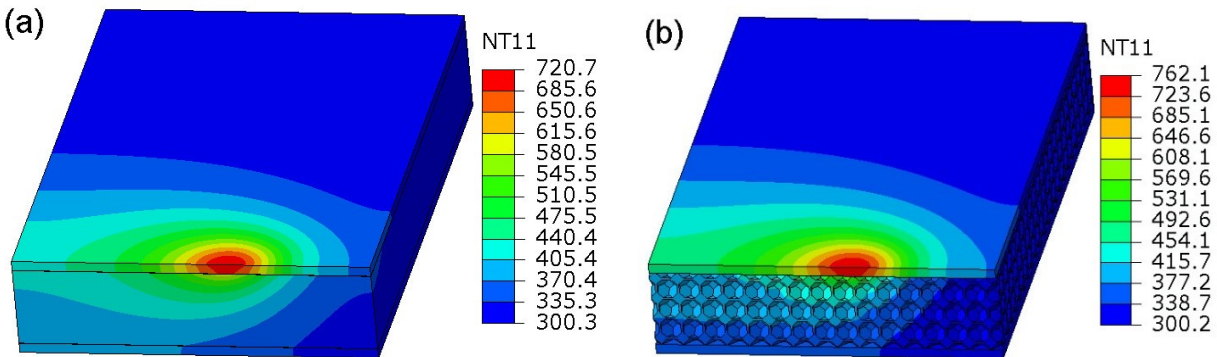


Fig. 75 Temperature distribution in a sandwich specimen scanned at $D = 12$ mm and $v = 10$ mm/s using a (a) equivalent sandwich model and a (b) Kelvin sandwich model. Half of the specimen is shown due to symmetry.

On the other hand, the foam core geometry does have a significant impact on the heat transfer between the facesheets and the metal foam core. In the equivalent sandwich model there is no geometric restriction to heat flow between the facesheet and metal foam, whereas the heat flow in the Kelvin sandwich model is channeled through thin cell walls. This leads to discrepancies in the temperature gradients as shown in Fig. 76 (analogous to Fig. 64). Due to the

geometrical restriction of the heat flow, more heat gets “trapped” in the top facesheet of the Kelvin sandwich model. As a consequence, the top facesheet heats up more and a greater temperature drop establishes across the interface. This discrepancy is more pronounced at $D = 12$ mm than at $D = 4$ mm, since heat has more time to dissipate due to the reduced scan speed [53], thereby rendering the interface property more important.

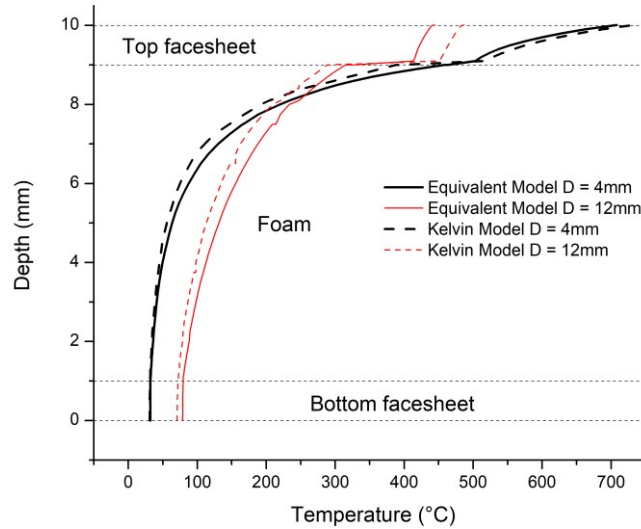


Fig. 76 Simulated temperature distributions at a cross-section (yz -plane) as the laser passes the section, predicted by the equivalent and Kelvin models, for the conditions $D = 4$ mm with $v = 30$ mm/s, and $D = 12$ mm with $v = 10$ mm/s. In the Kelvin sandwich model, the top facesheet temperatures and the temperature drop across the interface are greater due to the additional geometrical restriction of the heat flow at the interface.

The foam core geometry also has a significant impact on the mechanical interaction between the facesheets and foam core. In the equivalent sandwich model, the top facesheet thickens the same way everywhere along the laser scan path (see Fig. 67). In the Kelvin sandwich model, on the other hand, the foam core has high geometry-induced stiffness, which locally restricts facesheet expansion, a phenomenon that was also observed in experiments. At sections where a cavity is underneath the facesheet at the scan line (Fig. 77(a)), the facesheet can expand downwards unrestrictedly, and significant plastic compressive strain develops in the facesheet. At sections where a cell wall is located underneath the facesheet at the scan line (Fig. 77(b)), the

facesheet expansion is restricted and less plastic compressive strains develop. This phenomenon occurs predominantly at $D = 4$ mm, because the facesheet expansion is highly localized at the laser scan line. At $D = 12$ mm, the facesheet thickens over a larger distance from the laser scan line, and the impact of the foam core geometry is reduced.

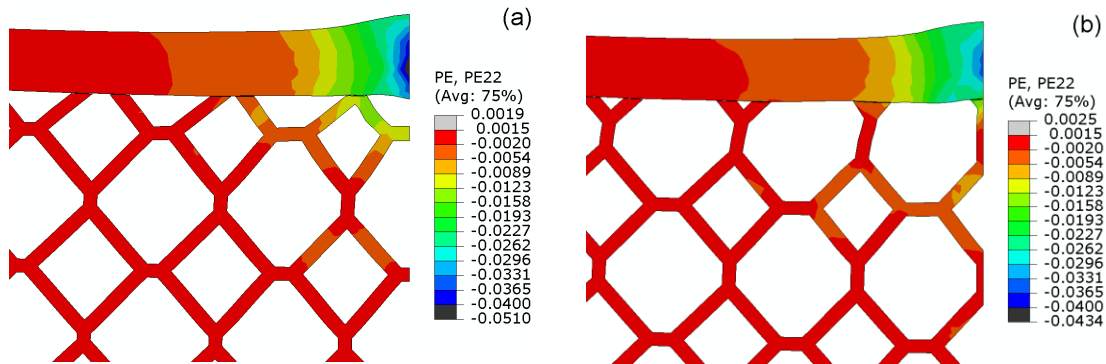


Fig. 77 Plastic strain distribution in the Kelvin sandwich model after a laser scan at $D = 4$ mm with $v = 30$ mm/s. A deformation scaling factor of 10 was used. Half of the specimen is shown due to symmetry. In (a), a cavity is located underneath the facesheet at the scan line, and the facesheet can expand downwards unrestrictedly. In (b), a cell wall is located underneath the facesheet, and the downward expansion of the facesheet is restricted.

Due to its increased geometrical accuracy, the Kelvin sandwich model has an increased sensitivity to changes in process conditions, as shown in Fig. 78. Whereas the equivalent sandwich model predicted little difference in bending angle between the small spot size ($D = 4$ mm) and the large spot size ($D = 12$ mm), the Kelvin sandwich model predicted a more significant difference between the two, which more closely agrees with experimental results. Both models over-predicted the bending angles at $D = 4$ mm, since neither of the models account for paint evaporation and possible local melting effects that occur at $D = 4$ mm.

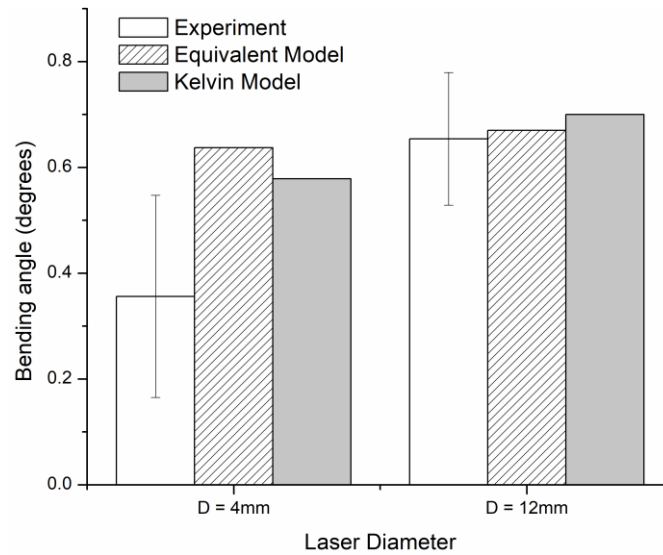


Fig. 78 Experimental and numerical bending angles after a single laser scan at $D = 4$ mm and $v = 30$ mm/s, and $D = 12$ mm and $v = 10$ mm/s ($P = 800$ W = const.). The Kelvin model is more sensitive to changes in process conditions due to its higher geometrical accuracy. Both models over-predicted the bending angles at $D = 4$ mm because they did not account for paint evaporation and localized melting.

4.6 Conclusions

This study demonstrated that sandwich panels with metal foam core can be laser formed with a wide range of process conditions. It was shown that both the top facesheet and the metal foam core bend via a laser forming mechanism and actively contribute to the bending deformation. The top facesheet bending mechanism depends on the laser spot size and varies between the TGM (for small spot sizes around $D = 4$ mm) and the UM (for large spot sizes around $D = 12$ mm). The metal foam core bends via the MTGM for all spot sizes. It was also demonstrated that sandwich panels bend more efficiently at large spot sizes than at small spot sizes, since larger segments of the top facesheet and the metal foam contribute to the compressive shortening. Moreover, it was shown that much greater bending angles can be achieved at larger spot sizes, due to the reduced impact of facesheet thickening on bending mechanism efficiency. Finally, it was shown that Kelvin sandwich models yield better predictions of bending angles and the

facesheet/foam core interaction than equivalent sandwich models, due to their higher geometrical accuracy.

From this study, it became clear that the facesheet/foam core interface plays a central role in laser forming of sandwich panels. Different adhesion types might significantly affect the heat transfer and the mechanics, and hence change the outcome of the laser forming process.

Acknowledgment

The authors gratefully acknowledge financial support from the National Science Foundation under a GOALI grant #CMMI-1725980. This work used the Extreme Science and Engineering Discovery Environment (XSEDE) Stampede through allocation TG-DDM160002, which is supported by National Science Foundation grant number ACI-1548562 [75]. The supply of aluminum foam sandwich material from Havel metal foam GmbH is greatly appreciated.

Chapter 5: Laser Forming of Metal Foam Sandwich Panels:

Effect of Manufacturing Method

5.1 Introduction

Metal foam has long been praised for its unique properties, notably its shock and noise absorption capacity and its high strength-to-weight ratio [2]. The material can realize its fullest potential in a sandwich configuration, where the metal foam is encapsulated by sheet metal on both sides. The solid metal “facesheets” of sandwich panels not only protect the foam core from wear and tear, but also create a high stiffness composite that still boasts a great shock absorption capacity while having a relatively low weight.

Many potential applications have been identified for sandwich panels with metal foam cores, ranging from parabolic mirrors in solar power plants, to rocket components and space equipment, to telescopic arms on construction equipment [7,9]. The material foremost has a great potential in the aviation industry, where it may be used for turbine casings to arrest failed turbine blades [11], for lightweight engine nacelles, or for airplane noses to absorb the shock during bird impacts [12]. In some applications, the material may even replace honeycomb structures that are widely used in airplanes nowadays, since it allows for a greater flexibility in its geometrical and structural attributes and has a uniform stiffness about all bending axes [2].

What currently hampers the implementation of sandwich panels with metal foam cores is that the material is challenging to manufacture in the shapes that are required in engineering applications. There do exist two near-net-shape methods that directly manufacture sandwich panels in non-straight shapes. The first process is 3D printing [13], which has a limited dimensional accuracy and is only suitable for small parts with a small production volume. The

second process is based on powder metallurgy. In this process, a “precursor” consisting of compacted metal and foaming agent powders is created and placed between two facesheets that are bent to the desired shape [9]. The entire assembly is placed into a mold and heated near the melting temperature of the precursor metal. The heating causes the foaming agent to release a gas that turns the precursor into a foam. Simultaneously, sintering occurs, joining the foam core to the facesheets via metallic bonds. While being convenient, this process is only suitable for relatively small parts, since it requires several molds that need to be uniformly heated. Moreover, the process is only adequate for a very large production volume, since much trial and error is required to achieve a uniform foam structure and density.

The alternative to the aforementioned processes is manufacturing the sandwich panel in a straightforward shape, such as a flat panel, and subsequently bending it to the required shape. In this fashion, panels with uniform properties can be manufactured at a lower cost. The challenge with this approach is that bending sandwich panels with metal foam cores is not possible with standard forming processes. 3-point bending causes many types of fractures ranging from core crushing to core failure or delamination [15]. Die stamping suffers similar defects [52], and hydroforming significantly densifies the foam core [17]. The only process that does not cause premature failures in the material is laser forming, as it is a non-contact process that induces deformation through heating and subsequent thermal expansion. The underlying bending mechanisms and numerical modeling considerations were analyzed in great detail in a previous study [91].

In [91] it was shown that laser forming can successfully bend a specific sandwich panel type, in which the facesheets and the foam core are joined directly during manufacture, discussed in detail in the following section. In this study, it was investigated whether laser forming is equally

capable of bending a fundamentally different sandwich panel type, in which the facesheets and the foam core are joined after having been manufactured separately. This sandwich panel type additionally has a different foam structure and facesheet type than the sandwich panel that was used in [91]. Through this analysis, it was determined whether the sandwich structure, composition, and manufacturing method have an impact on the bending mechanism, efficiency, and limit. The overarching goal of the study was to broaden the understanding of laser forming of sandwich panels with metal foam cores, and to deliver the insights necessary to implement a broader variety of sandwich panels in industrial applications.

5.2 Background

5.2.1 Sandwich Panel Manufacturing Methods

In this study, two fundamentally different types of sandwich panels with metal foam cores were compared. In the first type (referred to as *Type I*, shown in Fig. 79(a)), the foam core and the connection between the facesheets/foam core were established in the same step. In the second type (referred to as *Type II*, shown in Fig. 79(b)), the foam core and facesheets were manufactured independently and joined subsequently.

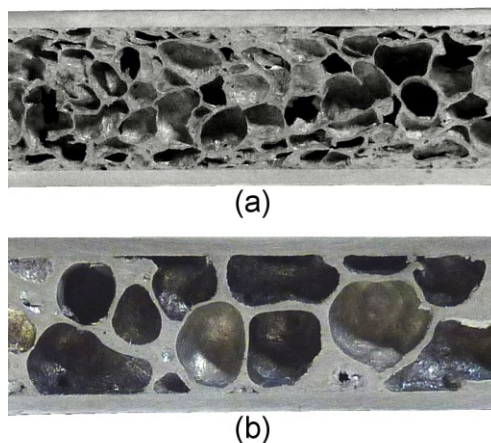


Fig. 79 (a) Type I sandwich panel, (b) type II sandwich panel

Only one method may be used to manufacture sandwich panels of the first type. This method is very similar to the near-net-shape method that was mentioned in the previous section [9]. A “precursor” consisting of compacted metal and foaming agent powders is placed in between solid metal facesheets and heated near the melting temperature of the precursor metal. During heating, the foaming agent releases a gas that creates bubbles, and simultaneously the metal powders are sintered together. As the precursor expands into a foam, its lateral expansion is restricted, thereby developing a pressure that causes the foam core to establish a metallic connection with the facesheets.

To manufacture sandwiches of the second type, many approaches may be taken to join the facesheets to the foam core. The simplest approach is to use an adhesive, which, though very affordable, is not adequate for laser forming since the adhesives cannot withstand the high temperatures that develop. The alternative is to establish metallic bonds via brazing [92] or diffusion bonding (i.e. sintering), which are generally stronger and more resistant to elevated temperatures. The latter metallic bond type was used in this study. In order to improve the bonding quality, pure aluminum powder was added between the facesheets and the foam core prior to vacuum sintering.

The advantage of type I sandwich panels is that the foam and the joints between the foam and the facesheets are created in the same step, whereas an additional joining step is required in type II sandwich panels. Also, the joint of type I sandwiches is more uniform and contains fewer defects than type II joints (as will be shown later), since the foam core does not have to be cut to the required dimensions prior to adhering it to the facesheets. At the same time, type II sandwich panels have a more uniform foam density than type I foams, which are typically denser near the facesheet and less dense in the center. Moreover, virtually any foam geometry (open-cell, closed-

cell, large/small pore) may be used in type II sandwich panels, provided that the foam composition is compatible with the facesheet and allows for diffusion bonding to occur. Type II sandwiches also do not require any molds, and the sandwich thickness can more readily be varied while still maintaining uniform foam properties.

Overall, type I sandwich panels would excel in structural applications where facesheet delamination could have catastrophic consequences. Type II sandwich panels would excel as shock absorbers where it is crucial to have consistent foam properties as well as a high flexibility in the foam geometrical attributes.

5.2.2 Thermally-Induced Stresses at the Interface

The thermo-mechanical behavior of the facesheets and the foam core during laser forming is well understood. In a previous study it was shown in great detail that the top facesheet bends via the temperature gradient mechanism (TGM) when a small laser spot size around 4 mm is used, and it bends via the buckling mechanism (BM) for large laser spot sizes around 12 mm (which turns into the upsetting mechanism (UM) in sandwich configuration). It was further shown that the metal foam bends via the modified temperature gradient mechanism (MTGM) regardless of the process condition [91]. The bottom facesheet is the only component that bends “mechanically” due to the bending moment induced by the top facesheet and the foam core. Detailed descriptions of all of the aforementioned mechanisms may be found in [22].

The behavior of the facesheet/foam core interface during laser forming, on the other hand, is comparatively poorly understood. The thermo-mechanical response of multilayered materials has only been studied in detail for the case where the entire composite is uniformly heated [96], which differs from the laser forming scenario where the temperature distributions are usually

non-uniform. Yet, the analysis still allows for a useful comparison of the two sandwich panel types that are investigated in this study.

The stress-state at the interface can be described in terms of tractions and displacement discontinuities across the interface, since both sandwich panel types have a finite yet exceedingly thin interface. Assuming that an interface of thickness η with normal and shear stiffnesses E_0, G_0 joins two layers with thicknesses s_i , thermal expansion coefficients α_i , and normal and shear stiffnesses E_0, G_0 (see Fig. 80), the normal and shear tractions t_n, t_s at the interface become [93]

$$t_n = E_0 \frac{z_1 - z_2}{\eta} \quad (5.1)$$

$$t_s = G_0 \frac{y_1 - y_2}{\eta} \quad (5.2)$$

where y_i and z_i are the displacements of both layers in y and z -direction, respectively (see Fig. 80).

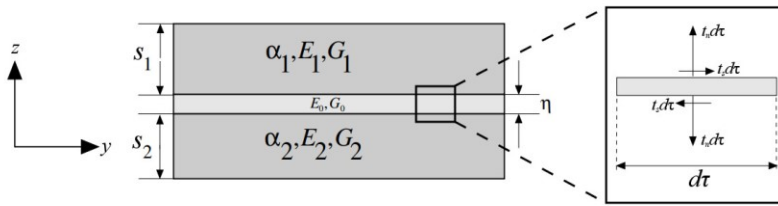


Fig. 80 Schematic of two layers of thicknesses s_1 and s_2 that are joined by an interface of thickness η , with a close-up of the traction components at the interface [93].

From eqns. (5.1) and (5.2) it is evident that the interfacial traction magnitude increases with decreasing interface thickness η . The interface thicknesses were measured using energy dispersive X-ray spectroscopy (EDS), and it was found that the average type I interface thickness of 80 μm was smaller than the average type II interface thickness of 120 μm . An example EDS line scan of a 350 μm segment of a type I sandwich is shown in Fig. 81, where the interface can be clearly identified as the transitional zone between the low Mg-content foam core and the high

Mg-content facesheet. Hence, the interfacial tractions are greater in type I sandwich panels, making them more prone to debonding. Interestingly, however, the EDS analysis also revealed that the interfacial thickness increases during laser forming. In the type I sandwich panel, for instance, the thickness increased from 80 μm to 120 – 130 μm after being laser formed at typical process conditions. Therefore, laser forming seems to alleviate the stress concentration at the interface by promoting more intermetallic diffusion.

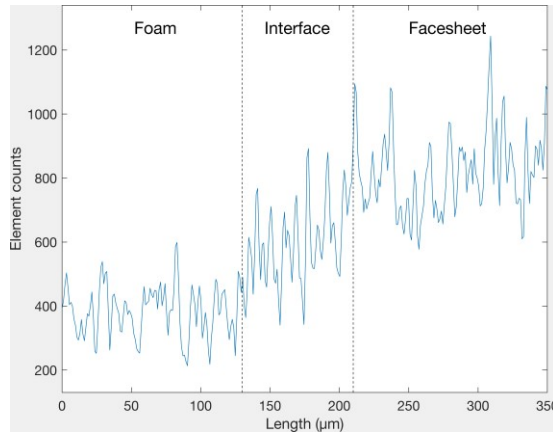


Fig. 81 Typical EDS line scan of a type I sandwich panel specimen, showing the magnesium content. The scan was performed across the interface between the facesheet and the foam core. The interface is the intermediary region between the high Mg-content facesheet and the low Mg-content foam.

The displacement discontinuities in eqns. (5.1) and (5.2) can be determined from the following equations, assuming that the displacements are infinitesimally small and only arise due to uniform heating of the facesheet and the foam core

$$\frac{dy_i}{d\tau} = \alpha_i \Delta T + \frac{P_i}{ws_i E_i} + \frac{s_i}{2R} \quad (5.3)$$

$$\frac{d^2 z_i}{d\tau_i^2} = - \frac{12(1-\nu_i^2)M_i}{E_i s_i^3} \quad (5.4)$$

where $d\tau$ is the width of the section over which the force analysis is performed (see Fig. 81) and ν_i is Poisson's ratio. The first term in eq. (5.3) represents the thermal expansion in y -direction of each layer due to the heating by ΔT . The second term in (5.3) is due to the load P_i that arises in

both layers (compressive in one and tensile in the other) because the layers are unable to slide past each other. w refers to the specimen width. The third term in (5.3) is due to the moments M_i that the layers exert onto each other since the radius of curvature R at the interface differs from the radii that the two layers strive to follow. These moments M_i also cause a displacement discontinuity in z -direction, shown in eq. (5.4), since they would cause each layer to bend by a different amount if the layers were separated [93].

From eqns. (5.1) – (5.4) it can be seen that substantial displacement discontinuities arise due to the different thicknesses of the foam core (8 mm) and the facesheets (1 mm). The equations further show that the displacement discontinuities, and hence the interfacial stresses, increase the more the material properties of the foam core and the facesheets differ. Based on this, the interfacial stresses are again predicted to be higher in the type I sandwich panel, where the AlSi10 foam core properties substantially differ from the AW 5005 facesheet properties, than in the type II sandwich panel where both the foam core and the facesheets consist mostly of aluminum (≥ 99.6 wt %).

Based on this theoretical analysis, the type I sandwich panel is more susceptible to develop high interfacial stresses that could lead to delamination. In reality, however, no delamination occurred during laser forming in either sandwich type as will be shown later. Therefore, the diffusion-based metallic bonds of the sandwich panels are strong enough to withstand the stresses caused by laser heating. This might in part be due to the ongoing intermetallic diffusion that occurs during laser forming.

5.2.3 Numerical Simulation

Three types of numerical models were used in this study, which may be grouped into the categories of *equivalent sandwich models* and *explicit sandwich models*. Equivalent sandwich models (Fig. 82(a)) approximate the foam geometry as a rectangular box and use metal foam material properties. Since metal foam is able to yield both due to shear stresses (Von Mises equivalent stress σ_e) as well as due to hydrostatic stresses σ_m , the yield criterion becomes [41]

$$F = \left[\frac{1}{1+(\beta/3)^2} (\sigma_e^2 + \beta^2 \sigma_m^2) \right]^{1/2} - Y \leq 0 \quad (5.5)$$

where Y is the yield strength and β the aspect ratio of the yield surface. When $F < 0$, elastic deformation occurs, while $F = 0$ initiates plastic deformation following the flow rule

$$\dot{\varepsilon}_{ij}^p = \frac{\dot{Y}}{H} \frac{\partial F}{\partial \sigma_{ij}} \quad (5.6)$$

where $\dot{\varepsilon}_{ij}^p$ is the plastic strain rate, and H is the hardening modulus defined as

$$H = \frac{\sigma_e}{\hat{\sigma}} h_\sigma + \left(1 - \frac{\sigma_e}{\hat{\sigma}} \right) h_p \quad (5.7)$$

where h_σ and h_p are the tangent moduli in uniaxial and hydrostatic compression, respectively, and $\hat{\sigma}$ is equal to the first term in eq. (5.5). The assumptions of the model were discussed in detail in a previous study [27]. In the finite element code Abaqus that was used in this study, this constitutive model is incorporated as *foam crushable model*. The mesh that was used for the foam model is shown in Fig. 85 and discussed in detail in [26,27].

Explicit models, in contrast, directly model the foam structure and use the bulk properties of the metal that comprises the foam (AlSi10 for type I and Al 99.7 for type II). Hence, they are governed by a constitutive model that describes the behavior of bulk metals. Similar to many

previous laser forming studies [53], the deformation is assumed to be incompressible, and Von Mises' yield criterion, the Von Mises flow rule, as well as strain hardening are assumed to hold. Two types of explicit models were used in this study that are discussed in detail in [26,27]. The first model, called *Kelvin cell sandwich model* (Fig. 82(b)), approximates the shape of a single cavity by a Kelvin cell geometry and assumes the wall thickness to be constant throughout. The model was obtained by cutting arrays of Kelvin cells out of a solid block. The second explicit model that was used is a *voxel sandwich model*. It was obtained by performing a micro computed tomography (CT) scan of 25 mm by 25 mm sandwich panel specimens at a resolution of 30 μm , and by converting high absorption points of the data cloud to cubical volumes that are called *voxels*. The resolution was then manually reduced to 150 μm in order to reduce the number of elements to around 400,000. Figure 82(c) shows a voxel model of the type I sandwich panel, next to the original, and Fig. 82(d) shows a voxel model of the type II sandwich panel. Due to their reduced size, the voxel models were only used for a qualitative analysis in this study.

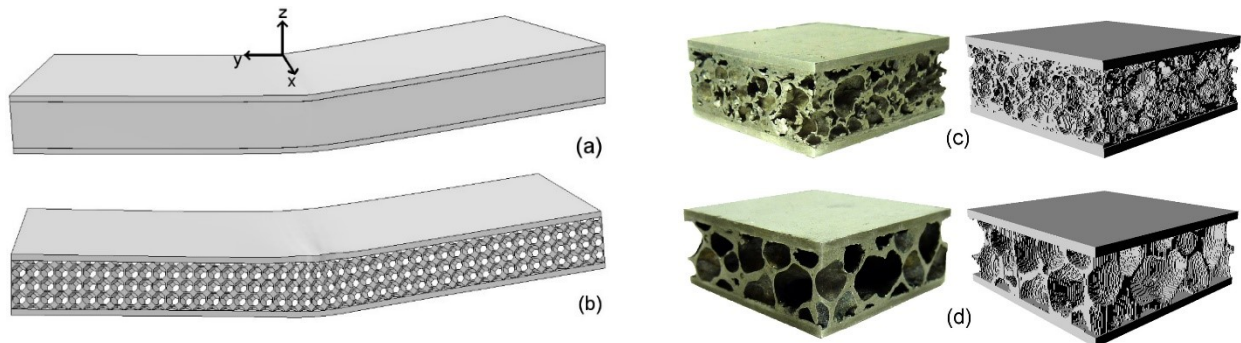


Fig. 82 (a) Equivalent sandwich model, (b) Kelvin-cell sandwich model, (c) type I sandwich panel specimen (left) and corresponding voxel model (right), (d) type II sandwich panel specimen (left) and corresponding voxel model (right).

In all three models, the facesheets were modeled as incompressible solids that follow Von Mises' yield criterion. In the equivalent and Kelvin sandwich models, 3 and 2 elements were used through the thickness of the top and bottom facesheets, respectively. In the voxel models, 4 and 3 elements were used, respectively, due to the finer mesh of the foam.

The interface between the facesheets and the foam was modeled using cohesive elements. The stress-state was described in terms of tractions and displacement discontinuities that were linearly related via the stiffness matrix K

$$\begin{bmatrix} t_n \\ t_s \\ t_t \end{bmatrix} = \begin{bmatrix} K_{nn} & 0 & 0 \\ 0 & K_{ss} & 0 \\ 0 & 0 & K_{tt} \end{bmatrix} \begin{bmatrix} u_n \\ u_s \\ u_t \end{bmatrix} \quad (5.8)$$

where the subscripts n , s , and t refer to the normal, 1st and 2nd shear directions, respectively. All stiffness components of the cohesive elements were set to a very large value (80 GPa) to ensure that the overall sandwich stiffness is unaffected by the presence of the interface [49].

All the simulations were performed in an uncoupled manner, using the results of the heat transfer analysis as input to the mechanical analysis. For the heat transfer analysis, DC3D20, DC3D10, DC3D8 elements were used for the equivalent, Kelvin, and voxel foams, respectively, and C3D20R, C3D10, C3D8R elements were used for the mechanical analysis. For the facesheet, DC3D20 and C3D20R elements were used for the heat transfer and mechanical analysis, respectively. DC3D8 and COH3D8 elements were used for the cohesive elements during the thermal and mechanical analyses, respectively.

The material properties for the type I foam (AlSi10) were extracted from [70], and the properties for the AW 5005 facesheet (AlMg1) were extracted from [94]. For the type II sandwich, Al 99.7 properties from [95] were used both for the facesheet and the foam core. An absorption coefficient of 0.6 was used. The laser source was modeled with the user subroutine *dflux*.

5.3 Experimental Methods

Two sandwich panel types were used in this study, whose manufacturing methods were explained in detail in Sec. 5.2.1. To maximize the scope of this study, the type I and type II sandwich panels additionally consisted of different facesheet types and foam structures. In the type I sandwich panel, the facesheets were made of AW 5005, containing Magnesium as major alloy element. The foam core was made of AlSi10 and had an average cavity size of roughly 2 mm. In the type II sandwich panel, both the facesheet and the foam had a high aluminum content (≥ 99.6 wt %), with the facesheet being made of Al 1060. In both sandwich panel types, the facesheet thickness was 1 mm. The foam core was manufactured using the melt foaming method [31], using TiH_2 as the foaming agent and having an average cavity size of roughly 4 mm. The foam cores of both sandwiches had an average density around 700 kg/m^3 (74% porosity) and a thickness of 8 mm.

Laser forming experiments were performed using a CO_2 laser with a wavelength of $10.6 \mu\text{m}$. The specimen surfaces were coated with black graphite paint to maximize the laser absorption. Between successive laser scans the specimens were allowed to cool back to room temperature. The specimens were scanned in x -direction shown in Fig. 82(a), and the deflection was measured using a dial indicator.

Two process conditions, which were also used in a previous study [91], were investigated. In the first process condition, a large spot size of 12 mm was used with a slow scan speed of 10 mm/s. In the second process condition, a small spot size of 4 mm was used with a fast scan speed of 30 mm/s. The power was set to 800 W for both conditions to maintain a constant area energy.

An infrared camera was used to measure the bottom surface temperature of the sandwich panels during laser forming. The frame rate of the camera was 120 Hz (8 ms per frame), and the

spatial resolution was roughly 0.1 mm. The specimens were placed above an aluminum shield to prevent the laser irradiation from damaging the IR camera. The measured surfaces were coated with highly emissive black graphite paint ($e = 0.92$) to maximize the measurement accuracy, and the results were averaged over a diameter of 1 mm.

5.4 Results & Discussion

5.4.1 Bending Efficiency & Limit

This study was initiated by investigating the impact of the sandwich composition and manufacturing process on the bending behavior, specifically the bending efficiency and the maximum achievable bending angle. Both sandwich panel types were laser formed at a small laser spot size ($D = 4$ mm, $v = 30$ mm/s) and a large laser spot size ($D = 12$ mm, $v = 10$ mm/s), and the bending angles were recorded over 8 scans (Fig. 83). At $D = 4$ mm, the two sandwich panel types bent by about the same amount over 8 laser scans. Also, the maximum achievable bending angle was similar, being $\sim 15^\circ$ for the type I panel and $\sim 12^\circ$ for the type II panel. At $D = 12$ mm, on the other hand, the type I panel bent at a much higher rate than the type II panel. Moreover, the maximum achievable angle was around 65° (Fig. 84(a)), while the maximum angle was $\sim 45^\circ$ for the type II panel (Fig. 84(b)).

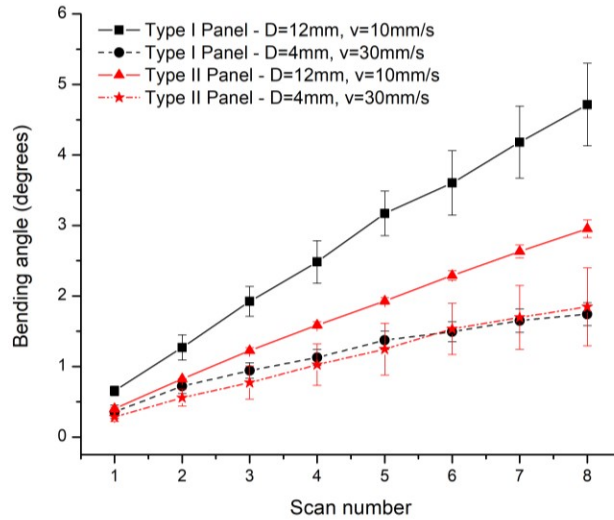


Fig. 83 Bending angles of both sandwich panel types over 8 laser scans at a large spot size ($D = 12 \text{ mm}$, $v = 10 \text{ mm/s}$) and a small spot size ($D = 4 \text{ mm}$, $v = 30 \text{ mm/s}$), the power was constant at $P = 800 \text{ W}$. The results were averaged over 3 specimens, standard errors are shown.

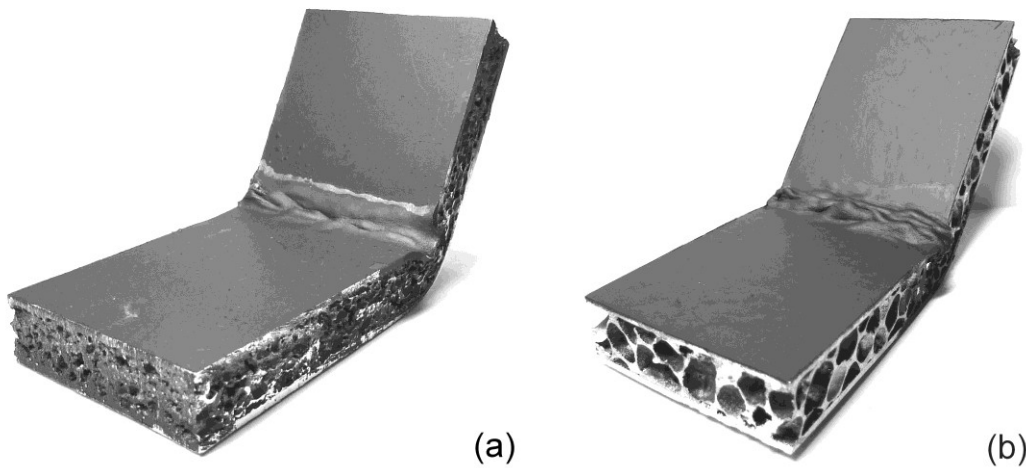


Fig. 84 The bending limit of the (a) type I and (b) type II sandwich panel at a large spot size ($D = 12 \text{ mm}$, $v = 10 \text{ mm/s}$) were around 65° and around 45° , respectively. In the type I sandwich panel, the top facesheet mostly deformed inwards, whereas it mostly deformed outwards in the type II sandwich panel.

Hence, some attribute(s) of the sandwich panels caused a significant deviation in the efficiency and bending limit at a large spot size. Due to the numerous differences between the sandwich panel types, a series of experiments and numerical studies were performed to identify the cause(s) of the aforementioned deviations.

5.4.2 Effect of Facesheet

The impact of the facesheet composition was investigated first. The type I (AW 5005) and type II (Al 1060) facesheets hardly differ in their thermal properties, but they have two notable differences in their mechanical properties. First, the yield strength of the type I facesheet is almost twice the yield strength of the type II facesheet. Second, the type II facesheet undergoes substantially more softening than the type I facesheet at elevated temperatures. Intuitively, one would expect the type II sandwich to bend more, due to its softness. Laser forming experiments of “isolated” facesheets (not attached to foam core) showed the opposite (Fig. 85), however, an unintuitive result that is characteristic to laser forming. The TGM that is induced at this process condition ($D = 4$ mm, $v = 30$ mm/s) relies on the fact that the thermal expansion of the heated material is restricted by the “cold” surrounding material, a condition that is better satisfied by a stiff material such as AW 5005, and less so by a material that undergoes substantial thermal softening such as Al 1060.

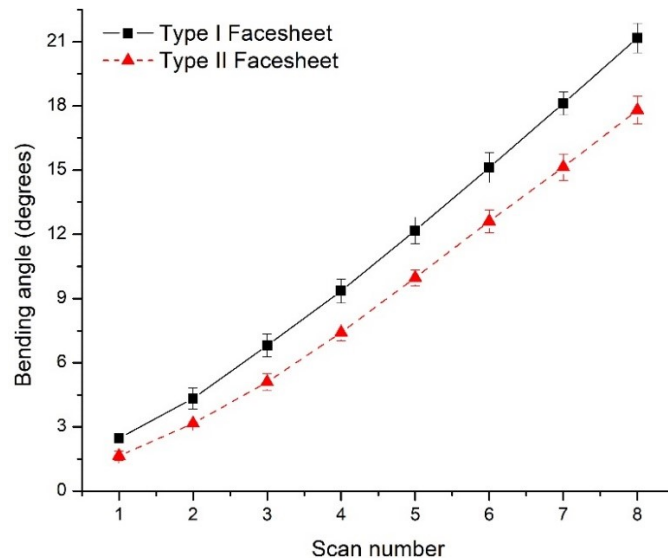


Fig. 85 Bending angles of the “isolated” facesheets (not attached to foam core) at a small spot size ($D = 4$ mm, $v = 30$ mm/s). The type I facesheet, made of AW 5005, bent more efficiently than the type II facesheet, which was made of Al 1060.

The same explanation applies when the entire sandwich panel is bent at a large spot size of $D = 12$ mm: the facesheet deformation via the UM is more efficient if the thermal expansion of the heated material is restricted by the “cold” surrounding material, which is again better satisfied by the type I facesheet. Numerical simulations confirmed this by showing that the plastic compressive strain in y -direction are much greater for the type I facesheet (Fig. 86(a)) than in the type II facesheet (Fig. 86(b)). The simulations also showed that the sandwich panel with type I facesheet properties bent by 0.68° , compared to the sandwich panel with type II facesheet properties that only bent by 0.56° (leaving all remaining properties the same).

Overall, the facesheet comparison showed that the type I facesheet bends at a higher rate than the type II facesheet, which is partially responsible for the difference in the bending efficiency in Fig. 83. Yet, the facesheet composition accounted for only around 20% of the difference in the bending efficiency, whereas the overall difference in efficiency in Fig. 83 was around 50%. Therefore, there are other factors that more significantly influenced the bending efficiency.

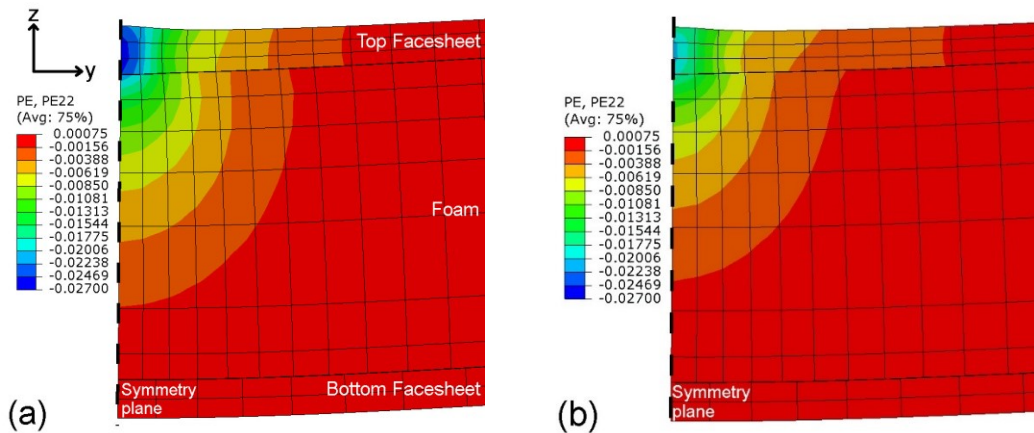


Fig. 86 Plastic strain distribution in y -direction after a laser scan at ($D = 12$ mm, $v = 10$ mm/s). AW 5005 facesheet properties were used in (a), and Al 1060 facesheet properties were used in (b). The remaining geometrical and material properties were identical. The deformation was scaled by a factor of 10 for viewing clarity. Only half of the model is shown due to symmetry.

5.4.3 Effect of Foam Core

The next component that was analyzed was the foam core. From a thermal standpoint, the two foams are hardly any different, as can be seen from their thermal response in Fig. 87. The results were obtained by machining two cylindrical foam pucks with a diameter of 25 mm and a thickness of 6 mm for both foam types. All the tested pucks had a similar density and surface area, and they were tested in both directions (4 tests per foam type). The pucks were placed between mirror-polished aluminum disks with a thickness of 1 mm (see diagram in Fig. 87). The assembly was clamped in a holder, a laser source with diameter of $D = 12$ mm was applied to the top surface, and the temperature history was recorded on the bottom surface using an IR camera. The exposed surfaces of the aluminum disks were spray-painted with black graphite paint to increase the laser absorption (top) and to ensure a high emissivity (bottom). The results in Fig. 87 show that the heat diffusion is very similar through both foam types, despite the fact that their structures are fundamentally different.

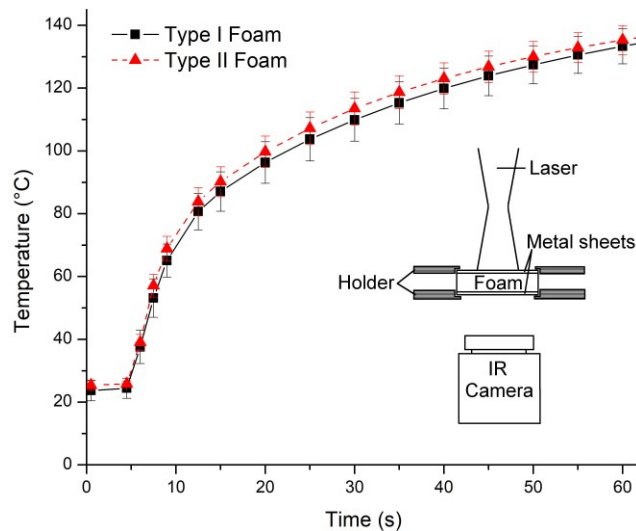


Fig. 87 Foam pucks were sandwiched between two solid aluminum disks. A laser with spot size $D = 12$ mm was applied to the top surface of the assembly and the temperature was measured underneath. The measured heat diffusion through the type I and type II foams was very similar. The results were averaged over 2 specimens that were tested from both directions, standard deviations are shown.

From a mechanical standpoint, the two foam types do not differ significantly either. The type I foam consists of an AlSi10 alloy and has a higher strength than the high aluminum-content type II foam (≥ 99.6 wt %). Hence, the type I foam is expected to bend more efficiently during laser forming. This effect is canceled out by the fact that the moment of area of the type I foam is on average 18% higher than the moment of area of the type II foam (Fig. 88), making it more resistant to bending deformation. The moment of area was calculated for each pixel of a particular micro-CT slice using the following relation

$$I = \int_{-s/2}^{s/2} z^2 y(z) dz \quad (5.9)$$

where s is the sheet thickness. The individual moments were then summed up using the parallel axis theorem. The moment of area was calculated about a horizontal axis at the center of specimens (not shown in Fig. 88).

Based on all the above results, both the thermal and mechanical responses of the type I and II foams are very similar. Therefore, the foam core behavior cannot possibly be the reason for the different bending efficiencies and bending limits observed in Figs. 83 and 84.



	Cross-section	Moment of area
Type I Foam		1.18
Type II Foam		1

Fig. 88 The moment of area of the type I foam is on average 18% greater than the moment of area of the type II foam, making it stiffer to bending deformation.

5.4.4 Thermal Response of Sandwich Panel

Neither the facesheets nor the foam cores are the major cause of the different behavior of the type I and II sandwich panels. Hence, the two sandwich panel types must differ in the way that their facesheets and foam cores interact. This interaction occurs on a thermal as well as a mechanical basis. The thermal interaction was investigated first by scanning both sandwich panel types at a small spot size ($D = 4$ mm, $v = 30$ mm/s) as well a large spot size ($D = 12$ mm, $v = 10$ mm/s), and by recording temperature on the bottom sandwich surface using an IR camera, shown in Fig. 89. For both sandwich types, the bottom surface reached higher temperature values at a larger spot size and a slower scan speed. This finding is consistent with previously reported results and relates to the fact that more heat diffusion can occur at slow scan speeds [26,43]. Figure 8 also shows that the type I sandwich panel reached slightly higher temperature magnitudes than the type II sandwich panel, which can be attributed to two causes. First, the facesheet adhesion quality is superior in type I sandwich panels, as will be shown later. Second, the type I foam is denser near the facesheet than at its center, allowing for an increased heat transfer between the facesheet and the foam compared to the type II sandwich panel. Overall, the temperature difference between the two sandwich types was rather insignificant, however, considering that their top surfaces were heated up to 600°C.

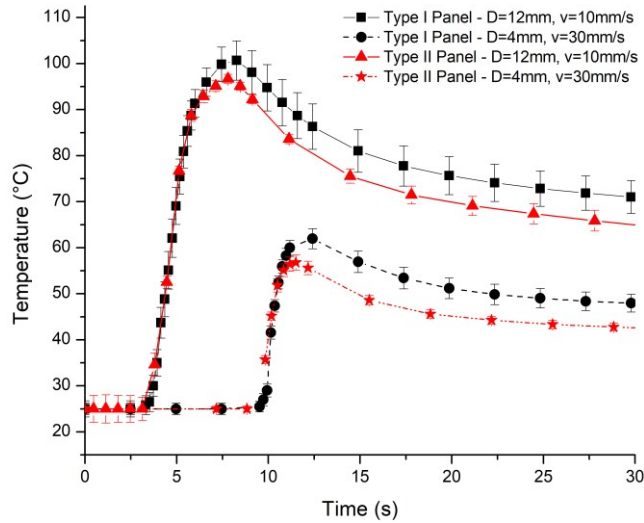


Fig. 89 Temperature history on the bottom surface of the sandwich panels during laser scans at a large spot size ($D = 12$ mm, $v = 10$ mm/s) and a small spot size ($D = 4$ mm, $v = 30$ mm/s). 4 specimens were tested for each sandwich panel type, standard deviations are shown.

Numerical simulations confirmed that the thermal response of both sandwich panel types is similar. Figures 90(a) and 90(b) show the temperature distributions in the type I and type II sandwich panels during a laser scan at $D = 12$ mm and $v = 10$ mm/s, performed using voxel models. The same temperature-dependent gap conductance relationship was used at the interface for both panels, discussed in detail in [91]. As was mentioned previously, heat can flow rather continuously from the top facesheet to the foam core in the type I sandwich panel (Fig. 90(a)) due to the small cavity size and the high foam density near the facesheets, whereas its flow is restricted to the sparsely spaced cell walls in the type II sandwich panel (Fig. 90(b)). As a consequence, the top facesheet heated up slightly more in the type II sandwich panel. Nevertheless, the thermal behavior of the two sandwich panel types was similar and must not have been the cause for the different bending efficiencies and bending limits.

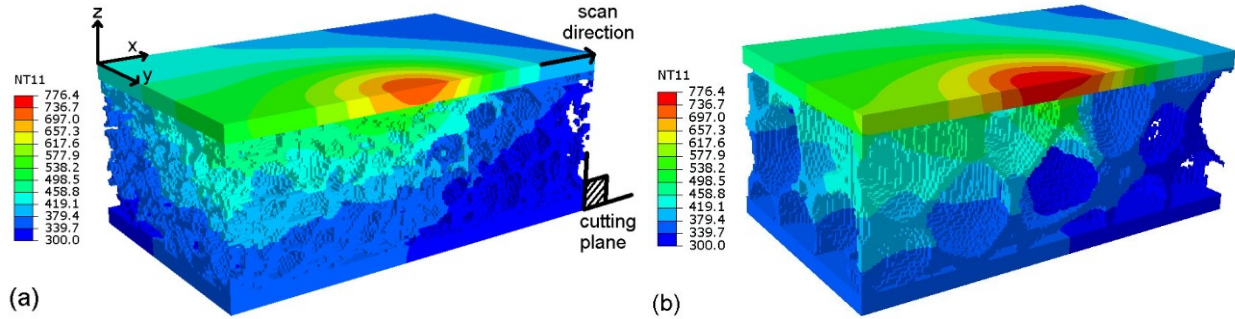
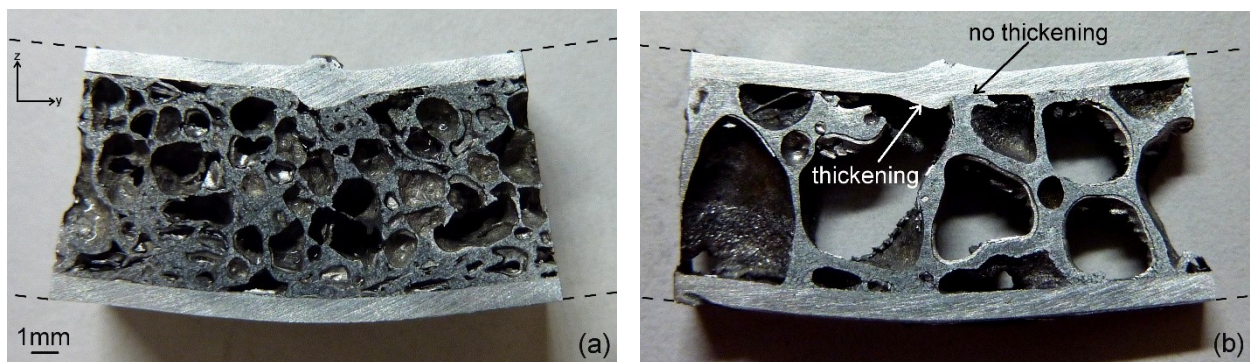


Fig. 90 Temperature distribution in voxel models of (a) type I sandwich panels and (b) type II sandwich panels, during a scan at a large spot size ($D = 12$ mm, $v = 10$ mm/s). The laser was scanned in x-direction. The models were sliced along the laser scan line for viewing clarity.

5.4.5 Mechanical Response of Sandwich Panel

Having ruled out the differences in the facesheets, the foam core, as well as the thermal interaction between the facesheets and foam core as major causes of the discrepancies in Figs. 83 and 84, the mechanical interaction of the facesheets and foam core is the last possible option. Results confirmed that the foam core structure is the key factor deciding how the facesheets and the foam core interact, thereby defining the bending behavior of the entire sandwich. While the type I foam core consists of many thin cell walls that can readily crush when subjected to compressive stresses, the type II foam core consists of fewer thick cell walls that only bend when subjected to very high compressive stresses. One consequence of this is that the deformation via the MTGM is less efficient in the type II foam. The second and more important consequence is that the top facesheet starts behaving differently during laser forming.



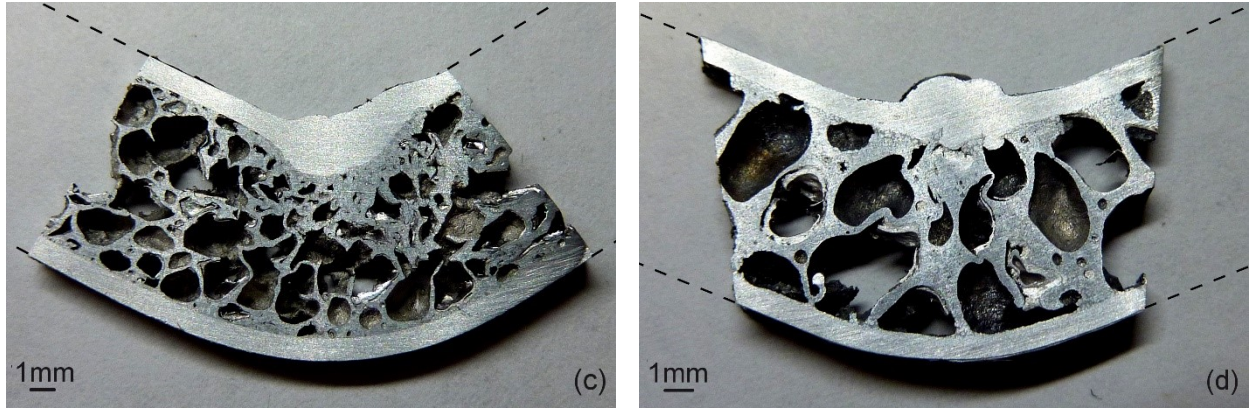


Fig. 91 Cross-sections of type I and type II sandwich panels that were bent to the bending limit. The laser was scanned into the page. At a small spot size ($D = 4$ mm, $v = 30$ mm/s), the bending limit of the type I sandwich panel is around 15° (a), and for the type II sandwich panel it is around 12° (b). At a large spot size ($D = 12$ mm, $v = 10$ mm/s) the limit is (c) around 65° for the type I sandwich panel and (d) around 45° for the type II sandwich panel.

In the type I sandwich panel, the top facesheet can readily penetrate into the foam core, both at small spot sizes (Fig. 91(a)) and large spot sizes (Fig. 91(c)), due to the high crushability of the foam core. In the type II sandwich, on the other hand, the top facesheet can penetrate into the foam core if a cavity is underneath, but not if a cell wall is underneath. Fig. 91(b) highlights this point, showing an example where the deformation at the scan line (in the center) is strictly divided between a left segment where the facesheet was able to thicken downwards (in negative z -direction) due to a cavity, and a right segment where no downward thickening occurred due to the presence of a cell wall.

This facesheet thickening behavior has a relatively minor impact on the bending efficiency and maximum bending angle at a small spot size of $D = 4$ mm, because the facesheet deformation via the TGM is relatively localized. At large spot sizes of $D = 12$ mm, however, the facesheet deformation is more widespread due to the UM, and the behavior of the top facesheet becomes more important. Unlike in the type I sandwich panel (Fig. 91(c)), where the top facesheet could significantly penetrate into the foam core, the top facesheet could hardly penetrate into the foam core in the type II sandwich panel (Fig. 91(d)). Instead, most of the

facesheet deformation occurred in an outward direction (positive z -direction). As a consequence, the overall thickness of the type II sandwich panel increased tremendously, rendering the sandwich stiffer and limiting the maximum achievable bending angle. The type I sandwich panel (Fig. 91(c)), in contrast, maintained almost the same thickness, allowing deformation up to larger bending angles.

Numerical simulations with voxel models qualitatively illustrate this point. Figures 92(a) and 92(b) show the plastic compressive strains in y -direction in a type II sandwich panel after a single laser scan at $D = 12$ mm, $v = 10$ mm/s and $P = 800$ W. Case (a) represents a scenario where a cavity is situated underneath the facesheet (by the scan line) and is contrasted with case (b), where a cell wall is located underneath the facesheet. In (a), the facesheet is able to thicken in downward direction, and high plastic strain magnitudes are reached due to the efficient action of the UM. In (b), the facesheet can only thicken in the upward direction, the UM becomes less efficient, and lower plastic strain magnitudes are reached.

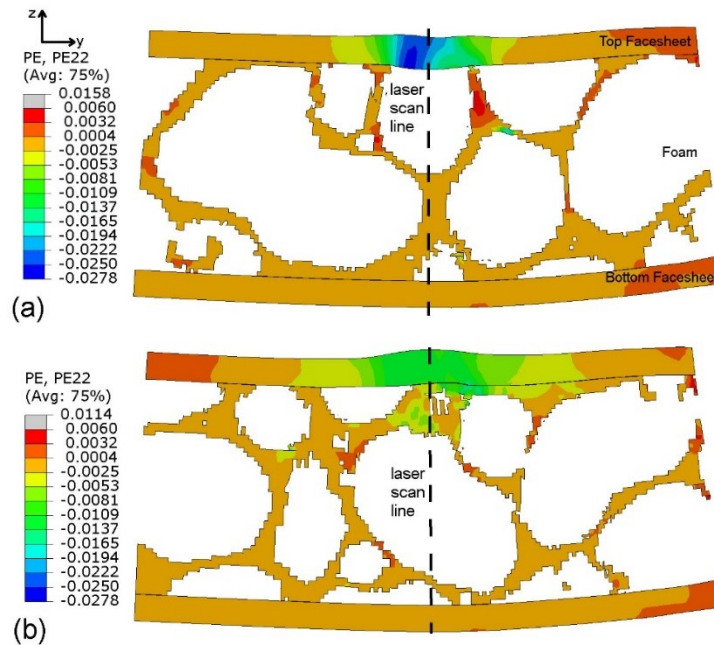


Fig. 92 Plastic strain distributions in y-direction in a type II sandwich panel after a laser scan at a large spot size ($D = 12$ mm, $v = 10$ mm/s), shown using a voxel model. The deformation was scaled by a factor of 10 for viewing clarity. The laser was scanned into the page, and the laser center was on the dashed line.

This effect can also be quantified using a Kelvin-cell model. In Fig. 93(a), the Kelvin-cell foam core was aligned such that most of the space underneath the top facesheet was occupied by cavities (representing case (a) from above). In Fig. 93(b), the Kelvin-cell foam core was aligned such that cell walls were located directly underneath the top facesheet (representing case (b) from above). All other parameters and geometrical properties were identical. The first scenario yielded a bending angle of 0.81° at the same condition as in Fig. 92, and the second scenario yielded a bending angle of only 0.73° . The simulation further yielded the same facesheet thickening behavior and plastic compressive strain distributions as the voxel models in Fig. 92.

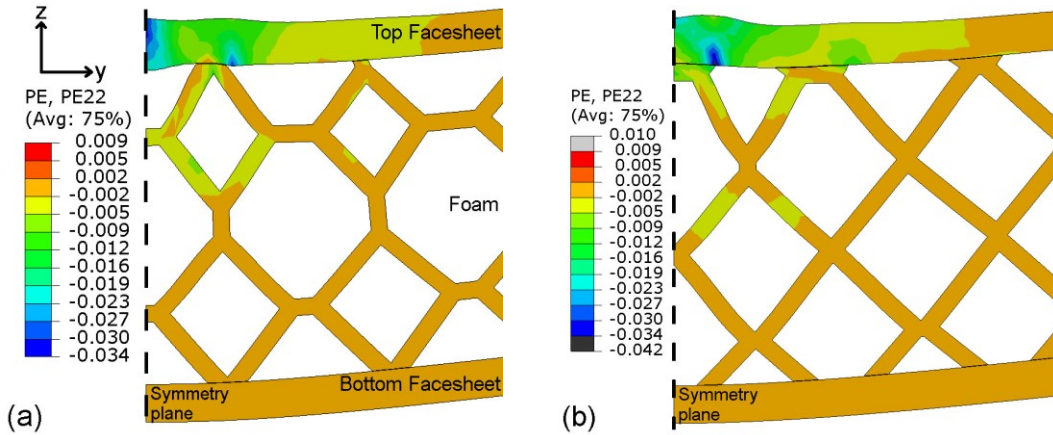


Fig. 93 Plastic strain distributions in y-direction in a Kelvin-cell sandwich model after a laser scan at a large spot size ($D = 12$ mm, $v = 10$ mm/s). Only half of the model is shown due to symmetry. In (a), the foam core was constructed such that cavities are underneath the top facesheet at the symmetry plane, whereas in (b) mostly cell walls are underneath the top facesheet. The remaining properties of both models are identical. The deformation was scaled by a factor of 10 for viewing clarity.

Overall, the previously shown results demonstrate that the foam structure of the type II restricts the downward expansion of the top facesheet. As a result, the top facesheet thickens mostly in an upward direction and bends less efficiently. This result is amplified at large laser spot sizes where the deformation region is large. Moreover, the maximum achievable bending

angle is reduced, because the upward facesheet thickening increases the overall sandwich panel thickness and renders the sandwich more resistant to bending deformation.

5.4.6 Importance of Facesheet Adhesion Quality

In the previous section it was shown that the foam core structure has a significant impact on the maximum achievable bending angle. The interface adhesion quality has an even greater impact on the bending limit. If the facesheets are completely bonded to the foam core via metallic diffusion bonds, large bending angles of 65° (type I sandwich panel) and 45° (type II sandwich panel) can be achieved, since laser forming does not cause any delamination. This fact can readily be accepted, looking at Fig. 91, where the adhesion between the facesheets and the foam core remained perfectly intact despite all the contortions of the top facesheet.

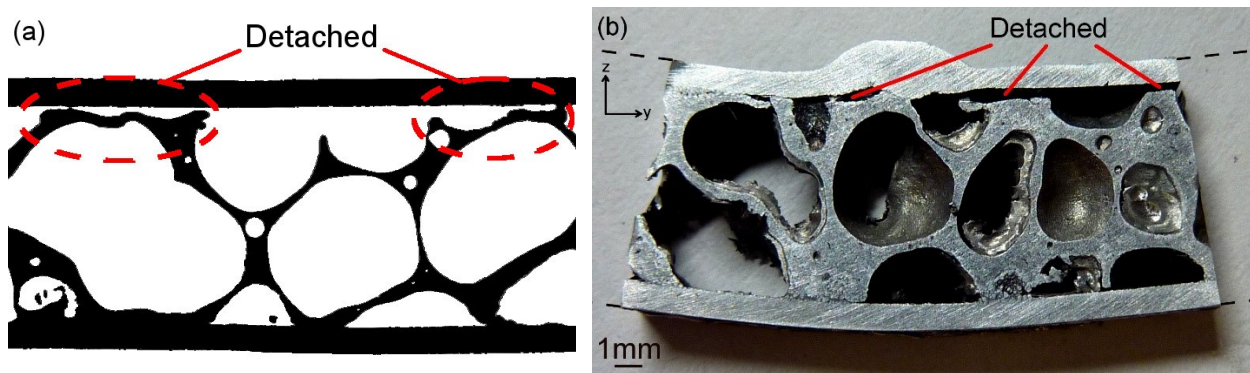


Fig. 94 (a) A cross-section of the type II sandwich panel, obtained using a micro-CT scan, shows that there are regions of detachment between the facesheet and the foam core. This detachment is detrimental to laser forming, since the maximum achievable bending angle drops from 45° to around 15° at a large spot size ($D = 12$ mm, $v = 10$ mm/s), shown in (b).

If, on the other hand, the facesheet adhesion is poor and there are regions of detachment after manufacture, the maximum achievable bending angle plummets. Pre-existing detachment has not been observed in the type I sandwich panel, as the adhesion quality is generally high due to the diffusion bonds being created during the formation of the foam core. In the type II sandwich panel, however, regions of pre-existing detachment do occur, as shown in Fig. 94(a). The reason why the type II sandwich is more prone to having pre-existing detachment is that the foam core

and the interfacial adhesion are created in separate steps. During cutting and handling the foam core might get locally damaged, so that it no longer is in contact with the facesheets during sintering. Gaps between the facesheets and the foam core may also occur if the pressure during the sintering step is not applied uniformly.

Given a situation with pre-existing detachment, the bending limit dropped from 45° (Fig. 91(d)) to merely 15° (Fig. 94(b)). Several factors are responsible for this significant drop in the bending limit. First, pre-existing detachment decreases the heat transfer from the top facesheet to the rest of the sandwich, reducing the temperature gradient in the foam core as well as its contribution to bending via the MTGM. Second, the bottom facesheet heats up less and undergoes less heat-induced softening. Finally, the top facesheet is completely unable to penetrate into the foam core. It was mentioned previously that the top facesheet penetrates less into the foam core in the type II sandwich panel than in the type I sandwich panel, but it still penetrates to some extent as can be seen in Fig. 91(d). In the detached case, however, the facesheet entirely thickens away from the foam core (positive z -direction), increasing the sandwich panel thickness and rendering it more resistant to bending deformation.

Numerical simulations again support the aforementioned arguments. Using an equivalent model, a case with perfect adhesion (Fig. 95(a)) was contrasted with a case where the top facesheet was detached from the foam core over half the beam spot size of $D = 12$ mm (Fig. 95(b)). In the detached case, the top facesheet underwent more heating and thus developed greater plastic compressive strains in y -direction. At the same time, the plastic compressive strain distribution in the foam core was reduced near the laser scan line, indicating less efficient bending via the MTGM [27]. The simulations also confirmed that the top facesheet only

thickened in an upward direction (positive z -direction) in the detached case, whereas it thickened in both directions in the intact case.

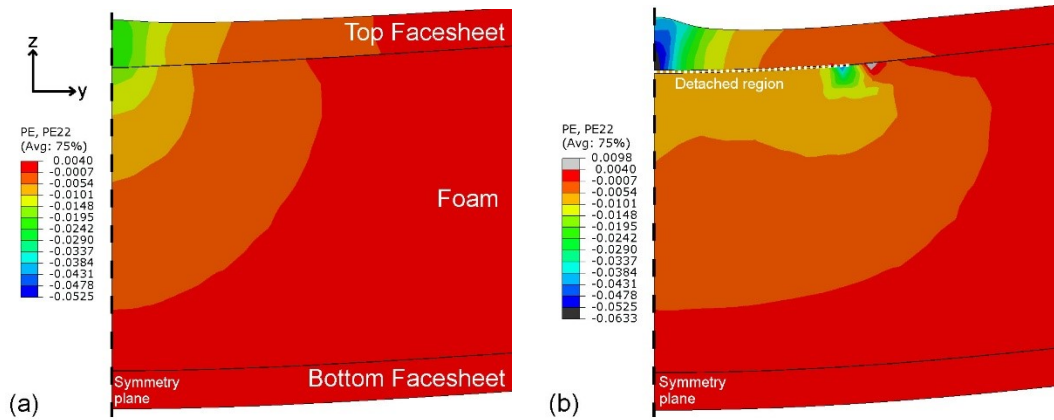


Fig. 95 Plastic strain distributions in y -direction after a laser scan at a large spot size ($D = 12$ mm, $v = 10$ mm/s). In (a), the adhesion between the top facesheet and the foam core is intact, whereas in (b) the top facesheet is detached from the foam core over a half the spot size of $D = 12$ mm. Only half of the model is shown due to symmetry. The deformation was scaled by a factor of 10 for viewing clarity.

5.4 Conclusions

This study comparatively studied the behavior of two types of sandwich panels with metal foam cores during laser forming. They differed in the facesheet type, foam core structure and composition, as well as the adhesion method. It was shown that the two sandwich panel types have a similar bending efficiency and bending limit when formed at small laser spot sizes ($D = 4$ mm). At large laser spot sizes ($D = 12$ mm) it was shown that type I sandwich panels bend at a much higher rate and achieve a higher bending angle.

Two major causes were identified for this discrepancy. First, it was shown that the type I facesheet bends at a higher rate, owing to its increased strength and stiffness. Second, it was demonstrated that the foam core structure determines how the top facesheet thickens during laser forming. In the type I sandwich panel, the top facesheet can penetrate into the foam core, allowing for a more efficient deformation via the upsetting mechanism. In the type II sandwich panel, on the other hand, the top facesheet mostly thickens away from the foam core, increasing

the overall thickness of the sandwich panel and rendering it more resistant to bending deformation.

Overall, this study demonstrated that a large variety of metal foam sandwich panel types can be laser formed, provided that the bond between the facesheets and the foam core is sufficiently strong to withstand the high temperatures and stresses that develop during the process. The bending efficiency and limit depend on the interactions between the panel properties and process conditions. Using the understanding developed in this study, potential applications in industry can be further explored.

Acknowledgment

The financial support from the National Science Foundation under a GOALI grant #CMMI-1725980 is gratefully acknowledged. Special thanks also go to Sam Robinson from the Bone Bioengineering lab at Columbia University for performing the micro CT scans, as well as to Connor Finn for proof reading the paper. This work used the Extreme Science and Engineering Discovery Environment (XSEDE) Stampede through allocation TG-DDM160002, which is supported by National Science Foundation grant number ACI-1548562 [75].

Chapter 6: 3D Laser Forming of Metal Foam Sandwich

Panels

6.1 Introduction

Throughout the past few decades, research studies have revealed that metal foam sandwich panels have an excellent stiffness, shock absorption capacity and strength-to-weight ratio [2,3]. Additionally, sandwich panels are more easily integrable in engineering structures than free-standing metal foam, and their metallic “facesheets” protect the foam core. Due to these favorable properties, numerous potential applications have been identified for the material [7,9]. Many of these applications have started becoming realizable thanks to the efforts of recent studies, showing that laser forming can successfully bend the material up to high angles without inducing failure [91,96]. These studies performed a detailed analysis of the process window, the laser-induced bending mechanisms, and the bending efficiencies and limits at different process conditions. The impact of the sandwich panel manufacturing method was also discussed. While a lot of ground has been covered, the work thus far has been limited to straight-line laser scans and shaping of Euclidean (2D) geometries. In industrial applications, however, non-Euclidean (3D) geometries are often necessary to meet design requirements. Karmann GmbH [2,72], for instance, is working on car body structures that are largely made of metal foam sandwich panels, due to their exceptional stiffness, reduced weight compared to steel panels, and vibration damping properties. There has also been talk about using metal foam sandwich panels as cone-shaped adaptors to support the payload in manned rockets [9], or as structural components in various intricately shapes airplane components, as discussed in Sec. 2.2.

Those concept studies considered two near-net-shape manufacturing methods for the industrial application of sandwich panels. The first method is based on powder metallurgy [9]; metal and foaming agent powders are compressed inside a mold that has the desired shape. The resulting precursor is placed between solid metal sheets, which have also been stamped to the desired geometry. The assembly is then heated near the metal melting point, causing the foaming agent to release a gas that turns the precursor into a foam. During foaming, the lateral expansion of the sandwich panel is restricted, giving rise to high pressures at the facesheet/foam core interface that promote the formation of metallic bonds. While being able to manufacture a wide range of shapes, this process is only economic for a large production volume because it requires several molds. Additionally, the part size must be small, due to the high cost of large dies, and the requirement of fitting the assembly into an oven. Another drawback is that the foam core cell distribution and density oftentimes becomes irregular during expansion and compression.

The second near-net-shape manufacturing method is 3D printing. Metal foam sandwich panels may either be 3D printed directly in the required shape, or a cast of the negative foam shape can be printed, out of which the foam can be cast [13]. Both approaches have the drawback that they are slow, can only manufacture relatively small parts, and are only applicable for low production volumes.

In order to overcome the aforementioned limitations, metal foam sandwich panels need to be manufactured in flat panels and subsequently be bent to the desired shape. Unfortunately, similar to 2D deformation, traditional bending methods are inherently unsuccessful at shaping 3D geometries. Hydroforming, for instance, causes severe foam crushing after forming sandwich panels into dome shapes [17]. Other traditional bending methods, such as die stamping [52], have not been attempted for 3D geometries, since they were unable to form 2D geometries

without significant defects. In this study, laser forming was investigated for 3D geometries, building upon the success of the method at shaping metal foam sandwich panels in 2D [91,96].

To date, 3D laser forming has only been investigated for sheet metal. Most of the effort has been spent generating two fundamental 3D shapes, which are the bowl and saddle shapes. The outcome of 3D laser forming experiments has been studied for a wide range of scan patterns, scan speeds, spot sizes, and powers [97-100]. Similarly, process synthesis has been studied in great detail, where the scan pattern and process conditions are determined using FEM based on a principal strain-based method [101,102]. However, it has never been attempted to bend metal foam sandwich panels into 3D geometries using lasers.

In this study, it was investigated whether laser forming of 2D Euclidean geometries can be extended to forming 3D non-Euclidean geometries. It was analyzed whether the fundamental knowledge that has been acquired for 2D laser forming regarding the bending mechanisms and the process window translates to 3D laser forming. Finally, it was investigated whether the numerical modeling techniques that were developed in previous studies [91,96] remain applicable when 3D laser forming is concerned.

6.2 Background

6.2.1 Laser Forming of Euclidean Geometries

Previous studies have shown that laser forming can successfully bend metal foam sandwich panels into Euclidean (2D) geometries using a series of parallel and straight scans [91,96]. Euclidean geometries, such as the channel geometry shown in Fig. 96, only require bending strains, which arise if the strain distribution through the sheet thickness is non-uniform. As shown in eq. (6.1), a bending strain vector $\underline{\varepsilon}_b$ develops if the minimum principal strain $\varepsilon_1^{s/2}$ at the top sandwich panel surface ($z = s/2$) differs from the minimum principal strain ε_1^0 at the mid-plane of the sandwich panel ($z = 0$)

$$\underline{\varepsilon}_b = \varepsilon_1^{s/2} \underline{n}_1^{s/2} - \varepsilon_1^0 \underline{n}_1^0 \quad (6.1)$$

where s is the sandwich panel thickness, and $\underline{n}_1^{s/2}$ and \underline{n}_1^0 are the directional vectors at the top surface and the mid-plane of the sheet, respectively [102]. The minimum principal strain is used instead of the maximum principal strain because laser forming mostly induces compressive deformation perpendicular to the scan path [27].

Laser forming can generate Euclidean geometries with very large amounts of deformation, and achieve bending angles up to 65° after repeated scans over single scan line. Additionally, small radii of curvature can be achieved, because the process shortens the top sheet segment relative to the bottom sheet segment, giving rise to large bending strains. The “shortening” is achieved through thermo-mechanical bending mechanisms that simultaneously occur in the top facesheet and the foam core. [91,96]. In the top facesheet, the bending mechanism depends on the process conditions. When the laser spot size is significantly smaller than the sandwich panel

thickness, the laser-irradiated material in the facesheet undergoes extreme heating, while the surrounding material remains at room temperature. As a consequence, the thermal expansion of the heated material is suppressed and converted to plastic compressive strain. This mechanism is well known as the temperature gradient mechanism (TGM) [22]. If, on the other hand, the laser spot size is equal to or greater than the sandwich panel thickness, the top facesheet heats up more uniformly. The thermal expansion is again converted to plastic compressive strain, due to the heated material being restricted by the surrounding material, causing a thickening of the top facesheet relative to the bottom facesheet. This mechanism is commonly referred to as upsetting mechanism (UM).

In the foam core, the bending mechanism responsible for the compressive shortening is independent of the process condition [27,91,96]. The compressive shortening is driven by temperature gradients, analogous to the TGM. However, the thermal expansion is not converted to plastic compressive strain as in the TGM. Instead, the thermal expansion causes cell wall bending and collapse, as postulated by the modified temperature gradient mechanism (MTGM).

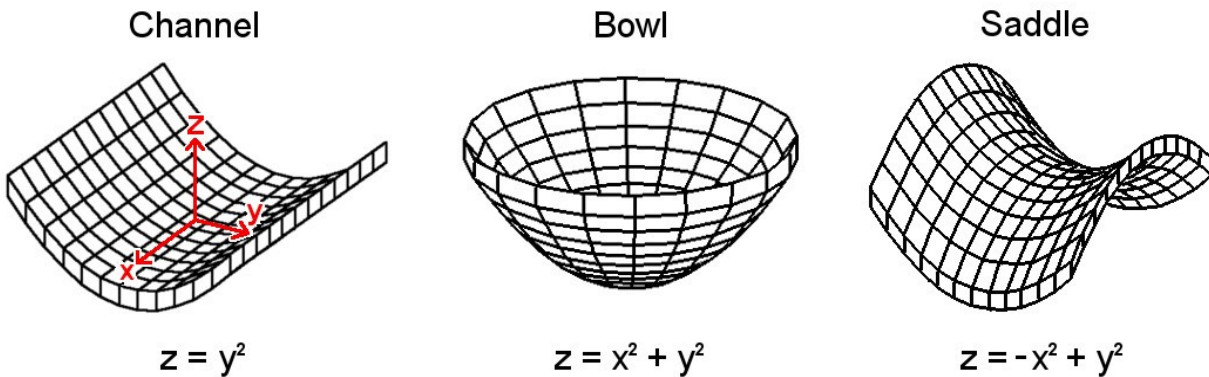


Fig. 96 The channel shape on the left is a Euclidean geometry. It can be obtained by bending strains alone, and the bending deformation is in the yz - plane. The bowl and saddle shapes are non-Euclidean geometries. Deforming a flat sheet into bowls and saddles requires both bending and in-plane strains, and the deformation occurs in three dimensions.

6.2.2 Shaping of Non-Euclidean Geometries

In many industrial applications, Euclidean (2D) geometries are not sufficient, and non-Euclidean (3D) geometries are required to realize design intents. Examples include airplane noses that could be used to protect aircraft against bird impacts [12], or airplane engine nacelles and car bodies [2]. Regardless of how complicated the 3D shape may be, it can be decomposed into the two fundamental non-Euclidean geometries, the bowl and saddle shapes (see Fig. 96). The airplane nose, for instance, has a distinct bowl shape, while the engine nacelle and car bodies consist of combinations of bowl and saddle shapes.

Unlike Euclidean geometries that have zero Gaussian curvature and only require bending strains, non-Euclidean geometries have a positive (e.g. bowl) or negative (e.g. saddle) Gaussian curvature. Hence, they require both bending strains as well as in-plane strains, especially if a large amount of deformation is required [101,102]. Mathematically, Euclidean shapes only include deformation in one direction such as the channel ($z = y^2$), while non-Euclidean shapes require shortening (e.g. bowl, $z = x^2 + y^2$) or stretching (e.g. saddle, $z = -x^2 + y^2$) of the entire material section in the second coordinate direction, as shown in Fig. 96. Whether laser forming is capable of inducing those in-plane strains was subject of this current investigation.

In order to specify scan patterns for the bowl and saddle shapes, inspiration was drawn from 3D laser forming of sheet metal. Several different approaches have been reported, depending on the complexity of the geometry. For simple geometries, such as the bowl shape, scan paths may be determined from laser forming principles. For all the bending mechanisms mentioned in Sec. 6.2.1 (TGM, UM, MTGM), compressive shortening is induced near the top surface, and the material bends about the laser scan line towards the laser. This knowledge can be used to devise straightforward scan patterns, such as radial [97] or circular scan patterns [98]. A radial pattern,

shown in Fig. 97(a), was used throughout Secs. 6.4.1 – 6.4.3, and contrasted with a circular scan pattern (Fig. 110) in Sec. 6.4.4. In both scan patterns, all the scans were performed on the top surface, represented by solid lines in Figs. 97(a) and 110. For the radial pattern, the scans were performed in an inward direction, terminating near the center of the specimen. The scans were initiated some distance away from the specimen edges to account for the delay between the laser shutter and the stage actuator. The scans were performed in the sequence indicated to allow for a smooth and more symmetric deformation of the entire specimen.

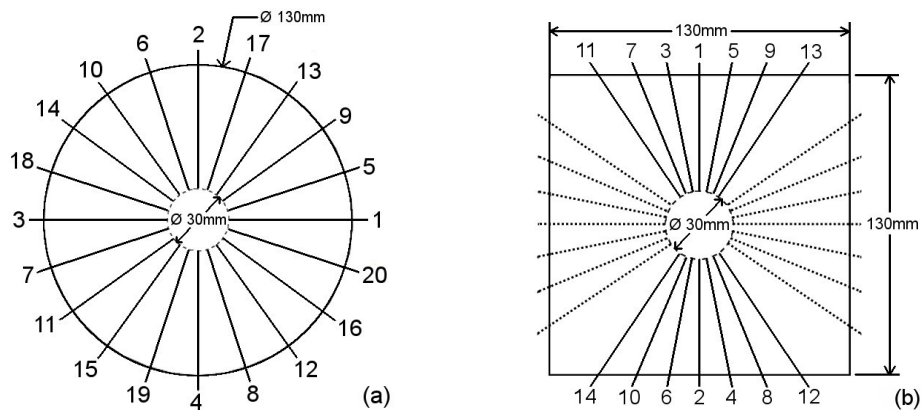


Fig. 97 Radial scan pattern that was used to obtain the (a) bowl shape and (b) saddle shape. Solid lines were performed on the top surface, dashed lines on the bottom surface. The numbering indicates the scan sequence. Scans were initiated on the outside and ended at the center. The diagrams apply for the condition of $D = 12$ mm and $v = 10$ mm/s. For $D = 4$ mm and $v = 30$ mm/s, the same overall area was treated, but the laser scans were closer together.

Using laser forming principles also allows for the determination of more complicated shapes such as the saddle shape, as was done in [99]. However, a more effective method of determining the scan paths for complicated shapes is process synthesis, which was briefly mentioned in the introduction [101,102]. In this approach, the desired geometry is modeled in FEM and compressed between rigid plates. Based on the resultant strain field, the scan paths can be drawn perpendicular to the directions of maximum plastic compressive strain. For a steel sheet of a thickness of 5 mm, this approach yielded a radial scan pattern [102] that was implemented in this study (see Fig. 97(b)) due to the high thickness of the sandwich panel of 10 mm. Since the

deformation is bi-directional, half of the scans were performed on the top surface (solid lines in Fig. 97(b)), and half of the scans were performed on the bottom surface (dashed lines in Fig. 97(b)). The scans were performed in an inward direction, terminating near the center of the specimen.

For the process conditions, the same overall approach was pursued as in 2D laser forming [91]. Using the hypothesis that the bending mechanisms are not vastly different (to be discussed in Sec. 6.4.3), it was assumed that 3D laser forming could be performed with the same two process parameter regimes that were mentioned in Sec. 6.2.1. In the first regime, the laser spot size of $D = 4$ mm was small compared to the sandwich panel thickness, and an elevated scan speed of $v = 30$ mm/s was employed. In the second regime, the laser spot size of $D = 12$ mm was slightly greater than the sandwich panel thickness, and a slower scan speed of $v = 10$ mm/s was used to maintain a constant area energy of 6.66 J/mm². The laser power was maintained at $P = 800$ W for both conditions.

6.2.3 Numerical Simulation

The same constitutive relations and overall modeling approach was used as in 2D laser forming of Euclidean geometries [91]. The facesheets were assumed to be incompressible and were modeled using Von Mises' yield criterion, Von Mises' flow rule, and isotropic (strain) hardening. Facesheet material properties were extracted from Ref. [94].

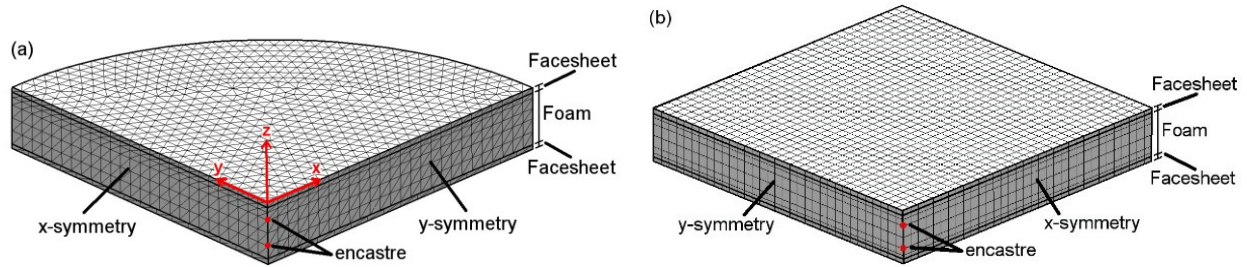


Fig. 98 (a) Bowl model and (b) saddle model. In both cases, only one quarter of the specimen was modeled, and an x and y symmetry was employed. Both models were fixed at two vertically aligned points using encastre constraints.

The foam was modeled using an “equivalent” modeling approach, which used a straightforward cylindrical and rectangular geometry for the bowl (Fig. 98(a)) and saddle (Fig. 98(b)) shapes, respectively. The foam behavior was modeled using the *crushable foam* constitutive model in ABAQUS. It was assumed that yielding can occur as a result of shear stresses, represented by Von Mises' equivalent stress σ_e in the following yield criterion, and in hydrostatic compression, represented by the mean stress σ_m

$$F = \left[\frac{1}{1 + (\alpha/3)^2} (\sigma_e^2 + \alpha^2 \sigma_m^2) \right]^{1/2} - Y \leq 0 \quad (6.2)$$

where α is the aspect ratio of the elliptical yield surface, and Y is the flow stress [41]. The deformation is elastic if $F < 0$ and plastic if $F = 0$. It was further assumed that the plastic strain increment is perpendicular to the yield surface pursuant Drucker's postulate, yielding the following flow rule

$$\dot{\varepsilon}_{ij}^p = \frac{\dot{Y}}{H} \frac{\partial F}{\partial \sigma_{ij}} \quad (6.3)$$

where $\dot{\varepsilon}_{ij}^p$ is the plastic strain rate, and H is the hardening modulus that is described by

$$H = \frac{\sigma_e}{\hat{\sigma}} h_\sigma + \left(1 - \frac{\sigma_e}{\hat{\sigma}}\right) h_p \quad (6.4)$$

where h_σ and h_p are the tangent moduli in uniaxial and hydrostatic compression, respectively, and $\hat{\sigma}$ is equal to the first term in the yield criterion. A detailed discussion of all the assumptions and their validity may be found in Refs. [26,27], along with a list of sources for the metal foam material properties.

The interface between the facesheets and the foam core was modeled using a cohesive layer. Due to the infinitesimal thickness of this layer, tractions and separations were used at the interface instead of stresses and strains. A linear traction-separation law was used

$$\begin{bmatrix} t_n \\ t_s \\ t_t \end{bmatrix} = \begin{bmatrix} K_{nn} & 0 & 0 \\ 0 & K_{ss} & 0 \\ 0 & 0 & K_{tt} \end{bmatrix} \begin{bmatrix} u_n \\ u_s \\ u_t \end{bmatrix} \quad (6.5)$$

where t is the traction, u the separation (jump discontinuity), and K the penalty stiffness. The subscripts n , s , and t refer to the normal, 1st and 2nd shear directions, respectively. A high stiffness of 850 GPa was assigned to the cohesive layer, so as to not affect the deformation behavior of the sandwich panel [49]. A temperature-dependent gap conductance relationship was used from Ref. [46], which is discussed in detail in Ref. [91].

Due to the large size of the specimens and the high number of laser scans, symmetry boundary conditions were assumed that allowed modeling a quarter of the bowl (Fig. 98(a)) and saddle (Fig. 98(b)) shapes. The symmetry boundary conditions assume no heat transfer across the symmetry plane, no translations perpendicular to the plane, as well as no out-of-plane

rotations. Unlike in 2D laser forming, symmetry boundary conditions induce some amount of error in 3D laser forming, since the problem is inherently asymmetric. However, the errors are relatively small and the predictions are still consistent with experimental values, as will be shown later. In addition to the symmetry boundary conditions, the specimens were anchored at two vertically aligned points at the center, marked in red in Fig. 98(a) and Fig. 98(b).

As will be discussed in Sec. 6.3, the sandwich panel showed substantial variations in the foam core thickness and density. To account for those variations and make a comparison with experiments possible, the thickness of each bowl and saddle model was adjusted to match the experimental average for that particular process condition. Changes in Young's Modulus, the flow stress, and the thermal conductivity with density were accounted for as well, using relations given in Ref. [27].

All the simulations were uncoupled into a thermal and mechanical part, which were performed subsequently, using the thermal results as initial condition for the mechanical analysis. In the bowl model, DC3D10/C3D10 elements were used for the facesheets/foam core, and DC3D6/COH3D6 elements were used for the cohesive layer in the thermal and mechanical analyses, respectively. In the saddle model, DC3D20/C3D20R elements were used for the facesheets/foam core, and DC3D8/COH3D8 elements were used for the cohesive layer in the thermal and mechanical analyses, respectively. An absorption coefficient of $A = 0.6$ was used for the thermal analysis, and all the simulations were performed in the FEM software ABAQUS.

6.3. Experimental Methods

The aluminum foam sandwich panel that was used in this study was manufactured using a powder-metallurgy technique by Havel Metal Foam GmbH. In this method, aluminum and foaming agent (TiH_2) powders are compressed, and the resulting precursor is sandwiched between solid metal “facesheets”. The assembly is then placed into an oven and heated near the metal melting temperature. The elevated temperatures cause the foaming agent to release hydrogen gas, which creates bubbles and turns the precursor into a foam. Simultaneously, the lateral expansion of the material is restricted, giving rise to substantial pressures that sinters the foam to the adjacent facesheets [9].

The facesheets were made of AW 5005, and their thickness was 1 mm. The foam core was made of AlSi10, and its thickness and density varied considerably, ranging between 8 – 10 mm and 500 – 650 kg/m^3 , respectively. The total sandwich panel thickness was between 10 – 12 mm. To account for the variations in the foam thickness and density, two experiments were performed for each condition per geometry, making sure that the average thickness and density were comparable.

The bowl specimens were cut to a diameter of 130 mm, while the saddle specimens were cut to squares with side lengths of 130 mm. Both specimen types were mounted at the center using a tapped hole. All specimens were painted with black graphite paint to increase the laser absorption. The specimens were laser formed using a CO_2 laser with a 1,500 W capacity and a wavelength of 10.6 μm . After each laser scan, the specimens were cooled to room temperature. The two process conditions that were contrasted were introduced in Sec. 6.2.2. Deflections were measured by attaching a dial indicator to a robotic stage. Cross-sections were cut using a diamond saw and polished using 1,200 grit sand paper before imaging.

6.4. Results & Discussion

6.4.1 Bowl Shape

Both process parameter regimes that were discussed in the background yielded a substantial amount of bending deformation, as shown in Figs. 99(a) and 99(b). For the regime employing the larger spot size of $D = 12$ mm, the scan pattern in Fig. 97(a) was used, which was repeated 8 times to obtain 160 scans. For the regime employing the smaller spot size of $D = 4$ mm, a denser line pattern with 50 scan lines was used. This modification was made based on the assumption that the bending mechanisms in 2D and 3D laser forming are similar (to be discussed in Sec. 6.4.3), and that consequently less bending deformation is induced per scan line at $D = 4$ mm. The 50 scan line pattern was repeated 6 times to obtain a total of 300 scans.

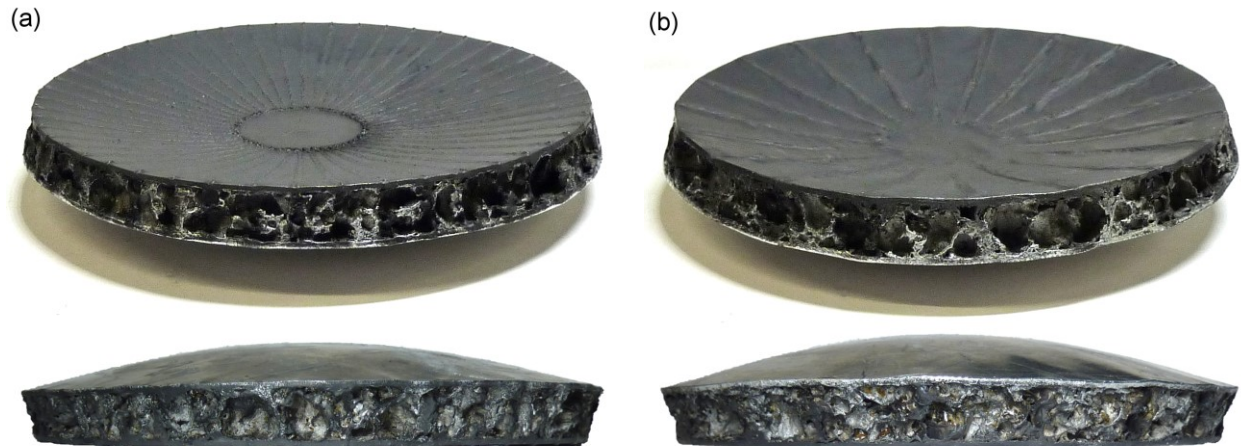


Fig. 99 Isometric and side view of bowl shape (a) after 300 scans at a laser spot size of $D = 4$ mm with scan speed of $v = 30$ mm/s, and (b) after 160 scans at a laser spot size of $D = 12$ mm with scan speed of $v = 10$ mm/s. The laser power was $P = 800$ W in both cases.

Despite using nearly half the scans, more bending was achieved at $D = 12$ mm than at $D = 4$ mm, as shown in Fig. 100. Hence, for the same area energy, the deformation is more efficient at $D = 12$ mm. The same result was obtained for Euclidean geometries in Ref. [91], where several factors were identified to explain this difference in the bending efficiency. It was shown that the upsetting mechanism (UM), which governs the deformation of the top facesheet at $D = 12$ mm,

induces plastic deformation over a larger region than the temperature gradient mechanism (TGM), which governs the deformation of the top facesheet at $D = 4$ mm. Similarly, it was shown that a larger segment of the foam core contributes to bending via the modified temperature gradient mechanism (MTGM) at $D = 12$ mm. Finally, it was shown that the bottom facesheet underwent more heat-induced softening at $D = 12$ mm, rendering the sandwich less resistant to bending deformation. In Sec. 6.4.3 it will be proven that all these factors are also valid for laser forming of non-Euclidean 3D geometries.

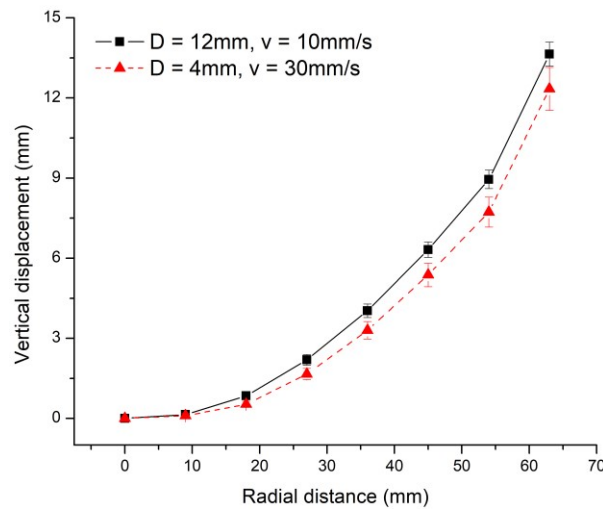


Fig. 100 Average radial deflection of the bowls in Fig. 99, shown with standard deviations. At a large spot size of $D = 12$ mm, a higher deflection was obtained even though the number of scans was lower than at a small spot size of $D = 4$ mm.

From Fig. 100, it can further be seen that the deviation in the bending deformation was slightly greater at $D = 4$ mm than at $D = 12$ mm. The same phenomenon was observed throughout the rest of the experimental results. Due to the localized plastic deformation occurring at $D = 4$ mm, the deformation of the top facesheet is more sensitive to the local foam structure, and hence the deviations in the bending results are greater.

The process was numerically simulated and a result is shown in Fig. 101. The simulation was carried out on a quarter of the circular specimen as shown in Fig. 98(a), and the visualization was based on mirroring the result in x and y – direction. The deflection was magnified by a factor

of 10 for viewing clarity, and only one iteration of the scan pattern in Fig. 97(a) was used. Despite using the symmetry constraints, laser scans lying on the symmetry planes yielded very similar plastic strain distributions as laser scans that were performed away from the symmetry planes.

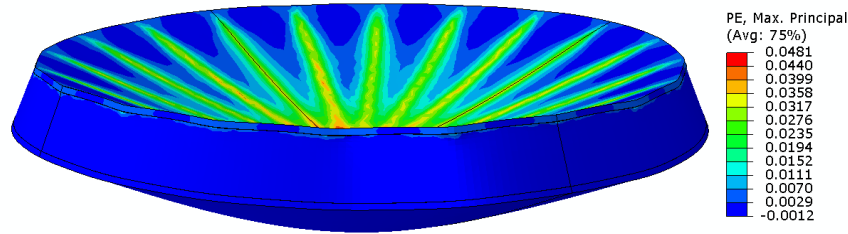


Fig. 101 Bowl shape predicted by the numerical model in Fig. 98(a), after performing one iteration of the scan pattern in Fig. 97(a). The model was mirrored in x and y - direction. The spot size was $D = 12$ mm and the scan speed was $v = 10$ mm/s. The deformation was magnified by a factor of 10 for viewing clarity.

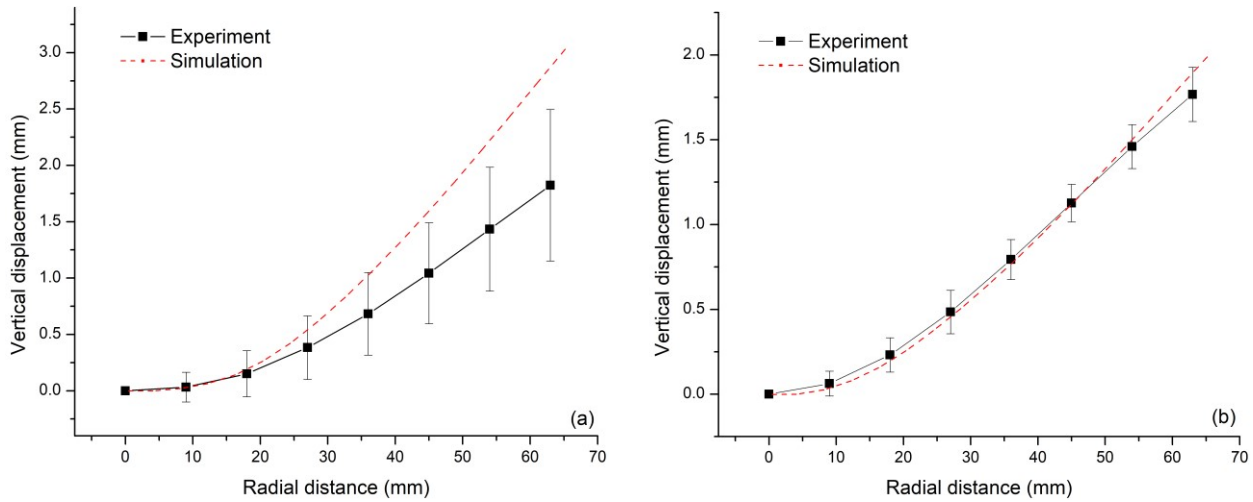


Fig. 102 Comparison of experimental and numerical deflections of the bowl shape at (a) a laser spot size of $D = 4$ mm with scan speed of $v = 30$ mm/s, and (b) a laser spot size of $D = 12$ mm with scan speed of $v = 10$ mm/s. One iteration of the scan pattern in Figs. 97(a) and 99(a) were performed. Average deflections and standard deviations are shown for the experimental data.

Only one iteration of the radial scan pattern in Figs. 97(a) and 99(a) was performed at the spot sizes of $D = 12$ mm and $D = 4$ mm, respectively. The experimental data was averaged over two specimens. The thickness and density of the foam core were set equal to the experimental average, and the density-dependent material properties were adjusted accordingly. At $D = 12$

mm, a good agreement was achieved, while at $D = 4$ mm, the simulation overestimated the deformation, especially near the specimen edge. The same trends were observed for 2D laser forming of Euclidean geometries [91], where it was shown that the overestimation at $D = 4$ mm can be attributed to localized melting and paint removal that occurred due to elevated temperatures. Both of these factors reduced the experimental bending deformation but were neglected in the simulation.

6.4.2 Saddle Shape

Laser forming of saddle shapes was equally successful at both $D = 4$ mm and $D = 12$ mm, shown in Figs. 103(a) and 103(b), respectively. At $D = 12$ mm, the pattern in Fig. 97(b) was used. This pattern of 28 scans was repeated 6 times, equating to a total of 168 scan, to allow for a meaningful comparison with the bowl shape in Fig. 99(a). At $D = 4$ mm, 48 scans were performed per iteration instead of 28 (12 per side instead of 7), due to the lower deformation per scan as discussed in Sec. 6.4.1. The laser treated area was the same as at $D = 12$ mm, maintaining the same distance between the outermost scans and the edges, but the scans were performed closer to one another because the deformation is more localized for this process condition. The scan pattern was repeated 6 times to obtain a total of 288 scans, which is again comparable to the number of scans used in forming the bowl shape in Fig. 99(b).

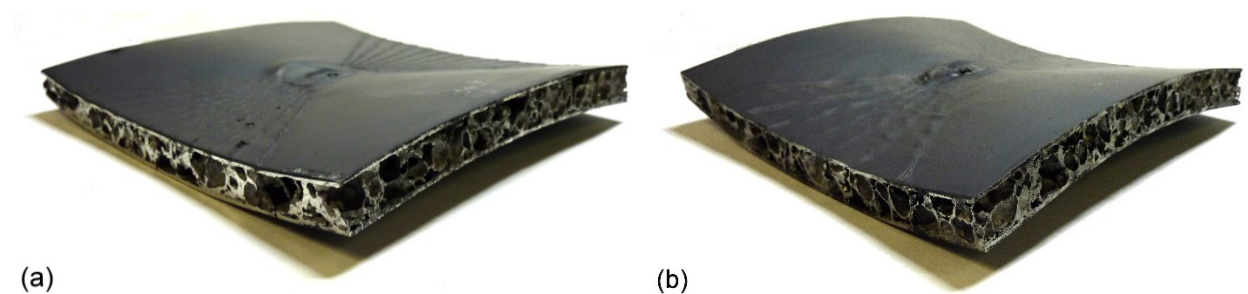


Fig. 103 Saddle shape (a) after 288 scans at a laser spot size of $D = 4$ mm with scan speed of $v = 30$ mm/s, and (b) after 168 scans at a laser spot size of $D = 12$ mm with scan speed of $v = 10$ mm/s. The laser power was $P = 800$ W in both cases.

Figure 104 shows the deflection of the outer edges (defined as *edge 1* and *edge 2* in Fig. 105), which were averaged over both sides. Just like for the bowl shapes, $D = 12$ mm yielded significantly more bending than $D = 4$ mm, despite being bent with fewer scans and using the same area energy. The reason for this behavior is the same as discussed in Sec. 6.4.1.

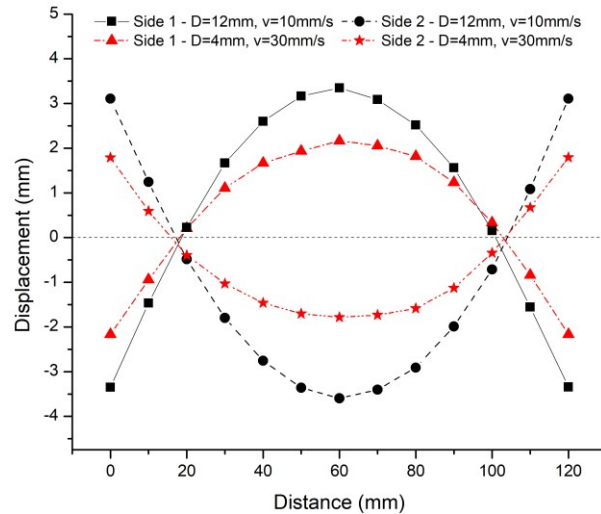


Fig. 104 Average deflection of the saddles in Fig. 103, measured at the outer edges marked as *edge 1* and *edge 2* in Fig. 105. The large spot size of $D = 12$ mm again yielded a higher amount of deformation than the small spot size of $D = 4$ mm.

Moreover, it is evident from Fig. 104 that the overall deflection in the saddle shape was smaller than in the bowl shape (Fig. 100). At $D = 12$ mm, for instance, the maximum deflection in the saddle shape was 6.7 mm, less than half the maximum deflection of 13.6 mm for the bowl shape. This discrepancy is due to the deformation taking place in two opposite directions. Particularly near the specimen diagonals, the material is simultaneously pulled in the positive and negative z – directions. Hence, the deformation induced by the top surface scans to some extent negates the deformation induced by the bottom surface scans and vice versa. This effect becomes less important as the specimen size and the distances between top surface and bottom surface laser scans are increased.

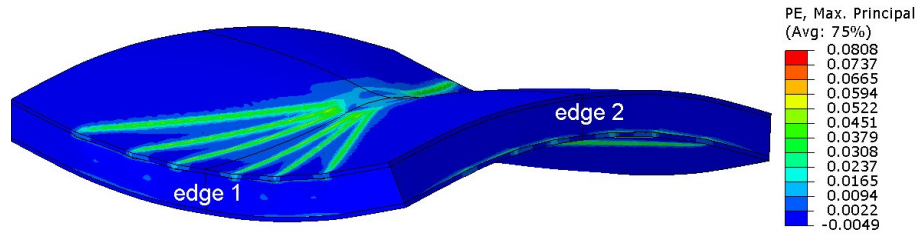


Fig. 105 Saddle shape predicted by the numerical model in Fig. 98(b) after mirroring the result in both x and y direction. The spot size was $D = 4$ mm and the scan speed was $v = 30$ mm/s. The deformation was magnified by a factor of 10 for viewing clarity. Only half the scans of Figs. 103 and 104 were modeled, skipping every other scan, to reduce the computational intensity.

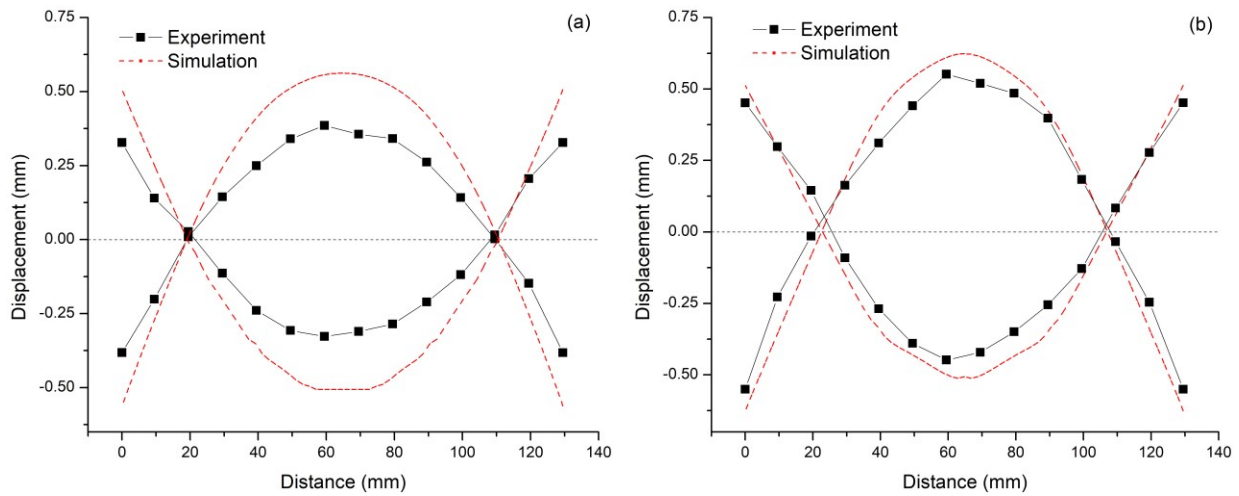


Fig. 106 Comparison of experimental and numerical deflections of the saddle shape at (a) a laser spot size of $D = 4$ mm with scan speed of $v = 30$ mm/s, and (b) a laser spot size of $D = 12$ mm with scan speed of $v = 10$ mm/s after one iteration of the scan pattern. Average deflections are shown for the experimental data.

Numerical simulations were capable of predicting the saddle shape, as shown in Fig. 105, with the aid of symmetry conditions. Due to the computational intensity of the saddle model (Fig. 98(b)), which were larger and required more elements than the bowl model, only every other scan line was modeled that is shown in Fig. 97(b). The plastic strain distribution in Fig. 105 again looks uniform on all scan lines, regardless of whether the laser scans were performed on or away from the symmetry planes.

The comparison with experimental data, shown for $D = 4$ mm and $D = 12$ mm in Figs. 106(a) and 106(b), respectively, again showed a better agreement at the latter condition. The

experimental results were averaged over two specimens for each condition, and the numerical models were adjusted for the foam core thickness and density. At $D = 4$ mm, the bending angles were again overestimated, due to the same reasons that were discussed in Sec. 6.4.1.

6.4.3 Bending Mechanism

In order to analyze the bending mechanism, the thermal and mechanical response of the metal foam sandwich panel was investigated during laser forming. All the results in this section were obtained for the bowl shape but are valid for the saddle shape as well.

The thermal response was analyzed using the numerical results in Fig. 107, which shows the temperature distribution that establishes across the sandwich panel as the laser passes the cross-section. At $D = 12$ mm, there is hardly any gradient across the top facesheet, implying that the thermal pre-requisites for the UM are met. At $D = 4$ mm, on the other hand, a steep temperature gradient established across the top facesheet, meeting the pre-requisites for the TGM. Across the foam core, there is a steep temperature gradient at both process conditions, satisfying the requirements of the MTGM. Hence, the thermal response of the sandwich panel suggests that the top facesheet and the foam core bend via separate bending mechanisms, which are the TGM/UM and the MTGM, respectively.

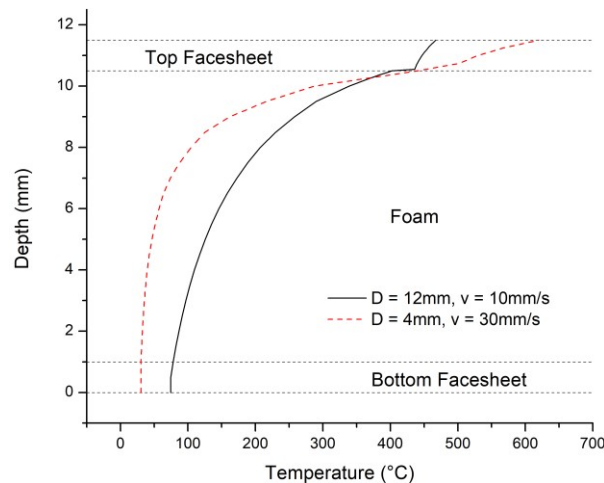


Fig. 107 Temperature distributions across the sandwich panel thickness right as the laser passes the cross-section, predicted by the numerical models. At $D = 12$ mm, there is hardly any gradient across the top facesheet, satisfying the thermal prerequisites for the UM. At $D = 4$ mm, there is a steep gradient across the top facesheet, satisfying the thermal prerequisites for the TGM. In both cases, there is a steep gradient across the foam, satisfying the thermal prerequisites for the MTGM.

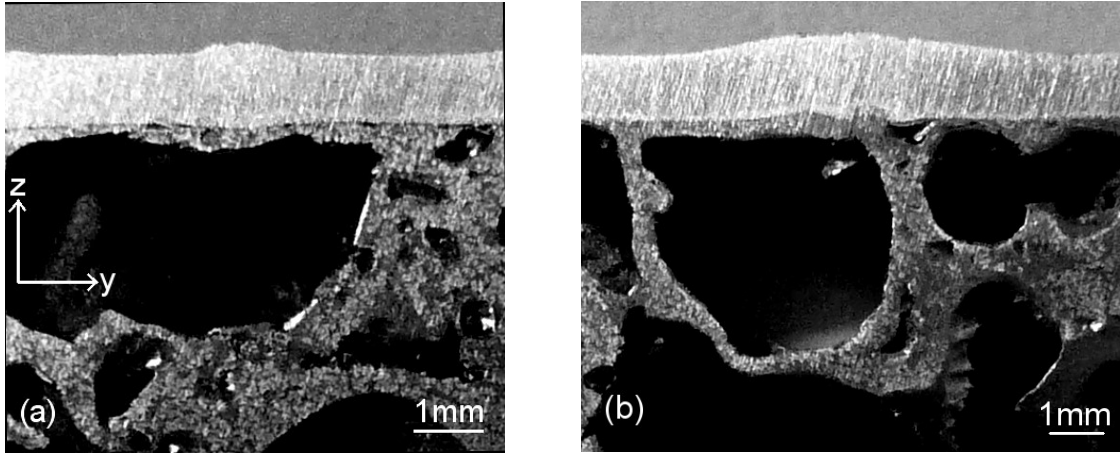


Fig. 108 Cross-sections cut perpendicular to the scan path at (a) $D = 4$ mm and $v = 30$ mm/s, and (b) $D = 12$ mm and $v = 10$ mm/s. The laser was scanned into the page. The cross-sections look very similar to cross-sections obtained in 2D laser forming [91].

To confirm the findings from the thermal analysis, cross-sections that were cut perpendicular to the laser scan direction were analyzed. At $D = 4$ mm (Fig. 108(a)), the top facesheet thickened slightly both into the foam core ($-z$ - direction) and away from the foam core ($+z$ - direction). The former is characteristic for the TGM, while the latter was also observed in 2D laser forming and was attributed to several factors [91]. First, the thermal expansion of the top facesheet during the laser scan is not suppressed, allowing the top facesheet to undergo some thickening in the negative z - direction. Second, the foam core densifies via the MTGM, leaving a void that needs to be filled by the top facesheet, leading to its thickening in the negative z - direction. Third, the foam core bends at a lower rate than the top facesheet, and thus limits the amount of tensile stretching the top facesheet can undergo on the bottom surface. This leads to a shear traction that the foam core exerts onto the top facesheet, which can also promote an expansion of the top facesheet into the foam core. At the larger spot size of $D = 12$ mm, whose cross-section is shown

in Fig. 108(b), the top facesheet also thickened in both directions similar to $D = 4$ mm. At the same time, the thickening occurred over a larger material section, which was shown to be characteristic for the UM [91].

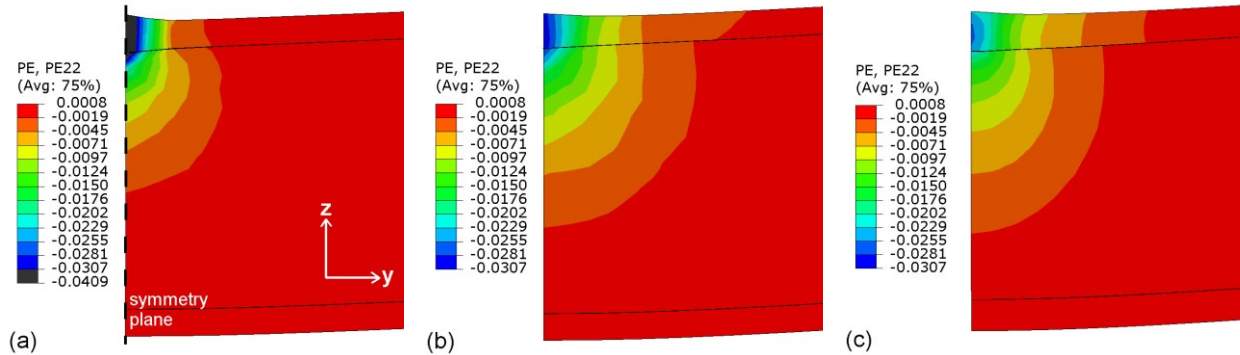


Fig. 109 Plastic strain distributions in y – direction (PE22) at a cross-section that is perpendicular to the laser scan at (a) $D = 4$ mm and $v = 30$ mm/s (3D case), and (b) $D = 12$ mm and $v = 10$ mm/s (3D case), and (c) $D = 12$ mm and $v = 10$ mm/s (2D case). The laser scan was performed on the symmetry plane, hence only half of the specimen is shown. The deformation was magnified by a factor of 10 for viewing clarity. The foam thickness differed between the 2D (c) and 3D (a,b) cases to reflect the experimental specimens used.

Numerical simulations confirmed the aforementioned findings. Figures 109(a) and 109(b) show the plastic strain distributions for $D = 4$ mm and $D = 12$ mm, respectively, at a cross-section in the yz - plane mid-way through the laser scan. Only half of the specimen is shown because the laser scan was located on the symmetry plane. It can be seen that a larger segment of the top facesheet underwent plastic compression at $D = 12$ mm than did at $D = 4$ mm, where the plastic compression was more localized near the scan line. This again confirms that the former case is governed by the UM while the latter is governed by the TGM. In the foam core, the plastic strain distribution was very similar to the distribution obtained in laser forming of freestanding metal foam [27], verifying that the MTGM was the governing mechanism. The bottom facesheet was again the only component that deformed due to the bending moment exerted by the top facesheet and the foam core, rather than a laser-induced bending mechanism.

Overall, the thermal and mechanical response of metal foam sandwich panels during 2D and 3D laser forming is nearly identical, both qualitatively and quantitatively. Qualitatively, the bending mechanisms are analogous, since the phenomena during 3D deformation shown in Figs. 107 – 109 are identical to those observed during 2D laser forming [91]. Quantitatively, nearly the same amount of plastic compressive strains are induced in 2D and 3D, as shown in Figs. 109(c) and 109(b), respectively.

The bending and in-plane strains required for 3D deformation as stated in Sec. 6.2.2 depend on process conditions. Laser spot sizes of $D = 4$ mm and $D = 12$ mm were considered. At $D = 4$ mm, the deformation in the top facesheet (TGM) and the foam core (MTGM) only involved bending strains, and a moderate amount of deformation was achieved, as shown in Figs. 99(b) and 103(b). At $D = 12$ mm, the bending strains in the top facesheet were largely replaced by in-plane strains (UM). Hence, the compressive shortening in the top facesheet was more efficient, and a slightly larger amount of deformation was achieved.

From the results in Figs. 107 - 109 it can also be concluded that in the absence of in-plane strains, deformation can still be induced, however, the amount of deformation increases considerably if the bending strains in the top facesheet are mostly substituted by in-plane strains. To obtain curvatures of greater magnitude than those in Figs. 99 and 103, in-plane strains need to be induced across the entire sandwich panel thickness, which cannot be achieved using laser forming.

6.4.4 Effect of Scan Line Length

One issue that becomes important, due to the high thickness of metal foam sandwich panels, is the length of the laser scan path. To investigate the effect of the scan length, a circular scan pattern shown in Fig. 110 was compared with the radial scan pattern shown in Fig. 97(a). To

allow for a meaningful comparison, a constant input energy was maintained. This was achieved by defining a circular scan pattern such that the overall scan length of the circular and radial scan patterns was identical for experiments of equal laser spot size. Several circular scan patterns with different spacings may satisfy this criterion, so no unique solution exists. Two scan patterns were investigated in this section. For the experimental results in Figs. 111 and 112, the pattern in Fig. 110 was used for the process condition of $D = 12$ mm and $v = 10$ mm/s, where the laser radii were $(R_1, R_2, R_3, R_4) = (30, 36.5, 43.1, 49.6)$ millimeters. At $D = 4$ mm and $v = 30$ mm/s, the same overall area was scanned, but more laser scan lines were employed that were more closely spaced with the radii $(R_1, R_2, \dots, R_{10}) = (30, 32.2, 34.4, 36.5, 38.7, 40.9, 43.1, 45.2, 47.4, 49.6)$ millimeters. For the numerical results in Figs. 113 and 114, on the other hand, a scenario was analyzed where the largest circular scan was only 10 mm away from the specimen edge. This scenario illustrated several points that could be used to explain the importance of the path length.

From Fig. 111 it can be seen that the circular scan pattern yielded significantly less bending than a radial scan pattern. Choosing a circular scan pattern with a larger spacing to the specimen edge increases the amount of bending, while a larger spacing decreases the amount of bending and can even cause delamination of the top facesheet.

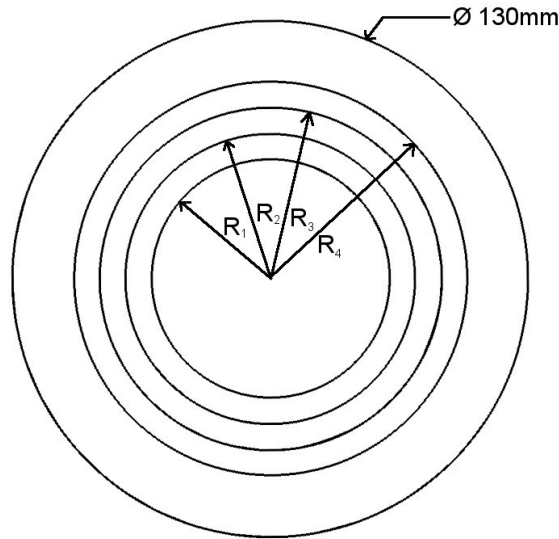


Fig. 110 Circular scan pattern that was used to obtain the bowl shape at $D = 12$ mm and $v = 10$ mm/s. The overall scan length is the same as in the radial scan pattern of Fig. 97(a). The radii are $R_1 = 30$ mm, $R_2 = 36.5$ mm, $R_3 = 43.1$ mm, $R_4 = 49.6$ mm. At $D = 4$ mm and $v = 30$ mm/s, the same overall area was treated, but 10 laser radii were used that were closer to one another.

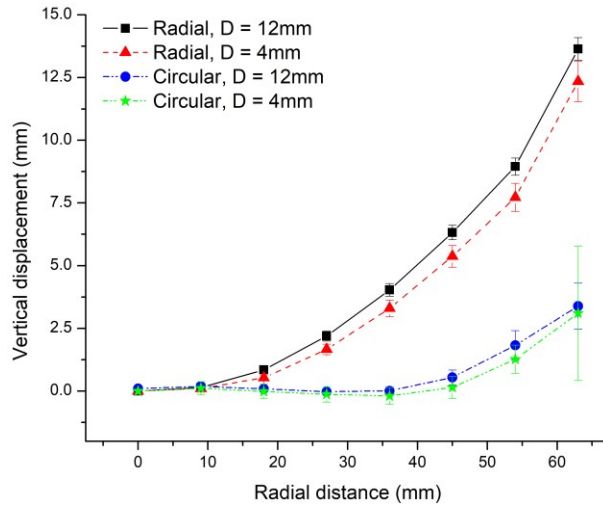


Fig. 111 Comparison between the average deflections of the bowl shape achieved using radial and circular scan paths. Standard deviation are shown. Much more deformation could be achieved using radial scan patterns.

In order to explain the difference between the deformation induced by the circular and radial scan patterns of equal energy input, the numerical results from Sec. 6.4.1 were compared with numerical results that were performed using a circular scan pattern (Fig. 112). The scan pattern used 4 concentric circles, where the outermost circle was very close to the specimen edge. No symmetry constraints were used in this simulation to capture the heat accumulation effects. The

process condition was $D = 12$ mm and $v = 10$ mm/s, and the overall scan length was the same as in the radial pattern.

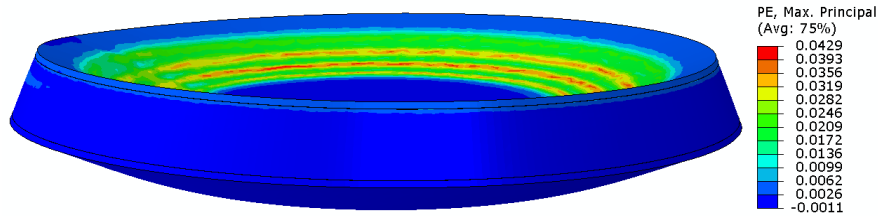


Fig. 112 Bowl shape obtained using a circular scan pattern. The spot size was $D = 12$ mm and the scan speed was $v = 10$ mm/s. The deformation was magnified by a factor of 10 for viewing clarity. The plastic strain magnitude is lower than when using a radial scan pattern (Fig. 101).

The temperature distributions were compared first, as shown in Fig. 113, during (a) a radial scan, (b) a circular scan far away from the specimen edge, and (c) a circular scan close to the specimen edge. For the circular scans, the temperature distributions are shown after $\frac{3}{4}$ of a revolution. Comparing scenarios (a) and (b), it is apparent that while little heat reaches the bottom surface in a radial scan, much more heat reaches the bottom surface in circular scans due to pre-heating of the material. Moreover, the temperature gradients are farther apart, and there is a longer “trail” where the material underwent significant heating. All of these factors imply that the temperature gradient in circular scans is smaller, and that the material surrounding the laser-irradiated material undergoes more heating. Hence, the thermal prerequisites of the bending mechanisms (TGM, UM, MTGM) are not satisfied. The thermal prerequisites are even more poorly satisfied when the circular scan is performed very close to the edge (Fig. 113(c)). The reason is that the gradients become even smaller, and the material surrounding the irradiated region undergoes even more heating.

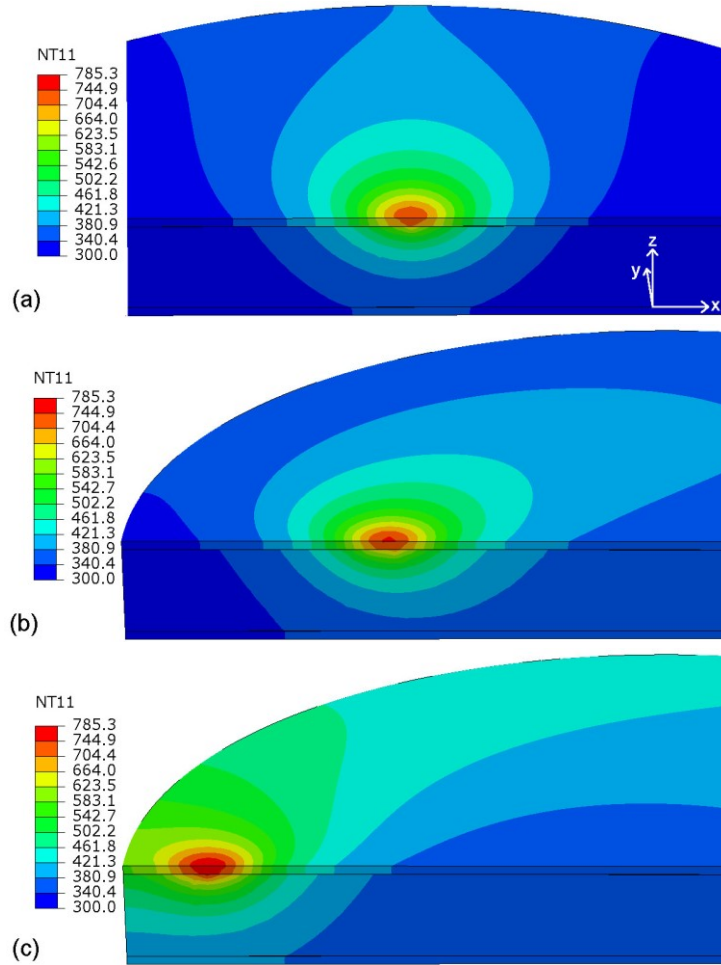


Fig. 113 Temperature distributions during (a) a radial laser scan, (b) a circular scan far away from the edge, and (c) a circular scan close to the edge. In circular scans, the temperature gradient is reduced, and the material surrounding the irradiated region undergoes more heating, especially if the scan is performed close to the edge.

How well the thermal prerequisites of the bending mechanisms are met translates into how much plastic compressive strain is generated. This becomes clear from Fig. 112, where the maximum plastic strain magnitude is significantly lower than in the radial case in Fig. 101. Figure 114 confirms this finding, showing the plastic strain distribution at a cross-section in the yz -plane at the center of circular specimen. Fig. 114(a) shows an asymmetric plastic strain distribution, generated from performing the outermost laser scan. By the specimen edge (left side), little plastic compressive strain developed both in the top facesheet and the foam core compared to the side that faces the center of the specimen (right side). The reason is that close to

the edge, the surrounding material underwent more heating and thermal softening, and consequentially allowed for more thermal expansion of the laser-irradiated material. Thus, a lower amount of the thermal strains in the laser-irradiated material turned into plastic compressive strains. Figure 115(b) confirms that as the distance to the edge increases (from the 1st to the 4th scan), the thermal prerequisite is better satisfied, and a higher amount of plastic compressive strain is generated.

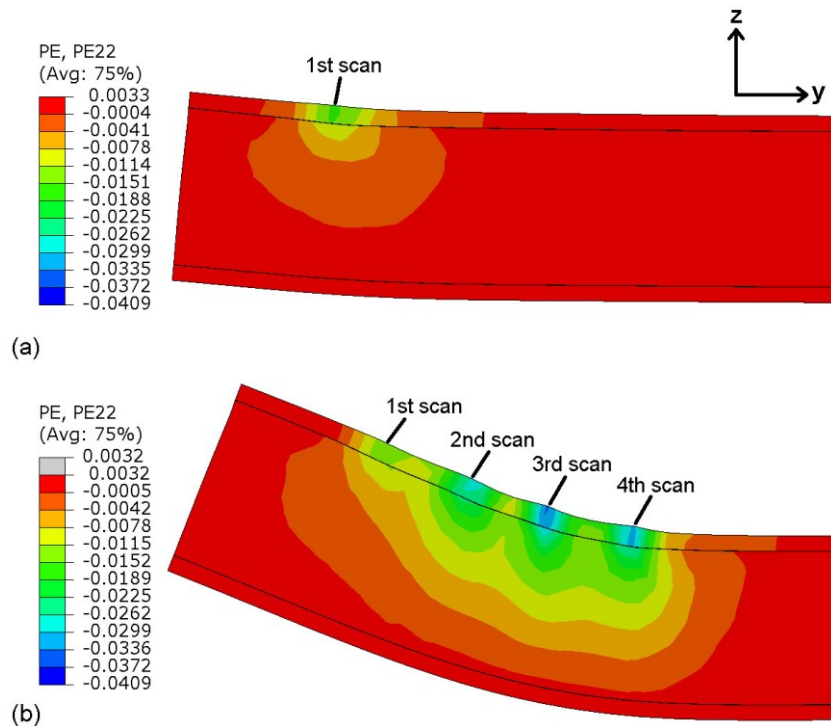


Fig. 114 Plastic strain distributions in y – direction after (a) a single laser scan close to the edge and (b) after 4 laser scans. The compressive strain increases with increasing distance from the edge, and its magnitude is higher on the side facing the center of the specimen.

In summary, it was shown that the scan path length becomes more important for metal foam sandwich panels, not because it changes the bending mechanisms, but because the thermal and mechanical prerequisites of the bending mechanisms are more difficult to satisfy. Especially for small specimens, the scan paths must be kept as short as possible.

6.5. Conclusions

This study demonstrated that laser forming could induce 3D deformation in metal foam sandwich panels. Both bowl and saddle shapes, the two fundamental non-Euclidean geometries, can be achieved under very different process conditions.

It was further shown that the mechanisms of laser-induced 3D bending are identical to laser forming of 2D geometries. At process conditions where the laser spot size is significantly smaller than the sheet thickness, only bending strains are present in the top facesheet and the foam core, and a moderate amount of deformation can be achieved. Increasing the laser spot size to the order of the sheet thickness converts most of the bending strains in the top facesheet to in-plane strains, and a slightly higher amount of deformation can be achieved. Even at large laser spot sizes, however, the 3D deformation is limited to moderate curvatures, because laser forming cannot induce in-plane strains throughout the entire sandwich panel section, which is necessary for producing large curvatures.

This study further showed that the choice of the scan path length is more important in metal foam sandwich panels than sheet metal, due to the larger thickness of the sandwich panels. The farther away laser scans are performed to the specimen edge, the better the thermal and mechanical pre-requisites of the laser bending mechanisms are satisfied, yielding more bending deformation. Lastly, this study demonstrated that accurate 3D bending predictions can be achieved in numerical simulations using the same modeling techniques that applied to 2D laser forming.

Acknowledgements

The financial support from the National Science Foundation under a GOALI grant #CMMI-1725980 is gratefully acknowledged. This work used the Extreme Science and Engineering Discovery Environment (XSEDE) Stampede through allocation TG-DDM160002, which is supported by National Science Foundation grant number ACI-1548562 [74].

Chapter 7: Conclusions

7.1 Laser Forming of Metal Foam

The work in this thesis made a significant contribution towards realizing the full potential of metal foam, a material that has been praised for its properties but that has failed to enter mass production thus far. Inspiration was initially drawn from a fellow research group that showed that lasers are capable of bending metal foams to large bending angles without causing failures. While still lacking in any conceptual understanding and predictive capabilities, the study demonstrated that it is possible to manufacture metal foam in simple shapes, such as flat panels, and bend the sheets to the required shapes.

Being inspired by all the possibilities that laser forming opens up, this work continued the experimental efforts and demonstrated that laser forming is also capable of bending metal foam sandwich panels to large bending angles without causing failures. It was shown that sandwich panels may be laser formed using two fundamentally different process parameter regimes. In the first regime, the laser spot size is significantly smaller than the sandwich panel thickness ($s/D > l$), while in the second regime the spot size is very close to the sandwich panel thickness ($s/D \sim l$). It was proven that the process window is not just limited to these two regimes, but encompasses all the laser spot sizes in between, provided the scan speed of laser power is adjusted to maintain a constant area energy. Lastly, it was shown that metal foam sandwich panels can be deformed into “3D” non-Euclidean geometries, such as bowl and saddle shapes. Overall, the experimental work made another tremendous amount of potential applications feasible that were purely in the conceptual realm before.

Throughout the remainder of the thesis, much effort was spent to go beyond the aforementioned parametrical study and develop a more fundamental understanding of the process. In order to do that, the thermo-mechanical bending mechanisms were analyzed that are responsible for the deformation of metal foam during laser forming. It was shown that a single bending mechanism is responsible for the deformation of metal foam. In metal foam sandwich panels, on the other hand, two bending mechanisms operate in tandem, one governing the deformation of the top facesheet and another governing the deformation of the foam core.

The thermal analysis of the bending mechanisms revealed that steep temperature gradients develop across metal foam, regardless of the process condition and whether the material is isolated or sandwiched between solid facesheets. Hence, from a thermal perspective, metal foam meets the pre-requisites postulated by the temperature gradient mechanism (TGM). The thermal analysis further showed that the bending mechanism governing the deformation of the top facesheet depends on the process condition. When the laser spot size is much smaller than the sandwich panel thickness ($s/D > 1$), steep gradients develop in the top facesheet, similar to the foam core, and the pre-requisites for the TGM are met. When the laser spot size is on the order of the sheet thickness ($s/D \sim 1$), on the other hand, there is hardly any temperature gradient across the top facesheet, and the thermal pre-requisites of the upsetting mechanism (UM) are met.

For the top facesheet, the mechanical analysis of the bending mechanisms confirmed the aforementioned findings. At a small laser spot size ($s/D > 1$), the plastic deformation in the facesheet was highly localized, and an increase in the facesheet thickness was obtained that is characteristic for the TGM. Similarly, at a large spot size ($s/D \sim 1$), a more wide-spread plastic

deformation was obtained, in combination with a uniform facesheet thickening in all directions, both of which are characteristic for the UM.

For the metal foam, on the other hand, the mechanical analysis revealed that the sheet metal bending mechanisms no longer hold. It was demonstrated that metal foam is unable to withstand high compressive stresses, since thin cell walls readily bend and cause cell collapse. From this result it was concluded that the plastic deformation in metal foam is achieved precisely through cell wall bending and cell crushing, as opposed to plastic compressive strains postulated by the TGM. This subtle yet important difference was summarized in a new bending mechanism, called the modified temperature gradient mechanism (MTGM), due to its similarity to the TGM.

The major consequence of the MTGM is that material densification occurs, a phenomenon that has not been observed in any “classic” laser forming bending mechanisms. Due to the densification, the thermal conductivity, Young’s Modulus and the flow stress increase, all of which reduce the driving force of the MTGM and cause a bending limit. Densification also reduces the compressibility of the material, however, due to the localized occurrence of densification the crushability of the material is hardly affected.

Throughout chapters 5 and 6, it was proven that the aforementioned bending mechanisms hold true regardless of the material manufacturing method and the deformation geometry (2D or 3D). While neither factors affect the nature of the bending mechanism, they affect the efficiency of the process, as well as the bending limit that can be achieved. If metal foam with extremely thick cell walls and large material accumulations between cavities is laser formed, cell crushing occurs less readily, dropping the efficiency of the MTGM. At the same time, the thickening of the top facesheet, a phenomenon that was attributed to the foam core/facesheet interaction, is impeded, again reducing the efficiency and bending limit that may be achieved.

Inducing deformations in 3D, such as bowl and saddle shapes, also reduces the overall achievable bending deformation. The reason is that laser forming is unable to induce in-plane strains throughout the entire sandwich panel section, which are required for large-scale 3D deformation. Nevertheless, a significant amount of deformation may be achieved, especially if large laser spot sizes are used that induce in-plane strains throughout the top facesheet.

7.2 Numerical Simulation of Laser Forming of Metal Foam

Besides the aforementioned experimental and conceptual work, a fundamental understanding was developed of how metal foam needs to be modeled, and how geometrical modeling affects the predictive capability. It was shown that accurate predictions can be made both with equivalent models, which are geometrically crude but accurately model the foam constitutive behavior, as well as explicit models that aim to replicate the foam geometry.

Equivalent models have the advantage of being simple to model and requiring fewer elements, which improves their CPU efficiency. At the same time, the models fail to accurately represent the laser absorption inside cavities, and also do not account for the tortuosity of the heat transfer path. In sandwich panels, equivalent foam cores overestimate the heat transfer between the facesheets and the foam core, requiring manual adjustment to account for the small contact area that exists in reality. From a mechanical standpoint, equivalent models make multiple assumptions such as isotropic behavior, symmetry of the yield surface, and isotropic hardening that are at the verge of oversimplification. Despite the abundance of assumptions and the limited accuracy in the thermal treatment, equivalent models were shown to be surprisingly accurate and predict experimental trends correctly.

Explicit models outperform equivalent models in the geometrical accuracy, particularly in the treatment of the thermal aspect. Due to their structure, the laser can penetrate into cavities, and the heat dissipation becomes tortuous due to the cellular structure. In sandwich panels, heat transfer between the top facesheet and the foam core is restricted due to the limited contact area, which again better corresponds with reality. The accuracy in the thermal treatment translates to the accuracy of the mechanical prediction as well. The bending angles predicted by the Kelvin cell model were slightly closer to the experimental values than the predictions of the equivalent model. Also, the high level of geometrical detail of the Kelvin-cell and in particular the voxel model was instrumental to develop a sound understanding of the bending mechanisms, particularly when it comes to the facesheet/foam core interaction in the sandwich panels. At the same time, the difference in predictive accuracy between explicit and equivalent models is relatively small, and oftentimes does not justify the extreme increase in CPU intensity that comes with the geometrical accuracy. In most cases, especially if multi-scan simulations are required, equivalent models provide sufficiently accurate predictions.

This thesis also investigated in great detail how the facesheet/foam core interface is to be modeled. In Abaqus, various paths lead to the same result, including a rigid connection, cohesive surfaces, or layers with cohesive elements. The first choice is often not desirable, as the extreme differences between the facesheet and foam core material properties can lead to convergence difficulties. The cohesive surface and element approaches are both based on traction-separation laws and accurately represent the sandwich panel behavior during laser forming. The cohesive element approach was used in this thesis, since it has the additional benefit of allowing the visualization of the damage progress (which ended up being redundant in this context though). It was shown that the sandwich panel behavior is only unaffected by the presence of the cohesive

layer if the layer stiffness is more than an order of magnitude greater than the stiffness of the joined layers.

7.3 Future Work

Overall, the work in this thesis delivered the theoretical, experimental and numerical groundwork, with which a more effective and versatile industrial implementation becomes possible. While the scope of this thesis project is comprehensive, some future work could be carried out.

First, a better understanding can be developed of how laser forming affects the material properties and structural attributes. Thus far, the impact of laser forming on the material properties was determined based on visual observation (experimentally) and densification plots (numerically). This work can be extended by performing various tests to quantify the impact of laser forming on the material properties. For instance, the 3D cell crushing behavior can be characterized more closely by taking a series of micro-CT scans at different levels of bending deformation. From this sequence of micro-CT scans, the development of the 3D strain fields can be determined using digital volume correlation (DVC), which in turn allows for the precise calculation of the cell crushing in 3D. Besides DVC, experiments can be performed to quantify changes in the material properties of the foam. Cylindrical coupons can be extracted from untreated and laser formed specimens, and compression tests can be performed to quantify losses in the crushability. Similarly, 4-point bending tests may be used to determine whether laser forming has a detrimental or beneficial impact on the bending stiffness and structural integrity. Additionally, cyclic tensile strength tests can be performed (within the linear regime) to investigate whether thermally-induced changes to the material properties affect the fatigue life of the material. In order to perform these tests, it would have to be ensured that a low number of

bending scans and small bending angles are used, to allow for a meaningful comparison with untreated specimens. Finally, experiments can be performed to quantify the changes in the material properties of the material that comprises the foam. This can be achieved by taking untreated and laser formed specimens, filling the cavities with resin, and puncturing the cell walls using a nano-indenter. From the test results, a comparison can be made of the hardness and the stress-strain curve for untreated cell walls and cell walls at varying distances from the laser, to determine how much laser forming causes hardening and embrittlement.

Second, the effect of the material composition and the facesheet adhesion method on the formability and bending mechanism can be investigated in more detail. A previous study has shown that the outcome of laser forming processes is strongly dependent on the material or alloy that comprises the foam [61]. Adding silicon carbide (SiC) as alloy element to aluminum, for example, rendered laser forming nearly impossible due to the significant drop in thermal expansion caused by SiC. Additionally, it can be investigated whether laser forming can bend sandwich panels in which the facesheets were bonded to the foam core using adhesives, which are currently the cheapest sandwich panels available. A successful bending result would allow for a significant reduction in the production cost, rendering numerous applications not just feasible but affordable.

Third, a subject requiring further study is the process synthesis of metal foam sandwich panels. For sheet metal, FEM-based methods were formulated based on thin-plate assumptions [56] to determine the required plain strain field, which in turn allows the synthesis of laser scan trajectory, power and speed. . Those assumptions no longer hold for metal foam, due to the large sheet thickness, and the algorithm needs to be revisited. A possible route is to extend the FEM-based methods to determine the required plain strain field in the top facesheet, which is relatively

thin, while additional algorithms are to be developed to determine the bending strain throughout the panel thickness. The synthesis then proceeds to determine process parameters to realize both strain fields.

A further advancement that could be carried out in the numerical simulations is to incorporate densification effects in the thermal analysis. In chapter 3, densification effects were already taken into consideration in the mechanical analysis by calculating the density as a field variable and providing density-dependent data for Young's Modulus and the flow stress. The same technique could be extended to the thermal analysis by providing density-dependent thermal conductivities. To update the thermal conductivity values with changes in density, one of two techniques may be chosen. In the first technique, the thermal and mechanical analyses are performed sequentially, i.e. the mechanical results are used as input to the next thermal analysis, whose results are used as input to the next mechanical analysis etc. Alternatively, the simulations can be performed in a coupled manner.

Finally, some changes in the laser processing parameters could be explored to increase the process window. For metal foams, it was shown that the process window is somewhat limited, and very specific area energies ought to be used. Area energies beyond the required value readily cause excessive melting, while area energies below the required levels do not cause any bending at all. The sensitivity of the process to the area energy might be reduced when pulsed lasers are used instead of continuous-wave lasers. Pulsed lasers might allow maintaining steep gradients while avoiding excessive thermal damage that is usually associated with high area energies. To achieve a better performance, the 3D shape of the laser may also be considered and potentially modified. Rather than focusing solely on the laser properties at the foam surface, the laser volume may be taken into account, since the laser is able to penetrate into the cavities of the

foam. In the simulation, the volumetric laser absorption could conveniently be modeled by employing a volumetric heat generation using the subroutine HETVAL.

References

- [1] Srivastava, V.C., and Sahoo, K.L., 2007, "Processing, Stabilization and Applications of Metallic Foams. Art of science," *Mater Sci-Poland*, 25(3), pp. 733-753.
- [2] Ashby, M.F., Evans, A.G., Fleck, N.A., Gibson, L.J., Hutchinson, J.W., and Wadley, H.N.G., 2000, *Metal Foams: A Design Guide*, Butterworth-Heinemann, Washington DC, USA.
- [3] Gibson, L.J., and Ashby, M.F., 1988, *Cellular Solids: Structure & Properties*, Pergamon, Oxford, UK.
- [4] Banhart, J., Cellular Metallic Material, www.metalfoam.net.
- [5] University of Gent, www.ugent.be.
- [6] Kremer, K., 2004, "Metal Foams for Improved Crash Energy Absorption in Passenger Equipment," Final Report for High-Speed Rail IDEA Program, Project 34, pp. 1-31.
- [7] Banhart, J., and Seeliger, H.W., 2012, "Recent Trends in Aluminum Foam Sandwich Technology," *Adv. Eng. Mater.*, 14(12), pp. 1082-1087.
- [8] Lu, T. J., and Chen, C., 1999, "Thermal Transport and Fire Retardance Properties of Cellular Aluminium Alloys," *Acta Mater.*, 47(5), pp. 1469–1485.
- [9] Banhart, J., and Seeliger, H.W., 2008, "Aluminium Foam Sandwich Panels: Manufacture, Metallurgy and Applications," *Adv. Eng. Mater.*, 10(9), p. 793.
- [10] Claar, T.D., Yu, C.J., Hall, I., Banhart, J., Baumeister, J., and Seeliger, W., 2000, "Ultra Lightweight Aluminum Foam Materials for Automotive Applications," SAE tech. pap. Ser., Detroit, MI, USA, pp. 1-9.
- [11] Hebsur, M., Noebe, R., and Revilock, D., 2003, "Impact Resistance of Lightweight Hybrid Structures for Gas Turbine Engine Fan Containment Applications," *J. Mater. Eng. Perform.*, 12(4), pp. 470-79.
- [12] Hanssen, A.G., Girard, Y., Olovsson, L., Berstad, L., and Langseth, M., 2006, "A Numerical Model for Bird Strike of Aluminium Foam-Based Sandwich Panels," *Int. J. Impact Eng.*, 32, pp. 1127-1144.
- [13] Kennedy, A., 2012, *Powder Metallurgy, Porous Metals and Metal Foams Made from Powders*, InTech, Rijeka, Croatia, Chap. 2.
- [14] American Elements, www.americanelements.com.

- [15] D’Urso, G., and Maccarini, G., 2011, “The Formability of Aluminum Foam Sandwich Panels,” *Int. J. Mater. Form.*, 5(3), pp. 243-57.
- [16] Zu, G.Y., Lu, R.H., Li, X.B., Zhong, Z.Y., Ma, X.J., Han, M.B., and Yao, G.C., 2013, “Three-point Bending Behavior of Aluminum Foam Sandwich with Steel Panel,” *Trans. Nonferrous Met. Soc. China*, 23(9), pp. 2491-2495.
- [17] Mata, H., Santos, A., Parente, M., Valente, R., Fernandes, A., and Jorge, N., 2013, “Study on the Forming of Sandwich Shells with Closed-cell Foam Cores,” *Int. J. Mater. Form.*, 7(4), pp. 413-24.
- [18] Steen, W.M., 1998, *Laser Material Processing*, Springer, London, UK.
- [19] Shen, H. and Vollertsen, F. (2009) ‘Modelling of laser forming – an review’, *Computational Materials Science*, Vol. 46, No. 4, pp.834–840.
- [20] Zhang, W., Liu, H., Shen, Z., Zhang, G., Ma, Y., and Wang, X., 2017, „Experimental Investigation on the Formation Behavior for Three-Layer Metal Sheets under Laser High Speed Flexible Micro-Forming“, *Int. J. Adv. Manuf. Technol.*, 93, pp. 3149-3157.
- [21] Edwardson, S.P., French, P., Dearden, G., Watkins, K.G., and Cantwell, W.J., “Laser Forming of Fibre Metal Laminates,” *Old City Publ.*, 15, pp. 233-255.
- [22] Geiger, M., and Vollertsen, F., 1993, “The Mechanisms of Laser Forming,” *CIRP Ann.*, 42(1), pp. 301–304.
- [23] Li, W., and Yao, Y. L., 2001, "Laser Bending of Tubes: Mechanism, Analysis, and Prediction," *J. of Manuf. Sci. Eng.*, 123(4), pp. 674-681.
- [24] Shi, Y., Yao, Z., Shen, H. and Hu, J., 2006, “Research on the mechanisms of laser forming for the metal plate,” *Int. J. Mach. Tools Manuf.*, 46(12–13), pp. 1689–1697.
- [25] Dowden, J., 2017, *The Theory of Laser Materials Processing*, Springer, New York, US.
- [26] Bucher, T., Bolger, C., Zhang, M., Chen, C., and Yao, Y.L., 2016, “Effect of Geometrical Modeling on Prediction of Laser-Induced Heat Transfer in Metal Foam,” *J. Manuf. Sci. Eng.*, 138(12), 121008.
- [27] Bucher, T., Young, A., Zhang, M., Chen, C.J., and Yao, Y.L., 2018, “Thermally Induced Mechanical Response of Metal Foam During Laser Forming,” *J. Manuf. Sci. Eng.*, doi: 10.1115/1.4038995.
- [28] Santo, L., Guglielmotti, A., and Quadrini, F., 2010, “Formability of Open-Cell Aluminium Foams by Laser,” *Proceedings of MSEC’10*, Erie, PA, USA, pp. 265-272.

- [29] Guglielmotti, A., Quadrini, F., Squeo, E.A., and Tagliaferri, V., 2009, "Laser Bending of Aluminum Foam Sandwich Panels," *Adv. Eng. Mater.*, 11(11), pp. 902-906.
- [30] Roohi, A.H., Naeini, H.M., Gollo, M.H., Soltanpour, M. and Abbaszadeh, M., 2015, "On the random based closed-cell metal foam modeling and its behavior in laser forming process," *Optics & Laser Technol.*, 72, pp. 53–64.
- [31] Yang, C.C., and Nakae, H., 2000, "Foaming Characteristics Control During Production of Aluminum Alloy Foam," *J. Alloys Compd.*, 313, pp. 188-191.
- [32] Sigworth, G. K., 2014, "Fundamentals of Solidification in Aluminum Castings," *Proc. of Am. Foundry Soc.*
- [33] Shankar, S., Riddle, Y.W., and Makhlouf, M.M., 2004, "Nucleation Mechanism of the Eutectic Phases in Aluminum–silicon Hypoeutectic Alloys," *Acta Mater.*, 52(15), pp. 4447-4460.
- [34] Haijun, Y., 2007, "Research on Acoustic, Mechanical and Other Properties of Closed-Cell Aluminum Foam," Ph.D. thesis, Northeastern University, Shenyang, Liaoning, China.
- [35] Sutton, M.A., Orteu, J.J., and Schreier, H.W., 2009, *Image Correlation for Shape, Motion and Deformation Measurements: Basic Concepts, Theory and Applications*, Springer, New York, NY.
- [36] Bastawros, A., Bart-Smith, H., and Evans, A.G., 2000, "Experimental Analysis of Deformation Mechanisms in a Closed-cell Aluminum Alloy Foam," *J. Mech. Phys. Solids*, 48(2), pp. 301-22.
- [37] Sutton, M.A., Yan, J.H., Tiwari, V., Schreier, H.W., and Orteu, J.J., 2008, "The Effect of Out of-plane Motion on 2D and 3D Digital Image Correlation Measurements," *Opt. Lasers Eng.*, 46(10), pp.746-57.
- [38] Bock, Jessica, and Anthony M. Jacobi. "Geometric Classification of Open-cell Metal Foams Using X-ray Micro-computed Tomography." *Materials Characterization* 75 (2013): 35-43.
- [39] Lorensen, William E., and Harvey E. Cline, 1987, "Marching Cubes: A High Resolution 3D Surface Construction Algorithm," *ACM SIGGRAPH Comp. Graph.*, 21(4), pp. 163-169.
- [40] Ulrich, D., B. Van Rietbergen, H. Weinans, and P. Rügsegger, 1998, "Finite Element Analysis of Trabecular Bone Structure: A Comparison of Image-based Meshing Techniques," *J. Biomech.* 31(12), pp. 1187-1192.

- [41] Deshpande, V., and Fleck, N., 2000, "Isotropic Constitutive Models for Metallic Foams," *J Mech. Phys. Solids*, **48.6**(7), pp. 1253-1283.
- [42] Ochsner, A., Murch, G. E., and De Lemos, M. J. S., 2008, *Thermal Properties Simulation and Prediction*, Wiley, Weinheim, Germany.
- [43] Li, W., and Yao, Y.L., 2000, "Numerical and Experimental Study of Strain Rate Effects in Laser Forming," *J. Manuf. Sci. Eng.*, **122**(3), p. 445.
- [44] Cheng, J., and Yao, Y.L., 2002, "Microstructure Integrated Modeling of Multiscan Laser Forming," *J. Manuf. Sci. Eng.*, **124**(2), pp. 379-388.
- [45] Parrinello, F, Failla, B., and Borino, G, 2009, "Cohesive-Frictional Interface Constitutive Model," *Int. J. Sol. Struc.*, **46**, pp. 2680-2692.
- [46] Skidmore, M., and Johnson, R., 1989, "Thermal Contact Conductance of Various Metals at Elevated Temperatures," *Proc. of 24th Thermophys. Conf.*, Raleigh, NC, USA, pp. 1-8.
- [47] Liu, D.H., and Shang, X.C., 2013, "The Physical-Mechanism Based High-Temperature Thermal Contact Conductance Model with Experimental Verification," *Chin. Phys. Let.*, **30**(3), p. 036501.
- [48] Dou, R., Ge, T., Liu, X., and Wen, Z., 2016, "Effects of Contact Pressure, Interface Temperature, and Surface Roughness on Thermal Contact Conductance between Stainless Steel Surfaces under Atmosphere Condition," *Int. J. Heat Mass Transfer*, **94**, pp. 156–163.
- [49] Turon, A., Davila, C.G., Camanho, P.P., and Costa, J., 2007, "An Engineering Solution for Mesh Size Effects in the Simulation of Delamination Using Cohesive Zone Models," *Eng. Fract. Mech.*, **74**(10), pp. 1665–1682.
- [50] Fuganti, A., Lorenzi, L., Hanssen, A. G., and Langseth, M., 2000, "Aluminium Foam for Automotive Applications," *Adv. Eng. Mater.*, **4**(2), pp. 200-204.
- [51] Davim, J. P., 2012, *Lasers in Manufacturing*, Wiley-ISTE, London.
- [52] Contorno, D., Filice, L., Fratini, L., and Micari, F., 2006, "Forming of Aluminum Foam Sandwich Panels: Numerical Simulations and Experimental Tests," *J. Mater. Process. Technol.*, **177**(1-3), pp. 364-367.
- [53] Li, W., and Yao, Y. L., 2001, "Laser Forming with Constant Line Energy," *Int. J. Adv. Manuf. Technol.*, **17**(3), pp. 196-203.
- [54] Cheng, J., and Yao, Y. L., 2001, "Cooling Effects in Multiscan Laser Forming," *SME J. Manuf. Processes*, **3**(1), pp. 60-72.

- [55] Cheng, P., Fan, Y., Zhang, J., Mika, D., Graham, M., Zhang, W., Marte, J., Jones, M., Yao, Y. L., 2006, "Laser Forming of Varying Thickness Plate – Part I: Process Analysis," *ASME J. Manuf. Sci. Eng.*, **128**, pp. 634-641.
- [56] Cheng, J., and Yao, Y. L., 2004, "Process Synthesis of Laser Forming by Genetic Algorithms," *Int. J. Mach. Tool. Manu.*, **44**(15), pp. 1619-1628.
- [57] Quadrini, F., Guglielmotti, A., Squeo, E. A., and Tagliaferri, V., 2010, "Laser Forming of Open-Cell Aluminium Foams," *J. Mater. Process. Technol.*, **210**(11), pp. 1517-1522.
- [58] Quadrini, F., Bellisario, D., Ferrari, D., Santo, L., and Santarsiero, A., 2013, "Numerical Simulation of Laser Bending of Aluminum Foams," *Key Eng. Mater.*, **554-557**, pp. 1864-1871.
- [59] Santo, L., Bellisario, D., Rovatti, L., and Quadrini, F., 2012, "Microstructural Modification of Laser-Bent Open-Cell Aluminum Foams," *Key Eng. Mater.*, **504-506**, pp. 1213-1218.
- [60] Quadrini, F., Bellisario, D., Ferrari, D., Santo, L., and Santarsiero, A., 2014, "Numerical Simulation of Laser Forming of Aluminum Sponges: Effect of Temperature and Heat Treatments," *Key Eng. Mater.*, **611-612**, pp. 731-738.
- [61] Zhang, M., Chen, C. J., Brandal, G., Bian, D., and Yao, Y. L., 2015, "Experimental and Numerical Investigation of Laser Forming of Closed-Cell Aluminum Foam," *ASME J. Manuf. Sci. Eng.*, **138**(2), p. 021006.
- [62] MacGregor, R. K., and Emery, A. F., 1969, "Free Convection Through Vertical Plane Layers – Moderate and High Prandtl Number Fluids," *ASME J. Heat Trans.*, **91**(3), p. 391.
- [63] Mukarami, T., Tsumura, T., Ikeda, T., Nakajima, H., and Nakata, K., 2007, "Anisotropic Fusion Profile and Joint Strength of Lotus-Type Porous Magnesium by Laser Welding," *Mater. Sci. Eng. A*, **456**(1-2), pp. 278-285.
- [64] Yilbas, B. S., Akhtar, S. S., and Keles, O., 2013, "Laser Cutting of Aluminum Foam: Experimental and Model Studies," *ASME J. Manuf. Sci. Eng.*, **135**(5), p.051018.
- [65] Randrianalisoa, J., and Baillis, D., 2014, "Thermal Conductive and Radiative Properties of Solid Foams: Traditional and Recent Advanced Modelling Approaches," *C. R. Phys.*, **15**(8-9), pp. 683-695.
- [66] Lu, T. J., and Chen, C., 1999, "Thermal Transport and Fire Retardance Properties of Cellular Aluminium Alloys," *Acta Mater.*, **47**(5), pp. 1469-1485.

- [67] Ma, M. Y., and Ye, H., 2014, “An Image Analysis Method to Obtain the Effective Thermal Conductivity of Metallic Foams via a Redefined Concept of Shape Factor,” *J. Appl. Therm. Eng.*, **73**(1), pp. 1277-1282.
- [68] De Giorgi, M., Carofalo, A., Dattoma, V., Nobile, R., and Palano, F., 2010, “Aluminium Foams Structural Modelling,” *Comput. Struct.*, **88**(1-2), pp. 25-35.
- [69] Mills, N. J., Stämpfli, R., Marone, F., and Brühwiler, P. A., 2009, “Finite Element Micromechanics Model of Impact Compression of Closed-cell Polymer Foams,” *Int. J. Solids Struct.*, **46**(3-4), pp. 677-697.
- [70] Spittel, T., Spittel, M., and Warlimont, H., 2011, *Non-ferrous Alloys – Light Metals*, Springer, Berlin, Vol. 2C2.
- [71] Bao, J., and Yao, Y. L., 2001, “Analysis and prediction of edge effects in laser bending,” *ASME J. Manuf. Sci. Eng.*, **123**, pp. 53-61.
- [72] Banhart, J., 2003, “Aluminum Foams: On the Road to Real Applications,” *MRS Bulletin*, **28**(4), pp. 290-295.
- [73] Reyes, A., Hopperstad, O.S., Berstad, T., Hanssen, A.G., and Langseth, M., 2003, “Constitutive Modeling of Aluminum Foam including Fracture and Statistical Variation of Density,” *Eur. J. Mech. A. Solids*, **22**(6), pp. 815-35.
- [74] Towns, J., Cockerill, T., Dahan, M., Foster, I., Gaither, K., Grimshaw, A., Hazlewood, V., Lathrop, S., Lifka, D., Peterson, G.D., Roskies, R., Scott, J.R., and Wilkins-Diehr, N., 2014 “XSEDE: Accelerating Scientific Discovery,” *Comput. Sci. Eng.*, **16**(5), pp. 62-74.
- [75] Nikanorov, S.P., Volkov, M.P., Gurin, V.N., Burenkov, Y.A., Derkachenko, L.I., Kardashev, B.K., Regel, L.I., and Wilcox, W.R., 2005, “Structural and Mechanical Properties of Al–Si Alloys Obtained by Fast Cooling of a Levitated Melt,” *Mater. Sci. Eng., A*, **390**(1-2), pp.63-69.
- [76] Mondal, D.P., Ramakrishnan, N., Suresh, K.S., and Das, S., 2007, “On the Moduli of Closed-cell Aluminum Foam,” *Scr. Mater.*, **57**(10), pp.929-32.
- [77] Brandal, G., and Yao, Y.L., 2016, “Dislocation Generation and Cell Formation as a Mechanism for Stress Corrosion Cracking Mitigation,” *ICALEO ‘16*, San Diego, CA, USA.
- [78] Edwardson, S.P., Abed, E., Bartkowiak, K., Dearden, G., and Watkins, K.G., 2006, “Geometrical Influences on Multi-pass Laser Forming,” *J. Phys. D: Appl. Phys.*, **39**(2), pp.382-89.

- [79] Sugimura, Y., Meyer, J., He, M.Y., Bart-Smith, H., Grenstedt, J., and Evans, A.G., 1997, "On the Mechanical Performance of Closed Cell Al Alloy Foams," *Acta Mater.*, 45(12), pp.5245-259.
- [80] McCullough, K.Y.G., Fleck, N.A., and Ashby, M.F., 1999, "Toughness of Aluminium Alloy Foams," *Acta Mater.*, 47(8), pp.2331-343.
- [81] Janssen, M., Zuidema, J., and Wanhill, R.J.H., 2004, *Fracture Mechanics*, DUP Blue Print, London, UK.
- [82] Blauel, J.G., 1985, "Ductile Fracture Material Characterization by J-R Curves," Proc. 4th Advanced Seminar on Fracture Mechancis, Ispra, Italy, pp. 117-143.
- [83] Han, M.S., Min, B.S., and Cho., J.U., 2014, "Fracture Properties of Aluminum Foam Crash Box," *Int. J. Automot. Technol.*, 15(6), pp. 945-51.
- [84] Crupi, V., Epasto, G., and Guglielmino, E., 2013, "Comparison of aluminium sandwiches for lightweight ship structures: honeycomb vs. foam," *Mar. Struct.*, 30, pp. 74-96.
- [85] Li, Z., Zheng, Z., Yu, J., Qian, C., and Lu., F., 2014, "Deformation and Failure Mechanisms of Sandwich Beams under Three-point Bending at Elevated Temperatures," *Compos. Struct.*, 111, pp. 285-90.
- [86] Hibbeler, R.C., and Vijay, K.S., 2013, *Mechanics of Materials*, Pearson Education, London, UK.
- [87] Chen, W., Hao, H., Chen, S., and Hernandez, F., 2015, "Performance of Composite Structural Insulated Panel with Metal Skin Subjected to Blast Loading," *Mater. Des.*, 84, pp. 194-203.
- [88] Camanho, P.P., Davila, C.G. and De Moura, M.F., 2003, "Numerical Simulation of Mixed-Mode Progressive Delamination in Composite Materials," *J. Compos. Mater.*, 37(16), pp. 1415-438.
- [89] Wang, H., Yao, Y.L., and Chen, H., 2015, "Removal Mechanism and Defect Characterization for Glass-Side Laser Scribing of CdTe/CdS Multilayer in Solar Cells," *J. Manuf. Sci. Eng.*, 137(6), 061006.
- [90] Bartkowiak, K., Dearden, G., Edwardson, S.P., and Watkins, K.G., 2004, "Development of 2D and 3D Laser Forming Strategies for Thin Section Materials Using Scanning Optics," Proceedings of the ICALEO 23', San Francisco, California, 97, paper # 559.
- [91] Bucher, T., Cardenas, S., Verma, R., Li, W., and Yao, Y.L., 2018, "Laser Forming of Sandwich Panels with Metal Foam Cores," *J. Manuf. Sci. Eng.*, accepted.

- [92] Raj, S.V., Ghosn, L.J., Lerch, B.A., Hebsur, M., Cosgriff, L.M., and Fedor, J., 2007, "Mechanical Properties of 17-4PH Stainless Steel Foam Panels," *Mat. Sci Eng. A*, **456**(1-2), pp. 305-16.
- [93] Abawi, A.T., 2004, "The Bending of Bonded Layers Due to Thermal Stress," Malibu, CA, Hughes Research Laboratories.
- [94] Spittel, T., Spittel, M., and Warlimont, H., 2011, *Non-ferrous Alloys – Light Metals Vol.VIII/2C2*, AlMg1, Springer, Berlin, Germany, doi: 10.1007/978-3-642-13864-5_53.
- [95] Spittel, T., Spittel, M., and Warlimont, H., 2011, *Non-ferrous Alloys – Light Metals Vol.VIII/2C2*, Al 99.7, Springer, Berlin, Germany, doi: 10.1007/978-3-642-13864-5_31.
- [96] Bucher, T., Zhang, M., Chen, J.J., Verma, R., Li, W., and Yao, Y.L., 2018, "Laser Forming of Metal Foam Sandwich Panels: Effect of Manufacturing Method," *J. Manuf. Sci. Eng.*, submitted.
- [97] Tavakoli, A., Naeini, H.M., Roohi, A.H., Gollo, M.H., and Shahabad, S.I., 2017, "Determining Optimized Radial Scan Path in 3D Laser Forming of Steel AISI 304 Plates to Produce Bowl Shapes," *Int. J. Adv. Manuf. Technol.*, **91**, p. 3457-3465.
- [98] Tavakoli, A., Naeini, H.M., Roohi, A.H., Gollo, M.H., and Shahabad, S.I., 2017, "Optimization of Circular Scan Path to Produce Bowl Shapes in 3D Laser Forming Process," *J. Laser App.*, **29**(4), p. 042001.
- [99] Edwardson, S.P., Watkins, K.G., Dearden, G., and Magee, J., 2001, "3D Laser Forming of Saddle Shapes," *Proceedings of the LANE '01*, Erlangen, Germany, pp. 559-568.
- [100] Edwardson, S.P., Moore, A.J., Abed, E., McBride, R., French, P., Hand, D.P., Dearden, G., Jones, J.D.C., and Watkins, K.G., 2004, "Iterative 3D Laser Forming of Continuous Surfaces," *Proceedings of the ICALEO '04*, San Francisco, California, **97**, p. 1-10.
- [101] Cheng, J., and Yao, Y.L., "Process Design of Laser Forming for Three Dimensional Thin Plates," *J. Manuf. Sci. Eng.*, **126**(2), pp. 217-225.
- [102] Liu, C., and Yao, Y.L., 2005, "FEM-Based Process Design for Laser Forming of Doubly Curved Shapes," *J. Manuf. Proc.*, **7**(2), pp. 109-121.

Appendix

This appendix contains information on where to find relevant archived files and how to run simulation files. The thesis may be found in folder “\1) Thesis”, and the proposal and defense presentation may be found in “\2) Presentation”. All the numerical files may be found in the folder “\3) Numerical Models”, which itself contains five sub-folders, three of which are related to the work mentioned in this thesis.

Chapter 2

All the models that were used in chapters 2 are located in the sub-folder “\3) Numerical Models\Foam”. There are three types of models in this folder, *equivalent models*, *Kelvin models*, and *voxel models*. Each of these folders contains a thermal analysis that was used in chapter 2. The thermal files are run by creating a job (or specifying job = thermal.inp), in which the subroutine file *dflux* is specified. This subroutine can be found in many subfolders, as well as in Sec. 1.6.6.1, both for straight laser scan lines as well as circular laser scan lines.

Chapter 3

The “\3)...Foam\Equivalent Model” and “\3)...Foam\Kelvin Model” folders contain the mechanical analyses that were used in chapter 3. The mechanical analyses were performed after the thermal analysis, i.e. the output of the thermal analysis was used as a predefined field in the mechanical part. This of course implies that the .odb file of the thermal analysis must be present. On your personal computer, the .odb file must be in the *temp* folder or wherever your computer puts output files, on the supercomputer the thermal .odb file must be located in the same folder in which you run the mechanical analysis. The mechanical model is run like any other simulation, by creating a job or using job = mechanical.inp.

The “(3)...Foam\Equivalent Model” folder also contains two different mechanical models, one including density-dependent material properties, the other containing density-independent material properties. Both were used in chapter 3. For a low amount of laser scans, the error induced by using density-independent material properties is negligible. For large bending angles and a large number of scans, I recommend using density-dependent material data for increased accuracy. The density-dependent properties are Young’s Modulus, the thermal conductivity, and the flow stress. Both density dependent and independent data may be found in the file *compiled material data.xlsx* in the folder “(4) What everybody ... (11) Material Properties”. The files *Material Properties Instructions.docx* and *Overview of properties, sources and assumptions.xlsx* give a detailed instruction of the origin of every single material property, along with the assumptions that went into their definition. Sources and references for the equivalent and explicit material properties may be found in the subfolder “(4)... (11)... Type I Foam Core”.

Instructions on how to run these analyses on the supercomputing facility XSEDE may be found in the folder “(4) What everybody ... (3) XSEDE application & procedure”. The folder contains example slurm files in the file *Example slurm file.docx*, along with detailed instructions in *XSEDE Instructions.docx*, *XSEDE Checklist2.docx*, and *XSEDE in a Nutshell.docx*.

Chapter 4

All the simulations pertaining to chapter 4 may be found in “(3) Numerical Models\Sandwich\Chapter 4”. There are two different types of numerical models. First, there is an *Equivalent sandwich model*, whose metal foam core is made using the equivalent approach. The folder again contains a thermal and a mechanical part. There are two different subroutines, one for the spot size of $D = 4$ mm, the other for the spot size of $D = 12$ mm. Please note that these subroutines both contain *dflux*, specifying the laser shape, as well as *gapcon*, which

specifies the gap conductance across the facesheet/foam interface (discussed in detail in Sec. 1.6.6.4). Second, there is a *Kelvin sandwich model*, whose metal foam core is made of a Kelvin cell model. The folder contains a thermal and mechanical part, and the subroutines are given for both spot sizes. Please note that there are two parts to the mechanical analysis, a part 1 and part 2. The reason is that the mechanical part takes more than 48 hours to complete on XSEDE, and the analysis has to be restarted.

How analyses are restarted is discussed in “(4) What everybody ... (3) XSEDE application & procedure”. *Restart1.inp* gives an example in which an analysis is restarted that was terminated mid-way through a step. *Restart2.inp* gives an example in which an analysis is restarted, and a separate new step is added to the analysis. Detailed instructions on how to modify the slurm file for restart jobs can be found in the file *Example slurm file.docx*.

The material properties of the foam core and the facesheet can be found in the file *Compiled material data.xlsx* in “(4)... (11) Material Properties”. The sources for the foam core are in the folder *Type I Foam Core*, and the sources for the facesheet are in the folder *Type I Facesheet (AW 5005 – AlMg1)*.

Chapter 5

All the simulations pertaining to chapter 5 may be found in “(3) Numerical Models\Sandwich\Chapter 5”. There are three sub-folders. The first sub-folder *Different Facesheet* contains the thermal and mechanical analysis of an equivalent sandwich panel model, in which the facesheet properties were changed to the Type II properties. I used this model to identify the impact of the facesheet properties (while leaving everything else constant). The second sub-folder *Type I Voxel Model* contains the thermal and mechanical voxel models of the type I sandwich panel. The third sub-folder *Type II Voxel Model* contains the thermal and

mechanical voxel models of the type II sandwich panel. The voxel models were created with the Matlab code that is explained in detail in the sub-folder “(4) What everybody...(5) Matlab code to create voxel model”.

The material properties for the type II sandwich panel can be found in the file *Compiled material data.xlsx* in “(4)...(11) Material Properties”. The sources for the foam core and facesheet are in the folder *Type II Facesheet & Foam Core*.

Chapter 6

All the simulations pertaining to chapter 6 may be found in “(3) Numerical Models\Sandwich\Chapter 6”. There are three types of models in this folder. First, there are models of the bowl specimen in *Bowl Radial*, which were scanned using a radial scan pattern. Only a quarter of the bowl is modeled due to symmetry. Once again there is a thermal and mechanical part. The fortran subroutine defining the radial scan pattern is *Bowl_D4_symmetry.for* at $D = 4$ mm, and the corresponding simulation for the spot size of $D = 12$ mm is *Bowl_D12_symmetry.for*. The radial pattern was created and drawn using *turtle graphics* in python. The files with the related python code are in the sub-folder “(4) What everybody...(13) Python code for radial scan patterns”.

Second, there are models of the saddle specimen in the folder *Saddle*, again containing subroutines defining a radial scan pattern at both spot sizes, as well as a thermal and mechanical part. Only a quarter of the saddle is modeled due to symmetry. The paths were again defined and drawn in python and can be found in the same place.

Third, the folder *Bowl Circular* contains a “complete” (no symmetries) model of the bowl, and a subroutine file that defines the circular scans. The folder again contains a thermal part, as

well as five mechanical parts. There are five parts because the simulation took five times 48 hours to complete, due to the CPU intensity of the model.

Miscellaneous

There are detailed instructions on how to create a sandwich panel model in the file *Instruction on How to Create a Sandwich Panel Model.docx* in the folder “\3) Numerical Models”. Using this guide, you will be able to re-create any model that I mentioned previously. The folder “\3) Numerical Models\4-Point Bending” contains a 4-point bending simulation of metal foam (no facesheets), which I used in chapter 3 to explain the bending mechanism. The folder “\3) Numerical Models\Scribing” contains a laser scribing model that I used while briefly working on the topic with Grant.

All my papers may be found in the folder “\5) Papers”.

Any remaining thing that you possibly need to know is in the folder “\4) What everybody should’ve done but didn’t do”, which again contains many subfolders. The sub-folder “\4)...\1) Micro Epsilon IR Camera” contains operation instructions, all the quotes, manuals, and specifications for the filter that was used for the CO₂ laser in chapters 4 & 5. The sub-folder “\4)...\2) DIC Procedure” contains DIC manuals and a brief instruction on how to go about DIC in general. The sub-folder “\4)...\3) XSEDE application & procedure” contains instructions on how to run models on the XSEDE supercomputer (regular jobs, restart, append step, etc.), as well as my startup and research requests. The sub-folder “\4)...\4) All issues I ever had with equipment” goes through all the problems I have ever encounter with lab equipment, and how they were solved. The sub-folder “\4)...\5) Matlab code to create voxel model” contains all the matlab files that I used to convert the micro-CT data cloud into a voxel model. The folder also contains detailed instructions of the code, which I used in chapters 2 and

5. The sub-folder “\4...\6 Matlab code to calculate moment of area” contains the Matlab code that took digital images and calculated the moment of area of a cross-section. I used this technique in chapters 3-5. The folder again contains detailed instructions of the Matlab code. The sub-folder “\4...\7 Calculating densification” contains the Matlab code that I used to create densification plots in chapters 3 & 4. The code uses displacement and strain data and computes the densification, as explained in the word document in the folder. The sub-folder “\4...\8 Machining & Preparing specimens” contains any information pertaining machining and preparing foam specimens of chapters 3 & 4. The sub-folder “\4...\9 Polishing & Photography” contains some instructions about polishing and photography techniques that I used. The sub-folder “\4...\10 Staubli Robot Programs” contains an example program for the Staubli robot, for the likely case where the memory of the robot and the laptop are wiped out at the same time. The sub-folder “\4...\11 Material Properties” contain all the material properties used in all simulations. The sub-folder “\4...\12 5th paper – ICALEO Version” contains my 5th paper in the ICALEO format. Finally, the sub-folder “\4...\13 Python code for radial scan pattern” contains python code with which the radial scan patterns of chapter 6 were defined and drawn (involves turtle graphics).

Publications under Candidature

- [1] **Bucher, T.**, Bolger, C., Zhang, M., Chen, C., Yao, Y.L., "Effect of Geometrical Modeling on the Prediction of Laser-Induced Heat Transfer in Metal Foam," ASME Trans. J. of Manufacturing Science and Engineering, **138**(12), 2016. (also presented at NAMRC conference)
- [2] **Bucher, T.**, Young, A., Zhang, M., Chen, C., Yao, Y.L., "Laser Induced Mechanical Response of Metal Foam During Laser Forming," ASME Trans. J. of Manufacturing Science and Engineering, **140**(4), 2018. (also presented at MSEC conference)
- [3] **Bucher, T.**, Cardenas, S., Verma, R., Li, W., and Yao, Y.L., "Laser Forming of Sandwich Panels with Metal Foam Cores," ASME Trans. J. of Manufacturing Science and Engineering, 2018, (accepted, also presented at ICALEO conference)
- [4] **Bucher, T.**, Zhang, M., Chen, C. Verma, R., Li, W., and Yao, Y.L., "Laser Forming of Metal Foam Sandwich Panels: Effect of Manufacturing Method," ASME Trans. J. of Manufacturing Science and Engineering, 2018, (under review)
- [5] **Bucher, T.**, and Yao, Y.L., "Advances in Laser Forming of Metal Foams: Mechanism, Prediction and Comparison," Int. J. of Mechatronics and Manufacturing Systems, 11(2/3), 2018, pp. 250-273.
- [6] **Bucher, T.**, Finn, C., Verma, R., Li, W., and Yao, Y.L., "3D Laser Forming of Metal Foam Sandwich Panels," ASME Trans. J. of Manufacturing Science and Engineering, 2018, (under review)
- [7] **Bucher, T.**, Brandal, G., Chen, H., Yao, Y.L., "Quantifying the Heat Affected Zone in Laser Scribing of Thin Film," Manufacturing Letters, Elsevier, 13, 2017, pp.11-14.
- [8] Bian, D., **Bucher, T.**, Shim, D.J., Jones, M., Yao, Y.L., "Effect of Deep Penetration of Interleaf on Delamination Resistance in GFRP," ASME Trans. J. of Manufacturing Science and Engineering, 138(7), 2016.
- [9] Brandal, G., **Bucher, T.**, Chen, H., and Yao, Y.L., "Shunt Loss and Thermally Induced Material Changes in Laser Scribing of Thin Film Solar Cells," Proceedings of the ICALEO '16, 2016, San Diego, CA.